CHARLES UNIVERSITY

Faculty of Science

Developmental and Cell Biology

Petra Novotná

The role of plectin deficiency in experimental colitis and colorectal cancer

Doctoral Thesis

Supervisor: RNDr. Martin Gregor, Ph.D.

Prague, 2024

DECLARATION

I hereby declare that I wrote this work independently and that I acknowledged all people involved in the production of this work and referenced the relevant literature. I did not use this work or its substantial part to obtain different academic degree.

Prague, 20th June 2024 Petra Novotná

ACKNOWLEDGEMENT

I would like to express my gratitude to my supervisor, RNDr. Martin Gregor, Ph.D., for his invaluable help, guidance, and advice throughout my Ph.D. studies. I am grateful to Mgr. Alžběta Kalendová, Ph.D., for her tireless energy and supervision. I would like to thank Miloslava Maninová, Ph.D. for her extensive work on our joint project. I highly appreciate the cooperation with Doc. MUDr. MVDr. Jozef Škarda, Ph.D., PhD., who helped us with the histopathological evaluation of our mouse model. I would also like to express my sincere gratitude to my partner for putting up with my unstable moods and to my friends and family for all the support and encouragement. Finally, I would like to thank the Department of Developmental and Cell Biology at Charles University for the scholarship that allowed me to complete this thesis.

Table of Contents

List of abbreviations

AA	acrylamide
ABD	actin-binding domain
AJ	adherens junction
AOM	azoxymethane
AP-1	activator protein 1
APC	adenomatous polyposis coli
ATB	antibiotics
BA	bisacrylamide
BM	basement membrane
BPAG	bullous pemphigoid antigen
BrdU	5-bromo-2'-deoxyuridine
BSA	bovine serum albumin
BVES	blood vessel epicardial substance
CA-CRC	colitis-associated colorectal cancer
CAR	coxsackie virus-adenovirus receptor
CBC cells	crypt base columnar cells
CD	Crohn's disease
CEC	colon explant cultures
ChgA	chromogranin A
Coll	collagen
CRC	colorectal cancer
Crubs-3	crumbs homologue 3
D	desmosome
DAB	3,3'-diaminobenzidine
DAI	disease activity index
DEG	differentially expressed gene
dH_2O	distilled water
DMEM	Dulbecco's modified Eagle medium
DSB	double-strand break
Dsp	desmoplakin
Dsg	desmoglein
DSS	dextran sodium sulphate
E-cad	E-cadherin
ECM	extracellular matrix
EEC	enteroendocrine cell
ERK	extracellular signal-regulated kinase
FA	focal adhesion
FACS	fluorescent activated cell sorting
F-actin	filamentous actin
FAK	focal adhesion kinase
FBS	fetal bovine serum
FDR	false discovery rate
FITC	fluorescein isothiocyanate
FN	fibronectin
GC	goblet cell
GO	gene ontology

GSEA	gene set enrichment analysis
H&E	haematoxylin-eosin
HD	hemidesmosome
HDAC3	histone deacetylase 3
HNPCC	hereditary non-polyposis colon cancer
HRP	horseradish peroxidase
HSE	high-salt extract
IBD	Inflammatory bowel disease
IEB	intestinal epithelial barrier
IEC	intestinal epithelial cells
IF	intermediate filament
IFBD	intermediate filament-binding domain
IHC	immunohistochemistry
IL	interleukin
ILK	integrin linked kinase
Itg	integrin
IQ	2-amino-3-methylimidazo[4,5-f]quinoline
JAM	junctional adhesion molecules
JNK	c-Jun N-terminal kinase
KASH	Klarsicht, ANC-1, and Syne homology
KEGG	kyoto encyclopedia of genes and genomes
KF	keratin filament
KO	knock-out
LINC	linkers of nucleoskeleton and cytoskeleton
LMN	lamin
LFC	log2FoldChange
M cells	microfold cells
Min	multiple intestinal neoplasia
MLCK1	myosin light chain kinase 1
MPO	myeloperoxidase
MRTF A	transcription factor A
MT	microtubules
MUC2	mucin 2
NF-κB	nuclear factor κB
NFR	nuclear fast red
MPO	myeloperoxidase
Nrf2	nuclear factor erythroid 2-related factor 2
ORA	over-representation analysis
OUT	Operational taxonomic unit
PAA	polyacrylamide
PALS1	protein associated with Lin-7 1
PARD3/6	partitioning defective 3/6 homologs
PAS	periodic acid Shiff
PC	paneth cell
PCoA	Principle Coordinate Analysis
PD	plakin domain
PDMS	polydimethylsiloxane

PFA	paraformaldehyde
PhIP	2-amino-1-methyl-6-phenylimidazo [4,5-b] pyridine
PI	propidium iodide
PI3K	phosphoinositide 3-kinases
PINCH	particularly interesting new cysteine-histidine-rich protein
PKB (Akt)	protein kinase B
PLEKHA7	PH domain-containing family A member 7
PM	plasma membrane
PRD	plectin repeat domain
SRA	Sequence Read Archive
PST	Plecstatin-1
qRT-PCR	quantitative reverse transcriptase polymerase chain reaction
RNA seq	RNA sequencing
SC	stem cell
SH3	Src homology 3
SI	small intestine
SR	sirius red
SRF	serum response factor
SUN	Sad1p, UNC-84
TA cells	transit-amplifying cells
TAZ	transcriptional coactivator with PDZ-binding motif
TEER	transepithelial electrical resistance
TEM	transmission electron microscopy
TJ	tight junction
TMX	tamoxifen
TNBS	2, 4, 6 - trinitrobenzensulfonic acid
TNFα	tumor necrosis factor α
TUNEL	terminal deoxynucleotidyl transferase dUTP nick end labeling
UC	ulcerative colitis
VASP	vasodilator-stimulated phosphoprotein
VF	vimentin intermediate filaments
Vim	vimentin
WBI	whole-body imaging
WT	wild-type
YAP	Yes-associated protein
ZO	zonula occludens

Abstract (in English)

Colorectal cancer (CRC) is one of the most prevalent cancer types. Patients suffering from inflammatory bowel disease (IBD) have an increased risk of CRC development. IBD is manifested by extensive intestinal inflammation, associated with perturbations in the intestinal epithelial barrier (IEB). Functional IEB relies on intestinal epithelial cells (IECs) and its integrity is dependent on cellular cohesion secured by cell-cell junctions such as adherens junctions (AJs) and desmosomes (Ds). IECs thus form epithelial sheets, which are integrated into a structural and functional continuum with subjacent dense extracellular matrix (ECM), also called basement membrane (BM), through cell-ECM adhesions called hemidesmosomes (HDs). The formation of functional Ds and HDs relies on the association of their transmembrane constituents with keratin filaments (KFs). Anchorage of KFs to junctions is mediated by plectin, a versatile cytolinker protein that integrates intermediate filaments (IFs) with cellular junctions and other cell structures, including the nucleus, thus providing mechanical stability to cells and tissues. Although mutations in plectin have previously been shown to negatively impact the integrity of skin tissue, its precise function in intestinal homeostasis has not been documented. Using a mouse model carrying constitutive ($Ple^{\Delta IEC}$) or inducible ($Ple^{\Delta IEC\text{-}ERT2}$) IEC-specific plectin deletion, we characterized the role of plectin in cytoskeletal architecture of IECs and IEB homeostasis. Moreover, our data reveal higher propensity of $Ple^{\Delta IEC}$ mice for development of colitis and colitis-associated CRC (CA-CRC). We also determined how altered cytoarchitecture impacts colorectal carcinogenesis and how mechanical forces threaten genome integrity, driving the oncogenic potential of plectin-deficient cells.

Our results reveal that plectin expression negatively correlates with the severity of inflammation in ulcerative colitis (UC) patients. $Ple^{\Delta IEC}$ mice spontaneously develop colitis characterized by extensive detachment of IECs from the BM, increased intestinal permeability, hyperproliferation, and inflammatory lesions. Such compromised epithelial barrier integrity, coupled with chronic inflammation, promotes spontaneous CRC development in $Ple^{\Delta IEC}$ mice. Mechanistically, plectin deficiency leads to disorganized KF networks, dysfunctional HDs, and intercellular junctions. Strikingly, expression profiling of UC patients reveals significant downregulation of plectin, KFs, and components of associated junctions. Consistent with these findings, plectin knock-out (KO) Caco-2/RPE cells exhibit reduced mechanical stability and

adhesion capacity. Spontaneous carcinogenesis in *Ple*$^{\Delta IEC}$ mice is associated with increased susceptibility to DNA damage. In cell monolayers, plectin deletion is associated with delayed adaptation to mechanical stress, resulting in increased nuclear deformability, DNA damage, and chromosomal instability, which together increases susceptibility to oncogenic transformation. Plectin-controlled architecture thus protects the genome from damage induced by mechanical stress.

Our study demonstrates that plectin-controlled cytoarchitecture is essential for maintaining the mechanical homeostasis of IECs, thereby protecting intestinal epithelia against DNA damage and carcinogenesis.

Abstrakt (v češtině)

Kolorektální karcinom (CRC) je jedním z nejčastějších typů nádoru. Pacienti trpící zánětlivým onemocněním střev (IBD) mají zvýšené riziko vzniku kolorektálního karcinomu. IBD se projevuje rozsáhlým zánětem střev, který je spojován s narušením střevní epitelové bariéry (IEB). Funkční IEB je tvořena střevními epitelovými buňkami (IECs) a její integrita závisí především na buněčné soudržnosti, kterou zajišťují mezibuněčné spoje, jako jsou adhezní spoje (AJs) a desmosomy (Ds). IECs takto tvoří epitelové vrstvy, které jsou začleněny do strukturálního a funkčního kontinua spolu se spodní hustou extracelulární matrix (ECM), také nazývanou bazální membránou (BM), pomocí buněčných spojů propojujících buňky s ECM, nazývanými hemidesmosomy (HDs). Tvorba funkčních Ds a HDs závisí na spojení jejich membránových složek se sítí keratinových filament (KF). Upevnění KFs do buněčných spojů je umožněno plectinem, mnohostranným vazebným proteinem, který propojuje buněčné spoje s intermediálními filament (IFs) a s různými buněčnými strukturami, včetně jádra, čímž poskytuje buňkám a tkáním mechanickou stabilitu. Ačkoliv bylo dříve ukázáno, že mutace v plectinu negativně ovlivňují integritu kožní tkáně, jeho přesná funkce ve střevní homeostáze dosud nebyla zdokumentována. Použitím myšího modelu nesoucího konstitutivní (*Ple*$^{\Delta IEC}$) nebo indukovatelnou (*Ple*$^{\Delta IEC\text{-}ERT2}$) IEC-specifickou deleci plectinu, jsme popsali roli plectinu na architekturu cytoskeletu IECs a na homeostázu IEB. Navíc, naše data odhalila vyšší náchylnost *Ple*$^{\Delta IEC}$ myší pro vývoj kolitidy a s kolitidou-asociovaným CRC (CA-CRC). Také jsme zjistili, jak změněná buněčná architektura ovlivňuje kolorektální karcinogenezi a jak mechanické síly ohrožují integritu genomu, vedoucí k onkogennímu potenciálu u buněk s delecí plectinu.

Naše výsledky ukazují, že exprese plectinu negativně koreluje se závažností zánětu u pacientů s ulcerózní kolitidou (UC). *Ple*$^{\Delta IEC}$ myši spontánně vyvíjejí kolitidu, která se vyznačuje rozsáhlým oddělením IEC od BM, zvýšenou střevní propustností, nadměrnou proliferací a výskytem zánětlivých ložisek. Toto narušení integrity epiteliální bariéry, spolu s chronickým zánětem, podporuje spontánní vývoj kolorektálního karcinomu u myší s delecí plectinu. Mechanisticky vede absence plectinu k dezorganizaci KF sítí, dysfunkčním HDs a mezibuněčným spojům. Pozoruhodně, podrobná analýza u pacientů s UC ukázala významné snížení exprese plectinu, KFs a komponent asociovaných s mezibuněnčnými spoji. V souladu s těmito zjištěními, Caco-2/RPE buňky s delecí plectinu (KO) vykazují sníženou mechanickou stabilitu a kapacitu adheze. Spontánní karcinogeneze u *Ple*$^{\Delta IEC}$ myší je spojena se zvýšenou

náchylností k poškození DNA. V buněčných kulturách je delece plectinu spojena se zpožděnou adaptací na mechanický stres, což vede ke zvýšené deformovatelnosti jádra, poškození DNA a chromozomální nestabilitě, která dále zvyšuje náchylnost buněk k onkogenní transformaci. Plectinem řízená architektura tedy chrání genom před poškozením způsobeným mechanickým stresem.

Naše studie ukazuje, že cytoskeletální architektura zprostředkovaná plectinem je nezbytná pro udržení mechanické homeostázy střevního epitelu, a tím chrání střevní epitel proti poškození DNA a karcinogenezi.

1 Introduction

1.1 Intestinal tract

The intestine is the longest part of the digestive system. In mammals, the intestine is divided into the small intestine (SI) and the large intestine, also known as colon. The SI, approximately 7 meters long in humans (40 cm in mice), is responsible for most digestive and secretory functions and nutrient absorption. In contrast, the colon is about 1.5 meters in humans (10 cm in mice) and ensures water, vitamins, and minerals absorption [reviewed in (Azzouz and Sharma, 2024; Houtekamer et al., 2022; Kiela and Ghishan, 2016)]. The SI consists of three parts: duodenum, jejunum, and ileum, while in the colon are distinguishible proximal and distal parts. As the digestive tract reaches its terminus, the colon transitions into the rectum and anus. The intestinal wall consists of four layers (Figure 1): mucosa consists of the epithelium, which comprises various cell types, the *lamina propria* composed of connective tissue, and the *muscularis mucosae*, a layer of smooth muscle. Submucosa is a layer of connective tissue formed by blood, neural, and lymphatic systems. Muscularis propria consists of inner circular and outer longitudinal layers of smooth muscle. Alongside the enteric nervous system, known as Auerbach's plexus, the muscularis propria orchestrates coordinated contractions, termed peristalsis. To withstand the mechanical strain from the passage of feces, the longitudinal muscle layer of the colon features three distinct longitudinal bands known as *the teniae coli*. Serosa or adventitia envelops the intestinal tube with a layer of connective tissue and mucus, protecting adjacent organs against mechanical harm resulting from the movements of the intestinal wall during digestion [reviewed in (Fish et al., 2024)].

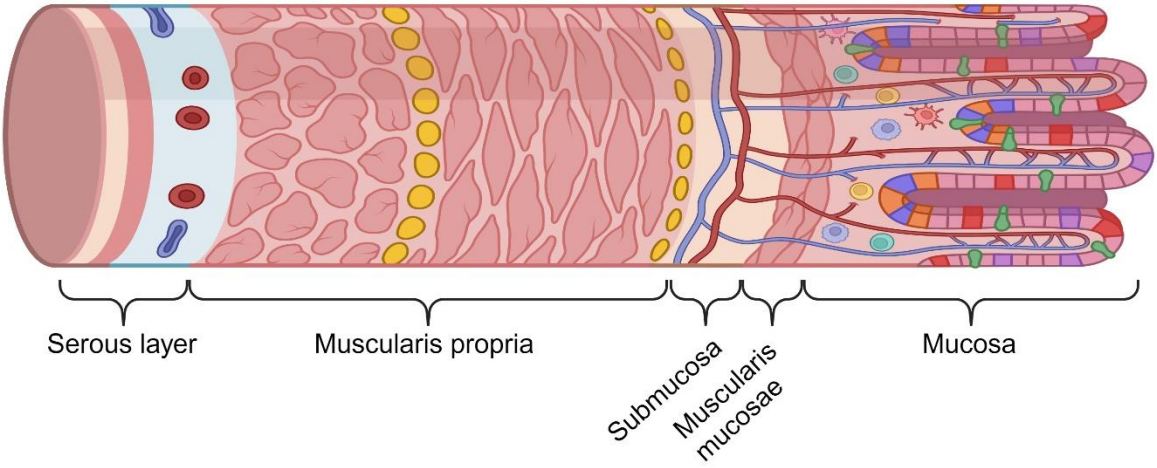

Figure 1 Architecture of the intestinal wall. The intestinal wall is composed of four layers: mucosa, submucosa, muscularis propria and serosa.

1.1.1 Intestinal epithelium

The distinct functions of the SI and colon are reflected in the epithelial structure of these organs. The mucosa of the SI forms protrusive structures called *plicae circularis* and villi, which increase the surface area for absorption. Glands known as crypts of Lieberkühn invaginate the underlying ECM in the SI. Conversely, the mucosa of the colon consists solely of crypts [Figure 2; reviewed in (Clevers, 2013)].

Figure 2 Histological compartmentalization of small intestine (SI) and colon. (A,B) The SI epithelium is structured into plicae circularis (A); scale bar 1mm**;** adopted from (AMBOSS, 2023) consisting of multiple finger-like projections villi and invaginations crypts of Lieberkühn (B). **(C)** The colonic epithelium if formed solely by crypts. Scale bar 100 µm.

The intestinal epithelium is formed by a single layer of columnar epithelial cells (Figure 3). There are 3 types of columnar epithelial cells: stem cells, transit-amplifying (TA), and differentiated cells. The intestinal environment poses significant challenges to epithelial cells, particularly to those, which are facing harmful mechanical and toxic luminal content [reviewed in (Watson and Hughes, 2012)]. Therefore, continuous renewal of epithelial cells is necessary

to maintain the integrity of the intestinal barrier. During the process of epithelial renewal, damaged/apoptotic epithelial cells are extruded from the villi tip/luminal area of crypts via intricate cytoskeletal remodeling, concurrently sealing the gap to preserve barrier integrity [reviewed in (Watson and Hughes, 2012)]. The intestinal crypt must produce millions of new epithelial cells daily to counterbalance the substantial cell loss. Regeneration primarily occurs at the crypt base, where adult stem cells divide regularly, yielding highly proliferative progenitor cells. These cells further undergo 2-3 divisions and differentiate as they ascend towards the villus base. Proliferation halts upon exit from the crypt as fully differentiated epithelial cells continue their upward migration. It takes 3 to 5 days to renew the entire crypt/villus.

1.1.1.1 Stem cells

As has been stated above, the crypt renewal process is enabled by crypt base columnar cells (CBCs), which serve as stem cells (SCs; Figure 3). These CBCs are characterized by their constant cycling, persistent throughout an individual's lifespan, and possession of the ability to self-renew, giving rise to all intestinal cell populations (Barker et al., 2007; Cheng and Leblond, 1974).

In addition to CBCs, another type of SCs known as +4 stem cells (Figure 3) has been identified. These +4 stem cells are situated at position 4, above the population of CBCs (Potten and Loeffler, 1990; Takeda et al., 2011). +4 cells share key marker genes with CBCs, indicating stem cell properties (Munoz et al., 2012). On the other hand, following an intestinal injury, the sensitive population of CBCs is eliminated, while the resistant +4 stem cells serve as a resilient source of epithelial regeneration and take over the role of the main pool of SCs (Metcalfe et al., 2014; Yan et al., 2012).

1.1.1.2 Proliferative cells

The intestinal epithelium undergoes rapid turnover, with a cell having a lifespan of 3-5 days. When SCs divide, they give rise to a population of TA cells (Figure 3). TA cells possess the ability to proliferate and eventually differentiate into specific cell types. During this process,

cells migrate upwards along the crypt-villus (SI) or crypt (colon), where they eventually undergo anoikis and are shed into the lumen [reviewed in (Gehart and Clevers, 2019)].

1.1.1.3 Differentiated cells

Based on their properties, mature differentiated cells are classified as either absorptive or secretory (Figure 3):

Absorptive lineage. Enterocytes and colonocytes represent the predominant differentiated cells in small and large intestines, respectively. These cells feature microvillar structures on their apical surfaces, collectively forming brush borders. These brush borders enlarge the surface area of these cells, facilitating absorption processes [(Cheng and Leblond, 1974); reviewed in (Snoeck et al., 2005)]. Microfold (M) cells are a type of immune cell characterized by their morphology resembling the letter “M”. Unlike other intestinal cell types, M cells typically lack or have shortened microvilli on their apical surface and possess unique pocket-like invaginations at the basal side. Their primary role involves antigen sampling: M cells capture antigens and microorganisms from the intestinal lumen and facilitate interaction with the underlying mucosal immune system, thereby facilitating immune responses. Due to their function, M cells are often located in follicle-associated epithelium near lymphoid follicles, such as Peyer’s patches in the small intestine, as part of the gut-associated lymphoid tissue [reviewed in (Jung et al., 2010; Mabbott et al., 2013; Ohno, 2016)].

Secretory lineage. The intestinal tract harbors a vast population of bacteria (Gu et al., 2013; Yuan et al., 2020). Paneth cells (PCs) play a crucial role as the primary producers of antimicrobial and immune molecules, aiding in the regulation of immune homeostasis and defending the intact intestinal epithelium against pathogenic invasion [(Wilson et al., 1999); reviewed in (Porter et al., 2002)]. Located within the crypts of the small intestine, PCs are intermingled with CBCs, which also contribute to stem cell homeostasis (Sato et al., 2011). In addition to PCs, another key player in antimicrobial protection are the Goblet cells (GCs). Unlike PCs, GCs are distributed throughout the epithelium of both the small and large intestines and are scattered along the entire crypt-villus or crypt axis. These cup-shaped cells are characterized by their large apical vacuoles filled with mucin glycoprotein granules (Zhou et al., 2020). Upon secretion, these mucin glycoproteins form a protective mucus layer

separating the epithelium from mechanical challenge and microbial agents. Recent studies indicate that GCs also participate in goblet cell-associated antigen passages, contributing to immune response homeostasis by transporting antigens from the lumen to underlying immune cells (Knoop et al., 2017a; Knoop et al., 2017b). Enteroendocrine cells (EECs) constitute less than 1% of the intestinal epithelium yet are the most abundant hormone-expressing cells in mammals. These chemosensory cells are distributed throughout the gastrointestinal tract [reviewed in (Gribble and Reimann, 2017; Worthington et al., 2018)]. Depending on the luminal content they sense, EECs secrete various hormones, cytokines, or neurotransmitters, thereby regulating physiological processes such as appetite, digestion, gut motility, and mucosal immunity [reviewed in (Gribble and Reimann, 2016; Yu et al., 2020)]. Tuft cells are dispersed throughout various organs, including the gastrointestinal tract. Upon encountering protists, helminths, bacteria, and viral infections, tuft cells release immunomodulatory molecules and play a role in regulating the immune response (Drurey et al., 2022; Howitt et al., 2016; Wilen et al., 2018; Xiong et al., 2022).

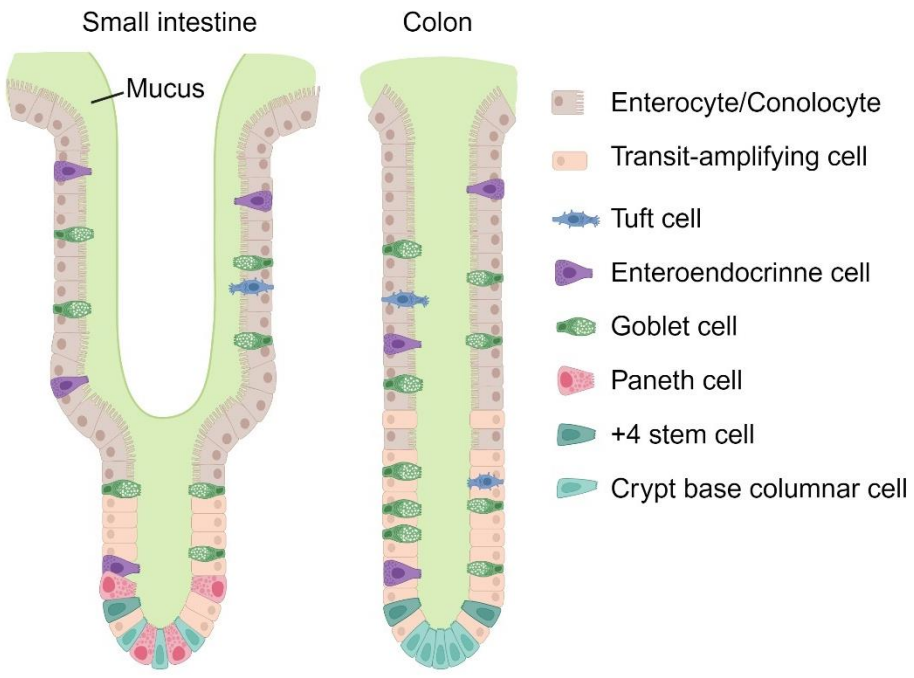

Figure 3 Epithelial cell types of SI and colon. The intestinal epithelium consists of multiple types of cell populations. The base of each crypt is occupied by crypt base columnar and +4 stem cells, which in the small intestine are interwoven by Paneth cells. The majority of the intestinal crypt is populated by transit-amplifying cells, which further give rise to differentiated cell types (Paneth cells, Goblet cells, Enteroendocrine cells, Tuft cells, and Enterocytes/Colonocytes) .

1.1.1.4 Barrier homeostasis

In various organs, specialized epithelial cells are of critical importance in forming protective barriers that separate organisms from the external environment. In the gastrointestinal tract, a vast population of commensal bacteria, known as the microbiome, resides within the intestinal lumen. Under normal conditions, these bacteria aid in developing the intestinal structure, provide essential nutrients to the host, facilitate digestion, and bolster the host's defense against pathogenic bacteria. Furthermore, the microbiome has been demonstrated to stimulate the immune system (Mazmanian et al., 2005). However, commensal bacteria, as well as various pathogens, represent a threat to the internal tissue. The intestinal barrier, therefore, ensures the physical segregation of luminal content, thus reducing the risk of infection and inflammation. There are three components essential for the integrity of the intestinal barrier. The epithelium strictly depends on a tightly sealed monolayer of IECs, which form the physical barrier. It maintains two important functions. First, to uphold the integrity of the barrier, thus restricting the entry of pathogens and toxins, and second, to permit the selective passage of vital nutrients and water into the tissue. This selective permeability is enabled by tight junctions [TJ; reviewed in (Suzuki, 2013)]. Junctional complexes are discussed in more detail (Chapters 1.2.3, 1.2.4).

Covering the epithelia, an additional protection in the form of a mucus layer is present. This hydrated gel is primarily composed of mucin glycoproteins produced by GCs and acts as the initial defense against luminal microorganisms. It physically separates the intestinal lumen from the epithelium, restricting microbiota access to the epithelial surface [reviewed in (Cornick et al., 2015)]. Furthermore, IgA antibodies can bind to mucus, thus facilitating bacterial attachment. The mucus comprises two layers, with the inner layer typically devoid of bacteria and the outer layer, where bacteria are highly abundant (Johansson et al., 2008). Mice lacking mucin 2 (MUC2) display a reduced inner mucus layer, leading to direct contact between microbiota and the epithelium. This contributes to the development of spontaneous colonic inflammation, known as colitis (Van der Sluis et al., 2006).

Important guardians of the intestinal barrier are immune cells, such as tuft cells and M cells, which interconnect the outer environment with the underlying immune system of the tissue. The maintenance of intestinal homeostasis depends on the delicate balance of

all - mucus, epithelial cells, and cells of the intestinal immune system. The altered function of any of these factors predisposes the development of gastrointestinal diseases.

1.2 Mechanical resilience of intestinal epithelium

Mechanical forces play a pivotal role in the functioning of nearly all biological systems. The early development, morphogenesis, and differentiation of cells are intimately connected to the sensing of physical forces within the external microenvironment [reviewed in (Mammoto and Ingber, 2010; Stooke-Vaughan and Campas, 2018)]. Cells perceive mechanical forces from the surrounding environment, including the stiffness of the underlying ECM, shear stress, stretch, and compression. Individual epithelial cells can transmit these forces via a process called mechanotransduction and generate intrinsic mechanical forces, for example, through actomyosin contractility. This may coordinate cell shape, proliferation, or motility and eventually orchestrate the tissue architecture [reviewed in (Houtekamer et al., 2022; Iskratsch et al., 2014; Murrell et al., 2015)]. With respect to the epithelial architecture of the intestine, it is essential that forces generated by the epithelium itself are maintained to ensure a proper balance in cell proliferation, maturation, crowding, and extrusion (Eisenhoffer et al., 2012).

The intestinal epithelium and intestinal tract experience and further propagate physical stress relevant to its inherent function – digestion. Food consumption induces shear forces on the epithelial surface as food particles move through the lumen. Additionally, it enhances peristaltic smooth muscle contractions, causing mechanical distention and compression of the intestinal wall [reviewed in (Beyder, 2018)]. The intestine's capacity to sense and react to these mechanical signals is essential for regulating digestive functions, such as promoting peristaltic contractions and triggering the secretion of mucus and hormones [reviewed in (Alcaino et al., 2017; Joshi et al., 2021)].

1.2.1 **Cytoskeleton**

The cytoskeleton is a structural framework that maintains cellular shape and mediates its resilience to mechanical deformation. Given the physically demanding environment, epithelial cells require robust and intact cytoskeletal support to withstand mechanical stress. The cytoskeleton comprises three major components: actin microfilaments, IFs, and

microtubules (MTs; Figure 4). Actin is one of the most abundantly expressed proteins in many cells. The vertebrate genome encodes three different isoforms: α-actin (encoded by three genes, in muscle cells), β-actin (one gene, in non-muscle cells), and γ-actin [two genes, one in smooth muscle cells, second in non-smooth muscle cells; (Hanson and Lowy, 1963); reviewed in (Dominguez and Holmes, 2011; Pollard, 2016)]. Actin undergoes reversible polymerization to form a dynamic network of polar filaments of 6 nm in diameter, which is rigorously regulated by various actin-binding proteins [reviewed in (Buracco et al., 2019; Dominguez, 2009; Pollard, 2016)]. The formation of prominent actin filament bundles is essential for the creation of various cellular structures, including intercellular junctions and apical microvilli in differentiated epithelial cell monolayers, cell-matrix adhesions in migrating cells, and the cleavage furrow in dividing cells [reviewed in (Braga, 2016; Crawley et al., 2014; Dekraker et al., 2018; Rothenberg and Fernandez-Gonzalez, 2019)]. It has been demonstrated that intestinal-specific dysfunction of β-actin in mice results in increased intestinal barrier permeability and enhanced susceptibility to mucosal inflammation (Lechuga et al., 2020). This observation documents that actin cytoskeleton plays an essential role in intestinal epithelial homeostasis maintenance.

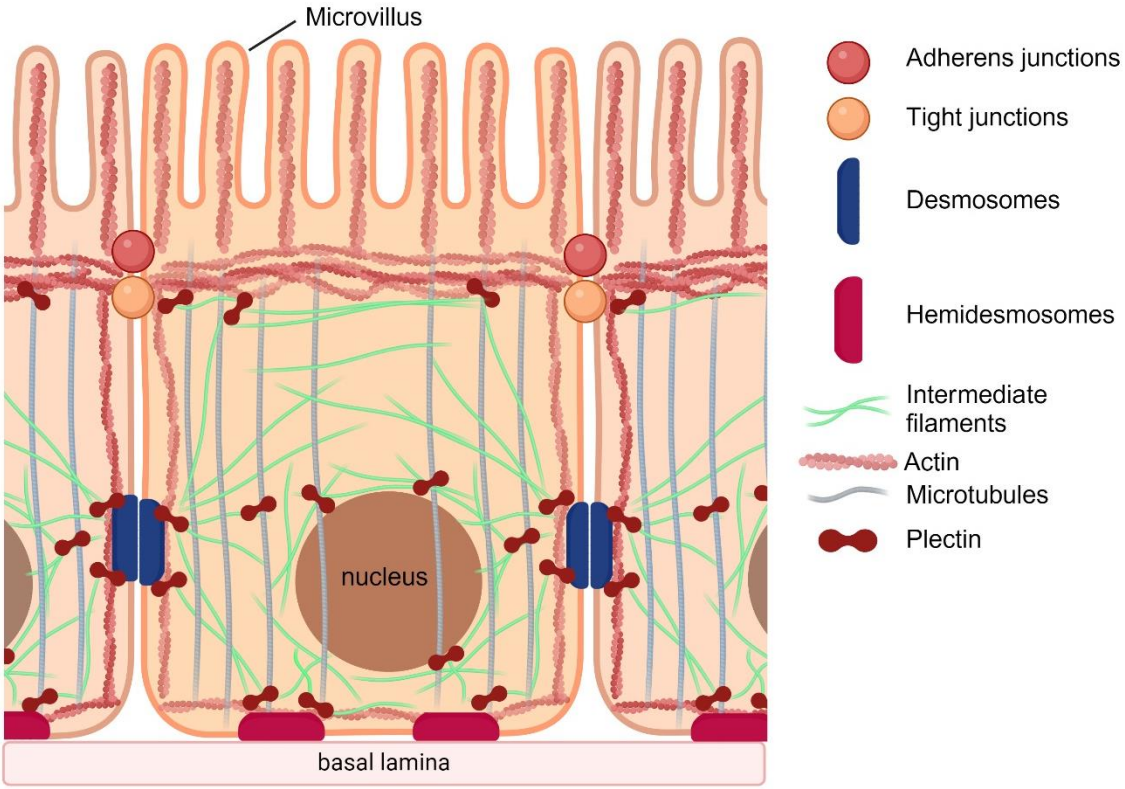

Figure 4 Architecture of intestinal epithelial cells (IECs). Simplified illustration of cytoskeletal crosstalk in intestinal epithelial cells. Via junctional complexes, cells are interconnected to their adjacent neighboring cells and to the subjacent extracellular matrix [ECM; modified from (Prechova et al., 2023)].

MTs are 15 nm thick polar fibers composed of α- and β-tubulin subunits (Nogales et al., 1998). Similar to actin filaments, MTs are dynamic structures experiencing continuous assembly and disassembly within the cell. In mammals, α- and β-tubulins are encoded by two different genes. They play a role in cell shape maintenance and are involved in cell motility, intracellular organelle transport, and chromosomal segregation during mitosis [(Goldman, 1971; Kaverina et al., 2000); reviewed in (Barlan and Gelfand, 2017; Maiato et al., 2004)]. Additionally, a third member, γ-tubulin, is encoded by a unique gene. The function of γ-tubulin is restricted to mitosis, where it localizes to centrosomes and forms the center of the mitotic spindle [reviewed in (Ikeda et al., 2010)].

IFs are fibers of 10 nm in diameter (Small and Sobieszek, 1977). IFs can be formed by a wide range of proteins, which are characterized by highly conserved structural and biochemical features that dictate their assembly into homo/hetero-polymers. The human genome contains 70 genes encoding all types of IFs. Although IFs are a diverse group of nonpolar filaments, they share a central α-helical rod domain flanked by nonhelical “head” and “tail” domains. Based on amino acid composition, protein structure, and tissue distribution, mammalian IFs are categorized into six groups (Szeverenyi et al., 2008).

The most abundant - type I (acidic) and type II (basic) IFs are keratins, which are encoded by 54 functional genes and predominantly expressed by epithelial cells [(Szeverenyi et al., 2008); reviewed in (Schweizer et al., 2007)]. Type I (K9-28 and K31-40) and type II (K1-8 and K71-80) keratins copolymerize and form heterodimers. While IFs type I are typical trichocytic keratins expressed in hair, nails, and horns, type II keratins are essential for epithelial cells [reviewed in (Jacob et al., 2018)].

Type III IFs consist of vimentin, expressed mainly by mesenchymal cells, leukocytes, smooth muscle, and endothelial cells; desmin, glial fibrillary acidic protein, and perinephrin found in muscle, glial, and peripheral neural cells [reviewed in (Strouhalova et al., 2020; Viedma-Poyatos et al., 2020)].

Type IV IFs constitute neurofilament proteins, including nestin, synemin, α-internexin, and syncoilin [(Luna et al., 2010; Yuan et al., 2006); reviewed in (Moorwood, 2008)].

Type V IFs represent a family of nuclear proteins, lamins. While other components of IFs are cytoplasmic proteins, lamins are found beneath and support the nuclear envelope in

all nucleated cells. Lamins can be classified into two groups: A-type lamins, encoded by a single gene which gives rise to two isoforms [lamin A and C; LMNA/C; (Lin and Worman, 1993)], and B-type lamins, containing lamin B1 and B2 (LMNB1/2) encoded by two different genes (Peter et al., 1989).

1.2.2 **Function of keratin and vimentin intermediate filaments**

In the digestive tract, the KFs include simple epithelial (single-layered) keratins, such as K7, K8, K18, K19, K20, and K23 [reviewed in (Omary et al., 2009)]. Similar to other IFs, these simple epithelial keratins exhibit specific expression patterns within the intestinal epithelium. For instance, K20 is predominantly present in the terminally differentiated cells.

Increased expression of keratins has been observed as a response to oxidative stress in the liver, exposure to toxins in the intestinal cells, stimulation by interleukin (IL)-6 in the intestine, intestinal injury, and during regenerative repair in the pancreas (Guldiken et al., 2016; Helenius et al., 2016; Wang et al., 2007a; Zhong et al., 2004). These findings document the protective role of KFs against various types of stress. Furthermore, mutation of *Krt5* or *Krt14* genes causes epidermolysis bullosa simplex, an inherited skin disorder characterized by enormous fragility of epidermal cells. This manifests as skin and mucous membrane blistering in response to mild mechanical injury or heat (Jerabkova et al., 2010). Similarly, mutation or deletion of *Krt18* gene in hepatocytes results in remarkable tissue fragility during isolation through liver perfusion (Ku et al., 1995; Loranger et al., 1997). These studies thus identified the keratin cytoskeletal network as one of the main contributors to mechanical homeostasis [reviewed in (Broussard et al., 2020)].

Furthermore, IFs serve as pivotal scaffolding proteins capable of binding diverse protein partners, sequestering them, or directing them to specific cellular locations. Notably, KFs were initially identified to interact with apical plasma membrane proteins, thereby facilitating the spatial organization of the apical domain in the polarized epithelium (Rodriguez et al., 1994). In intestinal tissue, KFs have been shown to interact with ion transporters and regulators (well-known interaction with cystic fibrosis conductance regulator) at the apical membrane. Additionally, they contribute to the targeted localization of ATPases and filamentous actin (F-actin) to apical/lateral domains (Duan et al., 2012; Toivola et al., 2004). Moreover, they play

indispensable roles not only in protein trafficking and the establishment of cellular polarity (Ameen et al., 2001) but also in maintaining organelle integrity. For instance, K8 has been demonstrated to support the integrity of nuclear envelope and lamina composition in colonocytes (Stenvall et al., 2022) and to influence the morphology and function of mitochondria [(Tao et al., 2009); reviewed in (Lowery et al., 2015)]. In mice lacking K8 (K8-null mice), there is an early manifestation of UC-like IBD and epithelial hyperproliferation, coupled with impaired IEB function and increased permeability. K8-null mice were highly susceptible to the development of colitis and CRC (Baribault et al., 1994; Habtezion et al., 2005; Liu et al., 2017; Misiorek et al., 2016; Stenvall et al., 2021). Collectively, these functions of IFs play essential role in the structural organization of the intestinal epithelial barrier [reviewed in (Salas et al., 2016)].

Vimentin is predominantly expressed in mesenchymal cells, which are prototypes for migratory and invasive cell types. Significant attention was drawn to the crucial role of vimentin in cell motility and invasivity (Gan et al., 2016; Strouhalova et al., 2020). Cell migration is a fundamental process in wound healing, tissue repair, and immune surveillance, where immune cells require migration to eliminate pathogens or infected cells. Additionally, cell migration is pivotal in various pathologies, including chronic inflammatory diseases and cancer, especially during metastasis [(Strouhalova et al., 2020); reviewed in (Satelli and Li, 2011)].

The migratory process involves several key steps, including spatiotemporal signaling transduction, establishment of cell polarity, extension of protrusions or cell adhesions, and activation of actomyosin contractility to facilitate movement [reviewed in (Ridley et al., 2003)]. Initially, the interaction between vimentin and MTs is crucial for establishing cell polarity. Subsequently, the actin cytoskeleton comes into action to facilitate the formation of protrusions and adhesions in order to generate contractile forces (Gan et al., 2016).

Importantly, similar to other IFs, vimentin network plays a pivotal role in maintaining the mechanical integrity of cells, enabling them to endure physical stress. Notably, during migration through interstitial spaces, cells undergo processes such as cytoskeleton reorganization and cell body reshaping to protect the nucleus and DNA from damage (Patteson et al., 2019). The vimentin network establishes connections with both the nucleus and the plasma membrane. Under physical stress, vimentin IFs (VFs) create a cage-like structure around the nucleus, acting as a mechanoprotective shield (Patteson et al., 2019). Moreover, in

mitotic cells, the vimentin network supports cortical actin structure, thus mechanically protecting chromatin and ensuring proper cell division in confinement (Serres et al., 2020).

1.2.3 **Cell adhesion**

Cell adhesion (Figure 4) is a process wherein cells establish physical contact with the ECM. Two primary junctional complexes, known as HDs and focal adhesions (FAs), facilitate such an adhesion. The transmembrane receptor proteins, integrins (Itgs) cluster into adhesive structures such as HDs or FAs, and they interconnect the cytoskeleton on the intracellular site with the ECM components [such as laminin, fibronectin (FN), and collagens (Coll)]. As a part of a process called mechanotransduction, HDs, and FAs sense, integrate, and convert mechanical forces arising from either the external environment or the internal cellular contractile apparatus into biochemical signals that regulate cell survival, gene expression, differentiation, proliferation, and cell migration (Gregor et al., 2014; Wang et al., 2020).

HDs (Figure 5) anchor epithelial cells to the underlying ECM or BM. The heterodimeric Itgα6/β4 complex is connected to KFs through plakin cytolinker proteins (Nahidiazar et al., 2015). In patients, mutations in *ITGB4* have been associated with the congenital disease junctional epidermolysis bullosa, characterized by epithelial fragility, skin blistering, and defects in respiratory and gastrointestinal tracts [reviewed in (Bardhan et al., 2020; Tsuruta et al., 2011)]. There are two types of HDs: HDs type I, found in stratified epithelium (such as skin), comprise Itgα6/β4, plectin, tetraspanin CD151, bullous pemphigoid antigen 1 (BPAG1; also known as BP230 or dystonin), BPAG180 [(synonymous BPAG2, Coll XVII; (Owaribe et al., 1990)]. In HDs type II, which are found in the simple epithelium (like the intestine), KFs are connected to Itgα6/β4 only via plectin, thus lacking BPAG1 and type BPAG180 [(Fontao et al., 1999); reviewed in (Walko et al., 2015)].

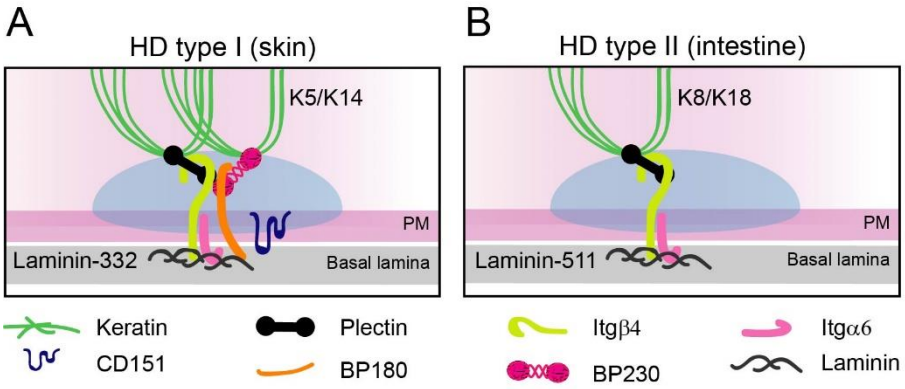

Figure 5 Schematic illustration of hemidesmosomes (HDs) type I and II. (A, B) The composition of HDs differs between stratified (skin; A) and simple (intestinal) epithelia (B). While type I HDs (A) consist of several crosslinking proteins, in type II HDs (B), plectin is the only crosslinking protein anchoring IFs to HDs. Plasma membrane [PM; (Korelova et al., unpublished)].

FAs (Figure 6) are adhesive complexes comprising Itg heterodimers (such as Itgα5β1 and ItgαVβ3) which traverse plasma membrane and interconnect actin and vimentin cytoskeletal networks with ECM [reviewed in (Geiger and Yamada, 2011)]. On the cytoskeletal side, FAs are composed of a complex of proteins such as vinculin, talin, paxillin, zyxin, α-actinin, vasodilator-stimulated phosphoprotein (VASP), Itg linked kinase (ILK), particularly interesting new cysteine-histidine-rich protein (PINCH-1), α-parvin, focal adhesion kinase, and other phosphotyrosine kinase proteins [reviewed in (Wu, 2007)]. Similar to HDs, FAs provide cells with mechanical support and stability. Additionally, they are essential for facilitating cell migration.

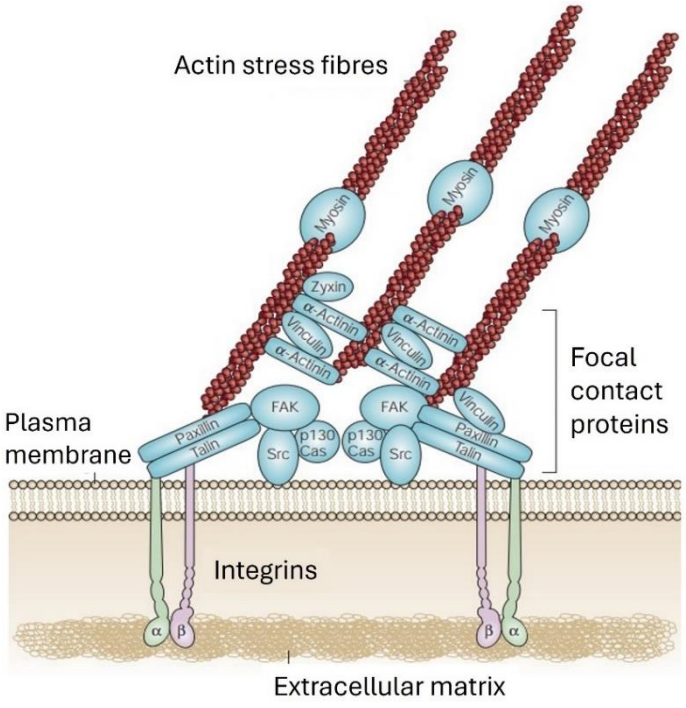

Figure 6 Schematic illustration of focal adhesions (FAs). The figure shows major consituents of the FA complex as they are described in chapter 1.2.3 [adopted from (Mitra et al., 2005)].

1.2.4 **Cell cohesion**

Cohesion between individual epithelial cells is required to form the functional epithelial layer. TJs, AJs, and Ds are the three types of intercellular cohesion complexes (Figure 4). TJs seal the barrier and enable paracellular transport, while AJs and Ds are essential for the mechanically robust interconnection of adjacent cells. Furthermore, these junctions contribute to establishing the apicobasal polarity of epithelial cells and the transepithelial transport of various compounds. Through their connection with the junctional plaque proteins and the cytoskeleton, cell-cell junctions actively transmit signals into the cell interior, consequently impacting gene expression and cellular behavior. Moreover, the assembly and maturation of junctional complexes are highly dependent on calcium levels [reviewed in (Groschwitz and Hogan, 2009)].

TJs (Figure 7) are located at the most apical position among intercellular junctional complexes. As the primary gate for paracellular diffusion, they control the passage of solutes with varying charge, electrical resistance, and sizes, regulated by their protein composition. TJs consist of transmembrane proteins such as claudin family proteins, MARVEL domain proteins (including occludin and tricellulin), blood vessel epicardial substance (BVES), junctional adhesion molecules (JAMs), angulin proteins, coxsackie virus-adenovirus receptor (CAR), and crumbs homologue 3 (Crubs3), which span the plasma membrane and connect neighboring cells through the paracellular space. Intracellularly, these transmembrane proteins are linked to a cytoplasmic plaque comprising scaffolding and effector proteins such as zonula occludens 1/2/3 (ZO-1/2/3), partitioning defective 3/6 homologs (PARD3/6), protein associated with Lin-7 1 (PALS1), and cingulin, ultimately connecting to the actin cytoskeleton [reviewed in (Anderson and Van Itallie, 2009; Heinemann and Schuetz, 2019; Zihni et al., 2016)]. Generally, paracellular epithelial permeability has three distinct pathways: the ‘leak’ and the ‘pore’ pathways, regulated by TJs, defining intestinal permeability. The leak pathway permits the transport of larger molecules. It is primarily controlled by myosin light chain kinase 1 (MLCK1), which triggers the endocytosis of TJ proteins such as occludins, thereby influencing barrier permeability. Conversely, the pore pathway facilitates the transport of small molecules through pores or channels formed by claudins. Additionally, there is a third pathway known as the ‘unrestricted’ pathway, associated with apoptotic leaks in pathological conditions, which

operates independently of TJs, allowing luminal antigens access to the lamina propria [reviewed in (Groschwitz and Hogan, 2009)].

AJs (Figure 8) are positioned below TJs and serve as a critical mediator of cell-cell adhesion. Similar to TJs, AJs consist of transmembrane proteins linked to actin filaments through cytoplasmic protein complexes [reviewed in (Hartsock and Nelson, 2008)]. The core transmembrane protein components belong to the cadherin family, with the primary transmembrane receptor in epithelial monolayers being E-cadherin (E-cad), which binds to adjacent epithelial cells. Cytoplasmic tails of cadherins interact with structural proteins from the Armadillo family (β-/γ-/p120-catenin), which in turn bind to actin via α-catenin. Moreover, studies have demonstrated that the cadherin/p120-catenin complex interacts with microtubules either through kinesin motors during cell surface trafficking (Chen et al., 2003) or via the adaptor protein PH domain-containing family A member 7 (PLEKHA7), which links p120-catenin to the protein NEZHA at the minus end of MTs (Meng et al., 2008). Furthermore, the transmembrane protein nectin, has been shown to cluster with cadherin-enriched clusters via PLEKHA7 and PDZD11 interaction, supporting the structural dynamics of AJs (Indra et al., 2013). Additionally, several other actin-binding proteins have been identified as part of

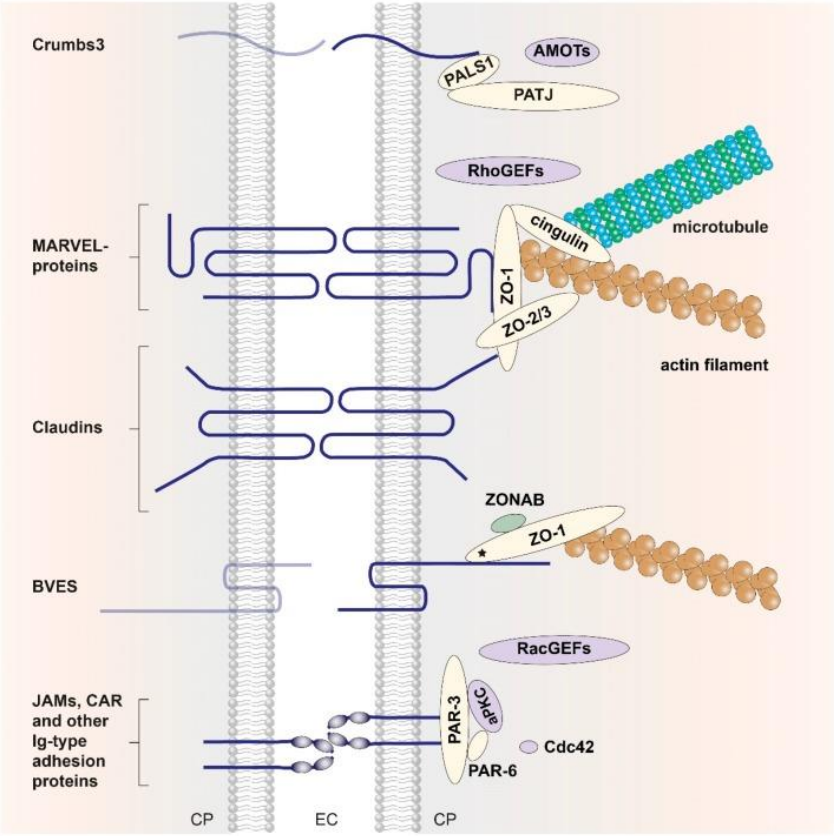

Figure 7 Schematic illustration of tight junction (TJ) complex. The individual proteins belonging to the core of TJ are depicted in the scheme and described in the chapter 1.2.4 [adopted from (Heinemann and Schuetz, 2019)]

adherens junctions, including vinculin, and afadin [reviewed in (Harris and Tepass, 2010; Lessey et al., 2022; Meng and Takeichi, 2009)].

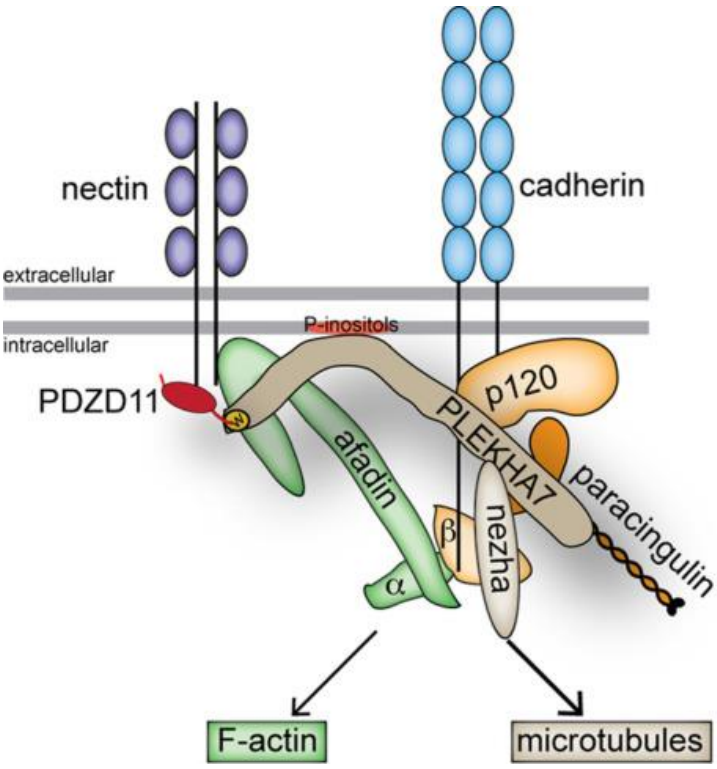

Figure 8 Simplified schematic illustration of adherens junction (AJ) complex. Via specific protein-protein interactions, AJs interconnect neighboring cells with the intracellular actin and microtubule (MT) cytoskeleton. α-catenin (α in green), β-catenin [(β in yellow; (Guerrera et al., 2016)].

Ds (Figure 9) are button-like junctional structures that are coupled to IFs at the plasma membrane, extracellularly connecting adjacent cells. During the development of cell-cell contacts, the establishment of Ds depends on the maturation of AJs. Since IFs provide cells with mechanical strength, Ds are particularly abundant in cells subjected to high mechanical stress, thus preserving the mechanical resistance of the tissue. Evolutionarily, given that the core transmembrane proteins of Ds are cadherins, and their assembly is temporally and spatially regulated in relation to AJs, Ds are considered akin to AJs (Koch and Franke, 1994). The primary components of Ds consist of heterodimeric transmembrane cadherins desmogleins (Dsg; 1-4) and desmocollins (1-3), further associating with junctional proteins plakoglobin and plakophillins (1-3). These are crosslinked by plakin proteins desmoplakin (Dsp), plectin, periplakin, and envoplakin, subsequently coupled to IFs [(Price et al., 2018); reviewed in (Green and Gaudry, 2000; Muller et al., 2021)].

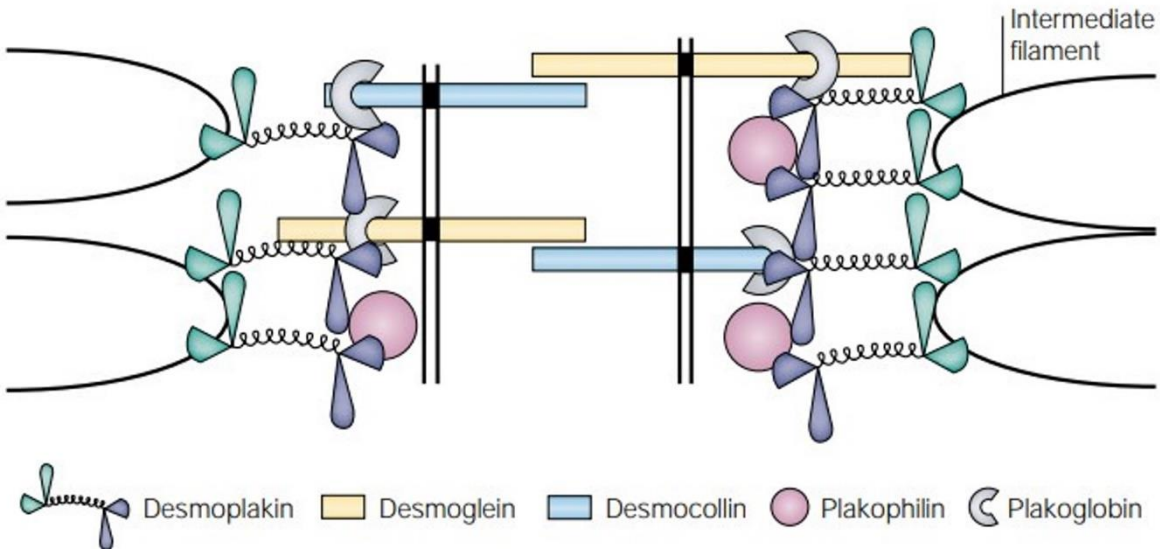

Figure 9 Schematic illustration of desmosomes (Ds). The figure shows the central members of the Ds complex, their mutual interactions and the anchoring of intermediate filaments [IFs; adopted from (Green and Gaudry, 2000)].

Analyses of samples from IBD patients have identified the aberrant expression of genes/proteins associated with the TJ, AJ and D junctional complexes (Consortium et al., 2009; Gassler et al., 2001; Piche et al., 2009). Over past years, multiple mouse models with genetically modified genes encoding TJ, AJ, and D constituents have been generated. Ablation or mutation of these genes resulted in changes in immune response, mucosal inflammation, and in some cases increased susceptibility for the development of CA-CRC or CRC [(Cuzic et al., 2021; De Arcangelis et al., 2017; Gross et al., 2018); reviewed in (Landy et al., 2016; Mehta et al., 2015; Schlegel et al., 2021; Zbar et al., 2004)].

1.2.5 **Plectin**

All cytoskeletal components are physically interconnected and anchored to the plasma membrane or other cellular structures. Such cytoskeletal interactions are mediated by cytoskeletal crosslinker proteins (cytolinkers) from plakin family. Moreover, plakins also promote the anchorage of the cytoskeletal network to cell-cell/cell-ECM junctions and intracellular organelles [reviewed in (Jefferson et al., 2004; Leung et al., 2002; Ruhrberg and Watt, 1997)]. In 1980, plectin, a plakin family member protein, was isolated (Pytela and Wiche, 1980). Plectin is the most versatile plakin and probably best-studied up to date. Even though

plectin is able to interact with all cytoskeletal filaments, it is preferentially an IF-binding protein (Prechova et al., 2022).

Plectin is a giant crosslinker protein (approx. 500 kDa) ubiquitously expressed in almost all cells and tissues. In humans, *PLEC* gene is localized in the q24 region of chromosome 8 and encoded by 32 exons (Liu et al., 1996), while in mice, it localizes on chromosome 15 (Fuchs et al., 1999). The analysis of transcript diversity in mice revealed that alternative splicing of *PLEC* gene gives rise to 14 plectin isoforms, which differ at their *N*-termini (Figure 10) and are expressed in a cell type-specific manner [(Fuchs et al., 1999; Liu et al., 1996; Rezniczek et al., 2003); reviewed in (Castanon et al., 2013)]. Nine of these isoforms differ in first exon and are alternatively spliced into common exon 2 (isoforms 1, 1a, 1b, 1c, 1d, 1e, 1f, 1g), three isoforms also differ in the first coding exon, but are spliced into exon 6 [isoforms 1h, 1i, 1j; (Rezniczek et al., 2003)]. Two isoforms are alternatively spliced in exons 2 and 4 (isoforms 2α and 3α). In epithelial cells, the most prevalent plectin isoforms are plectin 1 (P1), 1a (P1a), 1f (P1f), and 1c [P1c; (Fuchs et al., 1999)].

At the ultrastructural level, plectin assumes a dumbbell-like structure consisting a central 200-nm-long α-helical coiled-coil rod domain flanked by two globular domains (Foisner and Wiche, 1987; Wiche et al., 1991). Plectin's central rod domain facilitates the dimerization of plectin molecules, while the *N*- and *C*-terminal domains are crucial for interactions with binding partners (Figure 10). The *N*-terminal domain contains an actin-binding domain (ABD), which consists of 2 calponin homology domains that exhibit similarities to the spectrin family of proteins. Plakin domain, consisting of nine spectrin repeats along with a putative Src homology 3 (SH3) domain, is also located at the *N*-terminus (Ortega et al., 2016; Sonnenberg et al., 2007). The *C*-terminal domain harbors six plectin repeat domains encompassing the IF-binding domain (IFBD) and followed by a *C*-terminal tail [(Foisner et al., 1988; Janda et al., 2001; Wiche et al., 1991); reviewed in (Wiche, 2021)]. Intriguingly, vimentin can be bound not only by the *C*-terminal IFBD but also by the ABD located at the *N*-terminus (Sevcik et al., 2004).

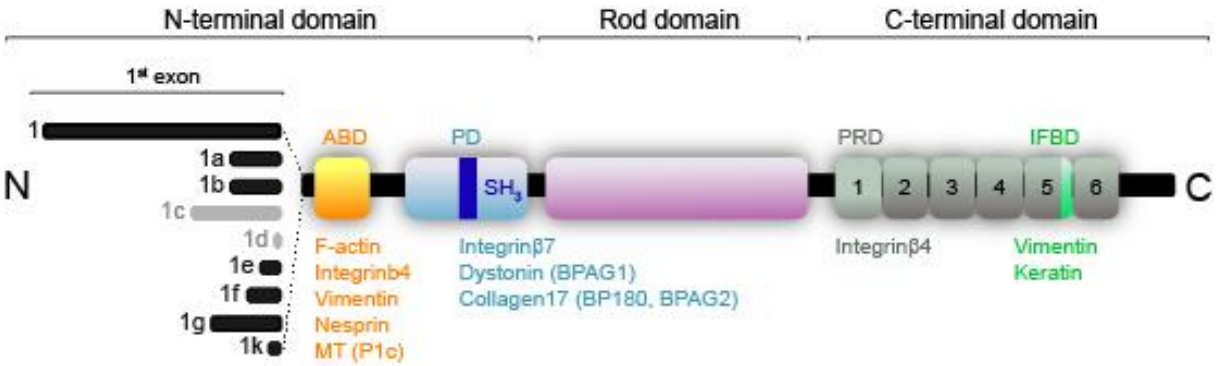

Figure 10 Structure of plectin. Schematic illustration showing a selection of plectin's binding partners and structural diversity of *N*-terminus (N) determining plectin isoform origins. *C*-terminus (C), actin-binding domain (ABD, yellow), plakin domain (PD, blue), plectin repeat domain (PRD, grey), IF-binding domain [IFBD, green; (Korelova et al., unpublished).

The ability to interact with a wide range of proteins enables plectin to link IFs with various cellular structures (Figure 11). By binding the Itgβ4 and BPAG1/2 (dystonin), plectin localizes and facilitates the assembly of HDs (de Pereda et al., 2009; Koster et al., 2003; Nievers et al., 2000; Rezniczek et al., 1998; Steiner-Champliaud et al., 2010). Plectin also anchors the cytoskeleton to Ds via periplakin binding domain (Boczonadi et al., 2007) or TJs via interaction with ZO-1 (Chen et al., 2006). Via ABD, plectin binds nesprin-3 and thus anchors IFs to the outer nuclear membrane. This altogether indicates its diverse roles in cellular architecture and organization (Ketema et al., 2007; Wilhelmsen et al., 2005).

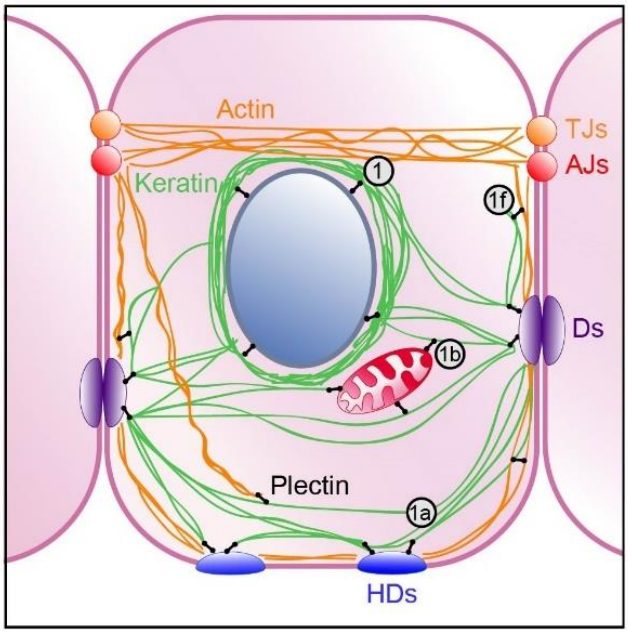

Figure 11 Plectin interacts with a plethora of subcellular structures. In the epithelial cells, plectin is present in several isoforms (1, 1a, 1b, 1f). Isoform diversity allows plectin to participate in the structural architecture of cell. TJs (yellow), AJs (red), Ds (purple), HDs (Korelova et al., unpublished).

1.2.6 **Plectinopathies**

Mutations in *PLEC* gene are associated with a broad spectrum of rare human disorders collectively known as “plectinopathies”. Currently, 116 identified variants of *PLEC* gene are associated with these disorders in 131 patients (Vahidnezhad et al., 2022). These multisystem disorders entail an autosomal dominant form of epidermolysis bullosa simplex, limb-girdle muscular dystrophy, aplasia cutis congenita, and an autosomal recessive form of epidermolysis bullosa simplex, which may manifest alongside muscular dystrophy pyloric atresia, and/or congenital myasthenic syndrome. The general mechanism underlying plectinopathies involves the pivotal role of plectin in preserving the mechanical stability of the tissue. When *PLEC* gene mutations occur, this stability is compromised, leading to pathologies such as tissue fragility, blisters, erosions, weakened and atrophic muscles, and cardiomyopathy, characteristic features observed across various plectin-related disorders [(Vahidnezhad et al., 2022; Walter et al., 2021); reviewed in (Kiritsi et al., 2021)]. In rare cases, patients with *PLEC* mutations diagnosed for epidermolysis bullosa simplex revealed signs of bloody diarrhea, intestinal malabsorption, protein-loosing enteropathy associated with intestinal mucosa fragility, intestinal wall thickening, and intestinal mucosa loss [(Kaneyasu et al., 2023; Verma et al., 2020); reviewed in (Mylonas et al., 2019)].

1.2.7 **Adaptation to mechanical stress**

The adaptability of cells defines their potential to survive and operate effectively under changing environmental conditions. In intestinal environment, cells are continuously exposed to various mechanical stimuli, including shear stress, compression, differences in tissue rigidity, and strain, to which they respond by activating robust mechanoprotective mechanisms [reviewed in (Houtekamer et al., 2022)]. This endurance is highly supported by cytoskeletal crosslinkers that carefully fine-tune the interplay between cytoskeletal elements, cell-cell and cell-ECM junctions, and facilitate mechanotransduction.

1.2.7.1 Adaptation at cellular level

Although excessive mechanical stress can potentially compromise tissue integrity, epithelial layers exhibit resilience against significant deformation by modulating the

morphology of individual cells within the layer. The change in extracellular mechanical force is primarily sensed by Itgs, which directly interact with ECM, or by cadherin, which mediate interactions with neighboring cells. These interactions allow cells to respond to various cues via actomyosin cytoskeleton, thereby upholding mechanical stability [reviewed in (Charras and Yap, 2018; Gauthier and Roca-Cusachs, 2018; Iskratsch et al., 2014)].

During uniaxial cyclic strain resulting from the environmental stretch, cells undergo adaptive changes in their cytoskeletal organization and cellular and nuclear morphology, aligning themselves nearly perpendicular to the direction of stretch. Activation of mechanoreceptors (cadherins and Itgs) propagates force into the cellular interior through direct conversion into a biochemical signal via downstream kinase activation or by triggering other mechanoresponsive proteins [reviewed in (Hu et al., 2017)]. Well-described is the impact of mechanical force on the conformational alteration of α-catenin. When epithelial monolayers experience uniaxial mechanical strain, cadherins within AJs detect force signals from neighboring cells and transmit them to the cell interior. This results in force-induced α-catenin conformational changes, vinculin binding, increased association with actin filaments, the formation of actin stress fibers, increased actomyosin contractility, and perpendicular reorientation of cytoskeleton followed by the nucleus (Hayakawa et al., 2001; Nava et al., 2020; Noethel et al., 2018; Yonemura et al., 2010). An additional force-induced response mechanism involves mechanosensitive ion channels Piezo 1/Piezo2 [(Coste et al., 2010); reviewed in (Murthy et al., 2017)]. These channels are situated both at the plasma membrane and the endoplasmic reticulum membrane (McHugh et al., 2010). Stretching results in strain-dependent nuclear deformation and increased nuclear stiffness, leading to the opening of Piezo-1 channels at the endoplasmic reticulum membrane and the subsequent intracellular release of Ca^{2+} from endoplasmic reticulum storage. This process facilitates chromatin mechanoresponse and the formation of the perinuclear F-actin ring (will be discussed more in Chapter 1.2.7.2). Furthermore, prolonged stretching causes increased plasma membrane tension, resulting in the influx of extracellular Ca^{2+} into the cytoplasm, thereby triggering supracellular patterning. Supracellular response is crucial for dissipating mechanical stress which could be harmful for the nucleus. This involves the reorientation of cells and the elongation of the nuclear long axis, as well as strengthening of cell-cell contacts and F-actin, driven by the remodeling of AJs (De and Safran, 2008; Faust et al., 2011; Hayakawa

et al., 2001; Lewis and Grandl, 2015; Nava et al., 2020; Prechova et al., 2022; Wang et al., 2001).

While extensive research has focused on unraveling the role of the actin cytoskeleton in cellular mechanotransduction, it's worth noting that IFs also play an important role in cell mechanics. Recent studies shed light on the crucial interactions between HDs or FAs and IFs, in particular in a plectin-dependent manner. This mechanical coupling between IFs and the cell periphery is critical for modulating cell stiffness, which is achieved by thickening of IF bundles in response to changes in the ECM environment. IFs form cage-like structure around the nucleus, which is essential to protect the nucleus from actomyosin-induced deformations through intricate crosstalk between IFs and actin. This process attenuates FAs and regulates Yes-associated protein (YAP) signaling. Perturbations in keratin organization due to plectin loss lead to increased nuclear deformability (Kechagia et al., 2023; Laly et al., 2021; Patteson et al., 2019; Wang et al., 2020). In addition, cortical IFs regulate the organization and mechanics of the actin network during mitosis, which is critical for successful cell division in confined spaces. Abnormalities in the IF network during mitosis prevent proper mitotic rounding and increase the likelihood of chromosomal aberrations (Serres et al., 2020).

Mechanical stimulation prompts rearrangements in the cytoskeleton and concurrently activates multiple mechanoresponsive signaling pathways. Given our understanding of the extensive remodeling of the actin cytoskeleton, it is not surprising that the transmission of force-induced signals often correlates with elevated levels of cytoplasmic Ca^{2+} and heightened actomyosin contractility. Mechanical stimuli can initiate the activation of mechanosensitive transcription factors, which subsequently instigate alterations in gene expression, dictating cell behavior and fate. Studies have demonstrated that mechanical strain triggers the activation of extracellular signal-regulated kinase (ERK1), c-Jun N-terminal kinase (JNK), and phosphoinositide 3-kinases (PI3K)/protein kinase B (PKB/Akt), leading to the expression of genes associated with proliferation or cell survival (Codelia et al., 2014; Gudipaty et al., 2017; Kaunas et al., 2006; Kippenberger et al., 2005). The contractility induced by mechanical force facilitates the translocation of mechanoresponsive transcription factors into the nucleus, including YAP/Transcriptional coactivator with PDZ-binding motif (TAZ) and myocardin-related transcription factor A (MRTF A)/serum response factor (SRF), which regulate genes involved in differentiation, proliferation, vascular remodeling, expression of α-smooth muscle actin, cell

polarization, fibroblast activation, and fibrosis (Benham-Pyle et al., 2015; Dupont et al., 2011; Kono et al., 2014; Liu et al., 2015; Musah et al., 2014; Talwar et al., 2014; Yamashiro et al., 2020; Zhao et al., 2007). Additionally, mechanically regulated factors such as β-catenin stimulate proliferation, while nuclear factor κB (NF-κB)/activator protein 1 (AP-1) induces the expression of pro-inflammatory genes, and nuclear factor erythroid 2-related factor 2 (Nrf2) stimulate the expression of anti-oxidant genes (Hsieh et al., 2009; Kumar et al., 2003; Samuel et al., 2011). Actin dynamics also impact global gene expression through histone modifications, including histone deacetylase 3 [HDAC3; (Jain et al., 2013)].

1.2.7.2 Nuclear/DNA level adaptation

Nucleus, the cells' largest and most rigid organelle, is separated from the surrounding cytosol by a lipid bilayer. The only type of IFs present within the nucleus are LMNA/C and LMNB1/2, which form nuclear lamina, a fibrilar network located at the inner nuclear membrane facing towards the nucleoplasm [reviewed in (Gruenbaum and Foisner, 2015; Gruenbaum et al., 2005)]. The cytoskeleton is connected to the nuclear membrane via linkers of the nucleoskeleton and cytoskeleton (LINC) complex, which is composed of Sad1p and UNC-84 (SUN) and Klarsicht, ANC-1, and Syne homology (KASH)-domain proteins. KASH proteins are embedded in the outer nuclear membrane and interact with all cytoskeletal components, namely via nesprin family of proteins. SUN proteins localize in the inner nuclear membrane and interact with lamina and chromatin. Since nuclear lamina associates with chromatin, mechanical forces acting at the cellular membrane can be transmitted onto a nucleus where they trigger chromatin remodeling or gene expression [reviewed in (Buchwalter et al., 2019)]. This process demonstrates that the nucleus also serves as an additional force-sensing barrier [mechanosensor; (Lombardi et al., 2011)].

The organization of chromatin within the nucleus is vital for proper regulation of gene expression. Chromatin at the nuclear periphery exists in a highly compacted form known as heterochromatin, tethered to the nuclear envelope through lamina-associated domains, which are characterized by low gene density and gene repression [reviewed in (Buchwalter et al., 2019; Lemaitre and Bickmore, 2015; van Steensel and Belmont, 2017)]. Heterochromatin is distinguished by repressive histone modification marks, such as H3K9me2, H3K9me3, and H3K27me3, which play roles in gene silencing, chromatin compaction, and localization [(Bian

et al., 2013; Nicetto et al., 2019; Yokochi et al., 2009); reviewed in (Buchwalter et al., 2019)]. Owing to its physical rearrangement, heterochromatin can act as a force-absorbing element in nuclear mechanosensing, along with the nuclear lamina and perinuclear actin.

As mentioned above (Chapter 1.2.7.1), the connection between the cell periphery and cell center transduces mechanoresponse onto the nucleus and chromatin. Nuclear IFs, like LMNA/C, can adapt to mechanical stress through changes in their expression, phosphorylation, or mechanical unfolding. This, in turn, may affect nuclear stiffness, gene expression, and migration to maintain nuclear shape and genomic integrity under force [(Denais et al., 2016; Heo et al., 2016; Nava et al., 2020); reviewed in (Cho et al., 2017; Lomakin et al., 2020)]. The actin cytoskeleton, specifically the F-actin perinuclear ring, plays a critical role in maintaining nuclear shape and volume under mechanical stress and regulating mechanoresponsive signaling pathways (Le et al., 2016; Nava et al., 2020; Shiu et al., 2018). The compaction state of chromatin heavily influences the mechanical properties of nuclei. Nuclei rich in heterochromatin tend to be rigid, while those with decondensed chromatin are softer, deformable, and more mobile. The association of chromatin with the nuclear lamina also modulates nuclear mechanical properties - uncoupling of chromatin from the nuclear envelope leads to increased chromatin flow, enhanced nuclear deformability, and alterations in nuclear shape (Chalut et al., 2012; Nava et al., 2020; Spagnol and Dahl, 2016; Stephens et al., 2017).

The presence of dysmorphic nuclei is characteristic of many tumors [reviewed in (Zink et al., 2004)]. Interestingly, variations in chromosome copy number, gene mutations, and genomic instability are strongly associated with tumor stiffness (Pfeifer et al., 2017). Under mechanical stress, nucleus undergoes pressurized deformation thus forming nuclear envelope blebs, which may in turn cause DNA damage. These blebs can rupture, causing leakage of nuclear factors and DNA into the cytoplasm, promoting senescence in non-transformed cells, and inducing an invasive phenotype in cancer cells (Nader et al., 2021). Repeated exposure to confinement can result in cell cycle arrest, alterations in chromosome copy number, and loss of heterozygosity (Irianto et al., 2017; Pfeifer et al., 2018). Force-induced DNA damage can occur even without nuclear rupture, as nuclear deformation increases replication stress, contributing to genomic instability, which can further promote tumorigenesis (Shah et al., 2021).

On the other hand, despite studies in cell cultures showing that nuclear deformation can induce DNA damage in non-transformed cells, tissues that undergo large-scale deformation under physiological conditions display mechanisms to counteract nuclear deformation and deformation-induced DNA damage. Subjecting cell monolayers to uniaxial stretch reduces levels of H3K9me3, making the nucleus and chromatin more elastic to dissipate mechanical energy and protect the genome from damage. Long-term mechanical strain can result in global transcriptional repression and chromatin remodeling, contributing to sustained mechanoprotection (Nava et al., 2020).

1.3 Pathologies of the intestinal epithelial barrier

It has been discussed in the previous chapter (1.1.1.4) that IEB ensures selective transport across epithelia and protects underlying tissues against pathogens. Disruption in the integrity of IEB caused by injury or infection can trigger the immune response. Persistent inflammation that is not healed or spreads to healthy tissue can, together with other factors, contribute to the development of IBD or CRC [(Vivinus-Nebot et al., 2014); reviewed in (Genua et al., 2021)].

1.3.1 **Inflammatory bowel disease**

IBD is characterized by severe inflammation in the gastrointestinal tract [(Leake, 2016; Schmidt and Stallmach, 2005); reviewed in (Hanauer, 2006)]. It is a chronic disorder affecting approximately 1 out of 250 individuals in the European population [reviewed in (Gonzalez-Lama et al., 2023)]. Patients diagnosed with IBD manifest symptoms including abdominal pain, fatigue/tiredness, high bowel frequency and diarrhea containing blood/mucus, and increased passage of gas (Perler et al., 2019). While the exact cause of IBD is still unknown, environmental factors, immune dysfunction, intestinal microbiota, and genetic predispositions are recognized as key risk factors associated with a poor prognosis and lifelong morbidity for patients [reviewed in (Karlinger et al., 2000)]. Up to date, two types of IBD have been described – UC and Crohn's disease (CD). In UC, inflammation is restricted to the rectum and colon, while in CD inflammation can affect any part of the intestine, including the small intestine. The mechanisms underlying disease progression differ between these two types of IBD. There is a

strong genetic predisposition to the disease, with many patients having family history of IBD (Sartor, 1995).

The IEB breakdown and increased intestinal permeability in IBD patients have been determined as high-risk factors for IBD onset [(McCole, 2014); reviewed in (Abraham and Cho, 2009; Martini et al., 2017). Interestingly, even patients with inactive IBD exhibit increased paracellular permeability (Vivinus-Nebot et al., 2014). Improving IEB function may therefore represent a promising therapeutic target for the treatment of IBD [reviewed in (Odenwald and Turner, 2017)]. Furthermore, mutations resulting in altered KFs have been observed in patients diagnosed with IBD and CRC (Evans et al., 2015; Owens et al., 2004; Tao et al., 2007). Additionally, clinical investigations shown that the expression patterns of K7 and K20 correlate with severity of IBD and some types of human CRCs. K7, which is absent in healthy tissues, may thus serve as a potential diagnostic marker for IBD (Moll et al., 1992; Polari et al., 2022; Stenling et al., 2007; Yun et al., 2000).

1.3.2 **Colorectal cancer**

CRC is recognized as the third most prevalent cancer on a global scale, representing approximately 10% of all cancer cases and ranking as the second leading cause of cancer-related mortality. A considerable proportion of individuals diagnosed with CRC are typically around 50 years of age, often presenting with advanced-stage tumors, thus posing challenges in terms of treatment options (Sung et al., 2021). Beyond genetic predisposition, a range of known risk factors contribute to CRC development. Some individuals have potential to mitigate these risk factors, thereby reducing the likelihood of tumor occurrence (Morgan et al., 2023). These factors include dietary patterns, such as the consumption of unprocessed foods, and lifestyle behaviors, including smoking, alcohol intake, inadequate physical activity, and obesity (Research, 2018). The change of the normal colonic epithelium to a precancerous lesion and, ultimately, an invasive carcinoma requires an accumulation of genetic mutations, either somatic (acquired) and/or germline (inherited), over an approximately 10- to 15-year period. Chromosomal instability, mismatch repair, and CpG hypermethylation are the major pathways to the onset of CRC (Grady and Markowitz, 2000).

It is well-documented that individuals with IBD face an elevated risk of developing CA-CRC (Lakatos and Lakatos, 2008; Long et al., 2017). Around 1-2% of CRC cases are attributed to CA-CRC, and this risk escalates over time (Eaden et al., 2001; Eluri et al., 2017; Selinger et al., 2014). Factors such as the duration and severity of inflammation, along with genetic predisposition within families, contribute significantly to this risk (Flores et al., 2017). CA-CRC typically manifests at younger age compared to sporadic CRC, leading to poorer survival rates. Notably, it accounts for approximately 15% of yearly deaths among individuals diagnosed with IBD [(Lu et al., 2022); reviewed in (Fornaro et al., 2016)]. The persistent inflammation in CA-CRC results in oxidative stress, causing DNA damage and double-strand breaks (DSBs). Like sporadic CRC, CA-CRC exhibits high genomic instability, particularly in critical driver genes such as *APC, P53, MYC, KRAS, PIK3CA, SMAD4,* and *ARID1* (Rajamaki et al., 2021; Robles et al., 2016; Yaeger et al., 2016). However, genetic alterations in IBD-associated CRC differ in timing and frequency compared to sporadic CRC. While mutations and loss of the *APC* gene are less common, mutations and loss of *P53* occur more frequently in earlier stages. *P53* mutations, present even in non-dysplastic mucosa, appear to have a more pronounced role in the development of IBD-associated CRC than in sporadic CRC (Du et al., 2017).

1.4 Mouse models of intestinal pathologies

Patients experiencing intestinal diseases, notably various forms of IBD or CA-CRC/CRC, demonstrate signs of compromised IEB function. Mouse models of intestinal pathologies have been developed to explore the treatment strategies of IBD and CRC. Such models help us to investigate the complex relationship between the intestinal microbiota, intestinal epithelium, and immune system during disease onset. The following chapters will describe some of the most frequently/commonly used mouse models.

1.4.1 **Colitis**

There are chemically-induced and genetically-engineered mouse models mimicking forms of IBD, namely CD, and UC:

1.4.1.1 **Chemically-induced colitis**

Dextran sodium sulphate (DSS). Because of its simplicity, DSS is the most commonly employed model for inducing experimental colitis in mice which closely mirrors human UC. DSS, a chemical colitogen, is typically diluted in drinking water and administered to mice in repeated cycles. Mice treated with DSS suffer from weight loss, diarrhea, and rectal bleeding (Chassaing et al., 2014). DSS interacts with medium-chain-length fatty acids, forming nanometer-sized vesicles with a diameter of approximately 200 nm. These vesicles fuse with the membranes of colonocytes, impacting major epithelial cell pathways and subsequently reducing intestinal barrier functions, triggering inflammatory signaling cascades within the intestine (Laroui et al., 2012). This disruption compromises the integrity of the IEB by affecting junctional complexes and the cytoskeleton (Poritz et al., 2007; Samak et al., 2015). The DSS model is clinically relevant for interpreting observations from mice to humans, as it has been shown to respond to drugs commonly used in the therapy of IBD (Melgar et al., 2008). DSS is accompanied by erosions/ulcers and loss of crypts, thereby exposing subepithelial immune cells to commensal bacteria. This effect is relatively independent of lymphocyte actions, as studies show that mice lacking T cells, B cells, and NK cells can still develop colitis in response to DSS (Axelsson et al., 1996; De Arcangelis et al., 2017; Dieleman et al., 1994).

2, 4, 6-Trinitrobenzensulfonic acid (TNBS). TNBS, a contact-sensitizing allergen, is a widely accepted model of IBD, in particular for CD in humans. Administration of 0.5 mg of TNBS in 50% ethanol induces in mice acute T cell-mediated, IL-12-driven transmural colitis, resulting in symptoms such as diarrhea, weight loss, and rectal prolapse (Neurath and Finotto, 2009; Neurath et al., 1995). Ethanol is utilized to perturb the mucosal barrier, while TNBS is hypothesized to haptenize microbiota or colonic autologous proteins, making them antigenic in susceptible mouse strains. The TNBS-induced model effectively mimics both the acute and

chronic stages of IBD, thereby being a valuable model for exploring innovative pharmacological approaches in patients (Silva et al., 2022).

4-ethoxymethylene-2-phenyl-2-oxazolin-5-one (Oxazolone). Oxazolone is a haptenizing reagent administered to mice via intrarectal enema. Both acute and chronic oxazolone colitis in mice is represented by superficial inflammation of the distal colon mucosa, extensive inflammatory infiltrate, depletion of GCs, formation of edema, loss of epithelial cells, hemorrhage, and vascular dilation, typically resembling UC histology (Boirivant et al., 1998; Kojima et al., 2004; Wang et al., 2004). This preclinical model presents several experimental obstacles, including rapid weight decline and increased mortality rates following oxazolone administration during the acute phase of the disease (Boirivant et al., 1998).

1.4.1.2 **Genetically engineered mouse models of spontaneous colitis**

IL-10-deficient (*IL-10*$^{-/-}$) mouse. IL-10 is a critical regulatory cytokine, representing a pivotal susceptibility gene in IBD (both UC and CD), owing to identifying mutations in the *IL10* gene among IBD patients. Mouse models, specifically *IL-10*$^{-/-}$ mice lacking the *IL10* gene, have provided valuable insights into disease pathogenesis. These mice exhibit spontaneous development of enterocolitis and adenocarcinoma (Anderson et al., 2011; Franke et al., 2008; Sturlan et al., 2001). The colitis phenotype observed in *IL-10*$^{-/-}$ mice is characterized by the presence of an inflammatory infiltrate consisting of lymphocytes, macrophages, and neutrophils (Kuhn et al., 1993). Intriguingly, a mouse model lacking IL-10 specifically in T cells mirrors a similar intestinal phenotype as *IL-10*$^{-/-}$ mice, emphasizing the importance of T cell-mediated immune response (Erdman et al., 2003).

Inhibitor of NF-κB kinase γ (*Ικκ-γ*$^{-/-}$) mouse. Deletion of the NF-kB essential modulator, also referred to as Ικκ-γ, specifically within the intestinal epithelium (ΔIEC), leads to the onset of severe, spontaneous inflammation in mice. This severe colitis coincides with aberrant apoptosis of epithelial cells induced by tumor necrosis factor α (TNFα), resulting in the disruption of IEB integrity, compromised expression of the anti-microbial peptide defensin-3, and the translocation of bacteria into the mucosal layer (Nenci et al., 2007). Noteworthy is the

observation that diminished defensin-3 expression has been documented in individuals suffering from IBD (Wehkamp et al., 2006).

1.4.1.3 **Immune cells induced colitis**

T cell adoptive mouse. The isolated undifferentiated CD45RB^{high}CD4^{+} T cells from healthy donors are transferred to severe combined immunodeficiency or the recombination activating genes 1/2 syngeneic immunodeficient mice, where they colonize the intestine and induce the onset of colonic inflammation (Powrie et al., 1994).

1.4.2 **Colitis-associated colorectal cancer/sporadic colorectal cancer**

1.4.2.1 **Carcinogen-induced mouse models**

Azoxymethane (AOM) model. AOM is a procarcinogen that undergoes metabolic activation in the liver into methylazocymethanol, a highly reactive alkylating species inducing O^6 methylguanine DNA adducts. Following excretion into the bile, it is absorbed by the colonic epithelium, leading to the initiation of mutagenesis (Sohn et al., 2001). AOM is intraperitoneally injected into mice in repeated cycles. Induced colonic carcinogenesis in treated mice displays histological features such as adenomas and adenocarcinomas, similar to sporadic colon cancers in humans [reviewed in (Boivin et al., 2003; Li et al., 2022)].

AOM/DSS model. The combination of AOM and DSS serves as a reliable method to induce CRC in mice, mimicking the pathogenesis of CA-CRC. Consequently, it stands as a highly replicable model suitable for both acute and chronic studies of intestinal colonic inflammation [reviewed in (Modesto et al., 2022)].

Heterocyclic amines. Heterocyclic amines, such as 2-amino-3-methylimidazo[4,5-f]quinoline (IQ) and 2-amino-1-methyl-6-phenylimidazo [4,5-b] pyridine (PhIP) are mutagens which require metabolic activation in the liver to be able to cause DNA adducts causing cancer. In contrast to AOM, IQ and PhIP promote multitarget carcinogenesis in the colon, mammary gland, and prostate (Hasegawa et al., 1993; Shirai et al., 1997). The time period before the

occurence of first tumors with IQ or PhIP is considerably long - it can require more than one year. However, when combined with DSS, the induction period of colon adenomas and adenocarcinomas is shortened to 6-24 weeks (Durmus et al., 2019).

1.4.2.2 **Genetically engineered mouse models**

Adenomatous polyposis coli (*Apc*$^{Min/-}$) mouse. In humans, polymorphisms in the *Apc* gene constitute a significant risk factor for sporadic CRC and familial adenomatous polyposis [reviewed in (Liang et al., 2013)]. Therefore, the multiple intestinal neoplasia (Min) mouse model has been engineered to investigate intestinal cancer in rodents. *Apc*$^{Min/-}$ mice exhibit spontaneous development of intestinal adenomas, which can be accelerated in the form of CA-CRC, where inflammation is induced by DSS treatment (Tanaka, Kohno et al. 2006).

Hereditary non-polyposis colon cancer. Hereditary non-polyposis colon cancer, also known as Lynch syndrome, arises from inherited mutations in DNA mismatch repair genes, notably *MLH1* and *MSH2*, which were among the first implicated in CRC. Mutations in these genes result in a high mutation rate and microsatellite instability (Bronner et al., 1994; Fishel et al., 1993; Lindblom et al., 1993). While Msh2-deficient mice exhibit lymphomas (Reitmair et al., 1995), the concomitant mutation of *Msh2* and *Apc* genes in mice accelerates intestinal carcinogenesis (Reitmair et al., 1996). To mimic hereditary non-polyposis colon cancer, a novel conditional KO mouse model was developed. Mice lacking Msh2, specifically in villin-expressing tissues (predominantly IECs of the SI and colon), exhibit similarities to hereditary non-polyposis colon cancer, as they do not manifest lymphoma development but show the formation of intestinal adenomas and adenocarcinomas (Kucherlapati et al., 2010).

2 AIMS OF THE THESIS

Plectin, a large cytolinker from the plakin protein family, binds IFs, interlinks them with other cytoskeletal components, and tethers crosslinked networks to junctional structures at the cell periphery, including Ds and HDs. Additionally, plectin anchors the cytoskeleton to the nuclear envelope. Mutations in the plectin gene predispose individuals to epidermolysis bullosa, a disorder characterized by severe skin blistering, muscular dystrophy, gastric obstruction, and various digestive disorders, such as IBD. Plectin ablation disrupts epithelial KF networks and alters cell junctions, compromising epithelial stability. In mouse models, plectin deletion negatively affects junction formation in the biliary epithelium and HD stability in keratinocytes. These disruptions lead to epithelial fragility and lesions similar to those in IBD patients. Despite these findings, the role of plectin in the intestinal epithelium remains unexplored.

The aim of my thesis is to investigate the role of plectin in the homeostasis and maintenance of the intestinal barrier. We hypothesized that plectin-controlled cytoarchitecture protects the cell nucleus and genome from damage induced by colitis-associated mechanical stress. To address this hypothesis, we utilized *Ple*$^{\Delta IEC}$ mouse model and KO cell lines. By examining the effects of aberrant cytoarchitecture on CRC development, we aim to better understand the relationship between mechanical stress, cytoskeletal integrity, and CRC progression in the context of CA-CRC.

2.1 Aim 1. Does plectin contribute to intestinal barrier homeostasis and colitis?

- Is plectin dysregulated in UC patients?
- What is the phenotype of *Ple*$^{\Delta IEC}$mice and plectin-deficient IEC cultures?
- Does the ablation of plectin disrupt the mechanical stability of intestinal epithelium?
- Are *Ple*$^{\Delta IEC}$mice susceptible to experimentally induced colitis?
- What is the underlying mechanism of the colitic phenotype in *Ple*$^{\Delta IEC}$ mice?

2.2 Aim 2. What is the role of plectin in mechanical stress-driven DNA damage and colorectal carcinogenesis?

- Are *Ple*$^{\Delta IEC}$mice susceptible to colorectal carcinogenesis?
- How does plectin-dependent cytoarchitecture protect the nucleus against DNA damage and genomic instability?
- What is the role of plectin in cell adaptation during mechanical stress?

3 Materials and Methods

3.1 Patients

Colon biopsy samples were collected from patients diagnosed with UC (*n* = 104) and from healthy controls (*n* = 31) admitted to the Hepatogastroenterology Department at the Institute for Clinical and Experimental Medicine (Prague, Czech Republic) for a colonoscopy from July 2016 to May 2019. Subjects were assigned to the healthy control group only after all clinical examinations excluded any signs of autoimmune disease, inflammatory disease, and colon cancer. All UC patients with concurrent primary sclerosing cholangitis were excluded from the study. Endoscopic UC activity at the time of a standard optical colonoscopy was categorized according to the Mayo endoscopic subscore and confirmed by histology examinations of the grade of inflammation. Standard endoscopic biopsies were extracted from the inflamed non-dysplastic mucosa of the left colon (rectum) and immediately placed in an RNAlater solution. Total RNA was extracted according to the manufacturer's instructions.

3.2 Mice

Plectin$^{flox/flox}$ (*Ple*$^{fl/fl}$) mice (Ackerl et al., 2007) were crossed with *villin-Cre* transgenic mice (MGI 2448639) to generate *Ple*$^{fl/fl}$*/villin-Cre* mice (*Ple*$^{\Delta IEC}$) and with *villin-creERT2* transgenic mice (MGI 3053826; both Cre strains were kindly provided by S. Robine (el Marjou et al., 2004)) to generate *Ple*$^{fl/fl}$*/villin-CreERT2* mice (*Ple*$^{\Delta IEC\text{-}ERT2}$). Age-matched littermate male mice were used in all experiments. Unless stated otherwise, mice were 12–14-week-old. Animals were housed under specific pathogen-free conditions with regular access to chow and drinking water and a 12 h light/12 h dark regime. To induce specific plectin deletion in *Ple*$^{\Delta IEC\text{-}ERT2}$ mice, 5 mg of tamoxifen (TMX; Sigma-Aldrich; dissolved in 200 µl of sunflower oil) was administered twice a day on days 1, 3, and 5 by orogastric gavage. Mice were sacrificed on day 10. *Ple*$^{fl/fl}$ mice received sunflower oil only.

3.3 Cells and CRISPR-mediated targeting of *plectin*

Human colorectal adenocarcinoma IECs (Caco-2) cells were grown in Dulbecco's modified Eagle medium (DMEM) supplemented with 20% fetal bovine serum (FBS) in a 5% CO_2/air humidified atmosphere at 37 °C. Human colonic cells (hCC; T0570, Applied biological

materials, Inc.) and human retinal pigment epithelial cells (hTERT- immortalized RPE1; RPE) were cultured in DMEM supplemented with 10% FBS in 5% CO_2/air humidified atmosphere at 37 °C. Plectin KO cell lines were generated by targeting genomic sequences of exon 6 of *plectin* using CRISPR/Cas9 plasmid pX330 Cas9-Venus. Two distinct gRNAs (5'-AGTTGTCGCATCGCAGGCCC-3') and (5'-GTCGGAGGACATGACGGCCA-3') were designed. Cells were transiently transfected using Lipofectamine LTX with Plus Reagent (Life Technologies). After 48 hours with the transfection complexes, cells were subjected to fluorescent activated cell sorting (FACS). Single-cell clones were obtained through dilution cloning in 96-well plates, and plectin KO was verified via DNA sequencing and immunoblot analysis.

3.4 DSS-induced colitis and disease activity scoring

12-week-old $Ple^{fl/fl}$ and $Ple^{\Delta IEC}$ mice were provided with a 2% (TdB Consultancy) dissolved in drinking water ad libitum over 4 days. Then mice were provided with drinking water over 3 days. Mice were sacrificed on day 7. As described previously (Brauer et al., 2016), body weight, stool consistency, and rectal bleeding (Hemoccult Fecal Occult Blood Test, Beckman Coulter) were assessed daily to calculate the disease activity index (DAI) and to monitor body weight loss over a time course of the experiment.

3.5 AOM-induced sporadic CRC

6-8-week-old $Ple^{fl/fl}$ and $Ple^{\Delta IEC}$ mice (minimum weight 18 g) received an intraperitoneal injection of 10 mg/kg AOM (Sigma-Aldrich) once per week for 6 consecutive weeks. Body weight was monitored throughout the experiment. If mice exhibited significant weight loss or rectal bleeding, the experiment was interrupted. Mice were sacrificed approximately 5 months after the first AOM injection. During dissection, developed tumors were captured by Zeiss Axio.Zoom V.16 microscope, and tissues from the SI and colon were processed for immunohistochemistry.

3.6 AOM/DSS-induced CA-CRC

6-8-week-old $Ple^{fl/fl}$ and $Ple^{\Delta IEC}$ mice (minimum weight 18 g) received an intraperitoneal injection of 10 mg/kg AOM (Sigma-Aldrich). After one week, the mice were provided with a

2% (TdB Consultancy) solution dissolved in drinking water ad libitum over 4 days. Throughout the experiment, body weight, stool consistency, and rectal bleeding (Hemoccult Fecal Occult Blood Test, Beckman Coulter) were assessed weekly to calculate the DAI and monitor body weight loss. If mice exhibited significant weight loss or rectal bleeding, the experiment was interrupted. Mice were sacrificed approximately 4 months after the first AOM injection. During dissection, developed tumors were captured by Zeiss Axio.Zoom V.16 microscope, and tissues from the SI and colon were processed for immunohistochemistry.

3.7 Depletion of gut microbiota by antibiotic treatment

Streptomycin 2 g/l (Carl Roth), gentamycin 200 mg/l (Carl Roth), enrofloxacin 100 mg/l (Sigma-Aldrich), and bacitracin 1 g/l (Carl Roth) were provided to 9-week-old $Ple^{fl/fl}$ and $Ple^{\Delta IEC\text{-}ERT2}$ mice in drinking water ad libitum over 2 weeks. To induce specific plectin deletion in 9-week-old $Ple^{\Delta IEC\text{-}ERT2}$ mice, 5 mg of tamoxifen (Sigma-Aldrich; dissolved in 200 µl of sunflower oil) was administered twice a day on days 6, 8, and 10 of the antibiotic treatment by orogastric gavage. Mice were sacrificed on day 14 of the treatment. $Ple^{fl/fl}$ mice received sunflower oil only.

3.8 Liquid diet feeding

9-week-old $Ple^{fl/fl}$ and $Ple^{\Delta IEC\text{-}ERT2}$ mice received a low-residue Ensure Plus (Abbott Laboratories) nutritional supplement diluted 1:1 in drinking water in the course of 2 weeks ad libitum in the absence of solid chow. Water was offered ad libitum. 5 mg of tamoxifen (Sigma-Aldrich; dissolved in 200 µl of sunflower oil) was administered twice a day on days 6, 8, and 10 of the liquid diet by orogastric gavage. Mice were sacrificed on day 14 of the liquid diet. Control mice received solid chow over the same time period. $Ple^{fl/fl}$ mice received sunflower oil only.

3.9 BrdU incorporation assay

14-week-old $Ple^{fl/fl}$ and $Ple^{\Delta IEC}$ mice received an intraperitoneal injection of 50 mg/kg 5-bromo-2'-deoxyuridine (BrdU; Sigma-Aldrich). Mice were sacrificed 2, 24, and 48 hours after

the injection. The small intestine and the colon were dissected and processed for immunohistochemistry. BrdU-positive cells were visualized by anti-BrdU antibody (BMC9318, Roche).

3.10 Whole-body imaging of inflammation

Myeloperoxidase (MPO) activity was detected by in vivo whole-body imaging using a specific XenoLight RediJect Chemiluminescent Inflammation Probe (PerkinElmer). A freshly thawed probe solution was administered by an intraperitoneal injection (200 mg/kg). Mice were immediately moved into the imaging chamber (Xtreme – whole-body imaging system, Bruker), and the number of photons produced by an inflammation probe was recorded (10 min after its administration) in anesthetized mice with 5 min exposure time.

3.11 Histology

Formalin-fixed, paraffin-embedded sections of the SI (ileum) and colon (5 µm thick) were deparaffinized and rehydrated as follows: 15 min in 100% xylene, 5 min in 100% ethanol, 3 min in 96% ethanol/water, 3 min in 80% ethanol/water, 3 min in 70% ethanol/water, and 5 min in distilled water (dH_2O). Slides were subsequently processed according to the required staining protocol:

3.11.1 **Haematoxylin-eosin staining**

The slides were stained with Mayer's hematoxylin for 10 min and rinsed under running tap water for 12 min. After rinsing in dH_2O, the slides were placed in a solution of 96% ethanol and water for 2 min, stained with Eosin Y for 30 seconds, and then washed in 96% ethanol and water for 2 min followed by 100% ethanol for 5 min. Finally, the slides were rinsed in xylene for 1 min and mounted using DPX hardening mounting media (Sigma Aldrich).

3.11.2 **Sirius Red staining**

The slides were stained with 0.1% Sirius red (SR) in picric acid for 1.5 hours, then rinsed in dH_2O. Subsequently, they were washed in a solution of 96% ethanol and water for 2 min,

followed by 100% ethanol for 5 min. Finally, the slides were rinsed in xylene for 1 min and mounted using DPX hardening mounting media (Sigma Aldrich).

3.11.3 **Alcian Blue staining**

The slides were stained with alcian blue solution in acetic acid for 30 min, then washed under running tap water for 2 min and rinsed in dH_2O. Next, they were counterstained with nuclear fast red (NFR) solution for 5 min, washed under tap water, followed by a wash in a solution of 96% ethanol and water for 2 min and then in 100% ethanol for 5 min. Finally, the slides were rinsed in xylene for 1 min and mounted using DPX hardening mounting media (Sigma Aldrich).

3.11.4 **Periodic acid Shiff staining**

Periodic acid Shiff (PAS) staining was conducted following the manufacturer's instructions (Sigma Aldrich). After rehydration, the slides were incubated in Periodic Acid Solution for 5 min, rinsed in dH_2O several times, and then incubated in Schiff's Reagent for 15 min. Subsequently, they were washed under running tap water for 5 min. Specimens were then counterstained in Hematoxylin Solution, Gill No. 3, for 90 seconds, rinsed under running tap water, and washed in a solution of 96% ethanol and dH_2O for 2 min, followed by 100% ethanol for 5 min. Finally, the slides were rinsed in xylene for 1 min and mounted using DPX hardening mounting media (Sigma Aldrich).

3.12 Immunohistochemistry and immunofluorescence

Rehydrated and deparaffinized sections were subjected to heat-induced antigen retrieval in either Tris- EDTA (pH 9) or citrate (pH 6) buffer supplemented with Tween 20 and further permeabilized with 0.1 M glycine and 0.1% Triton X-100 for 15 min. To block endogenous peroxidase activity and non-specific antigen interactions, sections were incubated with 0.3% hydrogen peroxide for 15 min followed by 5% bovine serum albumin (BSA; Sigma-Aldrich) in PBS supplemented with 0.1% Tween 20 (PBS-T) for 1 hour. Afterward, sections were incubated with primary antibodies at 4°C overnight, followed by incubation with

horseradish peroxidase- (HRP) or fluorophore-conjugated secondary antibodies at room temperature for 1 hour. The HRP signal was visualized with 3,3'-diaminobenzidine (DAB) detection kit (Roche).

Caco-2 and RPE cells seeded on coverslips or PDMS membranes were fixed with ice-cold methanol for 1 min or 2% paraformaldehyde (PFA)/PBS for 30 min, followed by permeabilization with 0,5% Triton X-100/PBS for 5 min. 2D organoids grown on polydimethylsiloxane (PDMS) membranes were fixed with 2% PFA/PBS for 30 min, followed by permeabilization with 0,5% Triton X-100/PBS for 20 min.

Non-specific antigen interactions were blocked with 5% BSA in PBS-T for 1 hour. Incubation with primary antibodies was 1 hour at room temperature or at 4°C overnight. The following primary antibodies were used: Ki-67 (GTX16667, GeneTex), keratin 8 (Troma I, Developmental Studies Hybridoma Bank), collagen IV (2150-1470, BioRad), pan-keratin (z0622, Agilent/Dako), E-cadherin (610181, BD Biosciences), desmoglein (611002, Progen), desmoplakin (651109, Progen), integrin α6 (ab181551, Abcam), plectin (GP21, Progen), chromogranin A (ab15160, Progen), keratin 20 (clone Ks20.8, Agilent/Dako), keratin 19 (Troma III, Developmental Studies Hybridoma Bank), β-actin (A2066, Sigma-Aldrich), lysozyme (A0099, Agilent/DAKO), mucin 2 (GTX100664, GeneTex), TROP2 (clone EPR20043, Abcam), phospho-Histone H2A.X (Ser139) (9718S, Cell Signalling; used for 2D organoid staining), phospho-Histone H2A.X (Ser139) (05-636, Millipore), vimentin (GTX100619, GeneTex), lamin A/C (SAB4200236, Sigma Aldrich), ad α-catenin (C2081, Sigma Aldrich). The following secondary antibodies were used: donkey anti-guinea pig Alexa Fluor (AF) 488, donkey anti-guinea pig AF594, donkey anti-guinea pig AF647, donkey anti-rabbit AF488, goat anti-rabbit AF594, donkey anti-rabbit AF647, goat anti-rabbit HRP-conjugated, donkey anti-mouse AF488, donkey anti-mouse RhodamineRedX, donkey anti-rat AlexaFluor488, donkey anti-rat Cross Adsorbed AF555, goat anti-mouse HRP-conjugated (all from Jackson ImmunoResearch). For immunolabelling of F-actin, samples were stained with phalloidin AF568 (A12380, Invitrogen). Nuclei were counterstained with Hoechst 33258 (Sigma-Aldrich) or DAPI (Biotechne, RnD). HRP-conjugated antibodies were visualized by DAB using the DAB Substrate (Roche Diagnostics) and counterstained with Mayer's hematoxylin (Sigma-Aldrich).

IHC samples were mounted into DPX hardening media (Sigma-Aldrich). Immunofluorescently labeled tissues were mounted into ProLong™ Gold Antifade Mountant

(ThermoFisher). Cell and organoid samples were mounted to 90% glycerol/N-propylgalate (Sigma-Aldrich) mounting media.

3.13 Visualization of Muc2 in colonic whole mounts

Staining was performed as described before (Brauer et al., 2016). Briefly, the intact colon was immediately fixed in Carnoy's fixative, and cut-open samples (5 x 8 mm) were incubated with an anti-Muc2 antibody (sc-15334, Abcam), at 4°C overnight followed by 1.5 hour incubation with fluorescently labeled secondary antibodies (donkey anti-rabbit AF488, Jackson ImmunoResearch) at room temperature. Nuclei were counterstained with Hoechst 33258 (Sigma-Aldrich). Samples were placed into 100% glycerol and immediately visualized using a Leica TCS SP8 confocal microscope.

3.14 Terminal deoxynucleotidyl transferase dUTP nick end labeling assay

Apoptotic cells were visualized on paraffin-embedded tissue sections using a Click-iT TUNEL Alexa Fluor 488 kit (ThermoFisher Scientific) according to the manufacturer's instructions.

3.15 Transmission electron microscopy

Immediately after a dissection, the distal colon free of feces, was cut into small pieces (3x3 mm) and fixed in 2.5% glutaraldehyde in Sorensen's buffer. Samples were post-fixed with 1% OsO4 in Sorensen's buffer, contrasted with 1% uranyl acetate in 50% ethanol overnight, dehydrated through a graded ethanol series followed by propylene oxide, and embedded into an Epon 812 substitute and Durkupan ACM (Sigma-Aldrich). Polymerized blocks were cut into 80-nm thin sections, contrasted with an aqueous solution of uranyl acetate, and inspected using a Morgagni 268 transmission electron microscope operated at 80 kV. Images were captured using a Mega View III CCD camera (Olympus Soft Imaging Solutions).

3.16 *In vivo* intestinal permeability assay

To measure intestinal permeability, fluorescein isothiocyanate (FITC)-dextran 4 (4000 MW; TdB Consultancy) dissolved in PBS was administered by oral gavage (0.6 g/kg body weight) to mice after a 4-hour fast. Blood was obtained by retro-orbital bleeding from anesthetized mice 4 hours later and collected in heparin-coated tubes (Microvette® CB 300, Sarstedt). Then plasma was separated. Serum-FITC levels were measured at 488 nm using an Envision 2104 MultiLabel Reader (PerkinElmer).

3.17 *Ex vivo* intestinal transepithelial electrical resistance measurement

The Ussing chamber technique was used to measure intestinal transepithelial electrical resistance (TEER). Whole thickness segments of the proximal and distal colon were mounted in Ussing chambers (exposed area 0.096 cm^2) filled with a Krebs-Ringer solution containing (in mM) Na^+ (140.5), K^+ (5.4), Ca^{2+} (1.2), Mg^{2+} (1.2), Cl^- (123.8), HCO_3^- (21), HPO_4^{2-} (2.4), $H_2PO_4^-$ (0.6), glucose (10), mannose (10), glutamine (2.5), and β-hydroxybutyrate (0.5). The segments were permanently oxygenated with a mixture of 95% oxygen and 5% carbon dioxide (pH 7.4, 37 °C). After 30 min of equilibration, TEER was measured using bipolar rectangular current pulses (10 µA, 200 ms) and a programmable voltage-clamp device (Müssler Scientific Instruments).

3.18 *In vitro* myeloperoxidase activity measurement

The distal colon was cut into small pieces and homogenized in a 50 mM phosphate buffer, pH 6, with 0.5% cetrimonium bromide (50 mg tissue/ml of buffer) and incubated at 60°C for 2 hours. MPO activity was assessed in a clear supernatant using 3,3',5,5'-tetramethylbenzidine (Sigma-Aldrich) as a substrate as described before (Pulli et al., 2013). Final activity is expressed in U per mg of protein.

3.19 Protein extraction and immunoblotting

Excised proximal and distal colons or ilea were cut open longitudinally and washed with PBS on ice. The colonic mucosa was scraped off using square coverslips. Snap-frozen mucosal

scrapings were homogenized in ice-cold RIPA (20 mM Tris-HCl pH 7.5, 150 mM NaCl, 1 mM Na_2EDTA, 1 mM EGTA, 1% NP-40, 0.5% SDS supplemented with Halt protease and a phosphatase inhibitor Cocktail (Thermo Fisher Scientific)) using the Tissue Lyzer II (Qiagen). Caco-2 and RPE cells were lysed in ice-cold RIPA by shearing through a 29G needle. Protein concentrations were determined using a BCA Protein Assay Kit (Thermo Fisher Scientific). Clarified lysates were resolved on SDS-PAGE and transferred to a nitrocellulose membrane for immunodetection. The following primary antibodies were used: ZO-1 (61-7300, ThermoFisher), E-cadherin (610181, BD Biosciences), desmoglein (611002, Progen), integrin α6 (ab181551, Abcam), integrin β4 (ab182120, Abcam), GAPDH (G9545, Sigma-Aldrich), keratin 8 (Troma I, Developmental Studies Hybridoma Bank), keratin 19 (Troma III, Developmental Studies Hybridoma Bank), keratin 18 (Ks18.04, Progen), Chk1 (sc-8408, Santa Cruz), ATR (13934, Cell Signaling), ATM (ab32420, Abcam), *p*-γH2A.X (05-636, Millipore), and pRb (ab181616, Abcam). The following secondary antibodies were used: HRP-conjugated goat anti-guinea pig IgG (Sigma-Aldrich), donkey anti-mouse IgG (IRDye 680RD), donkey anti-rabbit IgG (IRDye 800CW), and goat anti-rat (IgG IRDye 800CW; all Licor). Signals were detected with an ECL Plus Western Blotting Detection System (GE Healthcare Life Sciences) and recorded with a Luminescent Image Analyzer LAS-3000 (Fujifilm Life Science, Düsseldorf, Germany) or the Odyssey 9120 imaging system (Licor). The densitometry of blots was analyzed using QuantiScan version 1.5 software (Biosoft).

3.20 Quantitative reverse transcriptase polymerase chain reaction

RNA was isolated from snap-frozen mucosal scrapings (see above) using TRI reagent (Sigma-Aldrich) according to the manufacturer's instructions. The sample was placed in TRIzol reagent and incubated for 5 min at room temperature. Metal beads were added, and the samples were homogenized using a TissueLyser at 20 Hz for 4 min. The samples, including beads, were then centrifuged for 5 min at 17,000 RCF and 4°C. The supernatant was transferred to a clean Eppendorf tube, vigorously shaken with chloroform, incubated for 3 minutes, and centrifuged for 15 min at 17,000 RCF and 4°C. The upper phase was transferred to a clean tube, mixed with 2-propanol, incubated for 20 min at -20°C, and centrifuged for 10 min at 12,000 RCF and 4°C. The pellet was washed with 75% ethanol and centrifuged for 5 min at 7,500 RCF and 4°C. Finally, the pellet was air-dried and resuspended in 30 µl of RNase-free

water. The RNA concentration was determined using the NanoDrop ND-1000 (Thermo Fisher Scientific). If the samples were designated for RNA sequencing, they were provided to the Bioinformatics facility at this step. Otherwise, cDNA was prepared using M-MLV reverse transcriptase (ThermoFisher Scientific) with random oligo(dT)18 primers. qPCR was performed with SYBR Green JumpStart Taq ReadyMix (Sigma-Aldrich) using gene-specific primers (Table 1). Due to previously reported instability of reference genes in colitic mice (Eissa et al., 2016), expression of several reference genes was compared in $Ple^{fl/fl}$ and $Ple^{\Delta IEC}$ mice (Actb, Eef2, GAPDH, Hmbs and Tbp). As expression of none of these genes significantly differed between $Ple^{fl/fl}$ and $Ple^{\Delta IEC}$, relative RNA expression was calculated by the comparative threshold cycle method (ΔΔCt) (Pfaffl, 2001) using a GAPDH internal reference gene control.

GENE	**Forward (5'-3')**	**Reverse (5'-3')**
Plec	CGCTGTGACAACTTCACCAC *Plec*	CTCCAGGTTGGTCTGTCGAT
Krt18	TGAAGCGCTGGCTCAGAAGAAC	ACTGTGGTACTCTCCTCAATCTGC
Krt19	AGATCATGGCCGAGAAGAACCG	TGGGTGTTCAGCTCCTCAATCC
Krt8	AGGACTGACCGACGAGATCAAC	AACTCACGGATCTCCTCTTCATGG
Gapdh	AACTTTGGCATTGTGGAAGG	GTCTTCTGGGTGGCAGTGAT
Itga3	ATCAACCAGGATGGATTCCAGGAC	TTTGCCCAAGCCCTCAAATGGG
Itga5	ACTTGTCAGACACCCAGGGAAC	GCTCTGGTTCACAGCAAAGTAGTC
Itga6	AAGACCAGTGGATGGGAGTCAC	TCATATCGATGTGCACACGTCACC
Itgb1	TGTGGGTGGTGTACAAATACGAC	CATCACATCGTGCAGAAGTAGGC
Itgb4	CCTCTGGATTCCTGTGCAATGACC	AACCAGGCTCACACACACACTC
Dsp1/2	TCAGAGCCATGACTATTGCCAAGC	TGGAGCTCAAGGTCTTCGATGG
Dsg2	ACCGCCTTTCGGCATATTCGTC	TCCAATGCATAGCCTGTCAGCAG
Cdh1	TCATCGCCACAGATGATGGTTC	AACAGGACCAGGAGAAGAGTGC
Tjp1	TGCCCTGAAAGAAGCGATTCAGC	ACTTGTAGCACCATCCGCCTTC
Chek1	CAGCAAGGATCACCATCCCA	ACATACCACCTGATGTGGCG
Chek2	CTCGGCTATGGGCTCTTCAG	CCGGTACTTGTCCGTCCTTC
Brca1	GATCCAGCACCTCTCTTGGG	ACTTCTTGAATTTGGACGGCAG
Brca2	ACTGAGATTTGCAGAGGCCC	TCCTGCAGAGCATGGACTTG
Rb1	TCACCTCCTGCACTACTCAGA	GGGTGTTCGAGGTGAACCAT
Trp53	CCTCATCCTCCTCCTTCCCA	ATCCGACTGTGACTCCTCCA
Plk1	AGTTTTGGAGCTCTGTCGCA	TACTGGCAGCCCAGGACTAT
Cdkn1a	CGGTGTCAGAGTCTAGGGGA	AGGATTGGACATGGTGCCTG

Table 1 List of used RT-qPCR primers and their corresponding sequences.

3.21 RNA sequencing

RNA samples isolated from *Ple*$^{fl/fl}$ and *Ple*$^{\Delta IEC-}$ mice were subjected to RNA sequencing using the Illumina sequencer. For gene-level expression quantification, a bioinformatic pipeline nf-core/rnaseq was used. Individual steps included removing sequencing adaptors with Trim Galore!, alignment to the human reference genome GRCh38 (Ensembl annotation) with STAR, and quantifying expression on the gene level with Salmon. Per gene uniquely mapped read counts served as input for differential expression analysis using the DESeq2 R/Bioconductor package. Prior to the analysis, genes having less than 10 read counts in all samples were discarded. We supplied an experimental model assuming control group *Ple*$^{fl/fl}$ mice and *Ple*$^{\Delta IEC}$ mice as the main effect. The resulting per gene expression log2-fold changes (shrunken using the adaptive shrinkage estimator) were used for differential expression analysis. Genes exhibiting |Log2(Fold change)| > 1 and statistical significance adjusted p-value (False Discovery Rate; FDR) < 0.1 between compared groups of samples were considered as differentially expressed. Gene set enrichment analysis (GSEA) with differentially expressed genes was done using the clusterProfiler R/Bioconductor package against the Gene Ontology (GO) terms and Kyoto Encyclopedia of Genes and Genomes (KEGG) pathways.

3.22 Meta-analysis

The meta-analysis was aimed at studies comparing gene expression or protein abundance in human UC and healthy control samples. In the literature, we sought studies that used microarrays, RNA seq, or proteomics, and provided supplementary tables with the magnitude of change (fold change or log-fold change) and significance of the change (p-value or false discovery rate). Genes/proteins with |log2FoldChange| > 0.5 (LFC) and adjusted p-value (False Discovery Rate; FDR) < 0.05 were used for over-representation analysis (ORA) using fgsea R/Bioconductor package and our curated gene sets associated with mechanical resilience of the epithelium (keratin filaments, hemidesmosomes, desmosomes, actin).

3.23 Cell stretching

Stretch experiments were carried out on flexible PDMS (Sylgard) substrates with 4.0 cm^2 internal surface. The stretcher had a linear stage for a uniaxial stretch and was driven by a

computer-controlled stepper motor (Bonakdar et al., 2015). PDMS membranes were activated with Sulfo-SANPAH (0,5 mg/ml; Thermo Fisher Scientific). To monitor cell viability of Caco-2 and hCC cells in response to stretch, the PDMS membranes were coated with 50 µg/ml laminin or collagen type I (Coll I) in PBS at 4°C overnight, and 50,000 cells were seeded 24 hours prior to experiments. A uniaxial cyclic stretch was performed in an incubator under normal cell culture conditions (37°C, 5% CO2, 95% humidity) for 1 hour at 10, 20, 30 and 50% stretch amplitude (peak-to peak). For the analysis of DNA damage and genome instability of Caco-2 and RPE monolayers, the PDMS membranes were coated with either Coll I (Caco-2 cells) or fibronectin (FN; RPE cells) at a concentration of 50 µg/ml for 2 hours at 37°C, followed by seeding cells at a concentration of 250,000 cells/cm² onto these coated substrates 24 hours prior to the experiment. Mechanical stress was then applied under standard cell culture conditions. Cell monolayers were subjected to uniaxial cyclic stretch for 80 minutes with an amplitude 35% (Caco-2 cells) or 20% (RPE cells) and frequency 0.2 Hz. Cells were fixed immediately after stretching. To analyze chromosomal aberrations, cells were first subjected to a stretch, subsequently synchronized with nocodazole overnight, and fixed on the following day. Cells designated for anchorage-independent growth in soft agar experiment were trypsinized and counted for seeding immediately after the stretch.

3.24 Colon explant cultures

Excised distal colons were cut open longitudinally and washed with PBS on ice. The colonic tissue was cut into 1cm long pieces and placed into Advanced DMEM/F12 supplemented with 20% FBS and 1x penicillin/streptomycin. Colon explant cultures (CECs) were either pinned onto a PDMS membrane with the epithelium facing up and covered by 1 ml of media or left in a 6-well plate in a 5% CO_2/air humidified atmosphere at 37 °C as non-stretched controls. Colon explants underwent a 1-hour stretch with a 10% amplitude and a speed of 0.16 Hz.

3.25 Organoids

The colon was isolated from the mouse and placed in a Petri dish containing PBS on ice. The tissue was washed with ice-cold PBS using a plastic syringe, cut longitudinally, and placed

into a 50 ml falcon tube with ice-cold PBS. To thoroughly remove luminal content, the tube was shaken and the PBS was replaced until it remained clear. The colon was then incubated with 5 mM EDTA in PBS for 1 hour at 4°C on a rotator.

Meanwhile, colon organoid complete media was prepared using Advanced DMEM/F12 (Invitrogen), 1x Glutamax (Gibco), 1M HEPES, 1x penicillin/streptomycin (Sigma-Aldrich), R-spondin conditional medium, Noggin conditional medium, 1x B27 (Invitrogen), 1x N2 (Invitrogen), 50 ng/ml mouse EGF (Invitrogen), 1 mM n-acetylcysteine (Sigma-Aldrich), and 0.5 nM Wnt-Surrogate Fc fusion protein (ImmunoPrecise).

Colonic crypts were isolated by vigorously shaking the 50 ml tube and were then centrifuged at 300 RCF for 5 min at 4°C. The pellet was resuspended in Cultrex Reduced Growth Factor Basement Membrane Extract, Type 2 (Biotechne, RnD) and 20 µl drops containing the crypts were placed into pre-heated 6-well plates. After the gel solidified (approximately 15 min), 2 ml of colon organoid complete media was added to each well. The 3D organoids were passaged by mechanical pipetting once a week. After the third passage, the organoids were supplemented with 10 µM Y-27632 (Sigma-Aldrich) and 10 mM Nicotinamide (Sigma-Aldrich) and grown for 3-4 days.

Subsequently, the 3D organoids were mechanically disrupted into a suspension of single cells and very small organoids and seeded on Cultrex-coated (1:40 Cultrex/Advanced DMEM/F12) PDMS membranes, covered with media supplemented with Y-27632 and Nicotinamide. On day 2 after seeding, the media was changed to colon organoid complete media. On day 4, the media was changed and supplemented with 16 µM Plecstatin-1 (PST) or with DMSO as non-treated controls. After 16 hours of incubation, the 2D organoids were exposed to uniaxial cyclic stretch for 80 min, at 35% amplitude and 0.2 Hz speed. Immediately after stretching, the organoids were fixed with 4% PFA for 20 min, permeabilized with 0.5% Triton X-100 for 15 minutes, and then processed according to the immunofluorescence protocol.

3.26 Radial shear assay

Radial shear assay was performed on a customized spinning disk device (Branis et al., 2017) consisting of a rotating glass plate driven by compressed air. The glass plate was located

approximately 300 µm above a 35 mm plastic dish with adherent cells seeded at a density of 15000 cells/dish. The shear force was generated by a rotational speed of 1500 rpm and applied for 5 min. To assess the cell density, images of areas defined by radial distances 2-4 mm of the dish (corresponding to 0.7-1.5 Pa shear stress) were acquired before and after spinning. Then cells were stained with propidium iodide (PI; Fischer Scientific), and fractions of dead (PI-positive) and detached cells were calculated.

3.27 Magnetic tweezer microrheology

To determine the strength of cell-matrix adhesion, 5.09 µm carboxylated super-paramagnetic beads (microParticles GmbH) were coated with 20 µg/100 µl laminin or Coll I/ PBS. The bead slurry (50%) was added to Caco-2 and hCC cells grown on a 35 mm plastic dish and incubated for 1 hour under standard conditions. A magnetic field was generated as previously described (Kah et al., 2020) using a solenoid with a needle-shaped core (HyMu80 alloy, Carpenter). The needle tip was placed at a distance of 20 µm from a bead bound to the cell surface using a motorized micromanipulator (Injectman NI-2, Eppendorf). During measurements, bright-field images were taken by a CCD camera (ORCA ER, Hamamatsu) at a rate of 40 frames/s. The median of bead detachment (50% of adherent beads), determined under increasing forces of up to 15 nN, was used for calculating cumulative rupture forces.

3.28 Cell confinement

Cell confinement experiments were carried out using polyacrylamide gel pads prepared as described previously (Le Berre et al., 2014; Matthews et al., 2020). Gel pads were prepared in squared molds of size 1,3 x 1,3 cm. 5 ml solutions in water were prepared as follows: ~20 kPa: 927.5 µl acrylamide (AA) (40%, Bio-Rad), 500 ul bisacrylamid (BA) (2%, Bio-Rad), ~10 kPa: 927.5 µl AA, 237,5 ul BA, ~5 kPa: 927,5 µl AA, 150 ul BA. 50 ul APS (Sigma-Aldrich) and 10 µl TEMED (Sigma-Aldrich) was added to each and 850 µl of solution was pipetted into mold to prepare pad of thickness 1 mm. Gels were then incubated with cell culture media at least 1 hour before use.

Cells were seeded on Coll I (Gibco) or FN (Sigma-Aldrich) (both: 10 µg/ml, 37°C, 2 hours) coated coverslips in a density 100.000 cells/cm^2 and cultivated overnight to reach 90% confluency. To enrich the population with a fraction of mitotic cells, cells were treated overnight (14 hours) with a low dose of nocodazole (40 ng/ml) that arrested around 30% of the cell population in prometaphase. After washing out of nocodazole with PBS, cells were left to recover in a cell culture incubator for 15 min. The polyacrylamide (PAA) gel pads of specific stiffness were carefully placed on the cells on coverslips covered with half the amount of cultivation media. The second half of the media was layered slowly over the pad and placed on the coverslip to avoid the pad floating in the media. Cells were placed to cell culture incubator for 20 min and then PAAG pads were carefully removed. Cells were fixed immediately after pad removal or let to pass to further phases of mitosis or to the G1 phase.

3.29 Faecal microbiota analysis

Stool samples were collected from 6 *Ple*$^{fl/fl}$ and 6 *Ple*$^{\Delta IEC}$ mice at the age of 4, 12 and 20 weeks and analyzed for bacterial composition as described earlier (Kostovcikova et al., 2019). Briefly, genomic DNA was extracted with a MasterPure™Complete DNA and RNA Purification Kit (Epicentre) with repeated bead-beating in Lysing Matrix Y tubes using a FastPrep homogenizer (both MP Biomedicals). Next, the V3-V4 region of the 16S rRNA gene was amplified using barcoded bacterial 16SrRNA-specific primers 341F (5'-CCTACGGGNGGCWGCAG-3') and 806R (5'-GGACTACHVGGGTWTCTAAT-3'). PCR amplification was performed with KAPA 2G Robust Hot Start DNA Polymerase (Kapa Biosystems), with following concentrations: Buffer B 1×, Enhancer 1×, dNTP 0.2 mM each, primers 0.5 µM each, DNA sample 4 ng/µl, KAPA polymerase 0.5 U. Cycle parameters were 3 min 94°C, 25 cycles of 30 s at 94°C, 1 min at 54.2°C, and 1 min 15 s at 72°C; the final extension was at 72°C for 10 min. Three PCR products were pooled to minimize random PCR bias, and the length of PCR products was checked by agarose gel electrophoresis. Equal amounts of each sample were plate-purified using the SequalPrep™Normalization Plate (96) Kit (Invitrogen). Then equimolar amounts of PCR products from each sample were pooled, and MiSeq platform compatible adapters were ligated using a TruSeq DNA PCR-Free LT Kit (Illumina). The libraries were quantified using a KAPA Library Quantification Kit (Illumina) and sequenced on a MiSeq platform using a 2× 300bp kit at the CEITEC Genomics Core Facility.

Sequencing data were processed using QIIME (Quantitative Insights Into Microbial Ecology) version 1.9.1 (Caporaso et al., 2010). Quality filtering, chimera detection, read demultiplexing, and read clustering were done as described previously (Bajer et al., 2017). Raw reads were demultiplexed and quality filtered, and all sequences containing unknown base calls were excluded. Chimeric reads were detected and discarded using USEARCH algorithms (Edgar and Flyvbjerg, 2015). The final dataset contained 80,185 high-quality reads (median 1,306 reads per sample, range 28 - 8766). To make samples comparable, 4 samples with fewer than 460 reads were removed from the analysis, and the OUT table was rarefied at a depth of 460 sequences per sample. Operational taxonomic units (OTUs) were clustered at a 97% similarity level, and representative sequences were identified using a Ribosomal Database Project classifier (Wang et al., 2007b) against bacterial GreenGenes database 13.8 (DeSantis et al., 2006). For a microbiota analysis, PD whole tree metrics measuring the total descending branch length in the phylogenetic tree for each OTU was used to describe alpha diversity. The Principle Coordinate Analysis (PCoA) based on unweighted UniFrac distance metrics was used to describe beta diversity. The sequence data are available in the Sequence Read Archive (SRA; http://www.ncbi.nlm.nih.gov/sra) under BioProject accession number PRJNA561691.

3.30 High salt extraction of Caco-2 cells

High salt extraction of Caco-2 cells was performed as described previously (Toivola et al., 2002). Cell fractions were prepared by solubilizing cells for 2 min at 4°C with a buffer containing 1% TX-100, 5 mM EDTA, and Halt Protease Inhibitor Cocktail (Thermo Fisher Scientific) in PBS pH 7.4, followed by centrifugation (16,000 RCF, 10 min). The supernatant was collected as a soluble fraction. The pellet was homogenized in 1 ml of 10 mM Tris-HCl pH 7.6, 140 mM NaCl, 1.5 M KCl, 5 mM EDTA, 0.5% Triton X-100, supplemented with Halt Protease Inhibitor Cocktail. After 30 min (at 4°C), the homogenate was pelleted (16,000 RCF; 10 min), and the pellet (insoluble fraction) was rehomogenized with 5 mM EDTA in PBS pH 7.4. The resulting homogenate was further centrifuged (16,000 RCF; 10 min) to obtain the insoluble keratin-enriched high salt extract (HSE). All fractions were resolved by SDS-PAGE and their composition was analyzed by immunoblotting.

3.31 Double-strand break repair assay

Cells seeded on Coll I (Gibco) or FN (Sigma-Aldrich) (both: 1 µg/ml, 37°C, 2 hours) coated coverslips were exposed to ionizing radiation - 2 Gy of X-rays (X-RAD 225XL, Accella), fixed 10 min in 4% paraformaldehyde before or after radiation in indicated time points of recovery and immunostained with antibody against *phospho*-γH2A.X.

3.32 Anchorage-independent growth in soft agar

Well of a 12-well plate was coated with 1.5 ml of 0.5% low gelling temperature agarose (Sigma) solution dissolved in a standard culture medium. After solidification, 5×10^3 cells were suspended in 1 ml of 0.35% agarose in culture medium, seeded on top of 0.5% agarose, and overlaid with 1 ml culture medium after solidification. Cells were cultured for 40 days at 37 °C and 5% CO2, and culture medium was exchanged once a week. The colonies were stained and fixed with 0.01% crystal violet in 4% PFA and captured by Zeiss Axio.Zoom V.16 microscope. Size and area of colonies was analyzed from binary masks created using custom made ImageJ macro created by Jan Valecka, IMCF IMG.

3.33 Histological and morphometric analyses

Blinded histopathology evaluation of human colon biopsy samples stained with H&E was independently performed by two trained pathologist (E.S. and L.B.). Blinded histopathology evaluation of mouse colon sections stained with H&E and PAS was performed by a trained pathologist (J.S.). The numbers of Ki-67-, PAS-, ChgA-, K20-, lysozyme-, and TUNELpositive cells, and the numbers of detached cells per crypt (colon) or villus (SI) were counted and normalized to the total numbers of IECs. At least 7 crypts or villi were analyzed per mouse and genotype. Crypt and villus damage was assessed as a percentage of crypts/villi with >10% of IECs detached from the BM. To analyze migration of IECs in the colonic crypt, the relative position of each BrdU-positive cell within the crypt was assessed. For scoring the cell position, cells were numbered sequentially from the crypt base to lumen, with cell position 0 being occupied by the first cell at the base of each crypt. The Muc2-positive area was measured and quantified using Fiji software. At least 8 images were analyzed per genotype. The morphometry of IEC (the largest and the smallest orthogonal diameter) was evaluated from images immunolabeled

with anti-K8 and anti-Itgα6 antibodies using Fiji software. At least 250 IEC were assessed in 3 mice per genotype. To analyze *p*-γH2A.X positive foci in IECs, manually quantified cell counts were normalized to individual nuclei. The area of *p*-γH2A.X positive foci was then measure using Fiji software. Using Ki67 costaining, nuclei were separated into stem (first three positions from the crypt base), proliferative (Ki67 positive), and differentiated zones (Ki67 negative). At least 10 crypts were analyzed per genotype and condition. Measurement of angles during cell adaptation was assessed using staining against phalloigin (actin reorientation and cell mass reorientation and Ferret's diameter) and DAPI (nucleus reorientation). Nuclear wrinkles were analyzed using LMNA/C staining. Nuclei with or without wrinkles were then counted manually. At least 30 cells were quantified per genotype and condition.

3.34 Image acquisition and processing

Immunofluorescence images were acquired using a Leica TCS SP8 confocal fluorescence microscope (Leica Microsystems) with HC PL FLUOTAR 25×/0.75 NA and HC PL APO 63×/1.4 NA immersion oil objectives. For tissue sections, z-stacks were acquired, and representative maximal projections were shown. Super-resolution microscopy was performed using either a DeltaVision OMX microscope with a Blaze SIM module (GE Healthcare Life Sciences) and an U APO N 100×/1.49 NA immersion oil objective (K8 staining) or a Leica TCS SP8 STED 3X microscope (Leica Microsystems) with an HC PL APO 100×/1.4 NA immersion oil objective (actin and tubulin staining). Raw images were deconvolved using Huygens Essential 4.0.0 software (Huygens; Scientific Volume Imaging). Representative maximal projections of z-stacks are shown. Bright-field images were acquired on a Leica DM6000 wide-field microscope with an HC PLAN APO 20×/0.7 NA dry objective. Post-acquisition processing was performed with Photoshop CS6 (Adobe Systems Inc., Mountain View, CA) and the open-source Fiji image processing package (Schindelin et al., 2012). Fully automated wide-field image acquisition was performed using Scan^R system (Olympus IX81, UPLFLN 40x/1.3 OIL objective, sCMOS camera Hammamatsu ORCA-Flash4.0 V2) equipped with ScanR image acquisition and ScanR analysis software.

3.35 Statistics

All results are presented as mean ± SEM. All normally distributed parametric data were analyzed by two-tailed unpaired Student *t*-test. Comparisons of multiple groups to controls were performed using two-tailed one-way ANOVA. Multiple comparison test in analysis for *p*-γH2A.X populations, chromosomal aberrations, and micronuclei after cell stretching and confinement was assessed by the Bonferroni method. Comparisons of frequency distributions of BrdU-positive cells were analyzed with Mann–Whitney test. Survival curves were analyzed by Mantel–Cox test. Statistical analyses were performed using GraphPad Prism 5 (GraphPad Software, Inc., La Jolla, CA). Comparisons of detachment forces were done with bootstrapping (sampling with replacement) with 1000 replicates. Statistical significance was determined at the levels of *P < 0.05, **P < 0.01, †P < 0.001; *n* values are specified in the figure legends.

4 RESULTS

4.1 Aim 1.

4.1.1 Attenuated expression of plectin in human patients with UC

Our primary aim was to assess plectin expression in patients with UC. To achieve this, we obtained over 100 biopsy samples of non-dysplastic mucosa from UC patients and healthy individuals (in collaboration with the Hepatogastroenterology Department at the Institute for Clinical and Experimental Medicine, Prague, Czech Republic). Representative samples were analyzed for plectin expression using histological and immunohistochemistry (IHC) techniques (*n* = 5 UC; *n* = 5 healthy), while the remaining samples were used for RNA isolation (*n* = 104 UC; *n* = 31 healthy). Immunolabeling of healthy biopsies revealed a prominent plectin staining along the apical and BM of IECs (Figure 12A), a pattern that has been seen in colon and SI mouse tissue (Figure 12B). While plectin staining disclosed continuous signals in healthy patients, it appeared more fragmented in UC patients. The discontinued signal observed in UC patients likely corresponds to GCs, which were highly abundant in UC colon tissue (Figure 12C). Moreover, mRNA expression profiling showed decreased levels of plectin in patients with UC, with this reduction being directly proportional to the severity of inflammation (Figure 12D, E). These results suggest that plectin is involved in the pathophysiology of UC and that plectin may potentially serve as a biomarker for UC progression.

4.1.2 IEC-specific plectin-deficient mice develop a colitic phenotype due to intestinal barrier dysfunction

To investigate the role of plectin in intestinal pathophysiology, we generated a mouse model with IEC-specific deletion of plectin ($Ple^{\Delta IEC}$) using cre/loxP system (details can be found in Chapter 3.2). Immunohistochemistry verified the absence of plectin expression in the colonic epithelium of $Ple^{\Delta IEC}$ mice (Figure 13A). $Ple^{\Delta IEC}$ mice exhibited notable reductions in body weight (Figure 13B), diarrhea (Figure 13C), and also developed rectal prolapse as early as 17 weeks of age (Figure 13D).

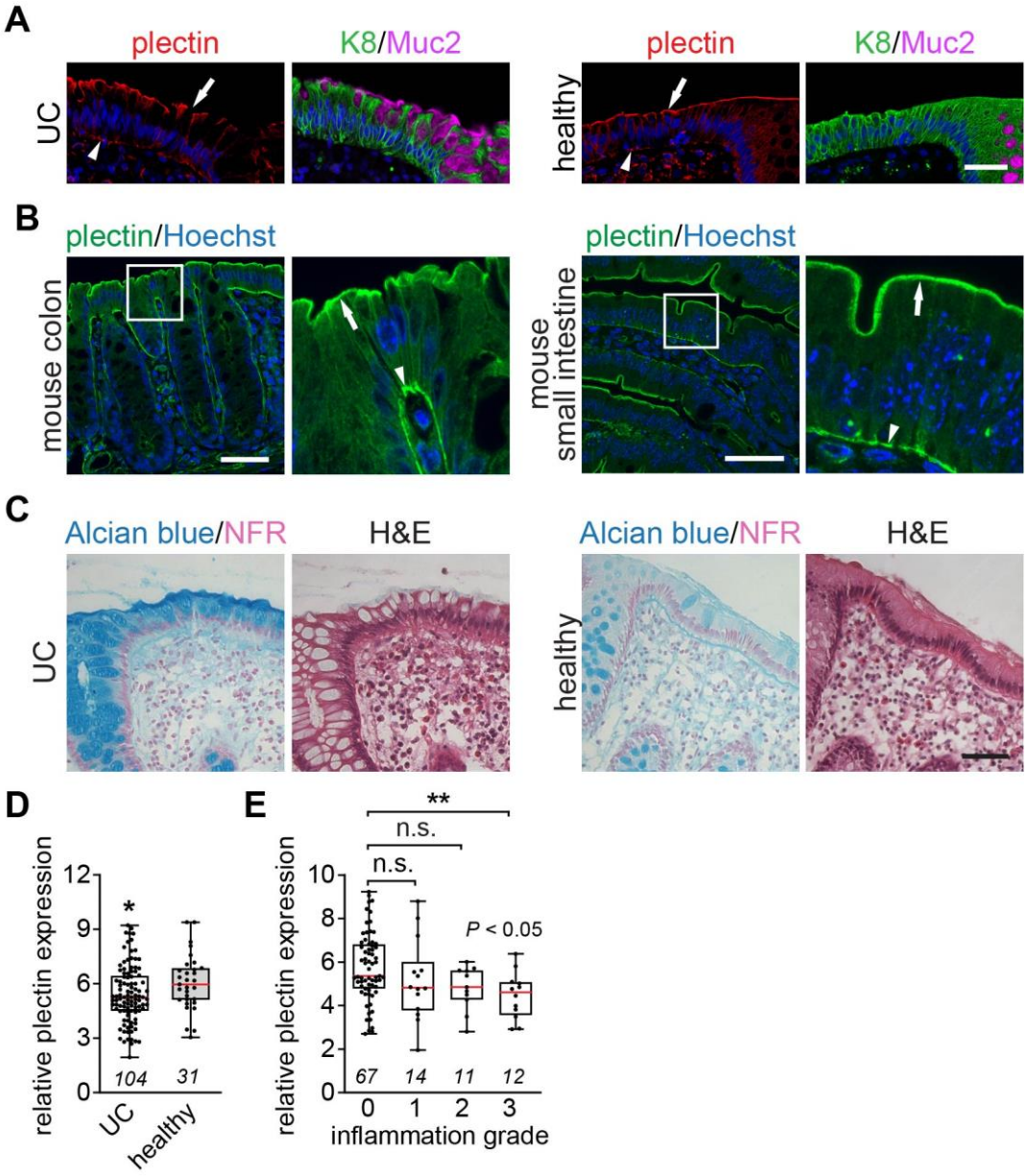

Figure 12 Loss of plectin is associated with ulcerative colitis (UC) in human patients. (A) Paraffin-embedded colon sections from UC patients (UC) and healthy controls (healthy) were immunolabeled with antibodies to plectin (red), keratin 8 (K8; green), and mucin 2 (Muc2; magenta). Nuclei were stained with Hoechst (blue). Arrows, apical IEC membrane; arrowheads, basal IEC membrane. Scale bar, 40 µm. **(B)** Paraffin-embedded sections from distal colon and small intestine of *Ple*$^{fl/fl}$ mice were immunolabeled with antibodies to plectin (green). Nuclei were stained with Hoechst (blue). Plectin staining at the apical (arrows) and basal (arrowheads) membranes. Scale bar, 50 µm. Boxed areas show ×4.5 images. **(C)** Paraffin-embedded colon sections from UC patients and healthy controls were stained with Alcian blue (mucus), nuclear fast red (NFR; nuclei), and hematoxylin-eosin (H&E). Scale bar, 50 µm. **(D)** Relative *plectin* mRNA levels in rectum biopsies collected from healthy controls and patients with active UC. Scattered boxplots show individual data points, median, 25th, and 75th percentile with whiskers reaching the last data point. The numbers of included participants per cohort are indicated in the graph. **(E)** Relative *plectin* mRNA expression in rectum biopsies collected from UC patients clustered based on inflammation scored in H&E-stained rectum sections. Scattered boxplots show individual data points, median, 25th, and 75th percentile with whiskers reaching the last data point. The numbers of included participants per cohort are indicated in the graph. Data are presented as mean ± SEM, n.s. not significant, **P* < 0.05, ***P* < 0.01, †*P* < 0.001.

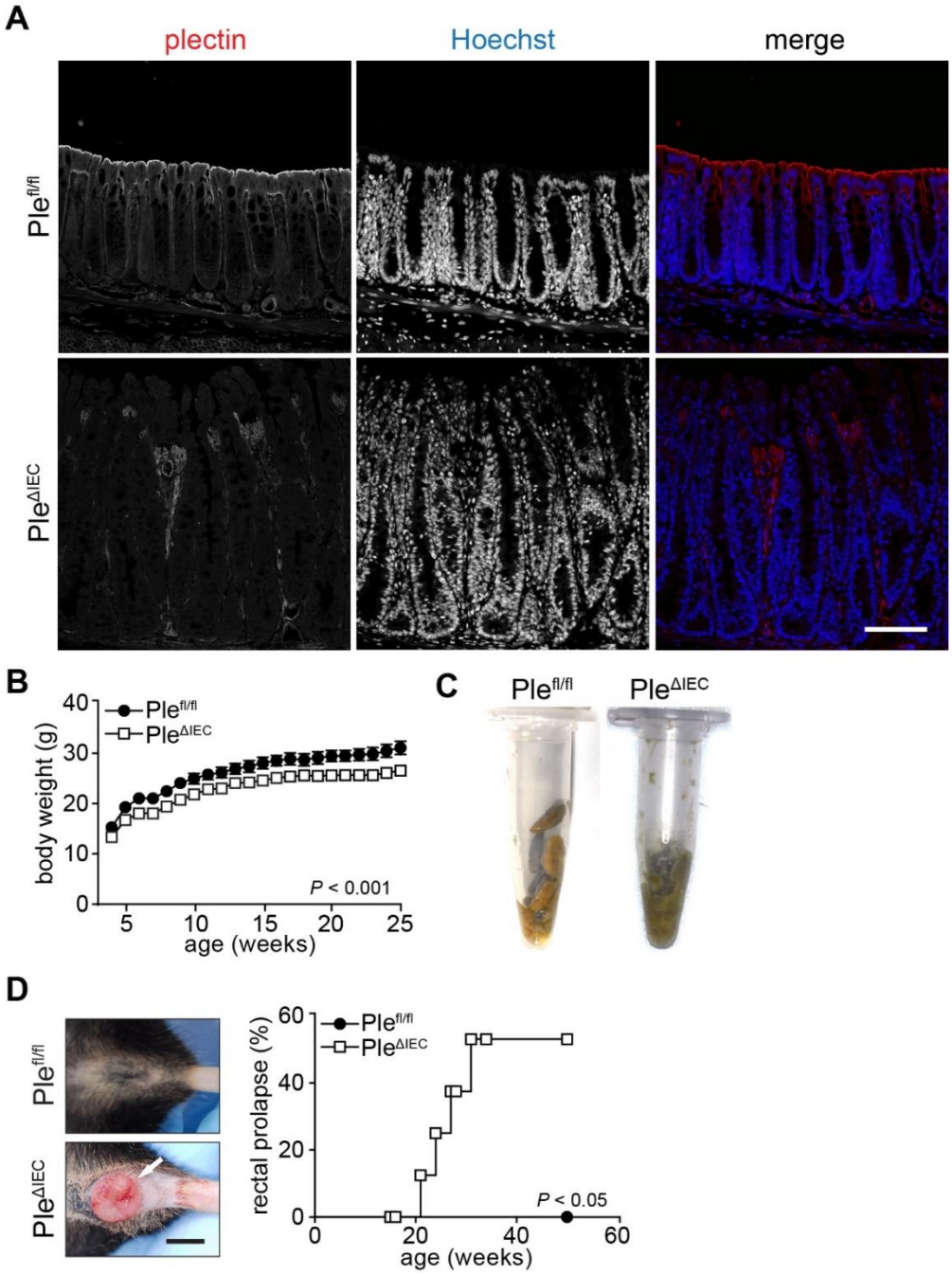

Figure 13 Characterization of mouse carrying IEC-specific deletion of plectin (*Ple$^{\Delta IEC}$*). (A) Paraffin-embedded distal colon sections from *Ple$^{fl/fl}$* and *Ple$^{\Delta IEC}$* mice were immunolabeled with antibodies to plectin (red). Nuclei were stained with Hoechst (blue). Scale bar, 100 µm. Note immunofluorescence signal in plectin-positive mesenchymal niche of both *Ple$^{fl/fl}$* and *Ple$^{\Delta IEC}$* colons. **(B)** Body weight of *Ple$^{fl/fl}$* and *Ple$^{\Delta IEC}$* mice was monitored for 25 weeks, $n = 7$. **(C)** Stool consistency in *Ple$^{fl/fl}$* and *Ple$^{\Delta IEC}$* mice. **(D)** Representative images of the rectum of 30-week-old *Ple$^{fl/fl}$* and *Ple$^{\Delta IEC}$* mice. Scale bar, 1 cm. Kaplan–Meier graph shows age-related rectal prolapse incidence. Data are presented as mean ± SEM, $^{*}P < 0.05$, $^{\dagger}P < 0.001$.

Previous studies have established a close relationship between the loss of IEB integrity and the onset of inflammation in patients with UC (Chang et al., 2017; Kiesslich et al., 2012; Vivinus-Nebot et al., 2014). Thus, we explored the integrity of the IEB in *Ple$^{\Delta IEC}$* mice. First, we performed the fluorescein isothiocyanate (FITC)-dextran intestinal permeability assay in mice

at ages ranging from 4, 6, 12, and 20-week-old (Figure 14A). *Ple*$^{fl/fl}$ mice exhibited consistently low intestinal permeability across all examined stages. In contrast to *Ple*$^{fl/fl}$ mice, FITC-dextran penetration into the bloodstream was markedly elevated in *Ple*$^{\Delta IEC}$ mice as early as 4-week-old mice. This heightened permeability persisted in *Ple*$^{\Delta IEC}$ mice at 6, 12, and 20 weeks, demonstrating a progressive increase over time, with the highest levels observed in the 20-week-old *Ple*$^{\Delta IEC}$ mice. Since FITC-dextran can cross the gut barrier and enter the bloodstream in both small and large bowels, we decided to specifically test colonic permeability of proximal and distal colons individually by the *ex vivo* transepithelial electrical resistance [TEER; (Figure 14B)]. Unless otherwise stated, all following experiments were performed with 12-week-old *Ple*$^{fl/fl}$ and *Ple*$^{\Delta IEC}$ mice. In *Ple*$^{\Delta IEC}$ mice, both proximal and distal colon segments displayed comparable and overall lower TEER values than in *Ple*$^{fl/fl}$ mice. Moreover, in *Ple*$^{fl/fl}$ mice, the TEER in the distal colon demonstrated a 2-fold elevation compared to the proximal part (Figure 14A). Collectively, these results indicate an extensively compromised IEB in *Ple*$^{\Delta IEC}$ mice.

The compromised IEB allows the infiltration of luminal bacteria into the submucosa, and subsequent development of the inflammation. Examination of hematoxylin-eosin (H&E) stained colonic tissue of 30-week-old *Ple*$^{\Delta IEC}$ mice uncovered colonies of bacteria colonizing the underlying mucosa (Figure 14C). Subsequently, we scrutinized *Ple*$^{fl/fl}$ and *Ple*$^{\Delta IEC}$ mice for intestinal inflammation. Using chemiluminescence-based whole-body imaging [WBI; (Brauer et al., 2016)], we visualized inflammatory lesions characterized by an infiltration of neutrophils positive for myeloperoxidase (MPO) signal. While the signal was completely absent in *Ple*$^{fl/fl}$ mice, in *Ple*$^{\Delta IEC}$ mice, these positive signals were concentrated in the intestinal region (Figure 14D). These findings were supported by *ex vivo* measurements, which showed significantly elevated MPO activity in *Ple*$^{\Delta IEC}$ mice (Figure 14E). Histopathological evaluation of colonic tissue substantiated the presence of inflammation, as evidenced by various parameters representing histological inflammation indices [such as the inflammation extent, lymphatic follicle numbers, lymphatic follicle maximal size, acute/chronic inflammation extent, acute/chronic inflammation intensity, lymphocytes in lesion, edema, and ulceration (Figure 14F, G)]. The data suggest that the absence of plectin in IECs increases intestinal barrier permeability, which leads to the translocation of luminal bacteria and causes persistent intestinal inflammation, symptoms collectively termed as colitis.

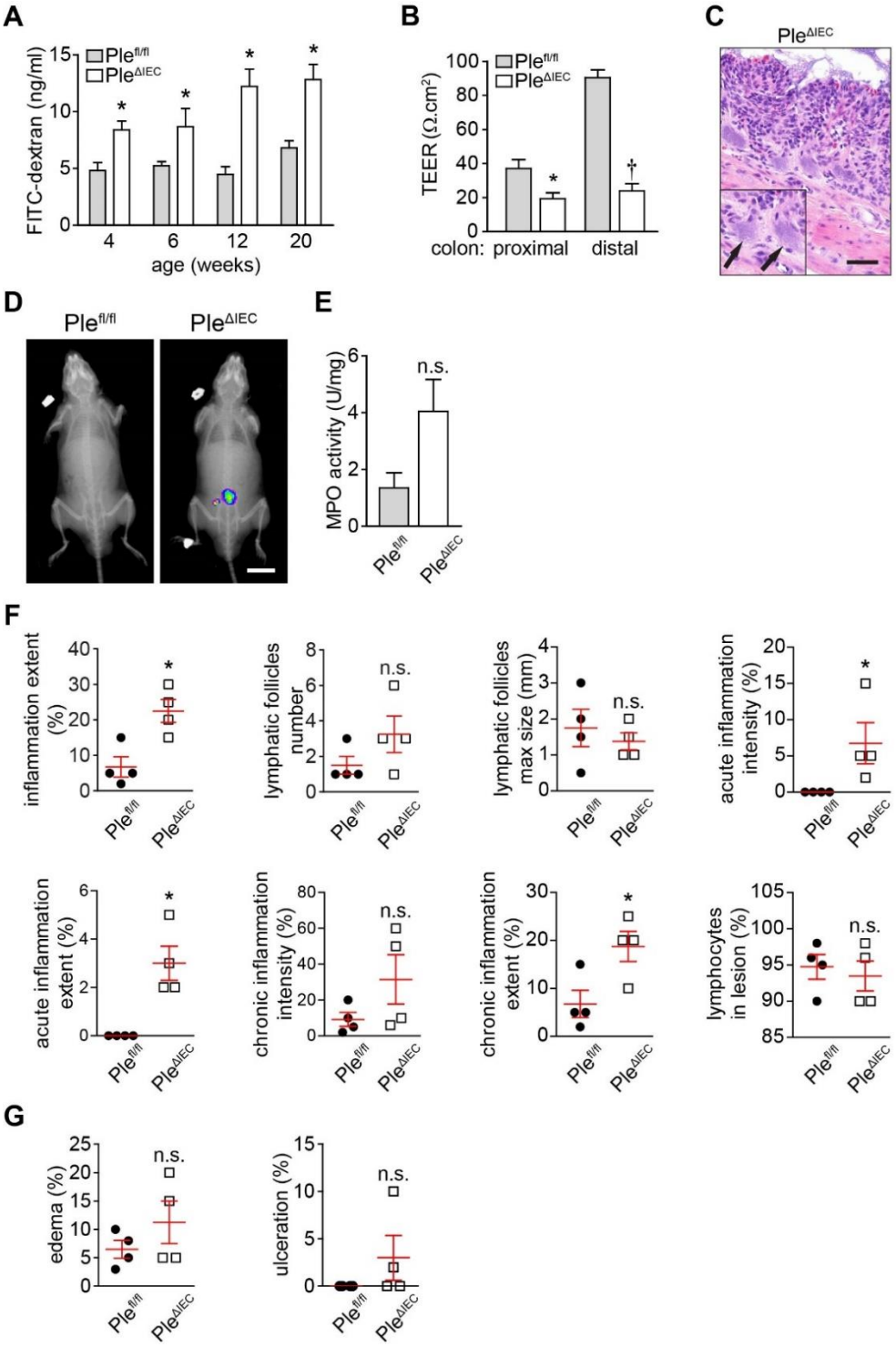

Figure 14 Loss of plectin leads to intestinal epithelial barrier dysfunction with concomitant intestinal inflammation in *Ple$^{\Delta IEC}$* mice. (A) Intestinal transepithelial electrical resistance (TEER) measured ex vivo in both proximal and distal colons of 12-week-old *Ple$^{fl/fl}$* and *Ple$^{\Delta IEC}$* mice, $n = 4$. **(B)** In vivo permeability of mucosa of *Ple$^{fl/fl}$* and *Ple$^{\Delta IEC}$* mice (at the age indicated) measured by monitoring 4-kDa fluorescein isothiocyanate (FITC)-dextran levels in plasma 4 h after orogastric gavage, $n = 3–7$. **(C)** Representative image of Ple$^{\Delta IEC}$ colon section from 30-week-old *Ple$^{\Delta IEC}$* mouse stained with H&E. Arrows, bacterial patches in the mucosa. Scale bar, 50 µm. **(D)** *In vivo* chemiluminescence images of 12-week-old *Ple$^{fl/fl}$* and *Ple$^{\Delta IEC}$* mice injected with myeloperoxidase (MPO) inflammation probe. **(E)** MPO activity (a marker of neutrophil infiltration) measured in colon lysates from 12-week-old *Ple$^{fl/fl}$* and *Ple$^{\Delta IEC}$* mice, $n = 3$. **(F)** Quantification of inflammatory parameters on H&E-stained sections of *Ple$^{fl/fl}$* and *Ple$^{\Delta IEC}$* colons. Graphs show percentage of inflammation extent, lymphatic follicles number, maximal (max) sizes of lymphatic follicles, percentage of acute inflammation intensity, acute inflammation extent, chronic inflammation intensity, chronic inflammation extent, and lymphocytes in lesion. **(G)** Quantification of tissue damage assessed from H&E-stained sections of *Ple$^{fl/fl}$* and *Ple$^{\Delta IEC}$* colons (percentage of edema and ulceration). $n = 4$. Data are presented as mean ± SEM, n.s. not significant, $^*P < 0.05$, $^\dagger P < 0.001$.

4.1.3 **Loss of plectin leads to hyperproliferation and aberrant differentiation of IECs**

Upon histological examination of H&E stained intestinal sections, we noticed that both colonic and SI mucosa of *Ple*$^{\Delta IEC}$ mice were markedly thicker with deeper crypts (Figure 15A and Figure 17A). Closer inspection revealed enormous crypt/villus damage (Figure 15A and Figure 17A) defined by a detachment of IECs from the subjacent BM. Moreover, compared to *Ple*$^{fl/fl}$ crypts, the enlarged crypts of *Ple*$^{\Delta IEC}$ mice were populated by an extended fraction of TA cells, marked by proliferative marker Ki-67 (Figure 15B). Interestingly, this hyperproliferation was not observed in the SI (Figure 17B), where the number of TA cells was comparable between *Ple*$^{fl/fl}$ and *Ple*$^{\Delta IEC}$ mice.

To address the spatio-temporal migratory potential of TA cells in *Ple*$^{\Delta IEC}$ crypts, we carried out the BrdU incorporation assay at 3 time points (2, 24, and 48 hours). In *Ple*$^{fl/fl}$ crypts, the 5-bromo-2'-deoxyuridine (BrdU)-positive (BrdU^{+}) populations inhabited bases of crypts. However, in *Ple*$^{\Delta IEC}$ crypts, BrdU^{+} cells inhabited almost all crypt areas and migrated even to the upper differentiated zone (Figure 15C). Interestingly, hyperproliferation and increased crypt damage were not caused/compensated by apoptosis in *Ple*$^{\Delta IEC}$ mice. Labeling of apoptotic cells via terminal deoxynucleotidyl transferase dUTP nick end labeling (TUNEL) did not show any differences between *Ple*$^{fl/fl}$ and *Ple*$^{\Delta IEC}$ mice (Figure 16A).

The increase in proliferative TA population prompted us to investigate proportions of differentiated IECs. First, we inspected GCs via periodic acid Shiff (PAS) staining as well as IHC of Muc2. Both stainings revealed hyperplasia of GCs in *Ple*$^{\Delta IEC}$ colonic crypts (Figure 15D) with deteriorated mucin architecture in *Ple*$^{\Delta IEC}$ mice (Figure 15E). In contrast, GC numbers were equal between *Ple*$^{fl/fl}$ and *Ple*$^{\Delta IEC}$ mice in villi of SI (Figure 17C). Next, specific labeling of chromogranin A (ChgA), a marker of EEC cells, showed equal populations between *Ple*$^{fl/fl}$ and *Ple*$^{\Delta IEC}$ mice in both colon and SI (Figure 16B and Figure 17D). K20, a marker of differentiated absorptive enterocytes, documented enlarged areas of differentiated cells in colonic crypts (Figure 16C and Figure 17) but showed reduced K20-positive (K20^{+}) populations in *Ple*$^{\Delta IEC}$ villi in the SI. PCs, immunolabeled for the marker lysozyme and found exclusively in the SI, showed no population differences between *Ple*$^{fl/fl}$ and *Ple*$^{\Delta IEC}$ mice (Figure 17F).

Overall, the data imply that plectin deficiency leads to epithelial damage, characterized by detachment of IECs from adjacent BM in both colon and SI. The damage is accompanied by hyperproliferation and compromised differentiation of IECs in the colon, resulting in altered

crypt organization. Surprisingly, except for smaller populations of K20^{+} cells, proliferation, and differentiation dysbalance changes between *Ple$^{fl/fl}$* and *Ple$^{\Delta IEC}$* mice were not observed in the SI.

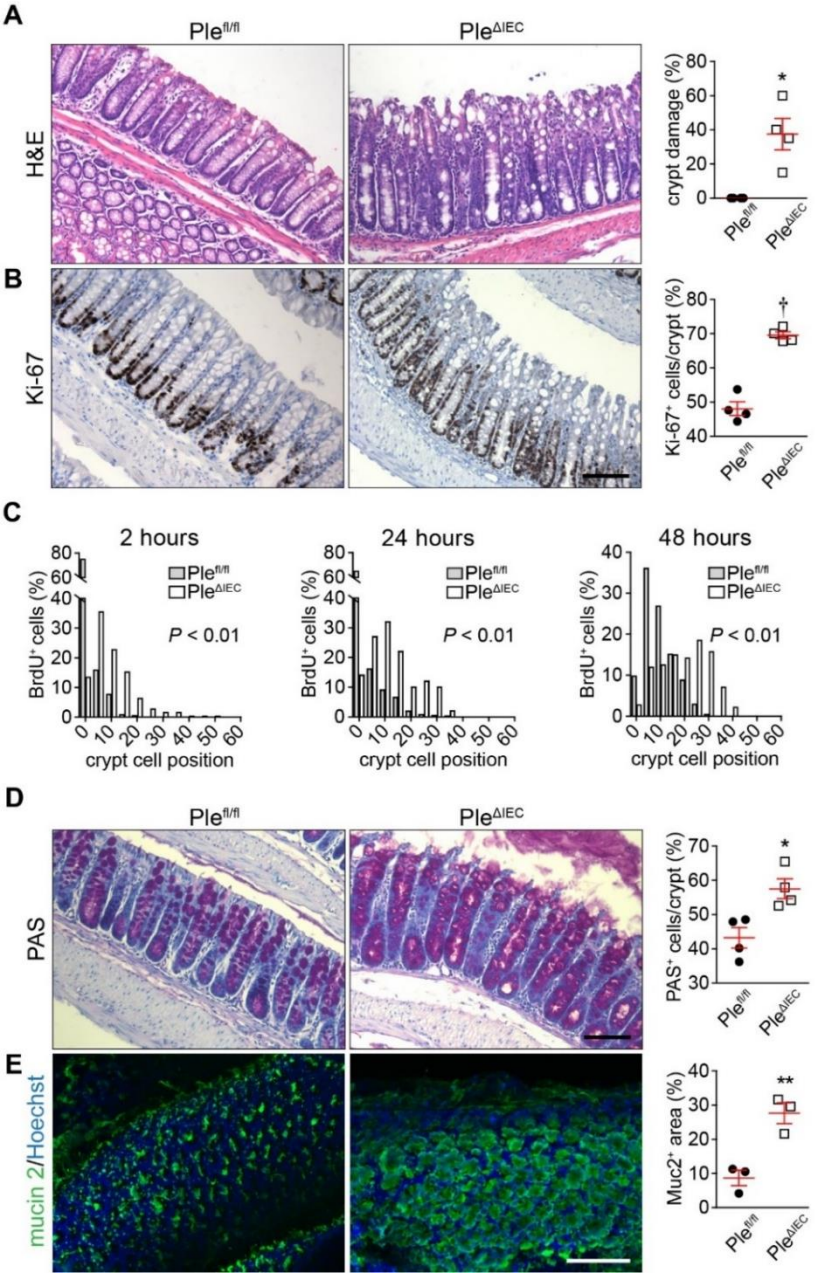

Figure 15 Plectin-deficient IECs in the colonic crypt exhibit aberrant proliferation and differentiation resulting in altered crypt organization. (A, B) Representative images of H&E staining (A) and Ki-67 immunohistochemistry (IHC; proliferating cells) (B) of *Ple$^{fl/fl}$* and *Ple$^{\Delta IEC}$* paraffin-embedded colon sections. Scale bar, 100 µm. Graphs show quantification of colonic crypt damage given as a percentage of crypts with >5% of IECs detached from basement membrane (BM; A) and percentage of the Ki-67-positive (Ki-67^{+}) IECs per crypt (B), n = 3–4. **(C)** Histograms showing the percentage of BrdU-positive (BrdU^{+}) cells in given positions of *Ple$^{fl/fl}$* and *Ple$^{\Delta IEC}$* colonic crypts at 2, 24, and 48 h after BrdU pulse. Cells were numbered sequentially from crypt base to lumen, with cell position 0 assigned to the first cell at the base of each crypt. At least nine crypts per mouse were analyzed from three mice per time point and genotype. **(D, E)** Representative images of PAS staining (goblet cells; GCs; D) and Muc2 immunofluorescence in mucus layer (E) of *Ple$^{fl/fl}$* and *Ple$^{\Delta IEC}$* distal colon sections (D) and colon whole mounts (E). Scale bars, 100 µm (D), and 200 µm (E). Graphs show quantification of percentage of periodic acid Shiff (PAS)-positive (PAS^{+}) IECs per crypt (D) and percentage of Muc2-positive (Muc2^{+}) area per whole mount area examined (E), n = 3–4. Data are presented as mean ± SEM, *P < 0.05, **P < 0.01, †P < 0.001

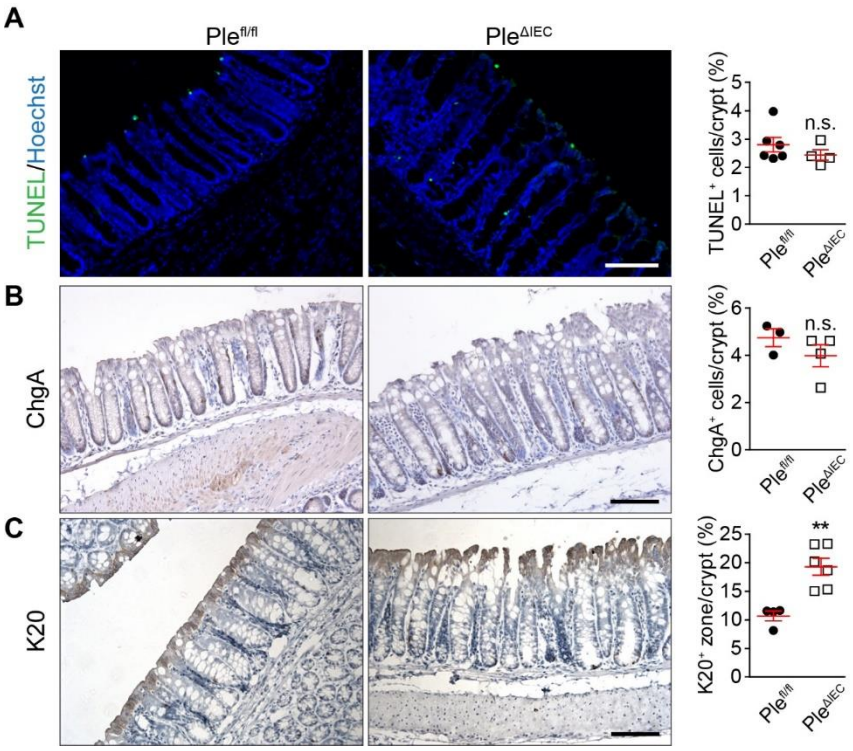

Figure 16 Plectin-deficient IECs exhibit alterations in differentiation but not in apoptosis. (A) Representative images of fluorescent TUNEL staining of apoptotic cells (green), **(B)** ChgA IHC (enteroendocrine cells), and **(C)** K20 IHC (mature IECs) of *Ple*$^{fl/fl}$ and *Ple*$^{\Delta IEC}$ colon sections. Nuclei in (A) were stained with Hoechst (blue). Scale bars, 100 µm. Corresponding graphs show percentage of positively labeled (+) IECs and K20 zone per crypt cells. *n* = 3-6. Data are presented as mean ± SEM, n.s. not significant, $^{**}P < 0.01$.

4.1.4 Plectin-deficient IECs form aberrant cell junctions and disordered KF networks

Previous research has demonstrated that IFs are recruited to cell junctions via plectin (Gregor et al., 2014; Jirouskova et al., 2018; Prechova et al., 2022; Walko et al., 2011). Our results document that *Ple*$^{\Delta IEC}$ IECs are detached from BM (Figure 15) and as a result, form a leaky intestinal barrier (Figure 12). Since the integrity of IEB is defined by junctional complexes, we examined their appearance in *Ple*$^{\Delta IEC}$ IECs.

To address the detailed structure and morphology of cell-cell (AJs, TJs, and Ds) and cell-ECM junctions (HDs), we employed transmission electron microscopy (TEM) and quantitatively analyzed their morphometry. The electron micrographs showing the cell-ECM contacts revealed large but low-electrodense HD plaques in *Ple*$^{\Delta IEC}$ IECs. When measured, we observed pronounced widening in the cell-ECM space in *Ple*$^{\Delta IEC}$ IECs. The dilatation was also observed when we measured intercellular spaces at the sites of AJs, TJs, and Ds between neighboring *Ple*$^{\Delta IEC}$ IECs (Figure 18A). This observation was also supported by decreased expression of some of the junctional components, such as Itgα6 and Itgβ4 (HDs; Figure 18B, C); E-cad (AJs); ZO-1

(TJs); Dsp1/2 (Ds) in *Ple*$^{\Delta IEC}$ IECs (Figure 18D, E) at both mRNA and protein levels. The analysis of junctional complexes implies that the absence of plectin leads to aberrant cohesion of IECs and their adhesion to BM, which results in the formation of compromised IEB seen in *Ple*$^{\Delta IEC}$ mice.

Another important aspect that determines the resilience of the IEB is the mechanical stability of the individual IECs. Therefore, we inspected the impact of plectin ablation on the KF network. The colonic tissue of *Ple*$^{fl/fl}$ and *Ple*$^{\Delta IEC}$ mice was stained for K8/K18 and K19, the most abundant KFs in IECs. Super-resolution microscopy revealed structural irregularities in KFs within *Ple*$^{\Delta IEC}$ IECs (Figure 19A). In contrast to *Ple*$^{fl/fl}$ IECs, where a typical network of KFs with clear apicobasal alignment was observed, the keratin networks in *Ple*$^{\Delta IEC}$ IECs were formed by KFs collapsed into bundles. *Ple*$^{\Delta IEC}$ IECs lacked also the characteristic enrichment of KFs at the apical membrane. The structural abnormalities in KFs were not due to the changes in keratin expression levels, as we observed comparable expression of keratins at mRNA and protein levels (Figure 19B, C).

The *in vivo* findings were further validated in cultured Caco-2 and hCC cells. We prepared plectin-deficient (KO) Caco-2 and hCC cells using CRISPR/Cas9 technology (details can be found in Chapter 3.3). Given that intestinal epithelium comprises proliferating and terminally differentiated cells, we allowed Caco-2 monolayers to grow for 16 days so they differentiate and resemble colonic epithelium seen in mice (Lea, 2015). In wild-type (WT) Caco-2 cells, the KFs form a network densely packed around the nucleus from which individual KFs stretch towards Dsp-positive Ds located at the plasma membrane (Figure 19D). In contrast, the keratin meshwork in KO Caco-2 was homogenously distributed throughout the cytoplasm. Dsp was continuously dispersed at the plasma membrane but did not form clearly discernible Ds.

Together, these results indicate that plectin deficiency destabilizes cells by (i) modifying keratin cytoskeletal architecture and (ii) disabling the formation of functional desmosomes, thus contributing to the destabilization of intestinal epithelium.

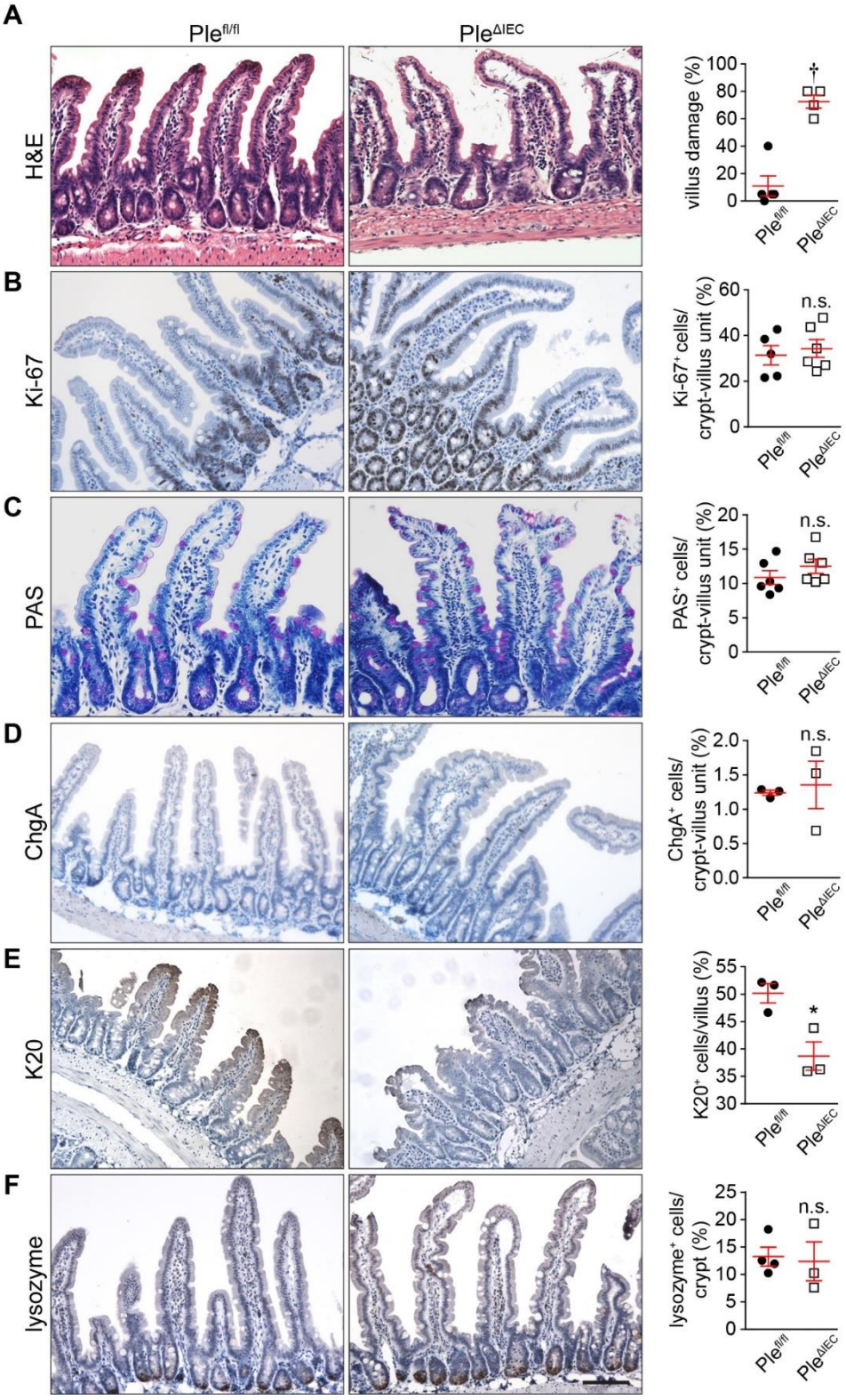

Figure 17 Plectin-deficient IECs in the SI manifest aberrant proliferation and differentiation, resulting in altered crypt-villus organization. (A-F) Representative images of H&E staining (A), Ki-67 IHC (B), PAS staining (C), chromogranin A (ChgA) IHC (D), K20 IHC (E), and lysozyme IHC (Paneth cells; F) of SI sections. Scale bar, 100 µm. Corresponding graphs show percentage of damaged crypt-villus units (villus damage given as percentage of villi with > 10% of IECs detached from BM (A) and percentage of the positively labeled (⁺) IECs per crypt-villus unit (B, C), villus (D, E) and crypt (F). *n* = 3-6. Data are presented as mean ± SEM, n.s. not significant, **P* < 0.05, †*P* < 0.001.

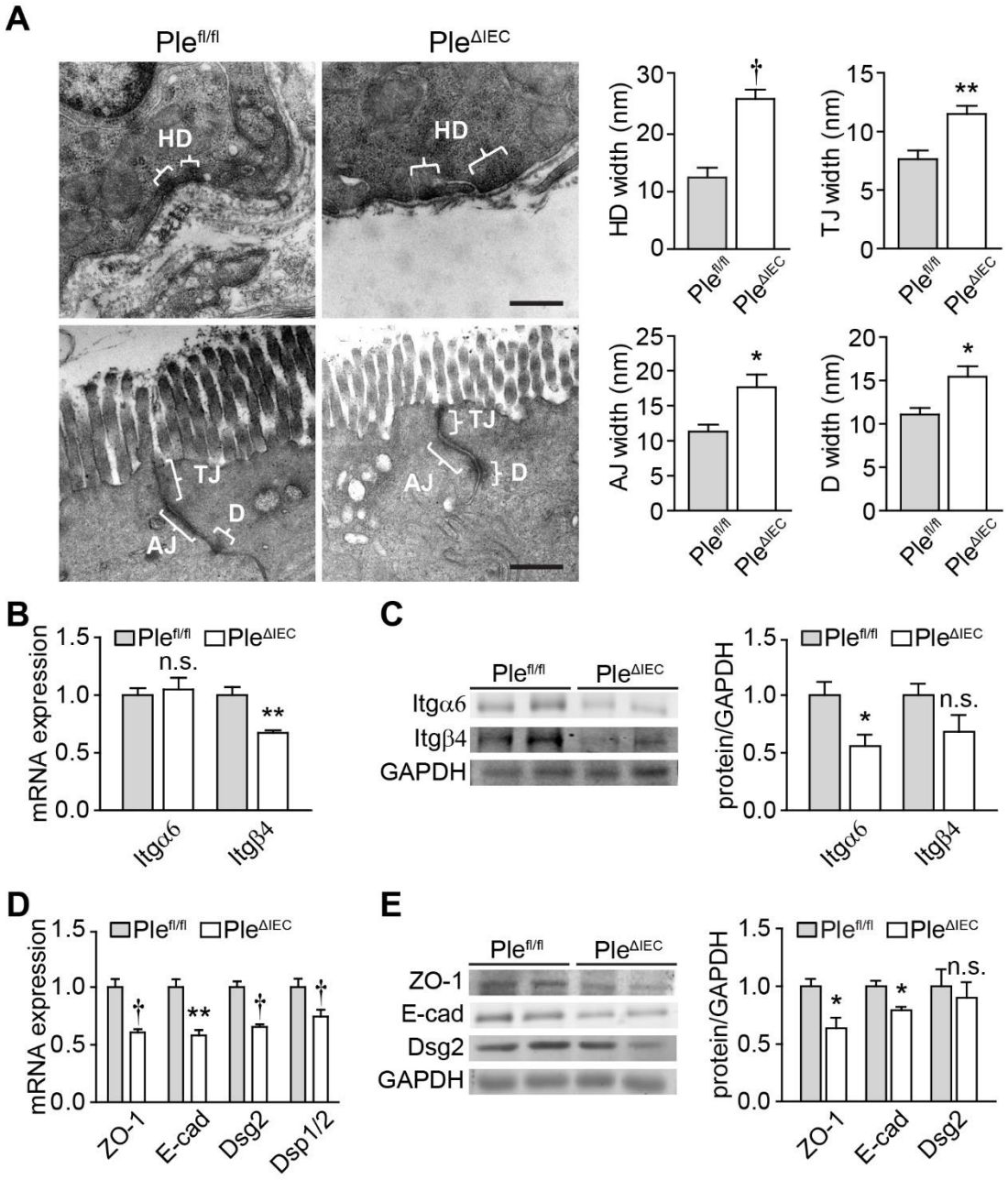

Figure 18 Formation of aberrant cell junctions in *Ple$^{\Delta IEC}$* IECs. (A) Representative transmission electron microscopy (TEM) micrographs of *Ple$^{fl/fl}$* and *Ple$^{\Delta IEC}$* IEC junctional complexes. Braces (white) indicate HD, TJ, AJ, and Ds. Scale bar, 500 nm. Graphs show quantitative analyses of junctional complex widths (measured as the distance from IEC to BM (HD) or distance from IEC to IEC membrane (TJ, AJ, and Ds)). Five to fifteen junctions were measured (two mice per genotype). **(B)** Relative mRNA levels of integrin (Itg) α6 and β4 in scraped mucosa from *Ple$^{fl/fl}$* and *Ple$^{\Delta IEC}$* distal colons, $n = 4–5$. **(C)** Quantification of Itgβ4 and Itgα6 in scraped distal colon mucosa from *Ple$^{fl/fl}$* and *Ple$^{\Delta IEC}$* mice by immunoblotting. GAPDH, loading control. The graph shows relative band intensities normalized to average *Ple$^{fl/fl}$* values, $n = 3$. **(D)** Relative mRNA levels of ZO-1, E-cadherin (E-cad), desmoglein 2 (Dsg2), and desmoplakin 1/2 (Dsp1/2) in *Ple$^{fl/fl}$* and *Ple$^{\Delta IEC}$* distal colons, $n = 5$. **(E)** Quantification of ZO-1, E-cad, and Dsg2 in *Ple$^{fl/fl}$* and *Ple$^{\Delta IEC}$* colon mucosa by immunoblotting. GAPDH, loading control. The graph shows relative band intensities normalized to average *Ple$^{fl/fl}$* values, $n = 3$. Data are presented as mean ± SEM, n.s. not significant, $*P < 0.05$, $**P < 0.01$, $\dagger P < 0.001$.

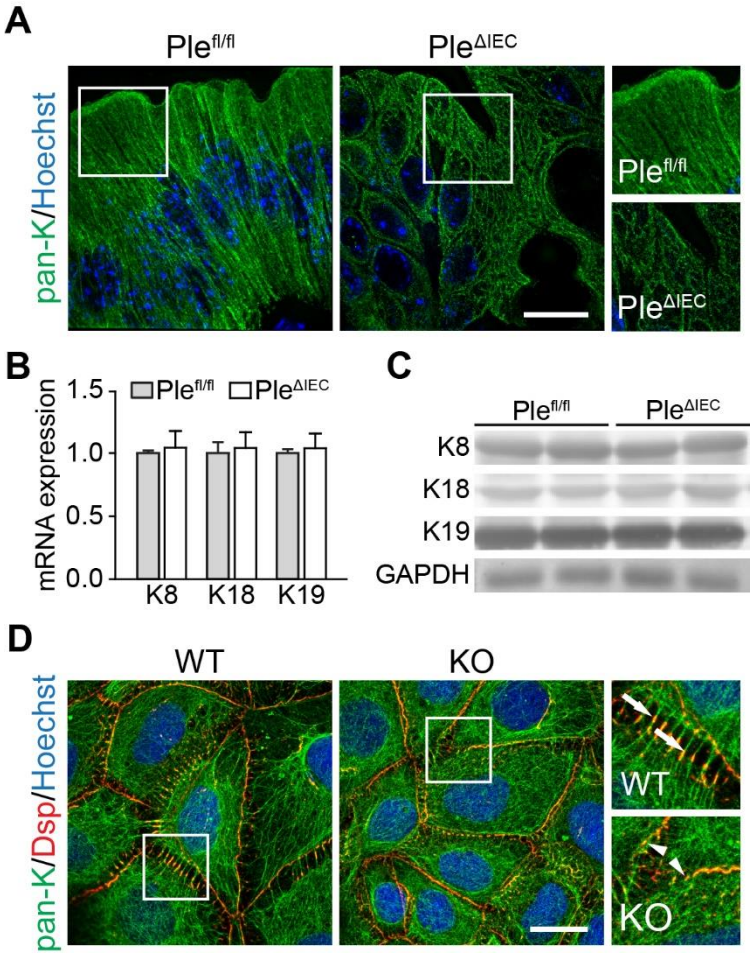

Figure 19 Plectin organizes KFs in IECs. (A) Representative super-resolution STED images of *Ple*$^{fl/fl}$ and *Ple*$^{\Delta IEC}$ distal colon sections immunolabeled for pan-keratin (pan-K; green) with nuclei stained with Hoechst (blue). Scale bar, 10 µm. Boxed areas show ×1.3 images. **(B, C)** Relative mRNA (B) and protein (C) levels of K8, 18, and 19 in *Ple*$^{fl/fl}$ and *Ple*$^{\Delta IEC}$ distal colon, $n = 3–5$. Data are presented as mean ± SEM, $P > 0.05$ by unpaired Student *t* test. **(D)** Representative immunofluorescence images of WT and KO Caco-2 cell monolayer cultures immunolabeled for pan-K (green) and Dsp (red). Nuclei were stained with Hoechst (blue). Arrows, straight K8 filaments anchored to Dsp-positive desmosomes; arrowheads, tangled K8 filaments. Scale bar, 20 µm. Boxed areas show ×2.5 images.

4.1.5 **Plectin preserves intestinal epithelial integrity through HD stabilization**

Previous studies have reported that plectin and its interaction with Itgα6β4 are indispensable for the mechanical stability of skin via the stabilization of HDs in keratinocytes. Disruption of this plectin-Itg linkage leads to detachment of epithelial cells and skin fragility (Kostan et al., 2009; Osmanagic-Myers et al., 2015). These findings together with our own observation of the IECs detachment from the BM (Figure 15 and Figure 17) and HD alterations (Figure 18) in *Ple*$^{\Delta IEC}$ IECs prompted us to focus on HDs and their components.

First, we analyzed the interaction of IECs with the underlying BM in *Ple*$^{fl/fl}$ and *Ple*$^{\Delta IEC}$ colon (Figure 20A) and SI (Figure 20E) using immunolabeling with specific antibodies or using

histological staining with Sirius red (SR). We co-stained K8-positive KFs together with either Itgα6 to visualize HDs, or Coll IV to visualize BM. Additionally, we performed SR staining to visualize BM (Figure 20C, F). The IECs of *Ple*$^{fl/fl}$ intestines delineated the subjacent ColIV-positive BM (Figure 20D, G) and formed Itgα6-positive HDs (Figure 20A, E). In contrast, IECs of *Ple*$^{\Delta IEC}$ colon showed remarkable detachment of IECs from the underlying substrate, mostly at the luminal part of colonic crypts (Figure 20D). The detachment of *Ple*$^{\Delta IEC}$ IECs was even more pronounced in the SI, where whole epithelial sheets were ripped off the BM (Figure 20G). Interestingly, the *Ple*$^{\Delta IEC}$ IECs were devoid of Itgα6 signal, which remained associated with the BM structure (Figure 20A, E). This suggests, that plectin deletion disrupts the Itg-keratin link, thus hampering IECs' anchorage to BM via HDs.

Next, we approached the interaction of IECs with BM biochemically. We performed a high-salt extraction of WT and KO Caco-2 cells, which yielded two fractions - a soluble fraction (cytosol) and a membrane-insoluble keratin-enriched fraction [HSE; (Osmanagic-Myers et al., 2006)]. We then compared the keratin and Itg content using immunoblotting. Not surprisingly, K8 was highly abundant in all cell fractions. On the other hand, while Itgβ4 content was comparable between WT and KO total cell lysates, the levels of Itgβ4 were significantly reduced in HSE fraction of KO cells (Figure 21A). This supports our previous histological findings (Figure 20), showing that interaction between KFs and Itg clusters is perturbed in plectin-deficient epithelium.

To find out whether plectin deficiency affects mechanical stability, we subjected WT and KO IECs to a series of mechanical challenges and quantitatively analyzed their biomechanical properties. First, we plated WT and KO Caco-2 or hCC cells on flexible polydimethylsiloxane (PDMS) membranes and tested their mechanical vulnerability using uniaxial cyclic stretch. Monitoring cell viability by propidium iodide (PI; dead cells), labeling revealed higher mechanical susceptibility of KO cells, which gradually increased with higher amplitudes of 10% - 50% stretch (Figure 21B, E).

Further, we tested cell adhesion strength by using radial shear assay. For that, we used a spinning disc device in which WT and KO cells were seeded on a plastic dish, and subsequently, the shear force was generated via an air-driven rotating glass lid. Consistently with cell stretching assay, radial shear rheometry showed a higher portion of PI-positive dead cells and a higher population of KO cells detached upon application of radial flow (Figure 21C,

F). Together, these data show that plectin deficiency weakens the adhesion of cells to the subjacent BM.

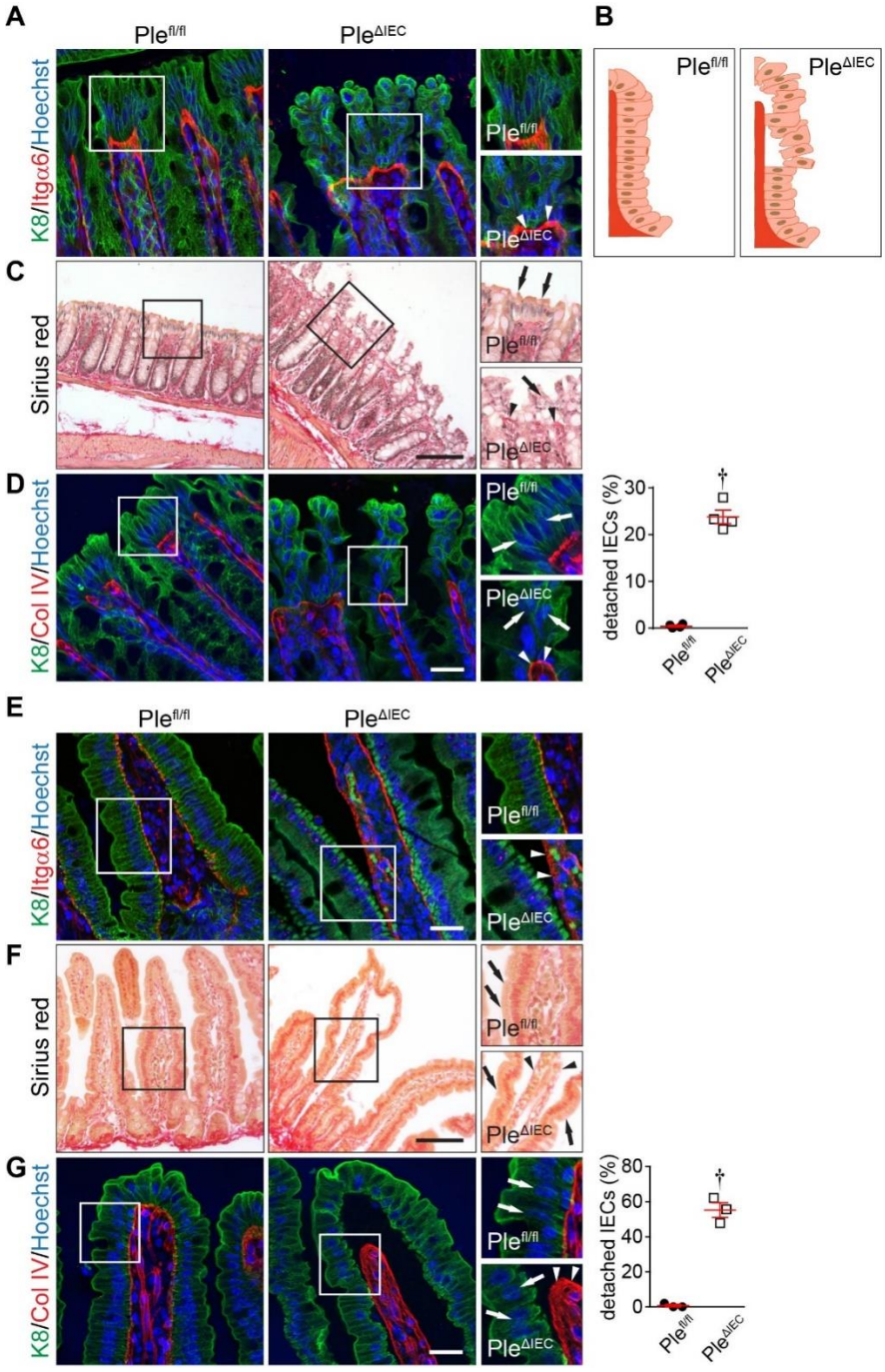

Figure 20 Detachment of IECs from BM and destabilization of HDs in *Ple$^{\Delta IEC}$* intestinal epithelium. (A, C, D) Representative immunofluorescence images of *Ple$^{fl/fl}$* and *Ple$^{\Delta IEC}$* distal colon sections immunolabeled for K8 (green) and Itgα6 (red; A), stained for fibrillar collagen with Sirius red (SR; C) and immunolabeled for K8 (green) and Coll IV (red; D); Hoechst-stained nuclei (blue). The arrows, IECs; Arrowheads, either Itgα6-positive clusters or BM. Scale bar, 25 µm. Boxed areas show ×1.5 images. **B** Drawn schematics depict aligned, BM-attached *Ple$^{fl/fl}$* IECs and mislocalized, detaching *Ple$^{\Delta IEC}$* IECs. **(E, F, G)** Representative immunofluorescence images of *Ple$^{fl/fl}$* and *Ple$^{\Delta IEC}$* SI sections immunolabeled for K8 (green) and Itgα6 (red; E), stained for fibrillar collagen with SR (F) and immunolabeled for K8 (green) and Coll IV (red; G); Hoechst-stained nuclei (blue). The arrows, IECs; Arrowheads, either Itgα6-positive clusters or BM. Scale bar, 25 µm. Boxed areas show ×1.5 images. Graphs show percentage of detached IECs per crypt (D) or villus (G). Data are presented as mean ± SEM, †$P < 0.001$.

Finally, we aimed to determine the strength of Itg-ECM binding quantitatively. To achieve this, we utilized magnetic tweezer microrheometry, allowing to measure the bond between ECM-coated paramagnetic beads and Itg clusters (Kah et al., 2020). Once the ECM-coated beads were attached to the cells, a magnetic field with an incremental force of up to 15 nN was applied using a needle-shaped core, causing the beads to detach from the cell surface. The entire process was monitored using a computer, allowing us to calculate the cumulative detachment probability of over 100 cells accurately. This calculation was then used to plot the rupture force representing the pulling force at which 50% of the beads were torn off the cell. The evaluation discerned reduced rupture force in KO cells when compared to WT cells (Figure 21D, G). In concert with the other experiments performed within this chapter (4.1.5), these results indicate that loss of plectin destabilizes HDs and compromises the mechanical stability of IECs.

4.1.6 **IEC-specific plectin deficiency exacerbates experimental colitis**

Ple$^{\Delta IEC}$ mice exhibit epithelial damage leading to a so-called “leaky gut” which is accompanied by chronic inflammation (Figure 14). This is reminiscent of the condition of UC patients, where the absence of plectin correlates with colitis severity. To investigate this, we experimentally induced colitis by 2% DSS treatment of *Ple*$^{fl/fl}$ and *Ple*$^{\Delta IEC}$ mice and monitored their susceptibility to intestinal inflammation. The experimental protocol involved exposing mice to 2% DSS in drinking water for 4 days, followed by a 3-day period of water consumption. During this time, *Ple*$^{\Delta IEC}$ mice suffered a significant weight loss compared to *Ple*$^{fl/fl}$ counterparts (Figure 22A). Additionally, based on the disease activity index (DAI), an index cumulatively describing body weight, rectal bleeding, and stool consistency, *Ple*$^{\Delta IEC}$ mice showed considerably worse health conditions than *Ple*$^{fl/fl}$ mice (Figure 22A). These poor health conditions were also reflected in a reduction in colon length (Figure 22B). WBI of mice at day 4 during DSS treatment and day 6 at the water recovery period showed MPO-positive luminescence signals in both *Ple*$^{fl/fl}$ and *Ple*$^{\Delta IEC}$ abdominal regions (Figure 22C). However, MPO-positive regions found in *Ple*$^{\Delta IEC}$ mice were larger, indicating the development of substantial inflammation. Histological examination of hematoxylin-stained colons supported the increased susceptibility of *Ple*$^{\Delta IEC}$ mice for epithelial injury (Figure 22D). Histological evaluation of colonic mucosa revealed severe ulcerations, crypt damage (Figure 22D), and overall

enhanced immune response parameters of histological inflammation indices in *Ple*$^{\Delta IEC}$ mice (Figure 22E).

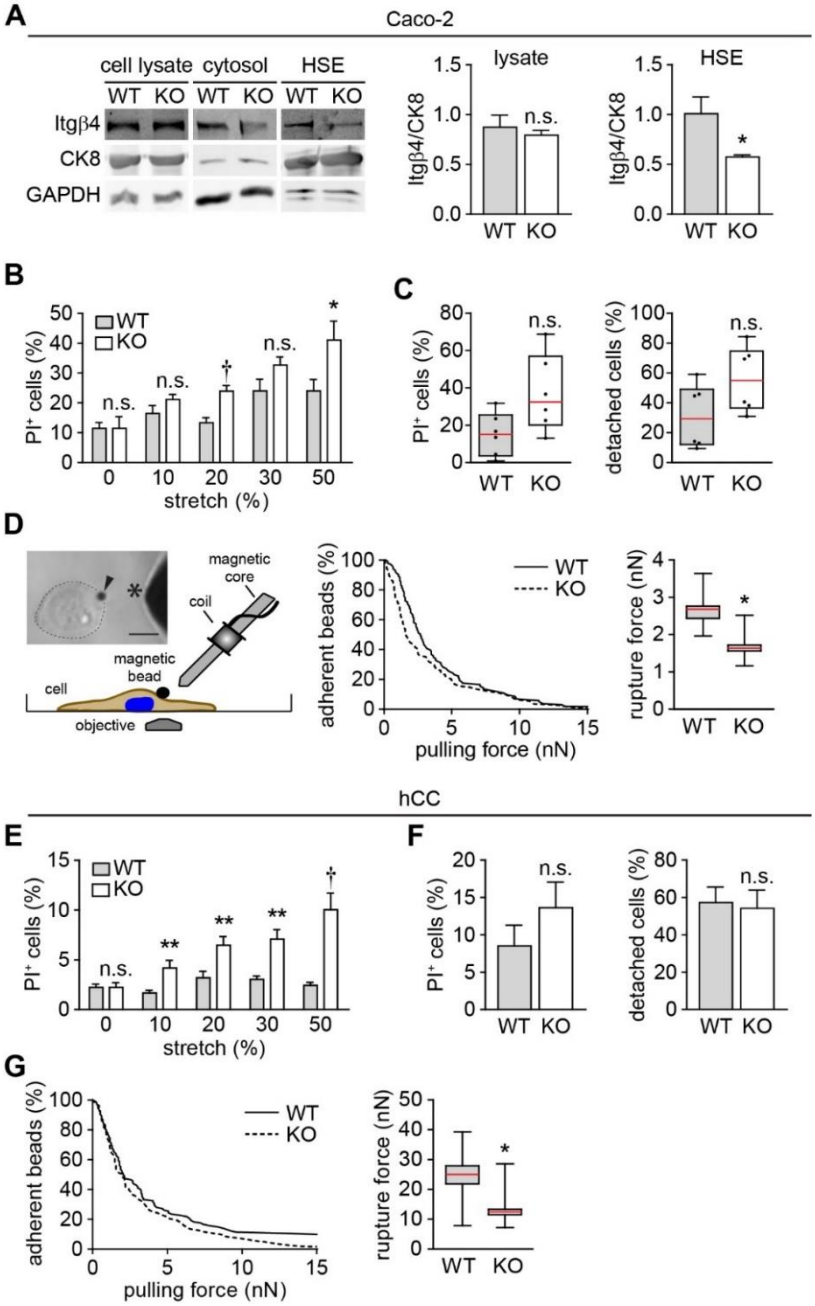

Figure 21 Plectin maintains the mechanical stability of IECs. (A) Cell lysates, cytosol fractions, and keratin-enriched high salt extracts (HSE) were prepared from WT and KO Caco-2 cells and subjected to immunoblotting with antibodies to Itgβ4 and K8. GAPDH, loading control. Graphs show relative band intensities normalized to average *Ple*$^{fl/fl}$ values, $n = 4–6$. **(B, E)** Viability of WT and KO Caco-2 (B) and hCC (E) cells exposed to uniaxial cyclic stretch presented as a percentage of dead (PI-positive; PI⁺) cells, $n = 9–12$. **(C, F)** Quantification of WT and KO Caco-2 (C) and hCC (F) cell viability (left) and adhesion (right) under radial shear flow shown as a percentage of dead and detached cells, respectively, $n = 6$-8. Boxplot data represent median, 25th, and 75th percentile with whiskers reaching the last data point. **(D, G)** Adhesion strength between ECM-coated superparamagnetic beads and WT and KO Caco-2 (D) and hCC (G) cells was quantified using magnetic tweezers that generated forces ramps at a speed of 1 nN/s up to a maximum force of 15 nN. Image and schematic depict magnetic tweezer setup. Arrowhead, paramagnetic bead; asterisk, magnetic tweezer tip; dotted circular line, cell border. Scale bar, 20 µm. The graph shows the percentage of beads in Caco-2 ($n = 103$ WT, 109 KO cells) and hCC ($n = 112$ WT, 103 KO cells) that remained adherent at a given pulling force. The boxplot shows the distribution of the median detachment force (calculated from bootstrapping by sampling with replacement, $n = 1000$ runs) and its distribution (25th, and 75th percentile with whiskers reaching the minimum and maximum sampled values). Bar graph data in all other subplots represent mean ± SEM, n.s. not significant, $^*P < 0.05$, $^{**}P < 0.01$, $^\dagger P < 0.001$.

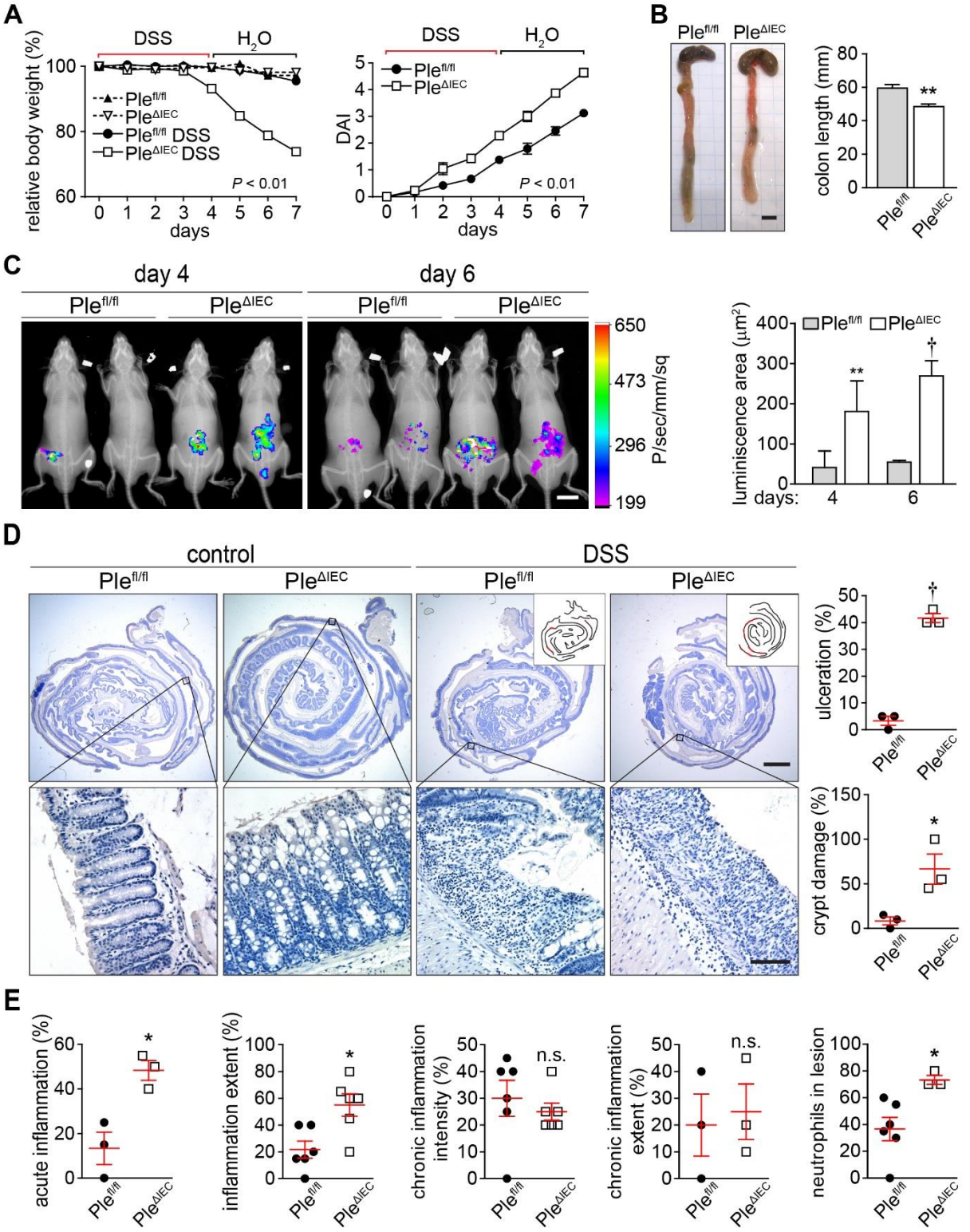

Figure 22 Ple$^{\Delta IEC}$ mice are more susceptible to DSS-induced colitis. (A) Relative bodyweight and disease activity index (DAI) of untreated and dextran sodium sulfate (DSS)-treated *Ple$^{fl/fl}$* and *Ple$^{\Delta IEC}$* mice during experimental colitis. Four to seven mice per genotype and time point were analyzed. **(B)** Representative images of colon and caecum of DSS-treated *Ple$^{fl/fl}$* and *Ple$^{\Delta IEC}$* mice. The graph shows colon length, $n = 4–6$. **(C)** *In vivo* chemiluminescence images and signal quantification (graph) of DSS-treated *Ple$^{fl/fl}$* and *Ple$^{\Delta IEC}$* mice injected with the myeloperoxidase substrate luminol on days 4 and 6 of DSS treatment, $n = 3–4$. **(D)** Representative hematoxylin-stained sections of Swiss roll mounts from untreated (control) and DSS-treated (DSS) mice. Scale bars, 2 mm, magnified boxed areas, 100 µm. Insets, outlines of lesions (in red) distributed along mucosa (black lines) in corresponding panels. **(D, E)** Graphs show quantification of colonic tissue damage given as the percentage of ulceration and crypt damage (D), percentage of acute inflammation, inflammation extent, chronic inflammation intensity and extent, and neutrophils in lesion (E), $n = 3-6$. Data are presented as mean ± SEM, $^*P < 0.05$, $^{**}P < 0.01$, $^{\dagger}P < 0.001$.

The proper composition of the microbiome and its interplay of with the intestinal immune system are believed to be one of the defense mechanisms in intestinal pathophysiology. Dysbiosis has been identified as an often-found feature in patients with UC (Bajer et al., 2017; Pascal et al., 2017; Sartor, 2006). Thus, we analyzed whether changes in microbiota composition accompany colitis found in *Ple*$^{\Delta IEC}$ mice. The fecal microbiota was isolated from unchallenged *Ple*$^{fl/fl}$ and *Ple*$^{\Delta IEC}$ mice at 4, 12, and 20 weeks of age. Surprisingly, we found no significant differences in microbiota composition between *Ple*$^{fl/fl}$ and *Ple*$^{\Delta IEC}$ mice at any age (Figure 23). Collectively, these data reveal that *Ple*$^{\Delta IEC}$ mice are highly prone to experimentally-induced colitis, which goes hand in hand with the high incidence of ulcerations and crypt damage while showing no alteration of microbial composition.

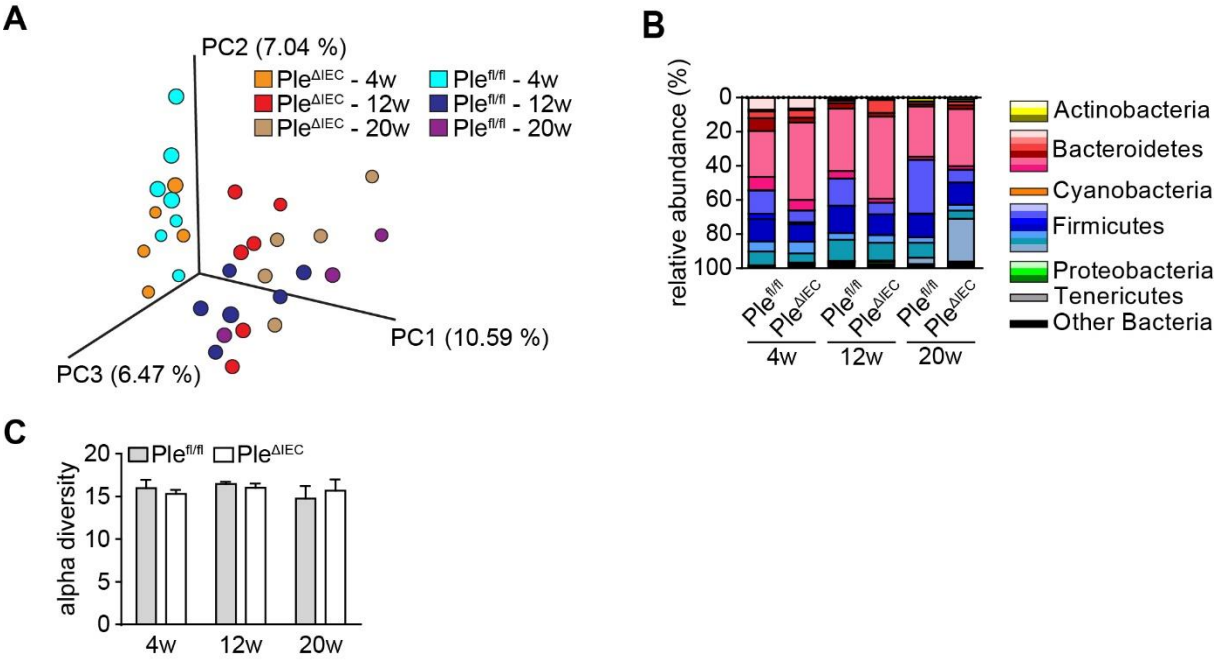

Figure 23 Colitic phenotype in Ple$^{\Delta IEC}$ mice is not accompanied with dysbiosis. (A) Fecal microbiota beta diversity in 4-, 12-, and 20-week-old untreated *Ple*$^{fl/fl}$ and *Ple*$^{\Delta IEC}$ mice as determined by 16S rDNA sequencing. Principal coordinate analysis plot, constructed with unweighted UniFrac distance metric, shows clustering of microbial beta diversity. PC1, PC2, and PC3 represent the top three principal coordinates that captured most of the diversity (given as a percentage). **(B)** Global composition of bacterial microbiota at phyla level shown as relative operational taxonomic unit (OTUs) abundance per time point and genotype. **(C)** Alpha diversity of fecal microbiota in 4-, 12-, and 20-week-old untreated *Ple*$^{fl/fl}$ and *Ple*$^{\Delta IEC}$ mice determined by 16S rDNA sequencing using PD whole tree metrics. *n* = 4–6.

4.1.7 **Reduced mechanical stability of epithelia accounts for intestinal injury in *Ple$^{\Delta IEC}$* mice**

Next, we determined the onset and progress of the intestinal injury in *Ple$^{\Delta IEC}$*. We assessed the epithelial damage in newborn, 21-day-old, and 12-week-old mice. The evaluation revealed that the intestinal epithelium in newborn pups was devoid of any injury. However, the crypt and villus damage already occurred in 21-day-old *Ple$^{\Delta IEC}$* mice that were weaned from liquid breast milk to solid chow (Figure 24A-C). This initial disruption of IEB in *Ple$^{\Delta IEC}$* mice was paralleled by histological indices of inflammation (Figure 25). In agreement with previous observations, 12-week-old *Ple$^{\Delta IEC}$* mice displayed remarkable epithelial damage (Figure 24A-C).

To precisely determine the timing of intestinal epithelial injury following plectin depletion, we established a new mouse model. Here, we employed a Villin-Cre-ERT2 system, which enabled us to deplete plectin specifically in IECs by tamoxifen (TMX) application (*Ple$^{\Delta IEC\text{-}ERT2}$*). We administered TMX via orogastric gavages to mice every other day for five consecutive days (detailed descriptions can be found in Chapter 3.2; Figure 24D, E). The mice were sacrificed on the fifth day after the last gavage. This approach allowed us to reach a maximal recombination efficiency, leading to a phenotype comparable to the constitutive *Ple$^{\Delta IEC}$* mouse model. To test the impact of dietary changes on epithelial, *Ple$^{fl/fl}$* and *Ple$^{\Delta IEC\text{-}ERT2}$* mice were subjected either to a low-residue liquid diet or a solid chow, starting six days before the first TMX application (Figure 24D). While *Ple$^{fl/fl}$* epithelium remained intact independently of the diet type, the damage to the colonic *Ple$^{\Delta IEC\text{-}ERT2}$* epithelium upon liquid diet mice was substantially improved by 20% compared to *Ple$^{\Delta IEC\text{-}ERT2}$* kept on a solid diet (Figure 24D-F).

When IEB integrity is compromised, luminal bacteria often colonize mucosa and trigger inflammation. Since we observed bacterial translocation to mucosa in *Ple$^{\Delta IEC}$* mice (Figure 14), we investigated whether eliminating microbiota improves epithelial damage (Figure 24G). To eliminate the intestinal microbiota, we treated *Ple$^{fl/fl}$* and *Ple$^{\Delta IEC\text{-}ERT2}$* mice with broad-spectrum antibiotic coctail [ATB; (De Arcangelis et al., 2017)]. While ATB treatment had no impact on epithelial integrity in *Ple$^{fl/fl}$* mice, it attenuated colonic crypt damage in *Ple$^{\Delta IEC\text{-}ERT2}$* mice (Figure 24H). The extent of the villus damage in *Ple$^{\Delta IEC\text{-}ERT2}$* mice was comparable regardless of treatment (Figure 24I).

Based on these observations, we concluded that the onset and progression of intestinal injury in *Ple*$^{\Delta IEC}$ mice are related to increased mechanical stress from luminal contents during the transition to solid chow. This is due to the reduced mechanical stability of HDs upon plectin deletion. In addition, broad-spectrum ATB treatment partially mitigated colonic epithelial damage in *Ple*$^{\Delta IEC\text{-}ERT2}$ mice, suggesting that the microbiota contributes to epithelial integrity.

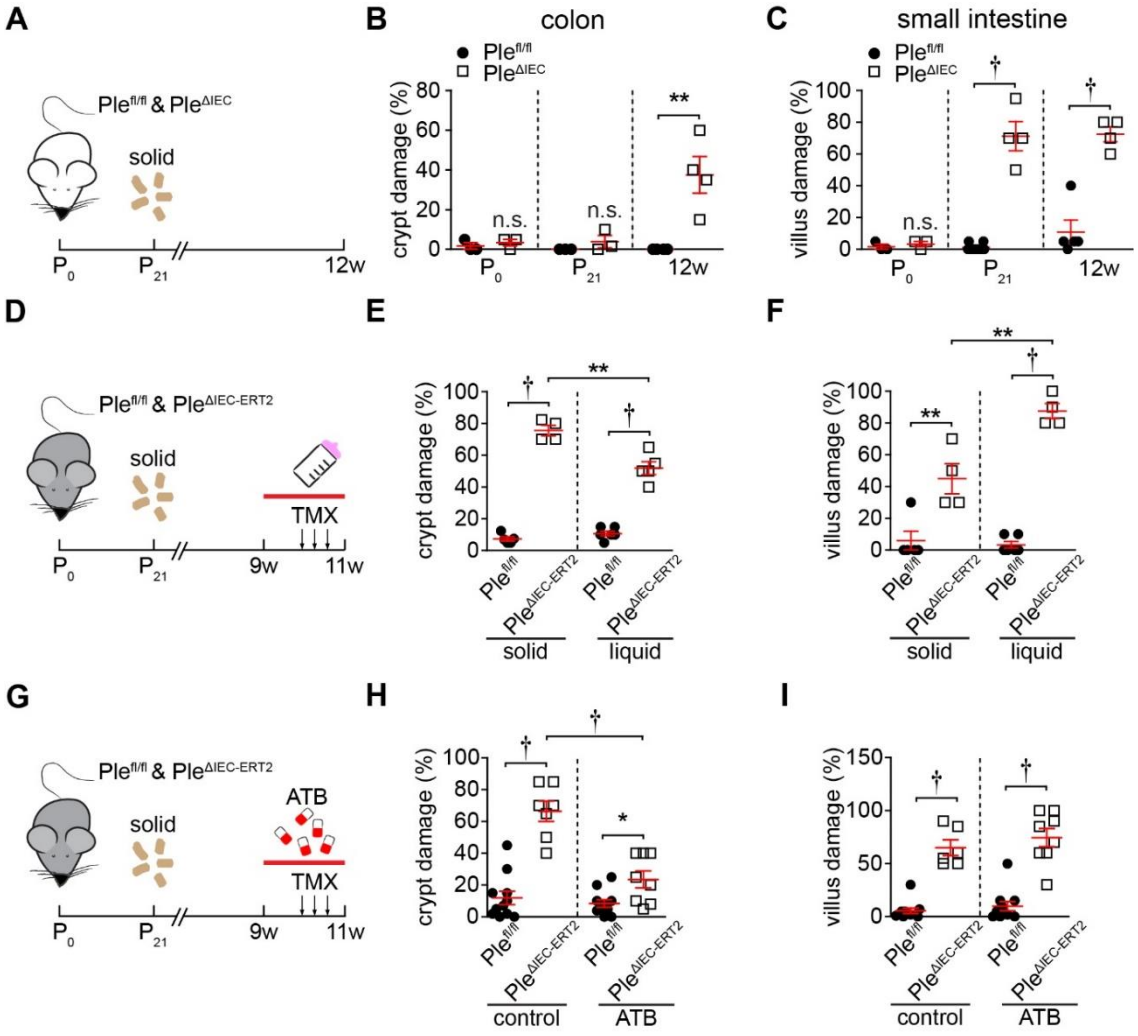

Figure 24 Intestinal epithelial damage in *Ple*$^{\Delta IEC}$ mice results from mechanical stress. **(A–C)** *Ple*$^{fl/fl}$ and *Ple*$^{\Delta IEC}$ mice were sacrificed on postnatal day 0 (P0), postnatal day 21 (P21), and at 12 weeks (12w) of age, and epithelial damage scores were assessed from colon and small intestine sections. Schematic illustrates the experimental setup (A). Solid, transition to solid chow at P21. Graphs show quantification of epithelial damage in the colon (B) and small intestine (C) at the age indicated. **(D–F)** Nine-week-old *Ple*$^{fl/fl}$ and *Ple*$^{\Delta IEC\text{-}ERT2}$ mice were either kept on solid chow or provided with a liquid diet for 14 days. Plectin inactivation was induced by three consecutive applications of tamoxifen (TMX) on days 6, 8, and 10; mice were sacrificed on day 14. The schematic illustrates the experimental setup (D). Solid, transition to solid chow at P21; arrows, TMX application; red bar, period on a liquid diet. Graphs show quantification of epithelial damage in the colon (E) and small intestine (F) on solid chow and liquid diet. **(G–I)** Nine-week-old *Ple*$^{fl/fl}$ and *Ple*$^{\Delta IEC\text{-}ERT2}$ mice were kept either untreated or treated with broad-spectrum antibiotics (ATB). Plectin inactivation and sample collection were identical to (B). Schematics illustrate experimental setup (G). Chow, the transition to solid chow at P21; arrows, TMX application; red bar, period of ATB treatment. Graphs show quantification of epithelial damage in the colon (H) and small intestine (I) on solid chow and ATB. Data are presented as mean ± SEM, n.s. not significant, *$P < 0.05$, **$P < 0.01$, †$P < 0.001$.

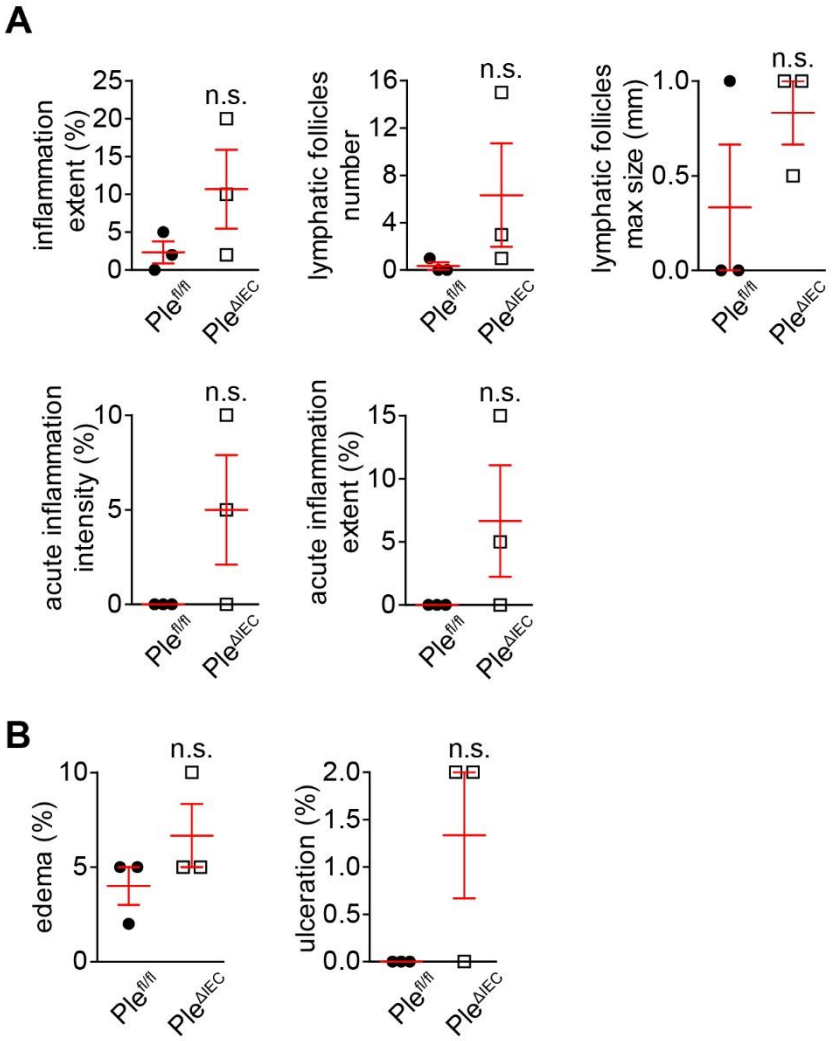

Figure 25 Histological assessment of colonic tissue damage and inflammation in 21-day-old *Ple*$^{\Delta IEC}$ compared to *Ple*$^{fl/fl}$ mice. **(A)** Quantification of inflammatory parameters on H&E-stained sections of *Ple*$^{fl/fl}$ and *Ple*$^{\Delta IEC}$ colons. Graphs show the number and maximal (max) sizes of lymphatic follicles, percentage of inflammatory extent, acute inflammation intensity, acute inflammation extent, and lymphocytes in the lesion. **(B)** Quantification of tissue damage assessed from H&E-stained sections of *Ple*$^{fl/fl}$ and *Ple*$^{\Delta IEC}$ colons (percentage of edema and ulceration). *n* = 3. Data are presented as mean ± SEM, n.s. not significant.

4.2 Aim 2.

4.2.1 Analyses of transcriptomic and proteomic signatures of UC patients reveal dysregulated expression of cytoskeletal and junctional components

The development of colitis is associated with a compromised IEB. Given the importance of mechanical resilience for a functional IEB, we investigated whether the expression of proteins/genes associated with epithelial mechanical stability is altered in UC patients. To achieve this goal, we combined results from publicly available transcriptomic and proteomic studies with meta-analyses from UC patients and healthy individuals (Haberman et al., 2019; Janker et al., 2023; Linggi et al., 2021; Massimino et al., 2021; Modos et al., 2021; Schniers et al., 2019; Taman et al., 2018). In these datasets, we analyzed expression profiles of genes/proteins associated with Ds, HDs, KFs, and actin (including AJs and TJs). Genes/proteins with |Log2(Fold change)| (|LFC|) > 0.5 and adjusted p-value (False Discovery Rate; FDR) < 0.05 were used for over-representation analysis (ORA). ORA revealed significant deregulation of the predefined set of genes in 1 transcriptomic meta-analysis, 2 transcriptomic studies, and 1 proteomic study. In addition, differentially expressed genes (DEGs) genes that were present in more than 2 studies, were visualized using heatmaps (Figure 26A, B). Taken together, our results indicated the downregulation of genes associated with the mechanical resilience of the intestinal epithelium, suggesting compromised IEB in UC patients.

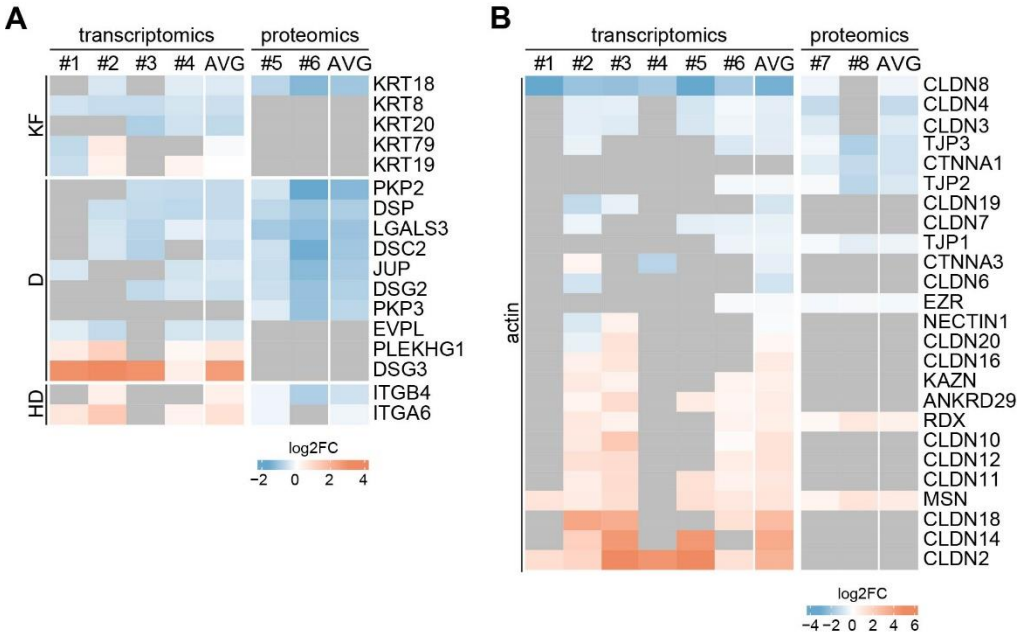

Figure 26 Colonic biopsies from UC patients exhibit changes in expression of proteins associated with cytoskeleton and junctional complexes. (A, B) Meta-analysis of UC patients' RNA and protein expression profiles. Heatmaps including genes significantly altered in the meta-analysis involved in the regulation of Ds, HDs, KFs (A), and actin (B). 8 studies included into the analysis indicated by #1 - #8.

4.2.2 **IEC-specific plectin-deficient mice show higher DNA damage and an increased propensity for CRC**

1-2% of patients with IBD, particularly those with UC, face an increased risk of CRC (Lakatos and Lakatos, 2008; Long et al., 2017). We have shown that colitis in $Ple^{\Delta IEC}$ mice was characterized by excessive detachment of IECs and hyperproliferation. To test whether $Ple^{\Delta IEC}$ mice follow the same paradigm as UC patients, we allowed them to age and monitored the epithelial damage and inflammation over the time course. The crypt damage steadily increased at 12, 25, and 50-week-old $Ple^{\Delta IEC}$ mice, while the inflammation reached the peak severity at the age of 12 weeks in $Ple^{\Delta IEC}$ mice in comparison to $Ple^{fl/fl}$ mice (Figure 27A). A similar trend was observed in $Ple^{\Delta IEC\text{-}ERT2}$ mice, with notable crypt damage and a mild increase in inflammation extent (Figure 27B).

Similar to the disease progression in UC patients, a substantial proportion (22%) of 50-week-old $Ple^{\Delta IEC}$ mice spontaneously developed CRC (Figure 27C). Histopathological examination of H&E-stained colonic sections from $Ple^{\Delta IEC}$ mice revealed epithelial erosions (#a; Figure 27D) together with high-grade dysplasia and tubular adenoma (#b; Figure 27D) predominantly in distal colon regions, particularly in rectal prolapses (Figure 27D). Mucosal hyperplasia was observed in 9% of 50-week-old $Ple^{fl/fl}$ and 33% of $Ple^{\Delta IEC}$ mice (Figure 27E). Adenomas were detected in 22% of $Ple^{\Delta IEC}$ mice, accompanied by low-grade dysplasia in 33% or high-grade dysplasia in 22% of cases (Figure 27E, F). Supporting the carcinogenesis in $Ple^{\Delta IEC}$ mice, immunolabeling of colon sections with oncogenic cell surface marker TROP2 (Huebner et al., 2022; Moretto et al., 2023; Ohmachi et al., 2006; Svec et al., 2022) identified positive areas in rectal regions (Figure 27G).

We employed two additional approaches to verify the increased susceptibility of $Ple^{\Delta IEC}$ mice for CRC development. In the first experimental approach, we induced sporadic CRC by administering AOM, while in the second approach, we induced CA-CRC by combining DSS treatment with AOM administration. The sporadic CRC model showed that only 9% of $Ple^{fl/fl}$ mice developed hyperplasia without signs of carcinogenesis. However, 50% of $Ple^{\Delta IEC}$ mice developed tumors together with hyperplasia (28%), carcinoma in situ (7%), adenoma (50%; tubular type 50%), low-grade dysplasia (50%), and high-grade dysplasia (29%; Figure 27H). The second model of CA-CRC revealed that 6% of $Ple^{fl/fl}$ mice developed tumors, together with hyperplasia (12%), adenoma (6%; tubular type 6%), and high-grade dysplasia (6%). The

incidence of developed tumors in *Ple*$^{\Delta IEC}$ mice was 79%, concurrently with hyperplasia (5%), carcinoma in situ (11%), adenoma (79%; tubular type 74%; tubulovillous type 5%), microcarcinoma (16%), adenocarcinoma (5%; tubular type 5%; well differentiated 5%), low-grade dysplasia (26%), and high-grade dysplasia (63%; Figure 27I). Based on these findings, we concluded that *Ple*$^{\Delta IEC}$ mice spontaneously develop CRC, which progresses into an invasive form when accelerated by chemical carcinogenes.

Genomic instability represents a key aspect in the process of carcinogenesis. Elevated accumulation of DNA damage and deficiencies in DNA damage repair mechanisms provide cancer cells with an essential advantage, enabling them to bypass cell cycle checkpoints and survive. Generally, DNA damage caused by DSBs is considered the most genotoxic insult for cells and represents a hallmark of carcinogenesis (Arnould and Legube, 2020; Huang and Zhou, 2021; Le Guen et al., 2015). To answer whether the accumulation of DNA damage contributes to carcinogenesis in *Ple*$^{\Delta IEC}$ mice, we immunolabeled colonic sections of 12-week-old and 50-week-old *Ple*$^{fl/fl}$ and *Ple*$^{\Delta IEC}$ mice for a marker of DSBs, histone γH2A.X phosphorylated on serine 139 [*p*-γH2A.X; (Rogakou et al., 1998)]. To gain deeper insights into DSBs in distinct populations of IECs, we co-stained *p*-γH2A.X with Ki-67 to distinguish between TA cells (pink; Figure 28A) and differentiated cells (yellow; Figure 28A). Cells located in the first three positions at the base of crypts were identified as SCs (green; Figure 28A). Analysis of *p*-γH2A.X-positive (*p*-γH2A.X^{+}) foci per nucleus revealed increased foci accumulation in differentiated cells of 12-week-old *Ple*$^{\Delta IEC}$ crypts (Figure 28B). These cells occupy the region of the crypt that is the most exposed to mechanical stress imposed by luminal content, suggesting the accumulation of DSBs may be driven by the vulnerability of *Ple*$^{\Delta IEC}$ epithelium to mechanical stress. This observation was accompanied by clearly discernible hyperproliferation in 12-week-old *Ple*$^{\Delta IEC}$ mice, which is consistent with our previous data (Aim 1 4.1; Figure 28B). Inspection of DNA damage showed an increase of *p*-γH2A.X^{+} foci in zones of proliferative and differentiated cells together with hyperproliferation (Figure 28C). These findings support the notion that DNA damage contributes to the development of spontaneous CRC in *Ple*$^{\Delta IEC}$ mice.

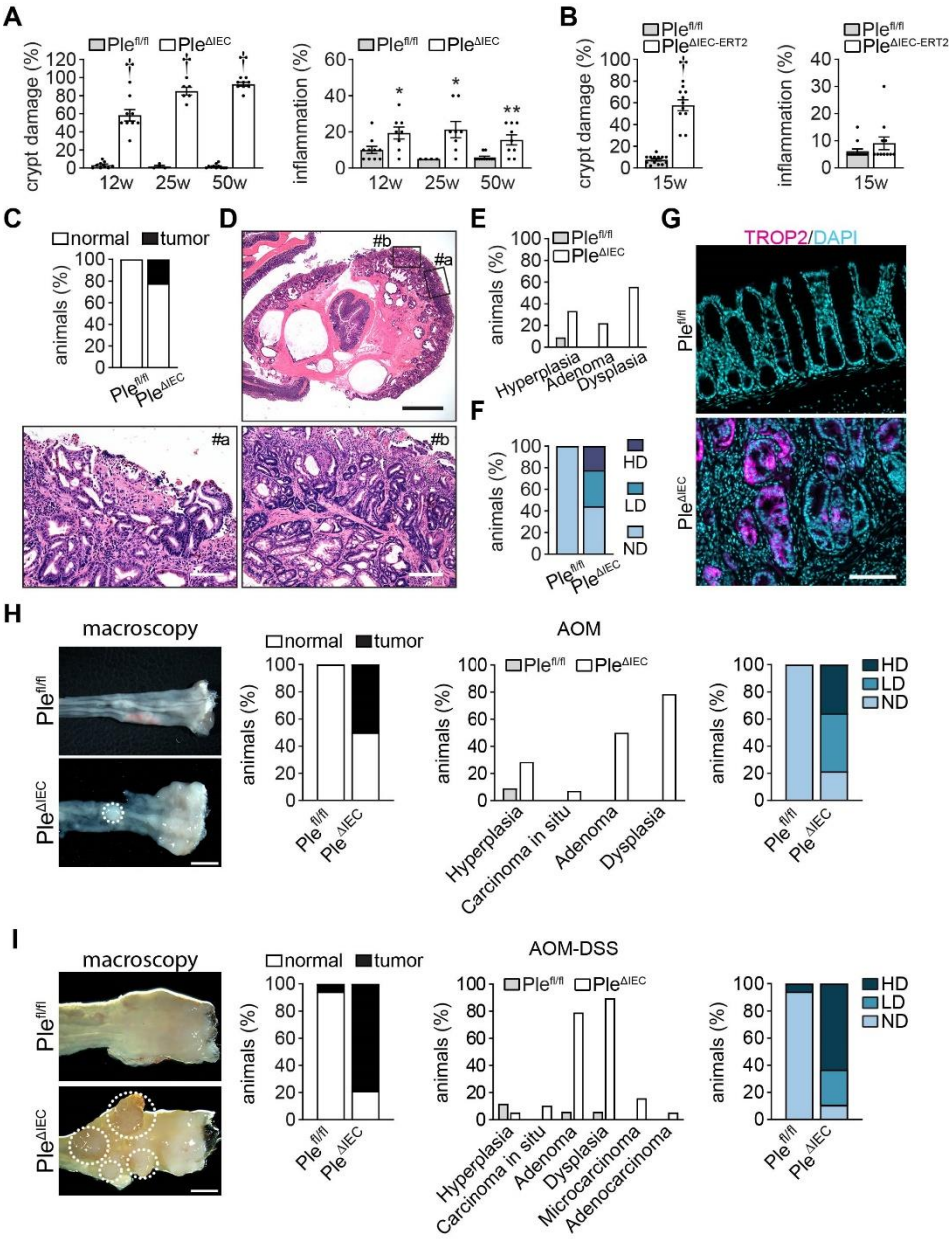

Figure 27 Loss of plectin leads to spontaneous development of colorectal cancer and higher susceptibilit to azoxymethane induced carcinogenesis. (A) *Ple$^{fl/fl}$* and *Ple$^{\Delta IEC}$* mice were sacrificed at 12, 25, and 50 weeks (12w, 25w, and 50w) of age. Graphs show quantification of epithelial damage scores and inflammation (%) assessed from H&E-stained colon sections, *n* = 4-11. **(B)** *Ple$^{fl/fl}$* and *Ple$^{\Delta IEC\text{-}ERT2}$* mice were sacrificed at 15 weeks. Plectin inactivation was induced by three consecutive applications of TMX on days 6, 8, and 10; mice were sacrificed on day 14. Graphs show quantification of epithelial damage scores and inflammation (%) assessed from colon H&E-stained sections at the age indicated, *n* = 11-13. **(C, D)** *Ple$^{fl/fl}$* and *Ple$^{\Delta IEC}$* mice were sacrificed at 50 weeks of age. Graph shows quantification of tumor incidence (%; C) assessed from H&E-stained colon sections (D), *n* = 9-11.**(D)** Reprezentative image of H&E-stained sections of rectal prolapse of 50w old *Ple$^{\Delta IEC}$* mouse. Scale bar, 2 mm. Boxed areas show magnified areas of inflammatory lesion (#a) and tubular adenoma with high grade dysplasia (#b). Scale bar, 200 µm. **(E)** Quantification of CRC parameters on H&E-stained colon sections of *Ple$^{fl/fl}$* and *Ple$^{\Delta IEC}$*. Graphs show the incidence of hyperplasia adenoma and dysplasia (%). **(F)** Specification of dysplasia, HD = high dysplasia (dark blue), LD = low dysplasia (light blue), ND = no dysplasia (cyan). **(G)** Representative immunofluorescence images of *Ple$^{fl/fl}$* and *Ple$^{\Delta IEC}$* distal colon sections immunolabeled for TROP2 (magenta). Nuclei were stained with DAPI (cyan). Scale bar, 100 µm. **(H)** Experimental induction of sporadic colorectal cancer (CRC) by azoxymethan (AOM) treatment in *Ple$^{fl/fl}$* and *Ple$^{\Delta IEC}$* mice. Pictures represent macroscopically visible tumors in distal colons. Scale bar, 3 mm. Graphs show quantification of incidence (%) of tumors, hyperplasia, carcinoma in situ, adenoma, and dysplasia; specification of HD, LD and ND, *n* = 11-14. **(I)** Experimental induction of colitis-associated CRC (CA-CRC) by combination of 2% DSS with AOM treatment in *Ple$^{fl/fl}$* and *Ple$^{\Delta IEC}$* mice. Pictures represent macroscopically visible tumors in distal colons. Scale bar, 3 mm. Graphs show quantification of incidence (%) of tumors, hyperplasia, carcinoma in situ, adenoma, dysplasia, microcarcinoma, and adenocarcinoma; specification of HD, LD and ND, *n* = 17-19. Data are presented as mean ± SEM, **P* < 0.05, †*P* < 0.001.

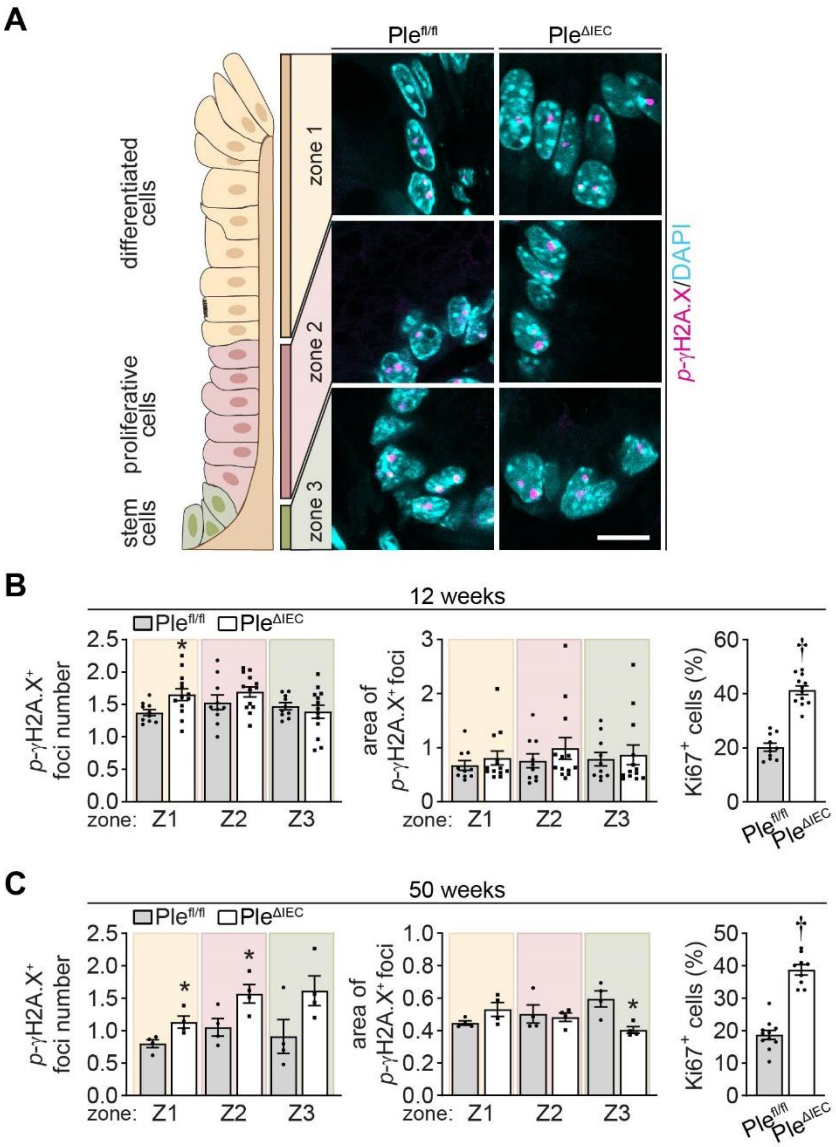

Figure 28 *Ple$^{\Delta IEC}$* mice are more susceptible to DNA damage. (A) Representative immunofluorescence images of 12 weeks old *Ple$^{fl/fl}$* and *Ple$^{\Delta IEC}$* IEC nuclei in distal colon crypts immunolabeled for histone γH2A.X phosphorylated on Ser139 (*p*-γH2A.X; magenta). Nuclei were stained with DAPI (cyan). Scale bar, 5 µm. Drawn schematics depicts distinct zones of colonic crypt. Zone of differentiated cells (zone 1; yellow), zone of proliferative cells (zone 2, pink), zone of stem cells (zone 3; green). **(B)** Graphs show quantification of numbers of *p*-γH2A.X-positive (*p*-γH2A.X$^+$) foci per nucleus, area of *p*-γH2A.X$^+$ foci, and percentage of Ki-67$^+$ cells separately for Z1/Z2/Z3 zones in crypts of 12 weeks old *Ple$^{fl/fl}$* and *Ple$^{\Delta IEC}$* mice. *n* = 10-13. **(C)** Graphs show quantification of numbers of *p*-γH2A.X$^+$ foci per nucleus, area of *p*-γH2A.X$^+$ foci, and percentage of Ki-67$^+$ cells separately for Z1/Z2/Z3 zones in crypts of 50 weeks old *Ple$^{fl/fl}$* and *Ple$^{\Delta IEC}$* mice. *n* = 4. Data are presented as mean ± SEM, $^*P < 0.05$, $^\dagger P < 0.001$.

To explore whether plectin deficiency is associated with altered gene expression, we performed RNA sequencing (RNA seq) analysis of colonic mucosa scrapings collected from adult 12-week-old *Ple$^{fl/fl}$* and *Ple$^{\Delta IEC}$* mice. Out of 17,095 genes with non-zero expression, 912 have been identified as differentially expressed genes (FDR <=0.1; |LFC| >=1). Gene set enrichment analysis (GSEA) using gene ontology (GO) and kyoto encyclopedia of genes and

genomes (KEGG) terms revealed a strong positive correlation with genes linked to increased cell cycle rate, DNA damage, and DNA repair (such as *H2A.X, ATR, ATM, Chek1, Chek2, BRCA1, BRCA2, PLK1,4*; Figure 29A, B). Expression of selected genes/proteins (cell cycle checkpoint and DNA damage kinases, tumor suppressors, and DNA damage markers) was validated by qRT-PCR and immunoblot analysis (Figure 29C, D). These data indicate that plectin-deficient intestinal epithelium suffers from increased DNA damage, accompanied by elevated levels of genes associated with DNA damage checkpoint signaling throughout all cell cycle phases, and the DNA damage repair pathways. These factors further predispose *Ple$^{\Delta IEC}$* mice to CRC, as evidenced by an increased intestinal adenoma signature.

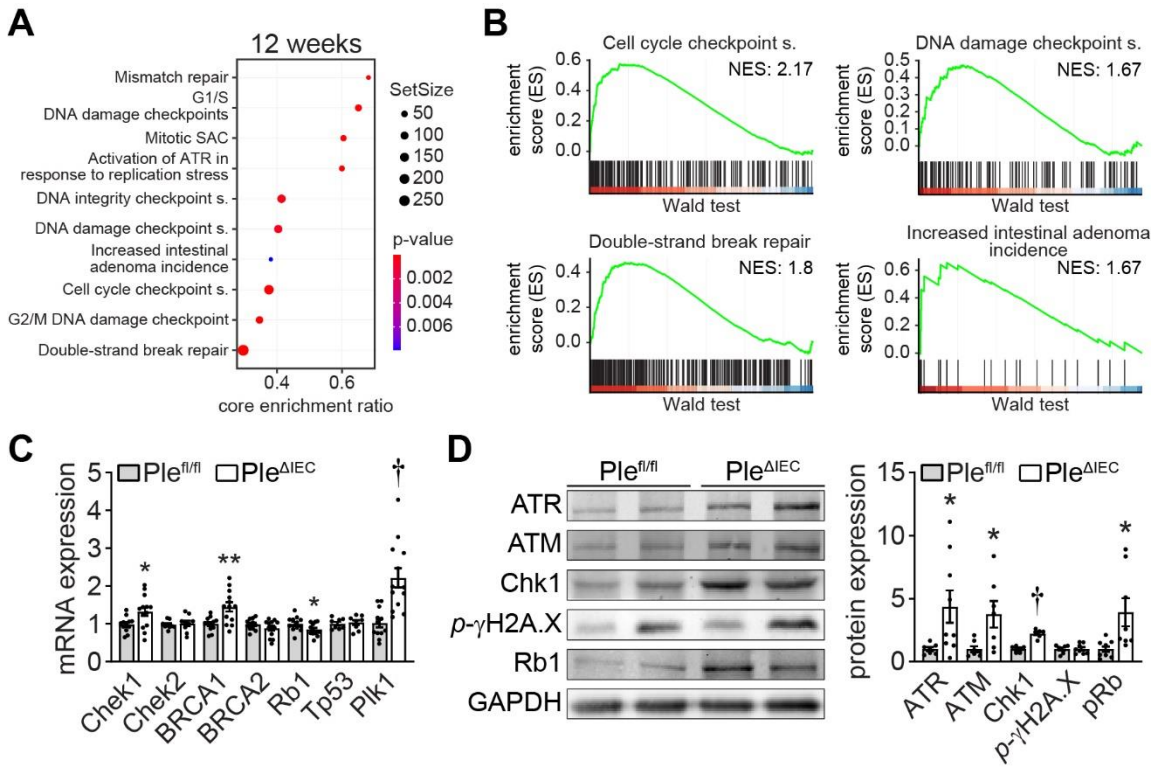

Figure 29 Expression of genes associated with cell cycle and DNA damage altered in 12-week-old *Ple$^{\Delta IEC}$* mice. (A) Representation of the most significantly deregulated processes identified in Gene set enrichment analysis (GSEA) on Gene Ontology (GO) and Kyoto Encyclopedia of Genes and Genomes (KEGG) gene sets. **(B)** GSEA enrichment score for selected processes – Cell cycle checkpoint signaling, DNA damage checkpoint signaling, Double-strand break repair, and Increased intestinal adenoma incidence. **(C, D)** Relative mRNA (C) levels of *Chek1/2, BRCA1/2, Rb1, Tp53*, and *Plk1* and protein (D) levels of ATR, ATM, Chk1, *p*-γH2A.X, and pRb in *Ple$^{fl/fl}$* and *Ple$^{\Delta IEC}$* distal colon. GAPDH, loading control. Graphs show relative band intensities normalized to average *Ple$^{fl/fl}$* values *n* = 6-13. Data are presented as mean ± SEM, **P* < 0.05, ***P* < 0.01, †*P* < 0.001.

To address whether the chronic inflammation triggers DNA damage and hyperproliferation in the mechanically fragile colonic tissue of *Ple$^{\Delta IEC}$* mice, we conducted RNA seq analysis on young, 2-3-week-old *Ple$^{fl/fl}$* and *Ple$^{\Delta IEC}$* mice. Given that these mice

primarily consumed breast milk, we anticipated a lower impact of mechanical stress imposed by intestinal peristalsis and, hence, reduced inflammation in the intestinal tract (Figure 25). Of 24,720 genes with non-zero expression, 512 have been identified as differentially expressed genes (FDR <=0.1; |LFC| >=1). In comparison to adult *Ple$^{\Delta IEC}$* mice, GSEA, using GO terms analysis, demonstrated that gene expression changes in young Ple$^{\Delta IEC}$ mice positively correlated with early inflammatory response and apoptosis while negatively correlating with DNA-damage binding (Figure 30A, B). RNA seq, in conjunction with mRNA and protein analysis (immunoblot and immunofluorescence analyses) revealed that 2-3-week-old *Ple$^{\Delta IEC}$* mice did not exhibit any signs of DNA damage. Moreover, proliferation was comparable between young *Ple$^{fl/fl}$* and *Ple$^{\Delta IEC}$* mice (Figure 30C-F). The RNA and protein profiling data support our hypothesis that mechanical stress affecting the mechanically vulnerable *Ple$^{\Delta IEC}$* intestinal epithelium may contribute to the increased accumulation of DNA damage and hyperproliferation, thereby predisposing *Ple$^{\Delta IEC}$* mice to carcinogenesis. These results, however, could not rule out contribution of another factor causing DNA damage - inflammation.

4.2.3 **DNA damage is in plectin-deficient IECs aggravated by mechanical stress**

In order to discriminate between the individual contributions of inflammation and mechanical stress to DNA damage, we employed several approaches to minimize the inflammatory component. First, we utilized the *Ple$^{\Delta IEC\text{-}ERT2}$* mouse, in which we depleted microbiota by ATB treatment (Figure 31A). The ATB treatment attenuated the inflammation in *Ple$^{\Delta IEC\text{-}ERT2}$* mice to the extent found in *Ple$^{fl/fl}$* mice (Figure 31B). Our previous investigations (Aim 1 4.1) showed that the attenuation of inflammation in *Ple$^{\Delta IEC\text{-}ERT2}$* mice led to a reduction in crypt damage. However, the level of crypt damage in *Ple$^{\Delta IEC\text{-}ERT2}$* mice was still higher than observed in *Ple$^{fl/fl}$* mice (Figure 24H). Interestingly, the attenuated inflammation had no effect on hyperproliferation (Figure 31C) or DNA damage in differentiated cells, as seen by comparable levels of *p*-γH2A.X^{+} foci in *Ple$^{\Delta IEC\text{-}ERT2}$* mice (Z1; Figure 31D). On the other hand, the ATB treatment in *Ple$^{\Delta IEC\text{-}ERT2}$* mice reduced the number of *p*-γH2A.X^{+} foci in the stem cell zone (Z3; Figure 31D). This suggests that while the inflammation contributes to the crypt damage, the hyperproliferation and DNA damage could be, to some extent, caused by inflammation-independent factors, such as mechanical stress.

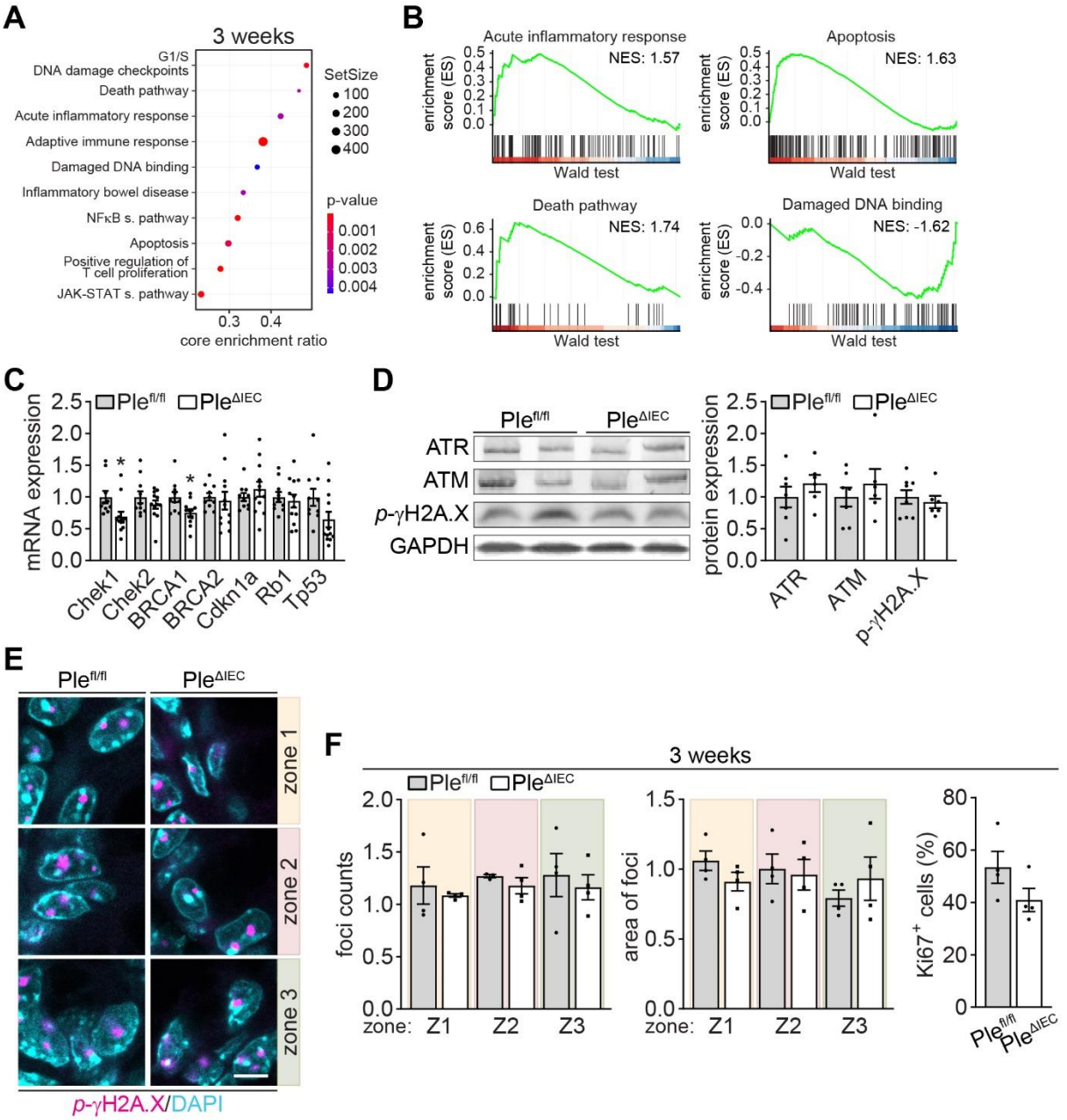

Figure 30 Enrichment of early inflammation and apoptosis associated signatures in 3-week-old *Ple$^{\Delta IEC}$* mice. (A) Representation of the most significantly deregulated processes identified in GSEA on GO and KEGG gene sets. **(B)** GSEA enrichment score for selected processes – Acute inflammatory response, Apoptosis, Death pathway, and DNA damage binding**. (C, D)** Relative mRNA (C) levels of *Chek1/2, BRCA1/2, Cdkn1a*, *Rb1*, and *Tp53* and protein (D) levels of ATR, ATM, and *p*-γH2A.X in *Ple$^{fl/fl}$* and *Ple$^{\Delta IEC}$* distal colon. GAPDH, loading control. Graphs show relative band intensities normalized to average *Ple$^{fl/fl}$* values, $n = 7–12$. **(E)** Representative immunofluorescence images of 3 weeks old *Ple$^{fl/fl}$* and *Ple$^{\Delta IEC}$* IEC nuclei in distal colon crypts immunolabeled for histone *p*-γH2A.X (magenta). Nuclei were stained with DAPI (cyan). Scale bar, 5 µm. **(F)** Graphs show quantification of numbers of *p*-γH2A.X$^+$ foci per nucleus, area of *p*-γH2A.X$^+$ foci (F), and percentage of Ki-67$^+$ cells separately for indicated crypt zones (see Figure 28A) of 3 weeks old *Ple$^{fl/fl}$* and *Ple$^{\Delta IEC}$* mice. Scale bar, 5 µm; $n = 4$. Data are presented as mean ± SEM, $^*P < 0.05$.

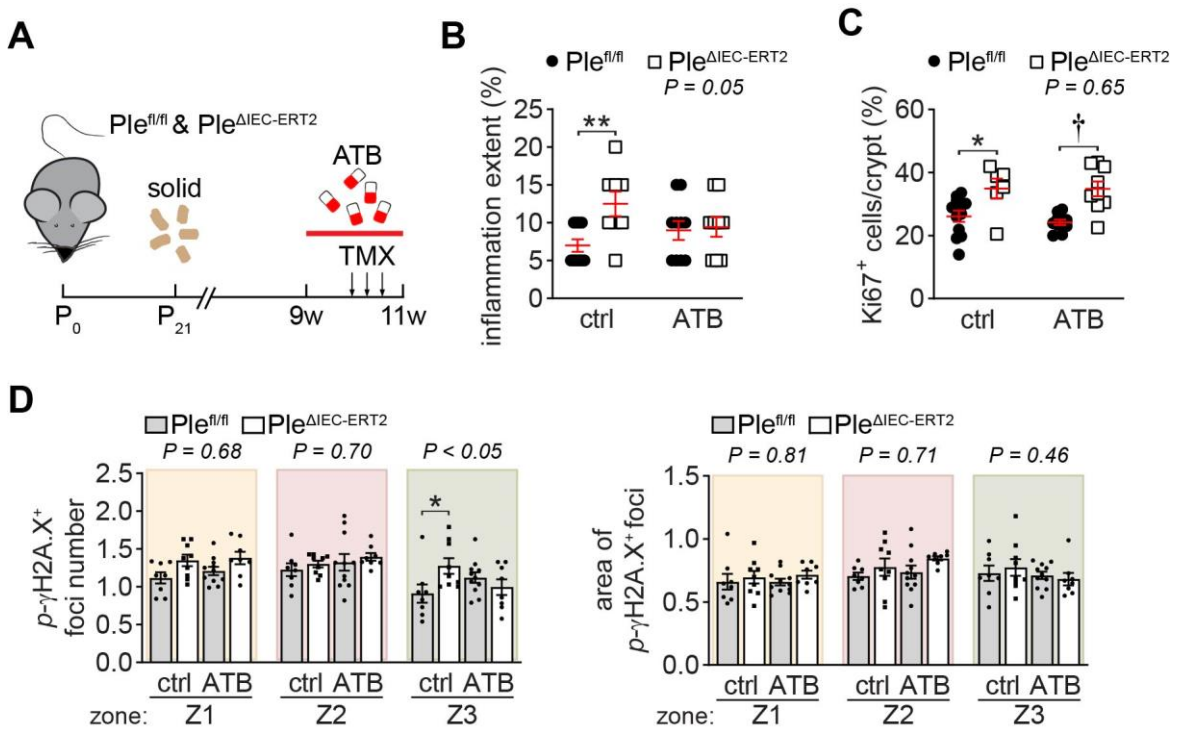

Figure 31 Inflammation contributes to the increased DNA damage in *Ple$^{\Delta IEC}$* mice. (A-C) 9 weeks old *Ple$^{fl/fl}$* and *Ple$^{\Delta IEC\text{-}ERT2}$* mice were kept either untreated or treated with broad-spectrum ATB. Schematic illustrates the experimental setup. Graphs show quantification of inflammation extent and Ki-67$^+$ cells (%) in *Ple$^{fl/fl}$* and *Ple$^{\Delta IEC\text{-}ERT2}$* colon crypts. **(D)** Graphs show quantification of numbers of *p*-γH2A.X$^+$ foci per nucleus, and area of *p*-γH2A.X$^+$ foci separately for indicated crypt zones (see Figure 28A) in crypts of *Ple$^{fl/fl}$* and *Ple$^{\Delta IEC\text{-}ERT2}$* mice with or without ATB. *n* = 8-12. Data are presented as mean ± SEM, **P* < 0.05, ***P* < 0.01, †*P* < 0.001.

To further investigate the effect of mechanical stress on the intestinal epithelium with minimal inflammatory component, we imposed a mechanical strain on the *ex vivo* colon explant cultures (CECs) derived from *Ple$^{fl/fl}$* and *Ple$^{\Delta IEC}$* mice. CECs from the distal colon were pinned to PDMS membranes and either exposed to 10% cyclic stretch or left in the media as non-stretched controls (Figure 32A). While one hour of cyclic stretch did not cause any changes in DNA damage in *Ple$^{fl/fl}$* crypts, we observed significantly increased DNA damage in *Ple$^{\Delta IEC}$* cells (Figure 32B).

Although we subjected isolated tissue to stretch *ex vivo*, we cannot rule out the contribution of ongoing inflammation in *Ple$^{\Delta IEC}$* environment. To avoid any contribution of inflammation, we established a 2D model of colonic organoids derived from *Ple$^{fl/fl}$* colonic primary cells and subjected them to mechanical strain (Figure 33A). The pattern of 2D colon organoid cultures stained for Ki-67 resembles the expansion of proliferative and differentiated cells typical for intestinal crypts (Figure 33B). In order to mimic plectin inactivation, we treated

organoids with plectin inhibitor, plecstatin-1 [PST; (Meier et al., 2017; Prechova et al., 2022)]. The immunolabeling of K8 showed upon PST treatment a pattern typical for KO cells, i. e. the coarse network composed of thick KF bundles (non-stretch; Figure 33C). A high-content screening microscopy together with data analysis unveiled that while plectin inactivation itself did not lead to the accumulation of DSBs, PST-treated *Ple*$^{fl/fl}$ organoids exposed to stretching exhibited significantly higher levels of DSBs compared to untreated stretched *Ple*$^{fl/fl}$organoids (Figure 33D-F). Overall, these data suggest that mechanical stress represents a potent driver of DNA damage within mechanically compromised plectin-deficient epithelial cells. Concomitant inflammation in *Ple*$^{\Delta IEC}$ colon may further aggravate this damage, thus contributing to tumorigenesis.

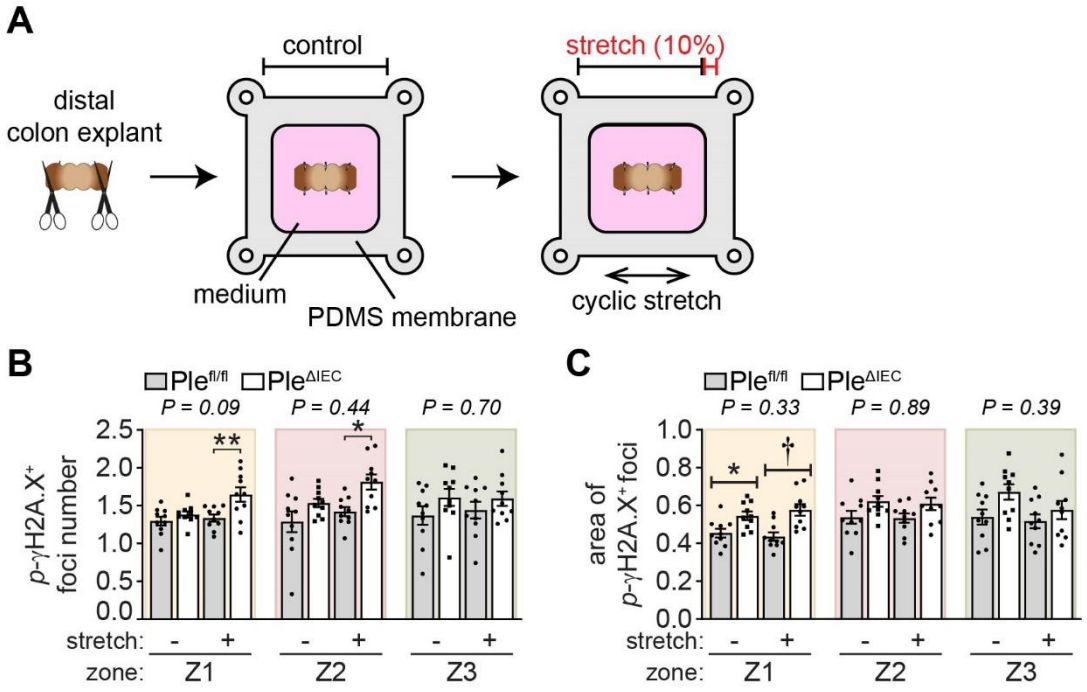

Figure 32 Mechanical stress induces DNA damage in *Ple*$^{\Delta IEC}$ colon explant cultures *ex vivo*. **(A)** Schematic illustration of the experimental setup. Colon explant cultures (CEC) were isolated from the distal colon of *Ple*$^{fl/fl}$ and *Ple*$^{\Delta IEC}$ mice, pinned onto elastic polydimethylsiloxane (PDMS) membrane, and exposed to 10% uniaxial cyclic stretch. **(B, C)** Graphs show quantification of numbers of *p*-γH2A.X$^+$ foci per nucleus (B) and area of *p*-γH2A.X$^+$ foci (C) separately for indicated crypt zones (see Figure 28A) in crypts of *Ple*$^{fl/fl}$ and *Ple*$^{\Delta IEC}$ mice. *n* = 10. Data are presented as mean ± SEM, **P* < 0.05, ***P* < 0.01, †*P* < 0.001.

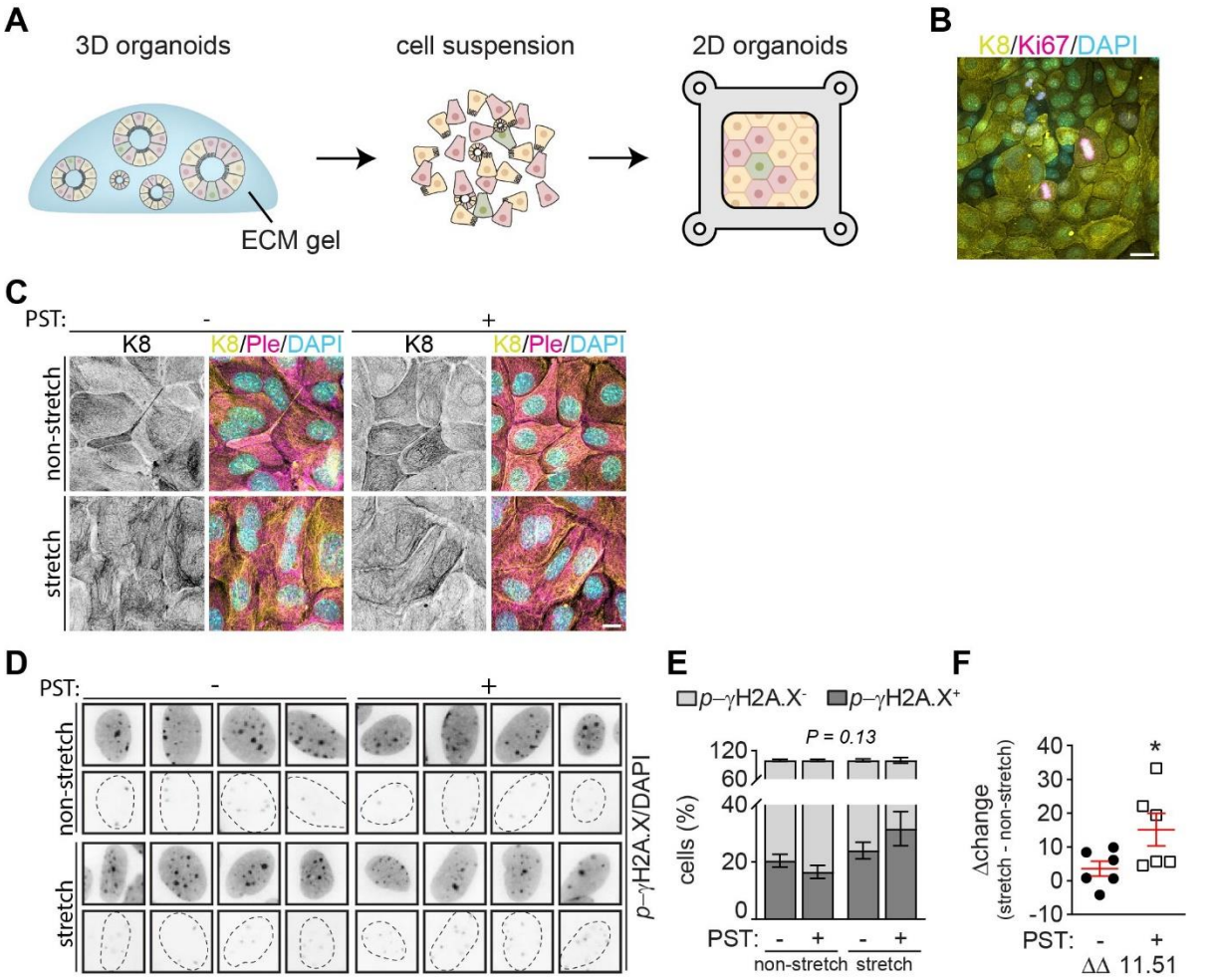

Figure 33 Mechanical stress induces DNA damage in colonic organoids upon plectin inactivation. (A) Schematic illustration of experimental setup. 3D colonic organoids grown in ECM domes were mechanically disrupted to suspension of single cells and small organoids, and seeded as a 2D monolayer onto PDMS membrane. **(B)** Representative immunofluorescence image of 2D monolayers immunolabeled for K8 (inverted single channel; yellow in overlap), and Ki-67 (magenta). Nuclei were stained with DAPI (cyan). Scale bar, 20 µm. **(C)** Representative immunofluorescence images of 2D organoids non-treated (-) or treated (+) with 16 µM plecstatin-1 (PST), and exposed to stretch (stretch) or non-stretched. 2D organoids immunolabeled with antibodies against K8 (yellow), and plectin (magenta). Nuclei were stained with DAPI (cyan). Scale bar, 10 µm. **(D)** Automatic segmentation and analysis of *p*-γH2A.X$^+$ foci. Dashed line areas show *p*-γH2A.X$^+$ nuclear signal. **(E, F)** Quantification of *p*-γH2A.X$^+$ and negative (*p*-γH2A.X$^-$) populations of cells (%; E), and delta (Δ) changes defined by the difference between stretch and non-stretch in PST – or + organoids. Data are presented as mean ± SEM, $^*P < 0.05$.

4.2.4 Mechanical stress-driven DNA damage and chromosomal instability are increased in plectin-deficient epithelial monolayers

To address inflammation-independent mechanically-driven effects on the epithelium, we used Caco-2 and RPE KO cell lines. Initially, we verified the successful targeting of plectin by immunoblot (Figure 34A) and immunofluorescence analyses (Figure 34B, C). The primary characterization of the IF network was in line with previous observations, demonstrating that plectin ablation resulted in the collapse of the KF network in Caco-2 and the VF network in RPE cells, manifesting with prominent IF bundles. Upon examining DSBs under non-challenged

conditions, we observed a comparable *p*-γH2A.X^{+} populations between monolayers grown from WT and KO Caco-2 and RPE cells (Figure 34D, E). When we exposed cells to 2 Gy X-ray irradiation, we noted a similar trend between WT and KO monolayers in the disappearance of *p*-γH2A.X^{+} foci throughout the time (Figure 35A, B). These data indicate that loss of plectin itself does not induce DNA damage or impair DNA damage repair mechanisms.

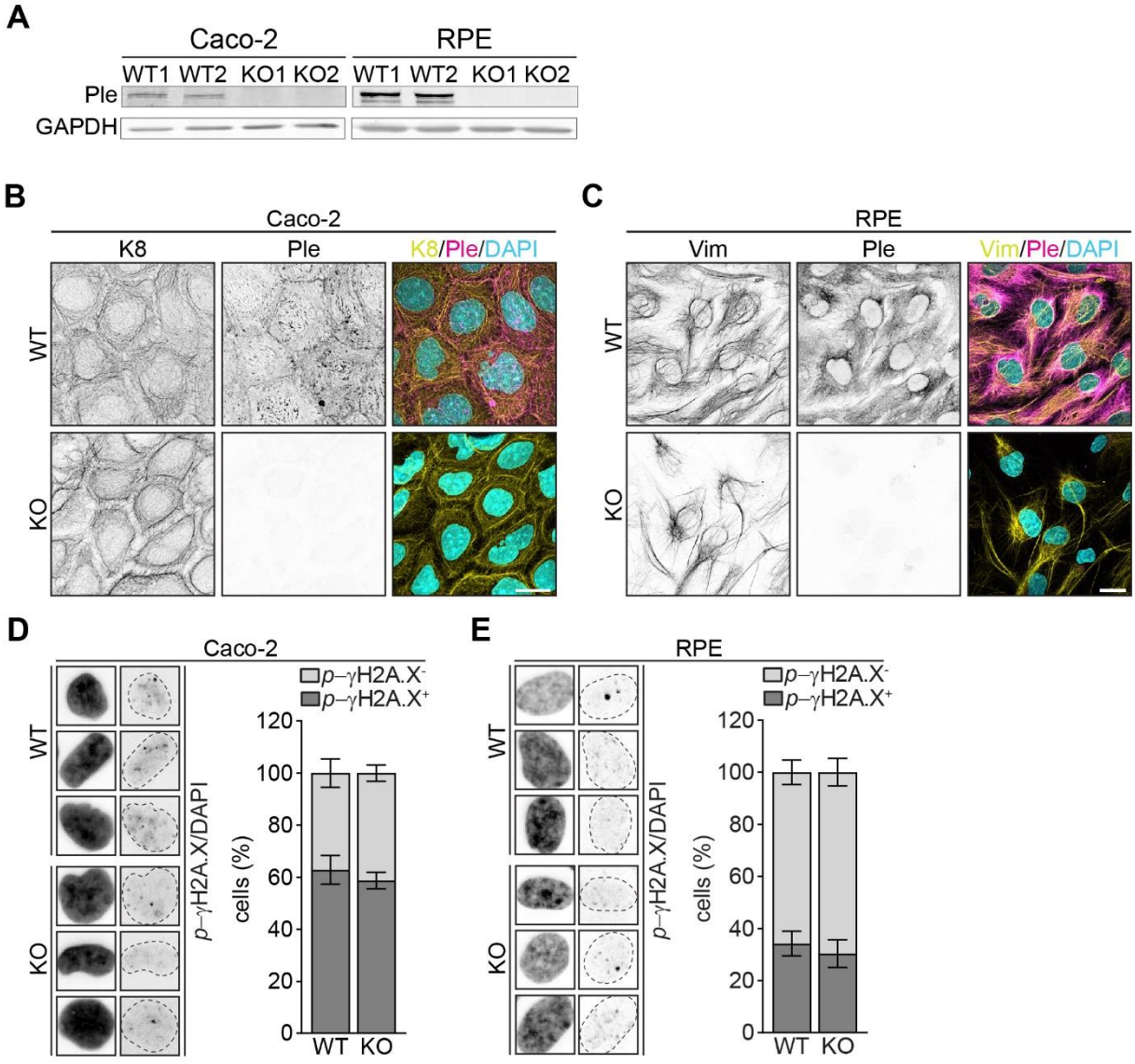

Figure 34 Verification of plectin targeting in Caco-2 and RPE cells. (A) Immunoblots showing depletion of plectin in individual clones of Caco-2 and RPE cells generated with two alternative guide-RNAs (KO1 and KO2). GAPDH, loading control. **(B, C)** Representative immunofluorescence images of WT and KO Caco-2 (B) and RPE (C) cell monolayer cultures immunolabeled for K8 (B) and vimentin (Vim; C; inverted single channel; yellow in overlap) and plectin (magenta). Nuclei were stained with DAPI (cyan). Scale bar, 10 µm. **(D, E)** Automatic segmentation and analysis of *p*-γH2A.X^{+} foci. Dashed line areas show *p*-γH2A.X^{+} nuclear signal. Quantification of *p*-γH2A.X^{+} and *p*-γH2A.X^{-} populations of Caco-2 (D), and RPE (E) cells. *n* = 8-12. Data are presented as mean ± SEM.

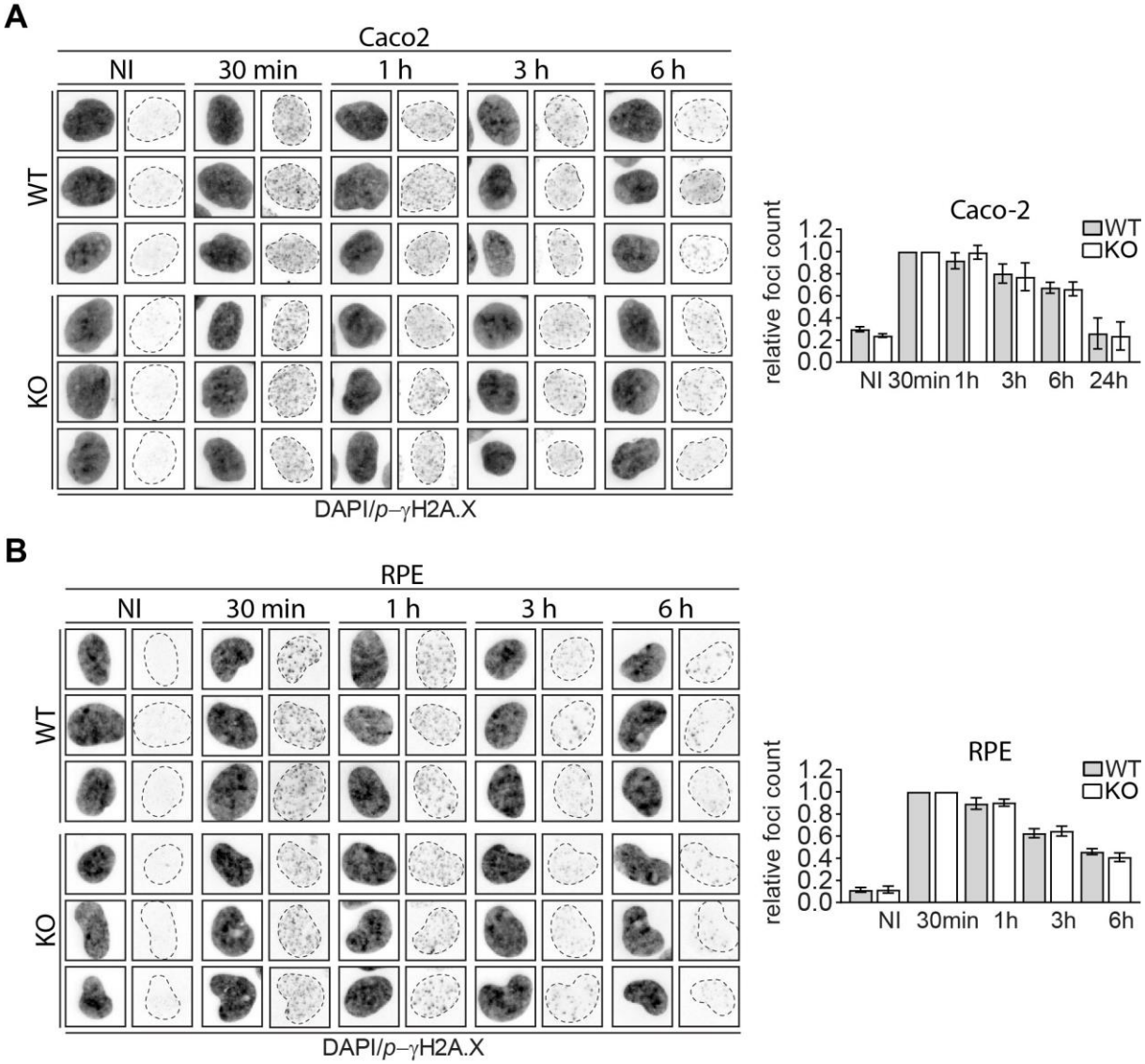

Figure 35 Loss of Plectin does not affect DNA damage repair. (A, B) Caco-2 (A) and RPE (B) cells were irradiated by 2 Gy X-ray and fixed at different time points. Automatic segmentation and analysis of *p*-γH2A.X$^+$ foci. Dashed line areas show *p*-γH2A.X$^+$ nuclear signal. Quantification of relative foci count in non-irradiated (NI) cells, and in 30 minutes (30min), 1 hour (1h), 3 hours (3h), and 6 hours (6h) after irradiation. *n* = 4. Data are presented as mean ± SEM (Maninová, unpublished).

The susceptibility of plectin-deficient cells to DNA damage under mechanical stress was assessed using the stretch device. WT and KO monolayers were seeded onto PDMS membranes coated with Coll I (Caco-2) or FN (RPE) and subjected to uniaxial cyclic stretch for 80 minutes with an amplitude 35% (Caco-2) or 20% (RPE). The analysis of non-stretched conditions confirmed our previous findings, where we did not observe any differences in the extent of DNA damage between KO and WT monolayers (Figure 34D, E). The quantification of *p*-γH2A.X$^+$ populations showed enhanced trends in stretched KO monolayers, which indicates a significant increase in DNA damage susceptibility when stretched and non-stretched

conditions were compared between WT and KO monolayers [Δchange (stretch – non-stretch) 6,9% in Caco-2 and 7,8% in RPE cells; Figure 36A, B].

Unrepaired DSBs can lead to cell death or neoplastic transformation. Also, incorrectly repaired DSBs, such as the misjoining of DSBs on different chromosomes, can cause genomic instability, chromosomal translocations, and mutagenic rearrangements (Cannan and Pederson, 2016; Mills et al., 2003; Zhang and Jasin, 2011). Throughout mitosis, various types of chromosomal aberrations, including multipolar spindles, chromosomal bridges, and lagging chromosomes, can be recognized. After a cell completes the mitosis and gives rise to a new population of daughter cells, such unrepaired chromosomal aberrations may manifest as micronuclei (Krupina et al., 2021). To score chromosomal aberrations in cells exposed to mechanical stress, we subjected WT and KO monolayers to stretch and synchronized them in prometaphase. Subsequently, we evaluated the occurrence of chromosomal aberrations in mitotic cells (namely multipolar spindles, chromosomal bridges, lagging chromosomes, and G1 cells for micronuclei; Figure 36C). In WT monolayers, stretch slightly enriched the fraction of multipolar spindles and micronuclei. Strikingly, the impact of mechanical stretch on KO monolayers was significantly more pronounced, leading to an increased frequency of all scored chromosomal aberrations and micronuclei in daughter cells within Caco-2 (Figure 36D) and RPE monolayers (Figure 36E).

IFs confer elastic spring-like properties, allowing cells to absorb energy and withstand tensile loads, thereby maintaining genome integrity and protecting the nucleus from mechanical deformation (Block et al., 2018; Patteson et al., 2019). In respect to the aberrant organization of IFs observed in KO cells, we inspected the impact of stretch on the cytoarchitecture of Caco-2 and RPE WT and KO monolayers (Figure 37). As expected, stretch induced reinforcement of the IF network, apparent in the IF bundle thickening in WT cells. This effect was more apparent in Caco-2 than in RPE monolayers. Remarkably, stretch triggered more profound architectural alterations in KO cells.

The initially compromised network of IFs caused by the plectin inactivation in the non-stretched condition, collapsed due to the stretch into even more prominent bundles, which were found densely packed around the nucleus. This suggests that the disorganized IFs in KO monolayers impair the responsiveness of IFs to mechanical stress. Consequently, the nucleus is ineffectively protected under mechanical stress, leading to genomic instability.

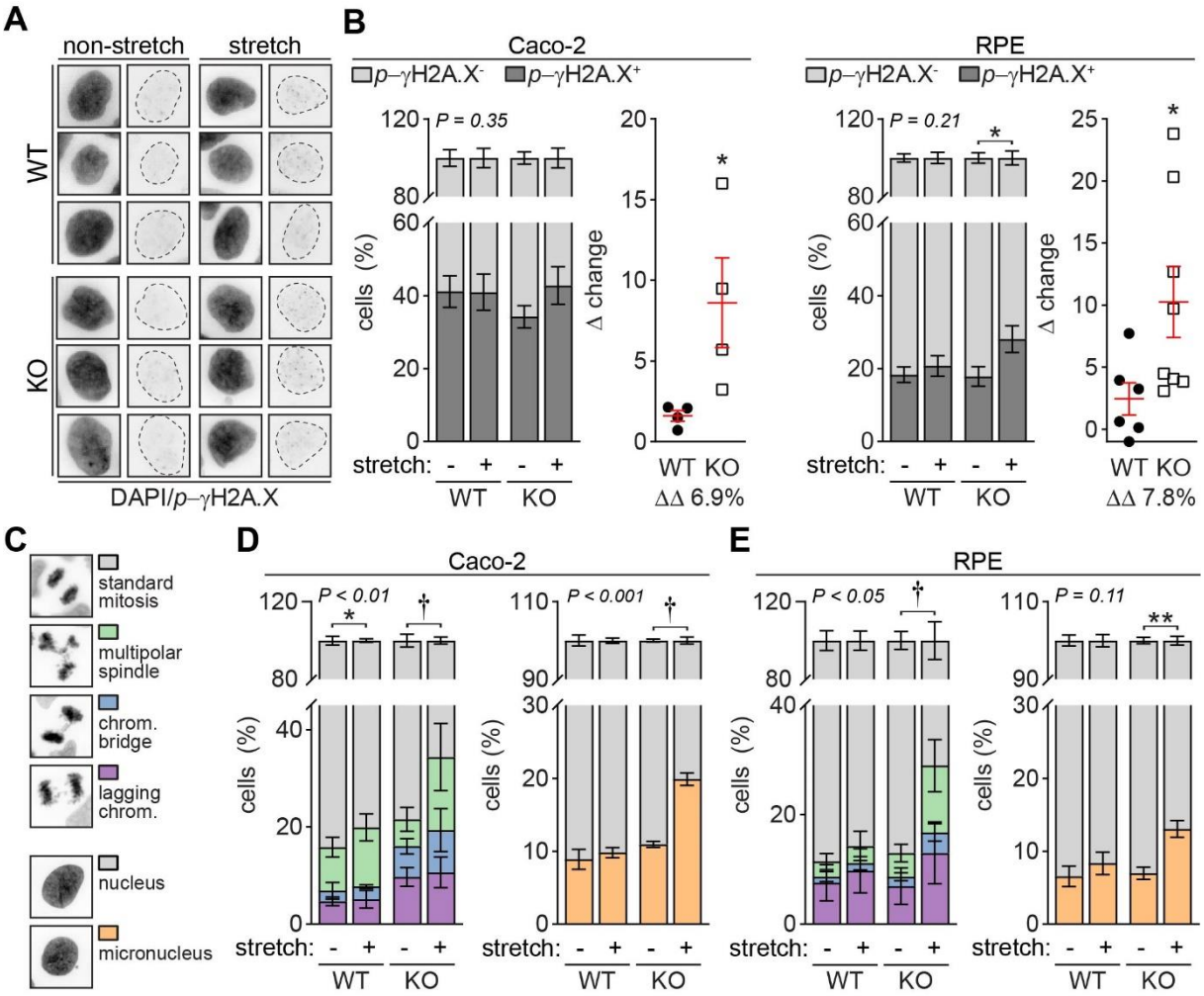

Figure 36 Plectin protects Caco-2 and RPE cell monolayers against stretch-driven DNA damage and chromosomal aberrations. (A, B) Automatic segmentation and analysis of *p*-γH2A.X⁺ foci. Dashed line areas show *p*-γH2A.X⁺ nuclear signal in Caco-2 cells (A). Quantification of *p*-γH2A.X⁺ and *p*-γH2A.X⁻ populations of Caco-2 (A) and RPE (B) monolayers in non-stretched (-) or stretched (+) conditions. Δchanges defined by the difference between stretch and non-stretch in WT and KO cells. **(C-E)** Quantification of chromosomal aberrations scored for standard mitosis (grey), multipolar spindle (green), chromosomal bridges (blue), and lagging chromosomes (purple) during mitosis; and G1-phase nuclei scored for nucleus (grey) and micronucleus (yellow; C) in Caco-2 (D) and RPE (E) cells in non-stretched (-) or stretched (+) conditions. *n* = 4-6. Data are presented as mean ± SEM, **P* < 0.05, ***P* < 0.01, †*P* < 0.001.

A precisely controlled cell rounding during mitosis is critical for supporting cell division, ensuring space required for mitotic spindle alignment and chromosome segregation. Moreover, the cell cortex composed of actin and underlying vimentin networks, provides mechanical support for cells during mitosis. In this process, vimentin is recruited to the mitotic cell cortex in a plectin-dependent manner (Serres et al., 2020). Since we observed increased DNA damage in intestinal proliferative cells *in vivo*, we considered whether plectin inactivation can exacerbate DNA damage in cells during mitosis. To explore this, we enriched the population of mitotic cells and confined them with polyacrylamide (PAA) hydrogels of different

stiffness [5, 10, 20 kPa; Figure 38A; (Le Berre et al., 2014; Matthews et al., 2020)]. The analysis of *p*-γH2A.X^{+} foci showed a slight increase in the DSB count as an effect of increasing stiffness in WT Caco-2 and RPE cells (Figure 38B, C). In contrast, a pronounced appearance of *p*-γH2A.X^{+} foci was evidenced even under softer 5 kPa-stiff hydrogel, with a gradual rise in the stiffer 20 kPa environment. The higher DSB occurrence in KO monolayers coincided with enhanced accumulation of chromosomal aberrations (Figure 38D, E). While WT cells showed minimal chromosomal aberrations and micronuclei, KO cells displayed higher numbers of the multipolar spindle, the lagging chromosomes, and micronuclei already under the confinement of softer PAA gel. The effects in mitosis were not due to the differences in mitotic speed progression as WT and KO cells proceeded through mitosis at comparable times (Figure 38F).

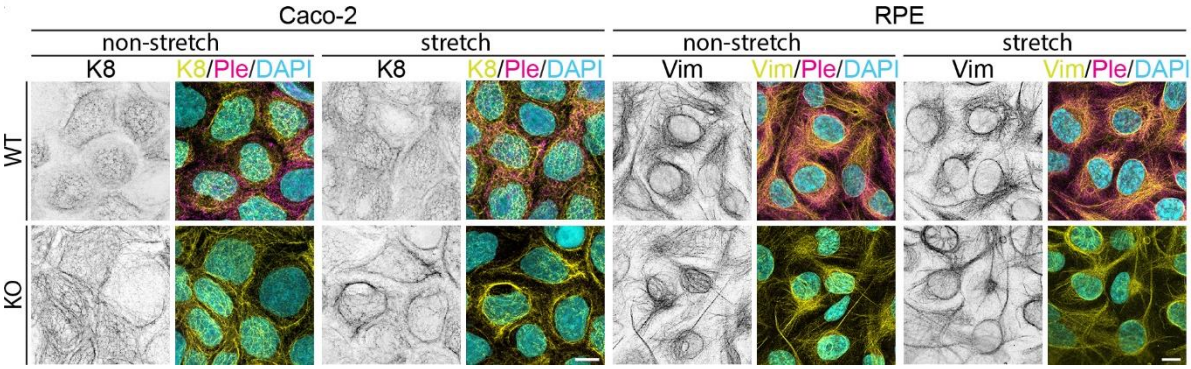

Figure 37 Formation of aberrant IF structures after stretch in plectin-deficient monolayers. Representative immunofluorescence images of WT and KO non-stretched and stretched Caco-2 and RPE monolayers. Monolayers were immunolabeled with antibodies against K8 (inverted single channel; yellow in overlap; Caco-2), Vim (inverted single channel; yellow in overlap; RPE), and plectin (magenta). Nuclei were stained with DAPI (cyan). Scale bar, 10 µm.

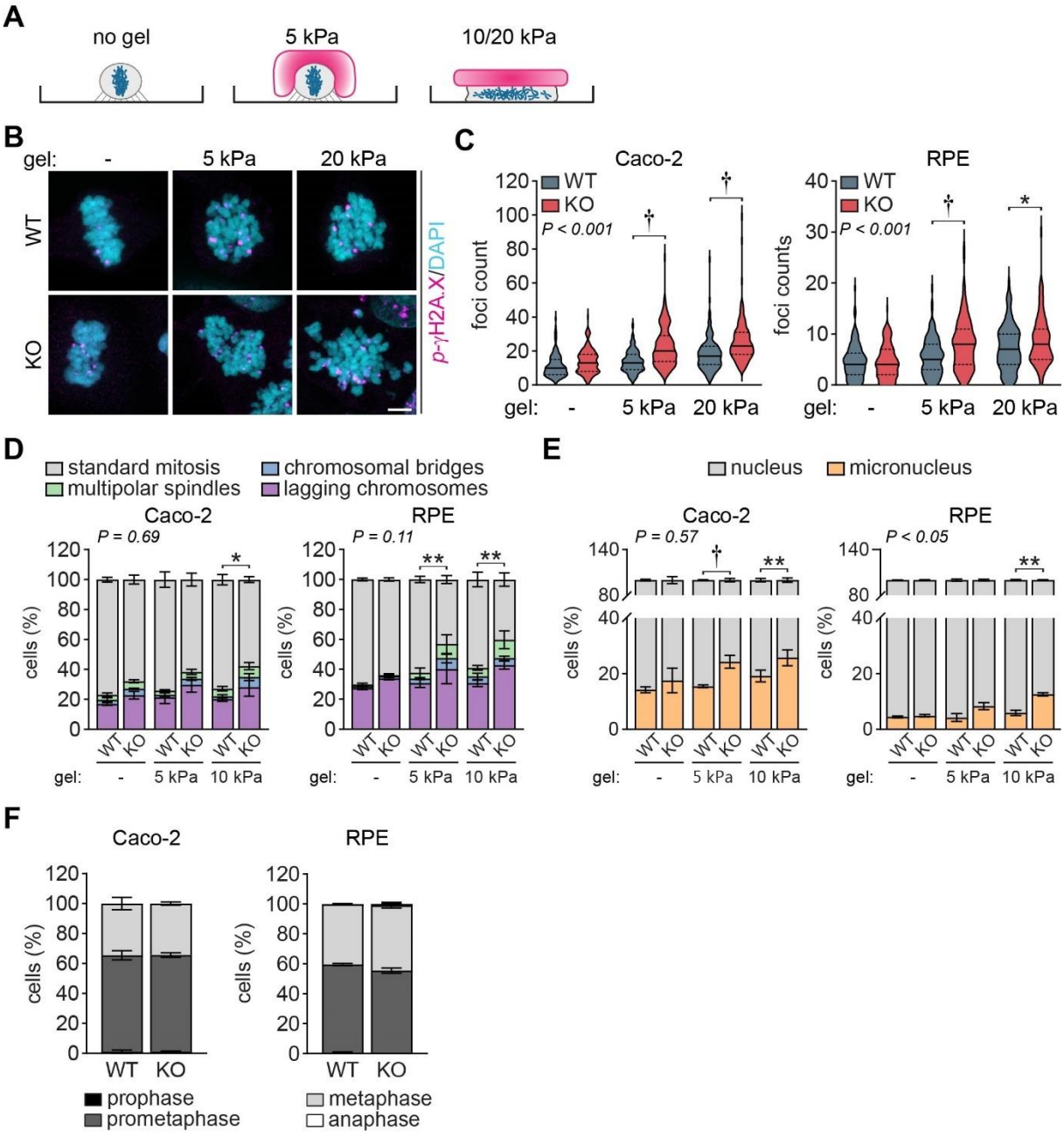

Figure 38 Plectin deficiency leads to DNA damage and accumulation of chromosomal aberrations under cell confinement. **(A)** Schematic illustration of the experimental setup. Polyacrylamide gels of indicated stiffness were placed on top of mitotic cells. **(B)** Reprezentative immunofluorescence images of WT and KO Caco-2 mitotic cells upon cell confinement. Cells were immunolabeled with an antibody against *p*-γH2A.X (magenta). Nuclei were stained with DAPI (cyan). Scale bar, 5 µm. **(C)** Quantification of *p*-γH2A.X$^+$ foci per mitotic cell in WT and KO Caco-2, and RPE cells in confinement. *n* = 105-166. **(D, E)** Quantification of chromosomal aberrations scored for standard mitosis (grey), multipolar spindle (green), chromosomal bridges (blue), and lagging chromosomes (purple) during mitosis (D); and G1-phase nuclei scored for nucleus (grey) and micronucleus (yellow; E) in Caco-2 and RPE cells in confinement, *n* = 3-4. **(F)** Quantitative analysis of mitotic progression speeds in WT and KO Caco-2 and RPE cells. Bars show the enrichment of mitotic cells in individual mitotic phases. Prophase (black), prometaphase (dark grey), metaphase (light grey), and anaphase (white), *n* = 2. Data are presented as mean ± SEM, **P* < 0.05, ***P* < 0.01, †*P* < 0.001 (Maninová, unpublished).

During mitosis, the cell cortex represents a major cytoskeletal structure, ensuring cellular shape and intracellular space required for individual mitotic events. Its mechanical

properties are defined mainly by its tension and stiffness. It has been demonstrated that in cells lacking vimentin, the cell cortex is thicker and softer, and mitotic cells are more prone to chromosomal instability upon mechanical stress (Serres et al., 2020). We checked the mechanical resilience of WT and KO Caco-2 and RPE cells under confinement by measuring cell height and width. While WT cells maintained their resistance, and their height and width did not differ in relation to the increasing stiffness of PAA gels. On the other hand, KO cells were deformable even under softer conditions, which was reflected by their significant flattening and widening at 5 kPa condition (Figure 39A-D). Detailed visualization of IFs revealed that while in WT cells, IFs form a well-organized cage surrounding the mitotic nucleus, in KO cells, the cage composed of thick bundles is disorganized, and some bundles were in close proximity to condensed chromatin (Figure 39E). Interestingly, closer insight indicated that these collapsed bundles encapsulated small DNA fragments, potentially explaining the high abundance of lagging chromosomes under cell confinement in KO cells. Taken together, compromised mechanical resilience of cell cortex governed by the plectin deficiency determines the high vulnerability of cells to DNA damage and chromosomal instability during mitosis.

4.2.5 **Plectin facilitates an adaptive cellular response to mechanical stress**

In epithelia, cells endure continuous exposure to diverse mechanical stresses. To maintain the integrity of the mechanical barrier, epithelial cells employ various mechanisms to absorb energy, resist force-induced deformations, and protect the genome from mechanical stress-induced DNA damage. When subjected to high amplitude uniaxial cyclic stretch, the cytoskeleton undergoes strain-induced reorganization, leading to the realignment of epithelial monolayers through rearrangement and strengthening of cell-cell adhesion [AJs; (Pinheiro and Bellaiche, 2018)]. This process is accompanied by the polarization of actomyosin fibres and reorientation of the nucleus perpendicularly to the stretch axis (De and Safran, 2008; Faust et al., 2011; Nava et al., 2020; Noethel et al., 2018; Wang et al., 2001). To inspect the role of plectin in the mechanical adaptation process, we exposed WT and KO Caco-2 and RPE monolayers to uniaxial cyclic stretch and assessed the status of F-actin (phalloidin staining) and nuclei reorientation at 0 (non-stretch), 20 and 60 minutes (Figure 40A, B). Quantitative orientation analysis showed that under non-stretched conditions, actin fibers were in both WT and KO cells directed over wide range of angles (20-90°) relative to the stretch axis, albeit actin

fibers formed thicker filaments in KO monolayers. Following mechanical stretch, F-actin aligned perpendicular to the stretch axis in WT cells in a time-dependent manner. In contrast, the reorientation of actin filaments in KO monolayers was significantly delayed. Similarly, the orientation of nuclei in WT and KO monolayers was almost random under non-stretched conditions. Upon stretch, a significant proportion of WT nuclei aligned at 90°, while KO monolayers exhibited delayed nuclear reorientation (Figure 40C, D).

The altered cytoskeletal distribution was evident at the supracellular level in KO Caco-2 monolayers. Cell body reorientation (defined by absolute Ferret's angle) depends on redistribution and dynamics of cell-cell contacts. Quantification revealed that cell body reorientation in WT monolayers mirrored the behavior of actin filaments, aligning perpendicularly to the stretch axis. In contrast, KO monolayers exhibited a delayed reorientation (Figure 40E). Additionally, ineffective adaptation was supported by the failed elongation of individual KO cells (Ferret's diameter; Figure 40F). Based on the data, we concluded that plectin-deficient cells lose the ability to adapt to mechanical load, thus failing to protect their DNA against mechanical damage.

To determine if the impaired protective function of IFs (Figure 37), together with the ineffective mechanical adaptation of KO monolayers, affect the integrity of the nuclear envelope, we immunolabeled non-stretched and stretched WT and KO RPE monolayers for LMNA/C. Quantitative analysis revealed a significant increase in wrinkled nuclear envelopes in KO monolayers upon stretch. Super-resolution microscopy of co-stained LMNA/C, actin, and vimentin in stretched KO monolayers revealed colocalization of nuclear envelope wrinkles with thick bundles of VFs (Figure 41). This finding supports our hypothesis that compromised cytoskeletal architecture in plectin-deficient cells results in strain-driven nuclear deformation, subsequent DNA damage, and chromosomal instability.

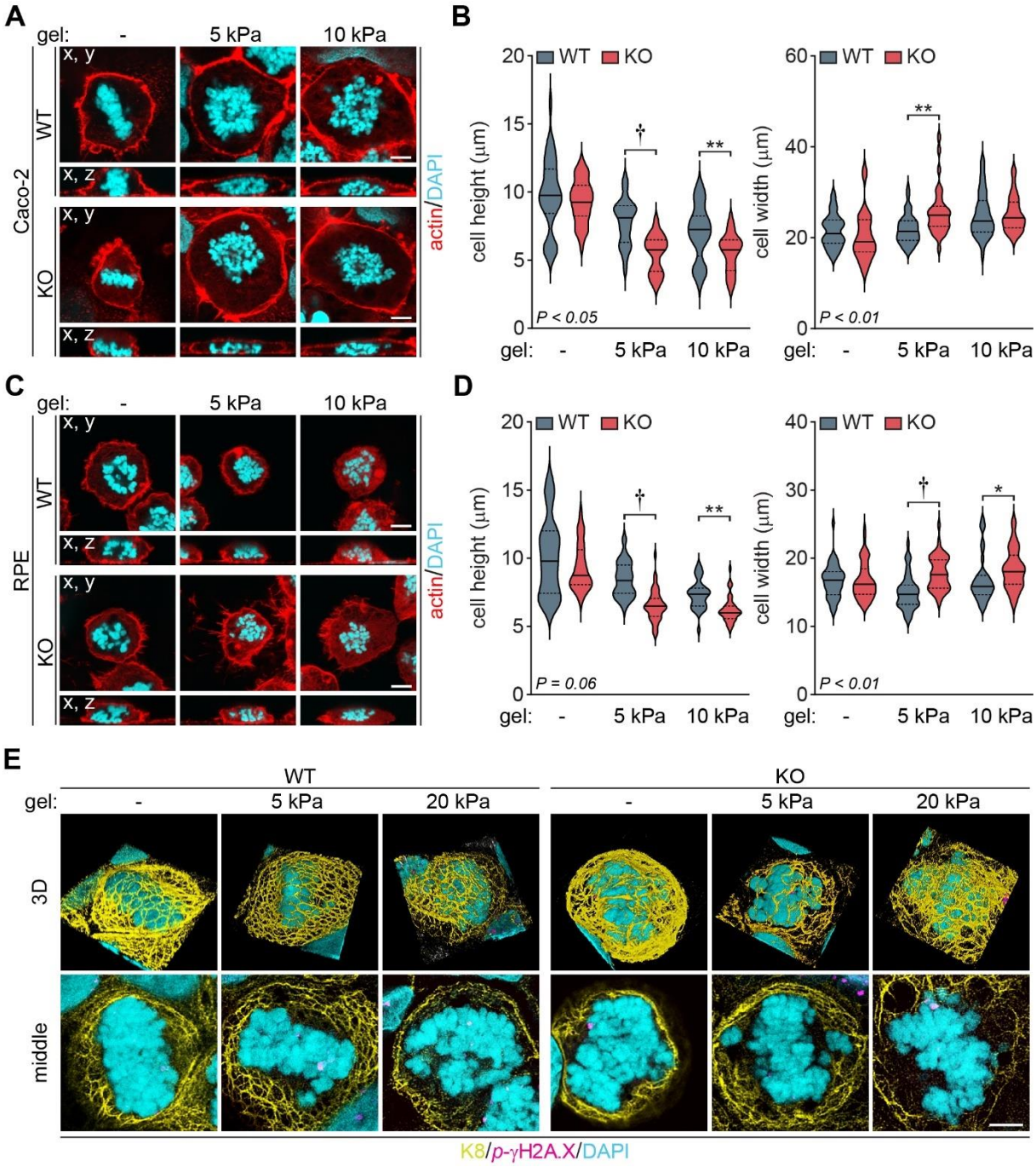

Figure 39 Plectin-controlled IF architecture maintains the mechanical resilience of mitotic cells. (A, C) Representative immunofluorescence images of WT and KO Caco-2 (A) and RPE (C) mitotic cells under confinement. Cells were immunolabeled with an antibody against F-actin (red). Nuclei were stained with DAPI (cyan). Scale bar, 5 µm. **(B, D)** Quantification of cell height and cell width of WT and KO Caco-2 (B) and RPE (D) cells under confinement, n = 34-42. **(E)** Representative immunofluorescence super-resolution images of WT and KO Caco-2 cells under confinement. Cells were immunolabeled with antibodies against K8 (yellow) and *p*-γH2A.X (magenta). Nuclei were stained with DAPI (cyan). Scale bar, 5 µm. Data are presented as mean ± SEM, $^{*}P < 0.05$, $^{**}P < 0.01$, $^{\dagger}P < 0.001$.

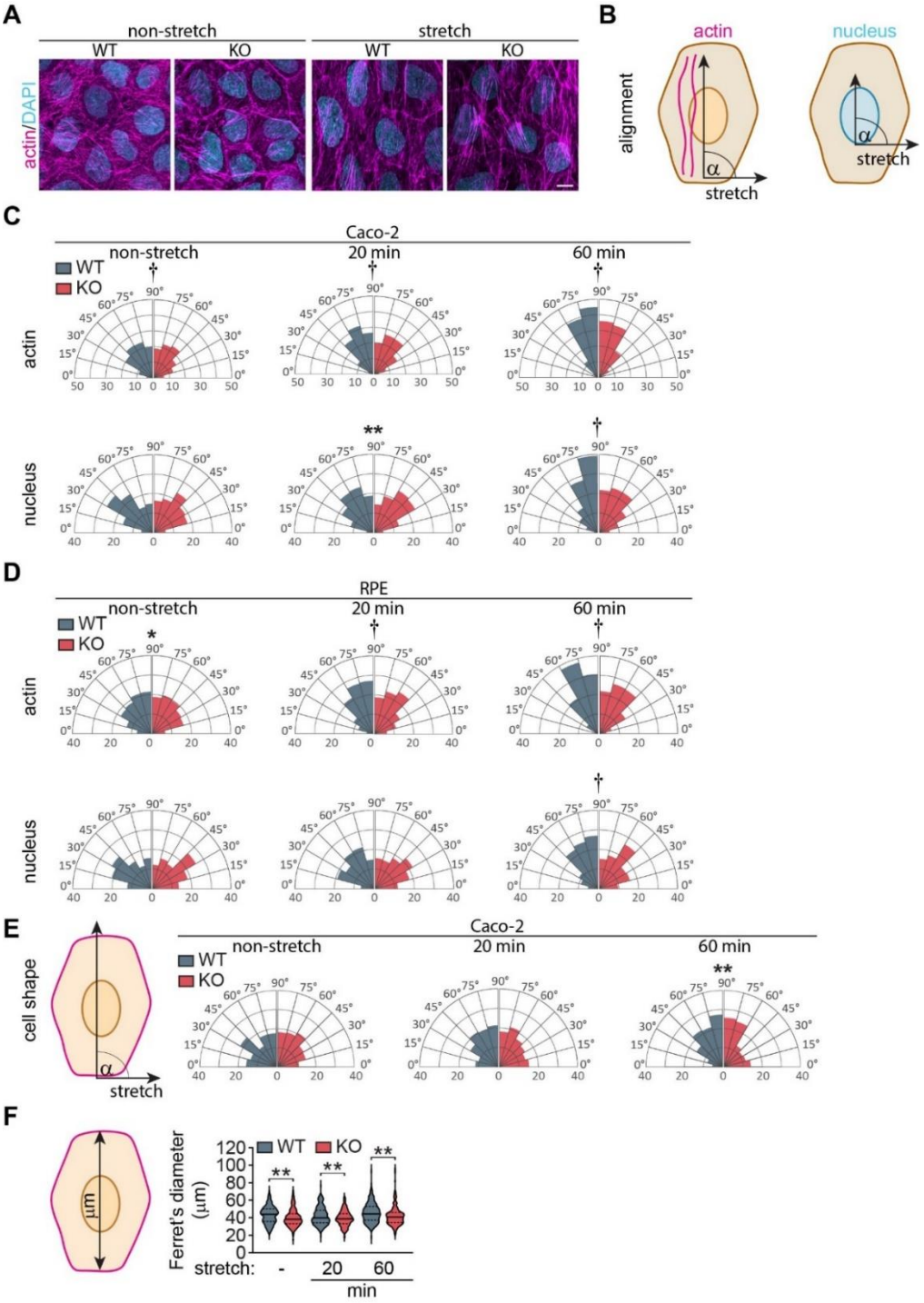

Figure 40 Plectin is required for effective cell and nuclear reorientation upon stretch. (A) Representative immunofluorescence images of WT and KO non-stretched and stretched (60 min) Caco-2 monolayers. Monolayers were immunolabeled with antibody against F-actin (magenta). Nuclei were stained with DAPI (cyan). Scale bar, 10 µm. **(B)** Schematic illustration of morphometric analysis. Alignment of F-actin fibers (magenta) and nuclei (cyan) into different angles (α) in respect to the stretch axis. **(C, D)** Rose graphs show changes in angles of F-actin fibers and nuclei in time-dependent stretch conditions (non-stretched, 20 minutes, 60 minutes of stretch) between WT (blue) and KO (red) Caco-2 (C), and RPE (D) cells. **(E)** Schematic illustration of morphometric analysis. Alignment of the cell body (absolute Ferre't angle). Rose graphs show changes in angles of cell body in time-dependent stretch conditions (non-stretched, 20 minutes, 60 minutes of stretch) between WT (blue) and KO (red) Caco-2 cells. **(F)** Schematic illustration of morphometric analysis. Violin plots show the measurement of maximal cell length (Ferret's diameter; µm) in time-dependent stretch conditions (non-stretched, 20 minutes, 60 minutes of stretch) between WT (blue) and KO (red) Caco-2 cells. Data are presented as mean ± SEM, **P* < 0.05, ***P* < 0.01, †*P* < 0.001.

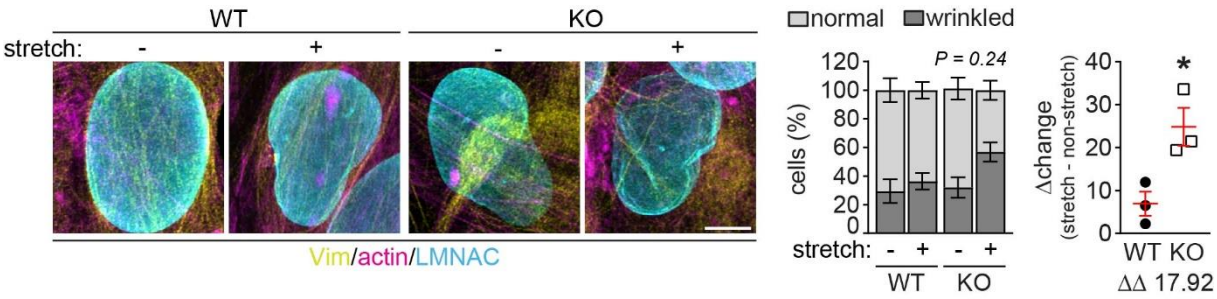

Figure 41 Plectin confers the integrity of the nuclear envelope under mechanical stress. Representative immunofluorescence super-resolution images of WT and KO non-stretched (-) and stretched (+) RPE monolayers. Monolayers were stained with antibodies against Vim (yellow), F-actin (magenta), and lamin A/C (LMNA/C; cyan). Scale bar, 5 µm. Quantification of cell populations (%) with normal (light grey) or wrinkled (dark grey) nuclei. Δchange defined by difference between stretch and non-stretch in WT and KO cells. *n* = 3. Data are presented as mean ± SEM, **P* < 0.05.

4.2.6 Mechanically-induced DNA damage increases the tumorigenic potential of plectin-deficient cells

Given the observed hyperproliferation in *Ple*$^{\Delta IEC}$ mice (Aim 1 4.1; Figure 28B, C), we tested proliferation rates in WT and KO Caco-2 and RPE cells. Cells were seeded on plastic plates, and their proliferation rates were measured over time. The analysis showed a reduced proliferation speed in KO cells compared to WT cells (Figure 42A). It has been reported that mechanical stretch can stimulate cell division (Gudipaty et al., 2017). Therefore, we quantified the population of mitotic cells under conditions where WT and KO monolayers experienced stretch. When Caco-2 and RPE monolayers were seeded on soft PDMS membranes under non-stretched conditions, no differences in mitotic populations were observed between WT and KO cells (Figure 42B). In contrast, exposure to stretch accelerated proliferation and enlarged mitotic populations in both WT and KO monolayers. The mitotic populations were notably more abundant in KO monolayers.

In *Ple*$^{\Delta IEC}$ mice, the combination of hyperproliferation, mechanical instability of the IEC, and increased DNA damage leads to increased susceptibility to CRC development. Our previous results showed that KO monolayers subjected to stretch accumulated significantly more chromosomal aberrations and micronuclei than stretched WT monolayers (Figure 36). To address whether stretched KO monolayers follow the same paradigm of tumorigenic potential, we employed a soft agar colony formation assay using non-stretched and stretched WT and KO RPE cells. After almost two months, the analysis of soft agars revealed a significant increase in the number of grown colonies from stretched KO monolayers (Figure 42C). The

data implies that stress-driven DNA damage in plectin-deficient cell sheets promotes tumorigenic potential and contributes to cancer development in epithelial tissues.

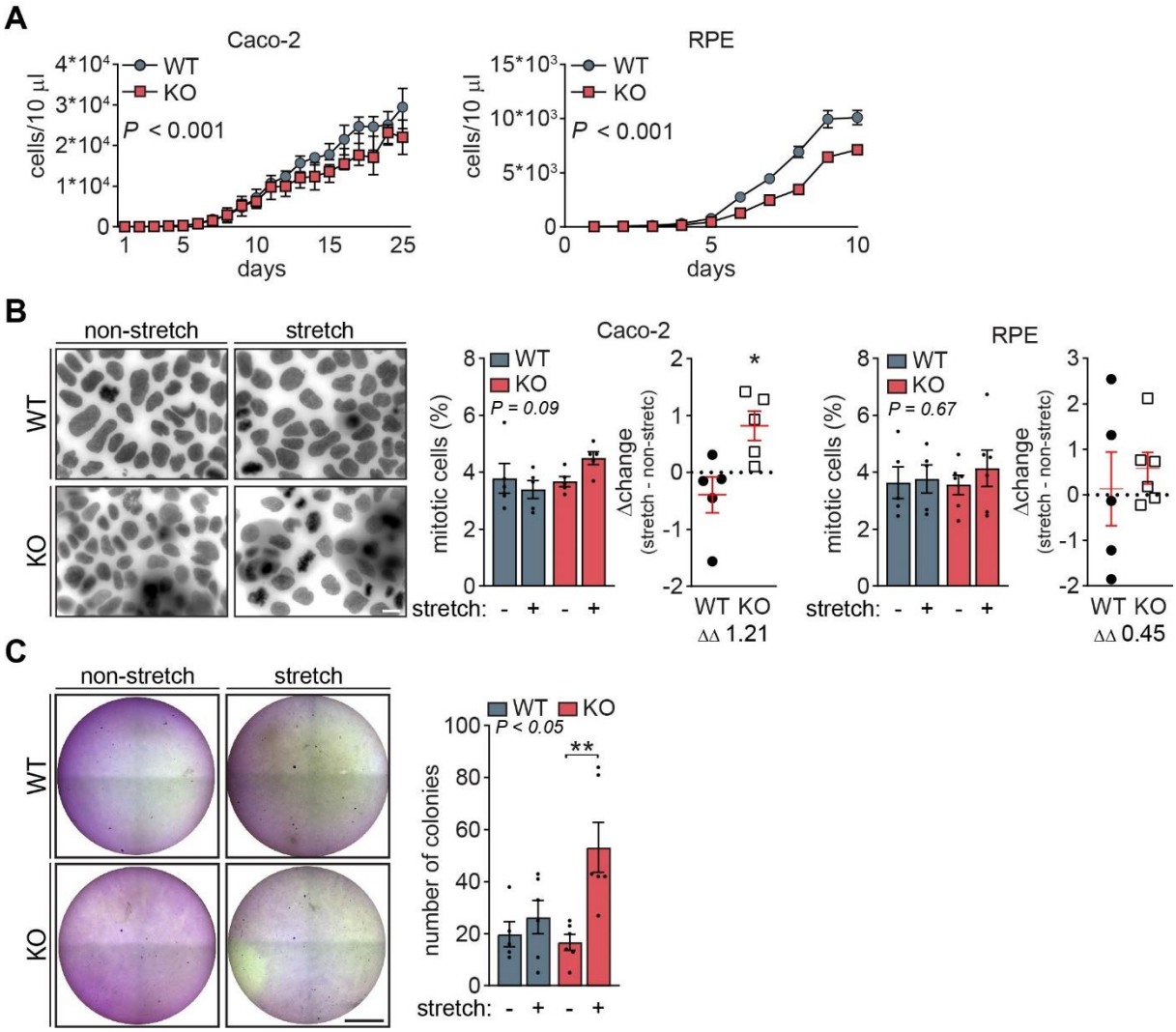

Figure 42 Mechanically-induced DNA damage increases tumorigenic potential of plectin-deficient cells. (A) Time-dependent growth curves of WT (blue) and KO (red) Caco-2 and RPE cells in non-challenged conditions. *n* = 12-18. **(B)** Reprezentative images of WT and KO non-stretched and stretched Caco-2 monolayers. Nuclei were stained with DAPI (grey). Graphs show quantification of mitotic cells frequency (%) in WT (blue) and KO (red) populations of non-stretched (-) and stretched (+) Caco-2 and RPE cells. Δchanges defined by difference between stretch and non-stretch in WT and KO monolayers. Scale bar, 10 µm. *n* = 5. **(C)** Soft agar colony transformation assay. Reprezentative pictures of non-stretched and stretched WT (blue) and KO (red) RPE cells. Colonies were stained with crystal violet. The graph shows numbers of grown colonies. Scale bar, 0.5 cm. *n* = 5-6. Data are presented as mean ± SEM, **P* < 0.05, ***P* < 0.01, †*P* < 0.001.

5 Discussion

5.1 Aim 1

Epithelial cells are in intestine constantly subjected to mechanical stresses, arising from stretch, compression, and shear forces [reviewed in (Beyder, 2018; Gayer and Basson, 2009; Houtekamer et al., 2022)]. Disruption of the IEB integrity is associated with intestinal epithelial injury and inflammation. To establish a functional intestinal epithelium capable of withstanding mechanical stress and protecting the mucosa from luminal pathogens, IECs must be supported by an intact cytoskeleton and well-formed cell-cell and cell-ECM junctions. Previous studies have demonstrated that mice deficient in genes associated with the mechanical resilience of the intestinal epithelium, including KFs and keratin-associated junctions - HDs (Itgα6), Ds (Dsg2) - exhibit increased susceptibility to the development of intestinal inflammation and CRC (Baribault et al., 1994; De Arcangelis et al., 2017; Gross et al., 2018; Habtezion et al., 2011; Habtezion et al., 2005). However, the contribution of mechanical stability to the development of these phenotypes remains understudied. This work describes the role of plectin, a cytoskeletal crosslinking protein, in the maintenance of mechanical homeostasis of intestinal epithelium. In epithelial cells, plectin organizes keratin networks and recruits them further to various cell structures, including cellular junctions. Here, we inactivated plectin *in vivo* in mouse IECs and in human IEC lines (Caco-2 and hCC) to address plectin-dependent molecular mechanisms that determine the mechanical stability of intestinal epithelium.

Microscopic examination of intestinal specimens from two mouse models – one with constitutive deletion of plectin in IECs ($Ple^{\Delta IEC}$) and the other with spatiotemporal TMX-inducible plectin deletion ($Ple^{\Delta IEC\text{-}ERT2}$) - revealed a significant detachment of IECs from the subjacent ECM. This detachment was associated with compromised selective permeability of the IEB and spontaneous development of chronic inflammation/colitis. Plectin is essential for the assembly and maintenance of HDs by linking KFs and Itgβ4 (Koster et al., 2001; Rezniczek et al., 1998). Notably, in areas where epithelial cells had sloughed off, the Itgα6 signal was absent from cells and was present on the ColIV-positive ECM sheets. TEM and quantitative analysis revealed elongated HD plaques and increased intercellular spaces between IECs and the ECM in $Ple^{\Delta IEC}$ mice compared to $Ple^{fl/fl}$ mice. The impaired HD formation in $Ple^{\Delta IEC}$ IECs correlated with decreased expression levels of Itgα6 and Itgβ4, as well as reduced content of

Itgβ4 in the keratin-enriched insoluble fraction of *Ple$^{\Delta IEC}$* mucosa. These findings indicate a compromised arrangement of HDs and their perturbed connection to KF network in the epithelium of *Ple$^{\Delta IEC}$* mice.

Plectin has the ability to self-assemble and form dimeric structures through its coiled-coil rod domain. In respect to plectin's role in HD assembly, previous investigations suggested that plectin may stabilize HDs through two different mechanisms. First, in concert with BPAG2, plectin facilitates the horizontal "lateral-association" - formation of plectin dimers enables oligomerization of Itgα6β4. This lateral association strengthens the clustering of Itgs, enhancing their capacity to anchor cells to the ECM. Second, plectin recruits KF vertically to Itgβ4, thereby forming a robust linkage between the intracellular cytoskeleton and the cell membrane. This vertical integration with cytoskeleton ensures that mechanical forces are effectively transmitted across the cell, contributing to cellular resilience and stability (Walko et al., 2015). We hypothesized that plectin inactivation, which disrupts the KF-Itgβ4 linkage, will compromise the functionality of HDs type II, where plectin is the only crosslinking protein present (Fontao et al., 1999; Litjens et al., 2006). This hypothesis was tested through a series of biomechanical experiments and *in vivo* analyses. Subjecting WT and KO cells to various forms of mechanical stress revealed a decreased mechanical stability of KO cells. Uniaxial stretch and radial shear assays showed that KO cells exhibited increased detachment and higher mortality rates compared to WT cells. The discrepancy between *in vivo* observations in *Ple$^{\Delta IEC}$* mice, which did not show significant differences in apoptosis, and the higher frequency of dead cells in cultured KO cells subjected to mechanical stress may be attributed to the non-physiological experimental conditions. Furthermore, optical tweezer rheology confirmed weaker adhesion of ECM-coated beads to KO cells. These findings, both *in vivo* and *in vitro*, support the essential role of plectin in the maintenance of the functional integrity of HDs type II. The disruption of HDs in plectin-deficient intestinal epithelium can serve as a predisposition to intestinal inflammation and CA-CRC (Beaulieu, 2018; De Arcangelis et al., 2018; De Arcangelis et al., 2017).

Previous study has shown that plectin-deficient endothelial cells display significant distortions of AJs and TJs, resulting in a breached barrier function and increased vascular permeability (Osmanagic-Myers et al., 2015). Our own results have revealed similar effects in cholangiocytes, where plectin deficiency favors the Ds disruption (Jirouskova et al., 2018).

Under mechanical stress from bile stasis, plectin-deficient cholangiocytes failed to upregulate the desmosomal protein Dsp, a known plectin binding partner (Eger et al., 1997). This resulted in mechanical instability of the biliary epithelium. Notably, case reports have documented patients with plectin mutations in the liver experiencing progressive familial intrahepatic cholestasis and liver failure (Thebaut et al., 2024; Wu et al., 2019). Furthermore, plectin deficiency in simple epithelial sheets resulted in aberrant KF architecture and increased actomyosin contractility, promoting enhanced cytoskeletal tension and distortion of Ds. When subjected to cyclic stretch, plectin-deficient epithelial monolayers failed to withstand external mechanical stress, resulting in reduced cellular cohesion and increased epithelial fragility (Prechova et al., 2022). In line with these findings, we observed not only inefficient formations of HDs but also defects in AJs, TJs, and Ds in the IECs of $Ple^{\Delta IEC}$ mice, which experience sustained mechanical stress. These data are supported by quantitative TEM analysis of intestine from $Ple^{\Delta IEC}$ mice, which revealed enlarged intercellular spaces between neighboring $Ple^{\Delta IEC}$ IECs. Further, expression analysis showed downregulation of several junctional members (ZO-1, E-cad, Dsg2, and Dsp1/2) both at mRNA and protein levels. The observed epithelial damage, characterized by detached IEC populations *in vitro*, suggests that the "leaky gut" phenotype (higher barrier permeability and bacteria translocation) in $Ple^{\Delta IEC}$ mice is primarily caused by HD instability. Additionally, the disruption of the KF network architecture and the destabilization of Ds due to plectin deficiency critically undermine the mechanical resilience and intercellular cohesion of the $Ple^{\Delta IEC}$ intestinal epithelium, contributing to its mechanical vulnerability.

Our data underscores the importance of plectin-mediated crosstalk between KFs, HDs, and Ds. The inactivation of plectin leads to impaired mechanical resilience of epithelium, predisposing plectin-deficient intestine to colitis. Beyond serving as a physical barrier, the intestinal epithelium is also reinforced by cells of the immune system. Histological examination of intestinal specimens from mice at early developmental stages and adulthood showed comparable mucosal damage, irrespective of maturity of the immune system. Additionally, DSS-induced inflammation was more prominent in treated $Ple^{\Delta IEC}$ mice compared to non-treated $Ple^{\Delta IEC}$ mice. Congruently with the results from the mouse model, clinical data from patients with UC showed a negative correlation between plectin expression and disease severity. Based on these findings, we concluded that perturbed intestinal barrier function upon

reduced expression of plectin, leading to a disorganized KF cytoskeleton and unstable HDs and Ds, contributes to the pathogenesis of IBD in humans. Generally, cells employ multiple mechanisms to protect against pathogenic infection and inflammation. This protection is provided by the mechanical integrity of the epithelium. On the other hand, the organization of KFs [(Habtezion et al., 2011; Habtezion et al., 2005); reviewed in (Geisler and Leube, 2016)], cell-ECM (De Arcangelis et al., 2017) and cell-cell adhesions (Gross et al., 2018; Hu et al., 2021; Pastorelli et al., 2013; Peterson and Artis, 2014; Weber et al., 2010) also provide non-mechanical protection. This entails for instance microflora-dependent resistance to apoptosis or modulation of the immune response by regulating cytokine production or facilitating antigen passage from the lumen to underlying intestinal immune system. It is conceivable that plectin influences other processes, such as coordination of reciprocal interactions between the microbiome, IECs, and the immune system, thereby contributing to the regulation of tissue homeostasis. However, additional studies are required to address these functions.

IFs are hard-wired with F-actin into complex cytoskeletal network via cytoskeletal linker proteins like plectin. Multiple studies have shown that cytoskeleton both physically and functionally interconnects HDs and FAs (Myllymaki et al., 2019; Pora et al., 2019; Wang et al., 2020). Consequently, the anchorage of IF-associated HDs contributes to the modulation of cellular traction forces produced by the actomyosin. The loss of HDs in keratinocytes has been demonstrated to promote the assembly of FAs, cell spreading, and the generation of traction forces (Wang et al., 2020). In addition, disruption of HDs stimulates cell migration by affecting FA dynamics in prostate epithelial cells (Schmidt et al., 2022) and promotes tumorigenesis in prostate cancer cells (Wenta et al., 2022). Mice with IECs-specific loss of Itgα6 developed invasive colorectal adenocarcinoma (De Arcangelis et al., 2017). Since we found that plectin in IECs affects keratin cytoarchitecture and HD stability, we hypothesized that plectin promotes the transformation of IECs. Loss of plectin could disrupt KF network, leading to altered cell adhesion dynamics and increased cellular motility. The disruption of HDs and the subsequent increase in FA formation and traction force generation could enhance the migratory and invasive capabilities of epithelial cells, contributing to tumor dissemination. Furthermore, the increased cellular traction forces and altered mechanotransduction pathways could promote oncogenic signaling, further driving the transformation process.

We found that *Ple*$^{\Delta IEC}$ intestinal crypts exhibit expanded zones of proliferating cells and larger GC populations. Similar hyperproliferation and a preference for differentiation toward secretory cell lineages have been documented in mice with IECs-specific deletion of Itgα6 (De Arcangelis et al., 2017) and K8 (Lahdeniemi et al., 2017; Toivola et al., 2004). These observations further strengthen the importance of the keratin-plectin-Itg linkage in maintaining functional intestinal homeostasis by regulating the appropriate balance between cell proliferation and differentiation. Possible mechanism involves the effects of K8 and K18 on Notch1 signaling, where decreased K8/18 levels reduce the expression of Notch1 target genes, thereby directing the cell fate toward the secretory lineage (Lahdeniemi et al., 2017). Intriguingly, activation of Notch1 signaling is regulated by intercellular tensional forces sensed by mechanosensitive receptors on the plasma membrane. Consequently, Notch1 signaling can dictate cell fate in response to changes in cytoskeletal tension (Hunter et al., 2019; Luca et al., 2017).

The crosstalk between Itgβ4 and plectin mediates mechanotransduction by inhibiting the RhoA-ROCK-MLC and FAK-PI3K pathways. Inhibition of these signaling pathways reduces cellular tension, which in turn prevents nuclear accumulation and dephosphorylation of the mechanosensitive transcription factor YAP (Wang et al., 2020). Alterations in YAP/TAZ signaling in the intestine, resulting from Itgβ4 depletion or changes in ECM stiffness, affect the proliferation of stem and progenitor cells, favoring differentiation towards the secretory lineage, particularly to GCs (He et al., 2023; Imajo et al., 2015). Moreover, YAP/TAZ plays a role in tissue regeneration and cell reprogramming following intestinal injury (Yui et al., 2018). Considering that plectin affects the cytoarchitecture of KF-HD networks, we can hypothesize that plectin depletion may determine intestinal cytoskeletal tension and regulate the cell fate of IECs by modulating mechanotransduction. This mechanism may be particularly relevant in the context of chronic inflammation, where tissue regeneration is continually required and may lead to cell reprogramming.

Plectin also binds nesprin-3 through its ABD at the N-terminus (Ketema et al., 2013; Ketema et al., 2007). A reduction in plectin-nesprin-3 binding can significantly affect signaling to the nuclear periphery, leading to changes in nuclear positioning and deformation. These changes can further affect chromatin modifications and gene expression (Almeida et al., 2015;

Staszewska et al., 2015). This highlights the critical role of the plectin-nesprin-3 interaction in maintaining nuclear structure and regulating genomic activity.

Ple$^{\Delta IEC}$ mice exhibited an increased epithelial injury by postnatal day 21, coinciding with the transition from breast milk to solid chow. This timing suggests that the elevated mechanical stress imposed by increased muscle contractions and digestion contributes to the development of an inflammatory phenotype in plectin-deficient tissue, where cells are mechanically unstable and fail to withstand mechanical load. Consistently, patients diagnosed with epidermolysis bullosa suffer from skin fragility characterized by epidermal blistering, erosions, and injured mucosa in response to relatively low levels of mechanical stress. Despite extensive research on the genetics and pathomechanics of epidermolysis bullosa disorders, the primary therapies focus on symptom relief and prevention of dermal injury (Has and Fischer, 2019; Uitto et al., 2018). Thus, we investigated whether a similar therapeutic approach could ameliorate intestinal epithelial injury in *Ple*$^{\Delta IEC}$ mice. Indeed, treatment with a low-residue liquid diet significantly improved epithelial damage in *Ple*$^{\Delta IEC}$ mice. However, inconsistent effects were observed in the SI, where the liquid diet exacerbated detachment of *Ple*$^{\Delta IEC}$ IECS in the villi. Further studies are required to understand whether varying plectin expression levels across the gastrointestinal tract lead to regional differences in clinical manifestation in patients.

Previous studies have demonstrated that broad-spectrum ATB treatment alleviates intestinal pathology, including epithelial damage and colitis, in K8- and Itgα6-deficient mice (De Arcangelis et al., 2017; Habtezion et al., 2011). Similarly, ATB treatment in *Ple*$^{\Delta IEC}$ mice resulted in an attenuation of inflammatory phenotype and epithelial damage. These findings suggest that intestinal microflora contributes to the exacerbation of colitis and epithelial injury in *Ple*$^{\Delta IEC}$ mice. In this study, we highlighted the importance of mechanical stability in maintaining epithelial homeostasis, emphasizing that intestinal microflora plays a role in epithelial injury. Thus, we propose that combining a low-residue liquid diet and ATB treatment could potentially serve as a therapeutic strategy for patients with tissue fragility disorders. However, before clinical application, it is essential to determine (i) whether this treatment modality would be suitable for long-term treatment and (ii) how this strategy would efficiently address broader systemic symptoms.

The intricate interplay within the gut-liver axis is of significant importance. Defects along this axis, such as those resulting from impaired gut barrier function and dysbiosis of the gut microbiota, can have significant consequences for liver function. In *Ple*$^{\Delta IEC}$ mice, the breakdown of the IEB allows the passage of microbial components and metabolites into the liver, where they can trigger inflammatory cascades and contribute to hepatic pathologies, including cancer. This scenario highlights the systemic impact of intestinal dysfunction and emphasizes the connection between different organs within the body (Ohtani and Kawada, 2019; Pabst et al., 2023).

5.2 Aim 2

IBD patients are at increased risk for CA-CRC, which accounts for 1-2% of colorectal cancers and 15% of IBD deaths annually [(Eaden et al., 2001; Eluri et al., 2017; Fornaro et al., 2016; Selinger et al., 2014); reviewed in (Long et al., 2017; Lu et al., 2022)]. Compared to sporadic CRC, CA-CRC patients are diagnosed at a younger age, resulting in poorer survival, with the severity and duration of inflammation being a significant risk factor [reviewed in (Flores et al., 2017)]. The genetic alterations in CA-CRC are different from those in sporadic CRC. While both show high genomic instability in critical driver genes, such as *APC, P53, MYC, KRAS, PIK3CA, SMAD4,* and *ARID1* (Rajamaki et al., 2021; Robles et al., 2016; Yaeger et al., 2016), CA-CRC shows mutations occurring more frequently and earlier, even in non-dysplastic lesions, contributing to a higher risk of developing tumors (Du et al., 2017; Wanders et al., 2020). Although driver genes contributing to tumorigenesis in CRC are well established, the molecular mechanisms in CA-CRC, where the inflammatory pathways predispose to the accumulation of genomic instability and mutagenesis, remain largely unexplored (Wanders et al., 2020).

Our study shows that genes/proteins crucial for maintaining the mechanical resilience of the intestinal epithelium, including IFs and IF-associated junctional complexes Ds and HDs, exhibit downregulation in patients with UC. The altered expression and structural changes of these proteins disrupt the mechanical stability of IECs, rendering them more susceptible to mechanical stress-induced DNA damage, and promoting the development of CRC. The presence of mutations in keratin encoding genes, altered keratin expression, and aberrant architecture of KFs in patients diagnosed with IBD and CRC/CA-CRC underscored the

significance of these structural proteins in intestinal health and disease (Evans et al., 2015; Moll et al., 1992; Owens et al., 2004; Polari et al., 2022; Stenling et al., 2007; Tao et al., 2007; Yun et al., 2000). Moreover, levels of K8 expression are associated with UC disease progression. During the acute phase of inflammation, K8 levels are reduced; during remission, expression levels are restored or even increased. Importantly, this dynamic restoration process is inefficient in UC patients at high risk of CA-CRC, suggesting that monitoring of KF expression levels can serve as a read-out for disease progression (Corfe et al., 2015).

As demonstrated in Aim 1, plectin deficiency results in aberrant cytoskeletal architecture of KFs and impaired cell-cell/cell-ECM junctions. Consequently, these changes result in reduced mechanical stability of the intestinal epithelium, which gives rise to a colitis-like inflammatory phenotype in $Ple^{\Delta IEC}$ mice. The plectin-dependent anchorage of IFs to Ds and HDs at the cell periphery (Dsp, Itgs) and the nuclear envelope (nesprin-3), facilitates the formation of a functional and mechanically robust IFs network that aids in resistance to mechanical forces and shields the cell nucleus against deformations and DNA damage. Such DNA damage can induce genomic instability, driving the accumulation of mutations that promote tumorigenesis (Almeida et al., 2015; Kechagia et al., 2023; Laly et al., 2021; Patteson et al., 2019; Shah et al., 2021). Our findings demonstrate that $Ple^{\Delta IEC}$ mice spontaneously develop CRC characterized by hyperproliferation and increased DNA damage in IECs. Chromosomal instability is evident in early adenomas, suggesting that chromosomal instability is an early event in tumorigenesis (Shih et al., 2001). Chromosomal instability often results from chromosomal missegregation during mitosis, where errors in segregation can lead to the partitioning of entire chromosomes into micronuclei. The nuclear envelope of micronuclei is inherently fragile, and DNA release from micronuclei can trigger DNA damage response and inflammatory pathways, ultimately promoting metastasis (Bakhoum et al., 2018). These findings imply that impaired epithelial stability and intestinal inflammation in $Ple^{\Delta IEC}$ mice, may contribute to DNA damage, predisposing these mice to CRC/CA-CRC development.

Notably, the highest increase in DSBs is observed in differentiated cells, which are the most exposed to friction forces from the intestinal lumen, highlighting the important role of mechanical stress in DNA damage. Interestingly, $Ple^{\Delta IEC}$ mice show signs of apoptosis prior to weaning, where mice experience even minimal mechanical stress exerted on the intestinal epithelium and early onset of intestinal inflammation. Furthermore, inflammation has been

shown to be an important risk factor for cancer [reviewed in (Anuja et al., 2017)]. During inflammation, a variety of mutagenic compounds are generated in the form of cytotoxic mediators. Reactive oxygen and nitrogen species generated by immune cells directly induce DNA damage, leading to the formation of cytotoxic and mutagenic DNA lesions and DSBs, ultimately resulting in genomic instability. In addition, proteins involved in DNA repair can promote proinflammatory gene transcription, creating a positive feedback loop which, when combined with inflammation-induced cell proliferation, greatly enhances the risk of exposure-related mutagenesis [(Kiraly et al., 2015); reviewed in (Friedrich et al., 2019)]. As a result, an uncontrolled inflammatory response can lead to chronic inflammation and the development of cancer (Meira et al., 2008). The data from ATB-treated mice implied that the interplay between mechanical stress and inflammation contributes to DNA damage in *Ple*$^{\Delta IEC}$ mice, where the inflammatory environment in *Ple*$^{\Delta IEC}$ mice can further aggravate DNA damage and promote colorectal carcinogenesis.

DNA damage can result from various sources, including exposure to external insults or internal processes such as replication, cell division, or repair [reviewed in (Cannan and Pederson, 2016)]. Deficiencies in genes encoding DNA damage repair factors are associated with increased sensitivity to DNA damage, severe chromosomal abnormalities, and oncogene activation [reviewed in (Cannan and Pederson, 2016; Mills et al., 2003; Tiwari and Wilson, 2019)]. Mechanical stress, an extrinsic factor, can induce nuclear deformations, contributing to DNA damage and genetic instability. Tumor stiffness correlates positively with genomic instability, and persistent cell migration through micro-constrictions can lead to nuclear envelope rupture, loss of repair factors (Cho et al., 2019; Irianto et al., 2017; Pfeifer et al., 2017; Pfeifer et al., 2018; Xia et al., 2019) or influx of exonucleases from the endoplasmic reticulum (Nader et al., 2021). Mechanical stress-induced DNA damage may occur even without nuclear envelope rupture, often linked to replication stress. During replication, DNA undergoes structural changes which allow synthesis of new DNA at places called replication forks. Mechanical stress induced by cell migration through micro-constrictions or cell compression leads to nuclear deformation, causing torsional stress and replication fork stalling. When mechanical insult persists, replication forks collapse and form DNA damage, resulting in replication stress (Shah et al., 2021). Lesions from DNA replication stress can be transmitted into the mitotic phase, resulting in chromosomal missegregation (Ichijima et al.,

2010). Interestingly, skeletal muscle tissues from mice and humans with muscular dystrophy and subsequent sarcoma development show significant DNA damage associated with somatic aneuploidy. DNA damage is detectable before the onset of macroscopic muscle degeneration, inflammatory responses, and cancer development. These findings suggest that the early accumulation of DNA damage in tissues exposed to mechanical stress may act as a precursor to later stages of disease progression, including inflammation and tumorigenesis (Schmidt et al., 2011). As we do not observe differences in DNA damage repair or nuclear envelope ruptures during mechanical stress, we speculate that DNA damage in plectin-deficient intestinal epithelium results, at least in part, from the mechanical stress-induced nuclear deformation and consecutive replication stress.

Epithelial sheets utilize specific mechanisms to protect the genome from damage when subjected to prolonged uniaxial cyclic stretch. For instance, cells can reduce heterochromatin occupancy at the nuclear periphery, thereby alleviating nuclear membrane tension. Epithelial cells also exhibit AJ-mediated supracellular alignment of epithelial sheets and engage in strain avoidance by reorganizing F-actin and nuclei perpendicularly to the direction of cyclic stretch, thus minimizing nuclear strain (Nava et al., 2020; Obbink-Huizer et al., 2014). Interestingly, plectin-deficient monolayers exposed to cyclic stretch display a significant delay in F-actin and nuclear realignment, along with reorientation of cell mass, which correlates with compromised nuclear envelope integrity. To investigate acute changes in nuclear adaptation, examining heterochromatin status in plectin-deficient cells is essential. It is hypothesized that ineffective supracellular adaptation prolongs the exposure of nuclei to mechanical stress, leading to nuclear deformation and increased DNA damage. Experiments to test this hypothesis are ongoing.

In *Ple*$^{\Delta IEC}$ crypts, we have observed an elevation in DSBs in highly proliferative TA cells. Plectin-mediated recruitment of IFs to the F-actin cell cortex, controls the cortical tension, providing mitotic cells with mechanical support. Depletion of plectin and vimentin reduces mitotic cortex tension, with vimentin deficiency leading to inefficient mitotic rounding and chromosomal missegregation under cell confinement (Serres et al., 2020). During interphase, cells activate checkpoints to facilitate DNA repair. However, once cells enter mitosis, these DNA damage checkpoints are absent, preventing the arrest of cell division for DNA repair. Thus, the DNA damage occuring during mitosis is likely to remain unrepaired, thereby promoting

chromosomal instability and increasing the risk of genetic aberrations during cell division. [reviewed in (Blackford and Stucki, 2020)]. Our findings suggest that compromised IF networks in plectin-deficient cells contribute to increased deformability and DNA damage during mitosis, resulting in chromosomal aberrations and accumulation of micronuclei under cell confinement.

Mechanical stress elicits a rigidity-dependent response from cells, triggering various mechanisms to cope with the tension. Recent studies have highlighted several pathways through which cells react to mechanical tension: (i) activation of mechanoresponsive signaling pathways such as ERK, PI3K/Akt, or ROCK; (ii) opening mechanosensitive ion channels Piezo 1/Piezo2; (iii) stretching nuclear pore complexes and translocation of mechanoresponsive transcription factors such as YAP into the nucleus. Through these pathways, mechanical stress can induce the expression of genes associated with cell cycle progression and cell survival (Andreu et al., 2022; Aureille et al., 2019; Benham-Pyle et al., 2015; Dupont et al., 2011; Elosegui-Artola et al., 2017; Gudipaty et al., 2017; Murthy et al., 2017; Tijore et al., 2021). Furthermore, studies mimicking tumor growth by applying mechanical pressure have demonstrated hyperproliferation and enlargement of colonic crypts in mice (Fernandez-Sanchez et al., 2015). These findings are consistent with our results, where stretching increases proliferation in plectin-deficient monolayers.

Of note, YAP/TAZ act as crucial coactivators enhancing the expression of core genes specific for CRC, thereby activated in many cancer cells (Della Chiara et al., 2021). Therefore, it is of interest to investigate the molecular mechanisms underlying mechanically-induced proliferation in plectin-deficient monolayers. By exploring these mechanisms, we can gain valuable insights into how plectin deficiency influences the activation of signaling pathways involved in CRC development.

In *Ple*$^{\Delta IEC}$ mice, we observed a higher degree of epithelial injury with increasing age (12-, 25-, and 50-week-old), while inflammation reached its peak at 12-week-old mice. This suggests that inflammation and mechanical instability are primary risk factors, exacerbating the carcinogenic process. Our data demonstrate that mechanical stress-induced proliferation and chromosomal instability have oncogenic potential. Previous studies have highlighted that the early onset of CRC correlates with the level and extent of chromosomal instability (Hoevenaar et al., 2020). Our observations that colonies grown from stretched plectin-

deficient monolayers do not expand in size suggest that some other stimulus is required for colony growth. Such stimulus can be either persistent mechanical stress or an inflammatory environment. Even though the effect of oxidative stress caused by inflammation cannot be excluded, our data show that mechanical stress significantly contributes to the proliferation and chromosomal instability in the plectin-deficient intestine, thereby conferring oncogenic potential.

Epithelial damage and tumor lesions in *Ple*$^{\Delta IEC}$ mice were found mainly in distal colon or rectal prolapse regions. In addition, the transition to a solid diet and increased muscle peristalsis in *Ple*$^{\Delta IEC}$ mice significantly exacerbated injury in the distal colon. Interestingly, in a mouse model of inducible chromosomal instability, CRC tumors arose exclusively in the distal colon and exhibited increased rates of aneuploidy and karyotypic heterogeneity (Hoevenaar et al., 2020). This propensity for tumor lesions in the distal part of the colon may be due to increased mechanical stress along the intestinal tissue. Under normal circumstances, when DNA damage occurs, cells typically activate mechanisms to repair the damage or induce programmed cell death to prevent the propagation of genetic abnormalities. However, our data indicate that mechanically-induced DNA damage, enhanced cellular proliferation, and concurrent inflammation create an environment promoting genomic instability. These factors not only exacerbate DNA damage but also promote oncogenic cell signaling pathways that further drive cellular proliferation and genomic instability. Consequently, the convergence of these factors ultimately paves the way for the development of CRC in *Ple*$^{\Delta IEC}$ mice.

6 Conclusions

6.1 Aim 1. Does plectin contribute to intestinal barrier homeostasis and colitis?

We assessed plectin expression in colon samples from UC patients and from healthy controls. We observed an inverse correlation between plectin expression and inflammation levels in UC patients. To elucidate the role of plectin in the intestinal barrier maintenance, we generated two novel mouse models with constitutive (*Ple*$^{\Delta IEC}$) or inducible (*Ple*$^{\Delta IEC\text{-}ERT2}$) IEC-specific plectin ablation. Our study demonstrates that *Ple*$^{\Delta IEC}$ mice exhibit reduced body weight, chronic diarrhea, hyperproliferation, and increased intestinal paracellular permeability. Histological examinations revealed significant detachment of plectin-deficient IECs from the BM accompanied by extensive inflammation. Microbiome analyses excluded inflammation-associated dysbiosis, as the gut microbiota composition remained similar between *Ple*$^{\Delta IEC}$ and *Ple*$^{fl/fl}$ mice. In a DSS-induced acute colitis model, *Ple*$^{\Delta IEC}$ mice experienced more severe body weight loss, a higher disease activity index, crypt damage, ulcerations and reduced survival rates. IHC and TEM analyses showed profound alterations in KF organization and intercellular junctions in plectin-deficient IECs. Additionally, plectin deficiency led to a diminished association of KFs with α6β4 integrin clusters and destabilization of β4-positive HDs. Analyses of cultured IEC cell lines confirmed that plectin-deficient cells exhibited decreased adhesion strength and greater vulnerability to dynamic mechanical stress. Taken together, our findings highlight that plectin is critical for the formation of functional HDs and thus maintains the integrity of the IEB.

6.2 Aim 2. What is the role of plectin in mechanical stress-driven DNA damage and colorectal carcinogenesis?

Our research demonstrates that *Ple*$^{\Delta IEC}$ mice spontaneously develop CRC. Furthermore, experimental induction of sporadic or CA-CRC revealed that *Ple*$^{\Delta IEC}$ mice exhibit increased susceptibility to and accelerated tumor development compared to *Ple*$^{fl/fl}$ mice. This increased tumorigenic potential was documented by faster tumor growth and higher tumor incidence in the *Ple*$^{\Delta IEC}$ mice. Spontaneous intestinal carcinogenesis in these mice is also associated with a higher frequency of *p*-gH2AX-positive foci, indicative of DSBs in DNA. Notably, the highest incidence of DSBs occurs in differentiated cells, which are exposed to frictional forces exerted by the luminal content. Additionally, elimination of intestinal microflora by ATB treatment revealed that inflammation also contributes to DNA damage in *Ple*$^{\Delta IEC}$ mice. This indicates that while mechanical stress is a primary driver of DNA damage in these cells, inflammatory processes also play a role in exacerbating this damage.

In cultured immortalized intestinal cells, deletion or inactivation of plectin results in the aberrant organization of IFs, which leads to higher nuclear deformability and increased DNA damage. This increased DNA damage results in accumulation of chromosomal aberrations within the plectin-deficient monolayers. The chromosomal instability results from the inefficient adaptive response of cells to mechanical stress, which is evidenced by delayed realignment of F-actin and the nucleus, along with altered reorientation of cell mass. Furthermore, our findings indicate that mechanically-induced DNA damage enhances the tumorigenic potential of plectin-deficient monolayers. When these cells experience mechanical stress, the resulting DNA damage promotes their transformation into cancer cells, thereby increasing their potential to form tumors.

Taken together, we demonstrate the importance of plectin for the mechanical integrity of IECs, which helps to protect against DNA damage and subsequent colorectal carcinogenesis in highly mechanically challenged tissue.

7 References

Abraham, C., and J.H. Cho. 2009. Inflammatory bowel disease. *N Engl J Med*. 361:2066-2078.

Ackerl, R., G. Walko, P. Fuchs, I. Fischer, M. Schmuth, and G. Wiche. 2007. Conditional targeting of plectin in prenatal and adult mouse stratified epithelia causes keratinocyte fragility and lesional epidermal barrier defects. *J Cell Sci*. 120:2435-2443.

Alcaino, C., G. Farrugia, and A. Beyder. 2017. Mechanosensitive Piezo Channels in the Gastrointestinal Tract. *Curr Top Membr*. 79:219-244.

Almeida, F.V., G. Walko, J.R. McMillan, J.A. McGrath, G. Wiche, A.H. Barber, and J.T. Connelly. 2015. The cytolinker plectin regulates nuclear mechanotransduction in keratinocytes. *J Cell Sci*. 128:4475-4486.

AMBOSS. 2023. Small intestine.

Ameen, N.A., Y. Figueroa, and P.J. Salas. 2001. Anomalous apical plasma membrane phenotype in CK8-deficient mice indicates a novel role for intermediate filaments in the polarization of simple epithelia. *J Cell Sci*. 114:563-575.

Anderson, C.A., G. Boucher, C.W. Lees, A. Franke, M. D'Amato, K.D. Taylor, J.C. Lee, P. Goyette, M. Imielinski, A. Latiano, C. Lagace, R. Scott, L. Amininejad, S. Bumpstead, L. Baidoo, R.N. Baldassano, M. Barclay, T.M. Bayless, S. Brand, C. Buning, J.F. Colombel, L.A. Denson, M. De Vos, M. Dubinsky, C. Edwards, D. Ellinghaus, R.S. Fehrmann, J.A. Floyd, T. Florin, D. Franchimont, L. Franke, M. Georges, J. Glas, N.L. Glazer, S.L. Guthery, T. Haritunians, N.K. Hayward, J.P. Hugot, G. Jobin, D. Laukens, I. Lawrance, M. Lemann, A. Levine, C. Libioulle, E. Louis, D.P. McGovern, M. Milla, G.W. Montgomery, K.I. Morley, C. Mowat, A. Ng, W. Newman, R.A. Ophoff, L. Papi, O. Palmieri, L. Peyrin-Biroulet, J. Panes, A. Phillips, N.J. Prescott, D.D. Proctor, R. Roberts, R. Russell, P. Rutgeerts, J. Sanderson, M. Sans, P. Schumm, F. Seibold, Y. Sharma, L.A. Simms, M. Seielstad, A.H. Steinhart, S.R. Targan, L.H. van den Berg, M. Vatn, H. Verspaget, T. Walters, C. Wijmenga, D.C. Wilson, H.J. Westra, R.J. Xavier, Z.Z. Zhao, C.Y. Ponsioen, V. Andersen, L. Torkvist, M. Gazouli, N.P. Anagnou, T.H. Karlsen, L. Kupcinskas, J. Sventoraityte, J.C. Mansfield, S. Kugathasan, M.S. Silverberg, J. Halfvarson, J.I. Rotter, C.G. Mathew, A.M. Griffiths, R. Gearry, T. Ahmad, S.R. Brant, M. Chamaillard, et al. 2011. Meta-analysis identifies 29 additional ulcerative colitis risk loci, increasing the number of confirmed associations to 47. *Nat Genet*. 43:246-252.

Anderson, J.M., and C.M. Van Itallie. 2009. Physiology and function of the tight junction. *Cold Spring Harb Perspect Biol*. 1:a002584.

Andreu, I., I. Granero-Moya, N.R. Chahare, K. Clein, M. Molina-Jordan, A.E.M. Beedle, A. Elosegui-Artola, J.F. Abenza, L. Rossetti, X. Trepat, B. Raveh, and P. Roca-Cusachs. 2022. Mechanical force application to the nucleus regulates nucleocytoplasmic transport. *Nat Cell Biol*. 24:896-905.

Anuja, K., S. Roy, C. Ghosh, P. Gupta, S. Bhattacharjee, and B. Banerjee. 2017. Prolonged inflammatory microenvironment is crucial for pro-neoplastic growth and genome instability: a detailed review. *Inflamm Res*. 66:119-128.

Arnould, C., and G. Legube. 2020. The Secret Life of Chromosome Loops upon DNA Double-Strand Break. *J Mol Biol*. 432:724-736.

Aureille, J., V. Buffiere-Ribot, B.E. Harvey, C. Boyault, L. Pernet, T. Andersen, G. Bacola, M. Balland, S. Fraboulet, L. Van Landeghem, and C. Guilluy. 2019. Nuclear envelope deformation controls cell cycle progression in response to mechanical force. *EMBO Rep*. 20:e48084.

Axelsson, L.G., E. Landstrom, T.J. Goldschmidt, A. Gronberg, and A.C. Bylund-Fellenius. 1996. Dextran sulfate sodium (DSS) induced experimental colitis in immunodeficient mice: effects in CD4(+) -cell depleted, athymic and NK-cell depleted SCID mice. *Inflamm Res*. 45:181-191.

Azzouz, L.L., and S. Sharma. 2024. Physiology, Large Intestine. *In* StatPearls, Treasure Island (FL).

Bajer, L., M. Kverka, M. Kostovcik, P. Macinga, J. Dvorak, Z. Stehlikova, J. Brezina, P. Wohl, J. Spicak, and P. Drastich. 2017. Distinct gut microbiota profiles in patients with primary sclerosing cholangitis and ulcerative colitis. *World J Gastroenterol*. 23:4548-4558.

Bakhoum, S.F., B. Ngo, A.M. Laughney, J.A. Cavallo, C.J. Murphy, P. Ly, P. Shah, R.K. Sriram, T.B.K. Watkins, N.K. Taunk, M. Duran, C. Pauli, C. Shaw, K. Chadalavada, V.K. Rajasekhar, G. Genovese, S. Venkatesan, N.J. Birkbak, N. McGranahan, M. Lundquist, Q. LaPlant, J.H. Healey, O. Elemento, C.H. Chung, N.Y. Lee, M. Imielenski, G. Nanjangud, D. Pe'er, D.W. Cleveland, S.N. Powell, J. Lammerding, C. Swanton, and L.C. Cantley. 2018. Chromosomal instability drives metastasis through a cytosolic DNA response. *Nature*. 553:467-472.

Bardhan, A., L. Bruckner-Tuderman, I.L.C. Chapple, J.D. Fine, N. Harper, C. Has, T.M. Magin, M.P. Marinkovich, J.F. Marshall, J.A. McGrath, J.E. Mellerio, R. Polson, and A.H. Heagerty. 2020. Epidermolysis bullosa. *Nat Rev Dis Primers*. 6:78.

Baribault, H., J. Penner, R.V. Iozzo, and M. Wilson-Heiner. 1994. Colorectal hyperplasia and inflammation in keratin 8-deficient FVB/N mice. *Genes Dev*. 8:2964-2973.

Barker, N., J.H. van Es, J. Kuipers, P. Kujala, M. van den Born, M. Cozijnsen, A. Haegebarth, J. Korving, H. Begthel, P.J. Peters, and H. Clevers. 2007. Identification of stem cells in small intestine and colon by marker gene Lgr5. *Nature*. 449:1003-1007.

Barlan, K., and V.I. Gelfand. 2017. Microtubule-Based Transport and the Distribution, Tethering, and Organization of Organelles. *Cold Spring Harb Perspect Biol*. 9.

Beaulieu, J.F. 2018. Integrin I+/-6 variants and colorectal cancer. *Gut*. 67:1747-1748.

Benham-Pyle, B.W., B.L. Pruitt, and W.J. Nelson. 2015. Cell adhesion. Mechanical strain induces E-cadherin-dependent Yap1 and beta-catenin activation to drive cell cycle entry. *Science*. 348:1024-1027.

Beyder, A. 2018. In Pursuit of the Epithelial Mechanosensitivity Mechanisms. *Front Endocrinol (Lausanne)*. 9:804.

Bian, Q., N. Khanna, J. Alvikas, and A.S. Belmont. 2013. beta-Globin cis-elements determine differential nuclear targeting through epigenetic modifications. *J Cell Biol*. 203:767-783.

Blackford, A.N., and M. Stucki. 2020. How Cells Respond to DNA Breaks in Mitosis. *Trends Biochem Sci*. 45:321-331.

Block, J., H. Witt, A. Candelli, J.C. Danes, E.J.G. Peterman, G.J.L. Wuite, A. Janshoff, and S. Koster. 2018. Viscoelastic properties of vimentin originate from nonequilibrium conformational changes. *Sci Adv*. 4:eaat1161.

Boczonadi, V., L. McInroy, and A. Maatta. 2007. Cytolinker cross-talk: periplakin N-terminus interacts with plectin to regulate keratin organisation and epithelial migration. *Exp Cell Res*. 313:3579-3591.

Boirivant, M., I.J. Fuss, A. Chu, and W. Strober. 1998. Oxazolone colitis: A murine model of T helper cell type 2 colitis treatable with antibodies to interleukin 4. *J Exp Med*. 188:1929-1939.

Boivin, G.P., K. Washington, K. Yang, J.M. Ward, T.P. Pretlow, R. Russell, D.G. Besselsen, V.L. Godfrey, T. Doetschman, W.F. Dove, H.C. Pitot, R.B. Halberg, S.H. Itzkowitz, J. Groden, and R.J. Coffey. 2003. Pathology of mouse models of intestinal cancer: consensus report and recommendations. *Gastroenterology*. 124:762-777.

Bonakdar, N., A. Schilling, M. Sporrer, P. Lennert, A. Mainka, L. Winter, G. Walko, G. Wiche, B. Fabry, and W.H. Goldmann. 2015. Determining the mechanical properties of plectin in mouse myoblasts and keratinocytes. *Exp Cell Res*. 331:331-337.

Braga, V. 2016. Spatial integration of E-cadherin adhesion, signalling and the epithelial cytoskeleton. *Curr Opin Cell Biol*. 42:138-145.

Branis, J., C. Pataki, M. Sporrer, R.C. Gerum, A. Mainka, V. Cermak, W.H. Goldmann, B. Fabry, J. Brabek, and D. Rosel. 2017. The role of focal adhesion anchoring domains of CAS in mechanotransduction. *Sci Rep*. 7:46233.

Brauer, R., J. Tureckova, I. Kanchev, M. Khoylou, J. Skarda, J. Prochazka, F. Spoutil, I.M. Beck, O. Zbodakova, P. Kasparek, V. Korinek, K. Chalupsky, T. Karhu, K.H. Herzig, M. Hajduch, M. Gregor, and R. Sedlacek. 2016. MMP-19 deficiency causes aggravation of colitis due to defects in innate immune cell function. *Mucosal Immunol*. 9:974-985.

Bronner, C.E., S.M. Baker, P.T. Morrison, G. Warren, L.G. Smith, M.K. Lescoe, M. Kane, C. Earabino, J. Lipford, A. Lindblom, and et al. 1994. Mutation in the DNA mismatch repair gene homologue hMLH1 is associated with hereditary non-polyposis colon cancer. *Nature*. 368:258-261.

Broussard, J.A., A. Jaiganesh, H. Zarkoob, D.E. Conway, A.R. Dunn, H.D. Espinosa, P.A. Janmey, and K.J. Green. 2020. Scaling up single-cell mechanics to multicellular tissues - the role of the intermediate filament-desmosome network. *J Cell Sci*. 133.

Buchwalter, A., J.M. Kaneshiro, and M.W. Hetzer. 2019. Coaching from the sidelines: the nuclear periphery in genome regulation. *Nat Rev Genet*. 20:39-50.

Buracco, S., S. Claydon, and R. Insall. 2019. Control of actin dynamics during cell motility. *F1000Res*. 8.

Cannan, W.J., and D.S. Pederson. 2016. Mechanisms and Consequences of Double-Strand DNA Break Formation in Chromatin. *J Cell Physiol*. 231:3-14.

Caporaso, J.G., J. Kuczynski, J. Stombaugh, K. Bittinger, F.D. Bushman, E.K. Costello, N. Fierer, A.G. Pena, J.K. Goodrich, J.I. Gordon, G.A. Huttley, S.T. Kelley, D. Knights, J.E. Koenig, R.E. Ley, C.A. Lozupone, D. McDonald, B.D. Muegge, M. Pirrung, J. Reeder, J.R. Sevinsky, P.J. Turnbaugh, W.A. Walters, J. Widmann, T. Yatsunenko, J. Zaneveld, and R. Knight. 2010. QIIME allows analysis of high-throughput community sequencing data. *Nat Methods*. 7:335-336.

Castanon, M.J., G. Walko, L. Winter, and G. Wiche. 2013. Plectin-intermediate filament partnership in skin, skeletal muscle, and peripheral nerve. *Histochem Cell Biol*. 140:33-53.

Chalut, K.J., M. Hopfler, F. Lautenschlager, L. Boyde, C.J. Chan, A. Ekpenyong, A. Martinez-Arias, and J. Guck. 2012. Chromatin decondensation and nuclear softening accompany Nanog downregulation in embryonic stem cells. *Biophys J*. 103:2060-2070.

Chang, J., R.W. Leong, V.C. Wasinger, M. Ip, M. Yang, and T.G. Phan. 2017. Impaired Intestinal Permeability Contributes to Ongoing Bowel Symptoms in Patients With Inflammatory Bowel Disease and Mucosal Healing. *Gastroenterology*. 153:723-731 e721.

Charras, G., and A.S. Yap. 2018. Tensile Forces and Mechanotransduction at Cell-Cell Junctions. *Curr Biol*. 28:R445-R457.

Chassaing, B., J.D. Aitken, M. Malleshappa, and M. Vijay-Kumar. 2014. Dextran sulfate sodium (DSS)-induced colitis in mice. *Curr Protoc Immunol*. 104:15 25 11-15 25 14.

Chen, V.C., X. Li, H. Perreault, and J.I. Nagy. 2006. Interaction of zonula occludens-1 (ZO-1) with alpha-actinin-4: application of functional proteomics for identification of PDZ domain-associated proteins. *J Proteome Res*. 5:2123-2134.

Chen, X., S. Kojima, G.G. Borisy, and K.J. Green. 2003. p120 catenin associates with kinesin and facilitates the transport of cadherin-catenin complexes to intercellular junctions. *J Cell Biol*. 163:547-557.

Cheng, H., and C.P. Leblond. 1974. Origin, differentiation and renewal of the four main epithelial cell types in the mouse small intestine. V. Unitarian Theory of the origin of the four epithelial cell types. *Am J Anat*. 141:537-561.

Cho, S., J. Irianto, and D.E. Discher. 2017. Mechanosensing by the nucleus: From pathways to scaling relationships. *J Cell Biol*. 216:305-315.

Cho, S., M. Vashisth, A. Abbas, S. Majkut, K. Vogel, Y. Xia, I.L. Ivanovska, J. Irianto, M. Tewari, K. Zhu, E.D. Tichy, F. Mourkioti, H.Y. Tang, R.A. Greenberg, B.L. Prosser, and D.E. Discher. 2019. Mechanosensing by the Lamina Protects against Nuclear Rupture, DNA Damage, and Cell-Cycle Arrest. *Dev Cell*. 49:920-935 e925.

Clevers, H. 2013. The intestinal crypt, a prototype stem cell compartment. *Cell*. 154:274-284.

Codelia, V.A., G. Sun, and K.D. Irvine. 2014. Regulation of YAP by mechanical strain through Jnk and Hippo signaling. *Curr Biol*. 24:2012-2017.

Consortium, U.I.G., J.C. Barrett, J.C. Lee, C.W. Lees, N.J. Prescott, C.A. Anderson, A. Phillips, E. Wesley, K. Parnell, H. Zhang, H. Drummond, E.R. Nimmo, D. Massey, K. Blaszczyk, T. Elliott, L. Cotterill, H. Dallal, A.J. Lobo, C. Mowat, J.D. Sanderson, D.P. Jewell, W.G. Newman, C. Edwards, T. Ahmad, J.C. Mansfield, J. Satsangi, M. Parkes, C.G. Mathew, C. Wellcome Trust Case Control, P. Donnelly, L. Peltonen, J.M. Blackwell, E. Bramon, M.A. Brown, J.P. Casas, A. Corvin, N. Craddock, P. Deloukas, A. Duncanson, J. Jankowski, H.S. Markus, C.G. Mathew, M.I. McCarthy,

C.N. Palmer, R. Plomin, A. Rautanen, S.J. Sawcer, N. Samani, R.C. Trembath, A.C. Viswanathan, N. Wood, C.C. Spencer, J.C. Barrett, C. Bellenguez, D. Davison, C. Freeman, A. Strange, P. Donnelly, C. Langford, S.E. Hunt, S. Edkins, R. Gwilliam, H. Blackburn, S.J. Bumpstead, S. Dronov, M. Gillman, E. Gray, N. Hammond, A. Jayakumar, O.T. McCann, J. Liddle, M.L. Perez, S.C. Potter, R. Ravindrarajah, M. Ricketts, M. Waller, P. Weston, S. Widaa, P. Whittaker, P. Deloukas, L. Peltonen, C.G. Mathew, J.M. Blackwell, M.A. Brown, A. Corvin, M.I. McCarthy, C.C. Spencer, A.P. Attwood, J. Stephens, J. Sambrook, W.H. Ouwehand, W.L. McArdle, S.M. Ring, and D.P. Strachan. 2009. Genome-wide association study of ulcerative colitis identifies three new susceptibility loci, including the HNF4A region. *Nat Genet*. 41:1330-1334.

Corfe, B.M., D. Majumdar, A. Assadsangabi, A.M. Marsh, S.S. Cross, J.B. Connolly, C.A. Evans, and A.J. Lobo. 2015. Inflammation decreases keratin level in ulcerative colitis; inadequate restoration associates with increased risk of colitis-associated cancer. *BMJ Open Gastroenterol*. 2:e000024.

Cornick, S., A. Tawiah, and K. Chadee. 2015. Roles and regulation of the mucus barrier in the gut. *Tissue Barriers*. 3:e982426.

Coste, B., J. Mathur, M. Schmidt, T.J. Earley, S. Ranade, M.J. Petrus, A.E. Dubin, and A. Patapoutian. 2010. Piezo1 and Piezo2 are essential components of distinct mechanically activated cation channels. *Science*. 330:55-60.

Crawley, S.W., M.S. Mooseker, and M.J. Tyska. 2014. Shaping the intestinal brush border. *J Cell Biol*. 207:441-451.

Cuzic, S., M. Antolic, A. Ognjenovic, D. Stupin-Polancec, A. Petrinic Grba, B. Hrvacic, M. Dominis Kramaric, S. Musladin, L. Pozgaj, I. Zlatar, D. Polancec, G. Aralica, M. Banic, M. Urek, B. Mijandrusic Sincic, A. Cubranic, I. Glojnaric, M. Bosnar, and V. Erakovic Haber. 2021. Claudins: Beyond Tight Junctions in Human IBD and Murine Models. *Front Pharmacol*. 12:682614.

De Arcangelis, A., M. Chamaillard, P. Simon-Assmann, and M. Labouesse. 2018. Integrin a6 loss promotes colitis-associated colorectal cancer. Response to: "Integrin a6 variants and colorectal cancer" by Beaulieu JF. *Gut*. 67:2227-2228.

De Arcangelis, A., H. Hamade, F. Alpy, S. Normand, E. Bruyere, O. Lefebvre, A. Mechine-Neuville, S. Siebert, V. Pfister, P. Lepage, P. Laquerriere, D. Dembele, A. Delanoye-Crespin, S. Rodius, S. Robine, M. Kedinger, I. Van Seuningen, P. Simon-Assmann, M. Chamaillard, M. Labouesse, and E. Georges-Labouesse. 2017. Hemidesmosome integrity protects the colon against colitis and colorectal cancer. *Gut*. 66:1748-1760.

de Pereda, J.M., M.P. Lillo, and A. Sonnenberg. 2009. Structural basis of the interaction between integrin alpha6beta4 and plectin at the hemidesmosomes. *EMBO J*. 28:1180-1190.

De, R., and S.A. Safran. 2008. Dynamical theory of active cellular response to external stress. *Phys Rev E Stat Nonlin Soft Matter Phys*. 78:031923.

Dekraker, C., E. Boucher, and C.A. Mandato. 2018. Regulation and Assembly of Actomyosin Contractile Rings in Cytokinesis and Cell Repair. *Anat Rec (Hoboken)*. 301:2051-2066.

Della Chiara, G., F. Gervasoni, M. Fakiola, C. Godano, C. D'Oria, L. Azzolin, R.J.P. Bonnal, G. Moreni, L. Drufuca, G. Rossetti, V. Ranzani, R. Bason, M. De Simone, F. Panariello, I. Ferrari, T. Fabbris, F. Zanconato, M. Forcato, O. Romano, J. Caroli, P. Gruarin, M.L. Sarnicola, M. Cordenonsi, A. Bardelli, N. Zucchini, A.P. Ceretti, N.M. Mariani, A. Cassingena, A. Sartore-Bianchi, G. Testa, L. Gianotti, E. Opocher, F. Pisati, C. Tripodo, G. Macino, S. Siena, S. Bicciato, S. Piccolo, and M. Pagani. 2021. Epigenomic landscape of human colorectal cancer unveils an aberrant core of pan-cancer enhancers orchestrated by YAP/TAZ. *Nat Commun*. 12:2340.

Denais, C.M., R.M. Gilbert, P. Isermann, A.L. McGregor, M. te Lindert, B. Weigelin, P.M. Davidson, P. Friedl, K. Wolf, and J. Lammerding. 2016. Nuclear envelope rupture and repair during cancer cell migration. *Science*. 352:353-358.

DeSantis, T.Z., P. Hugenholtz, N. Larsen, M. Rojas, E.L. Brodie, K. Keller, T. Huber, D. Dalevi, P. Hu, and G.L. Andersen. 2006. Greengenes, a chimera-checked 16S rRNA gene database and workbench compatible with ARB. *Appl Environ Microbiol*. 72:5069-5072.

Dieleman, L.A., B.U. Ridwan, G.S. Tennyson, K.W. Beagley, R.P. Bucy, and C.O. Elson. 1994. Dextran sulfate sodium-induced colitis occurs in severe combined immunodeficient mice. *Gastroenterology*. 107:1643-1652.

Dominguez, R. 2009. Actin filament nucleation and elongation factors--structure-function relationships. *Crit Rev Biochem Mol Biol*. 44:351-366.

Dominguez, R., and K.C. Holmes. 2011. Actin structure and function. *Annu Rev Biophys*. 40:169-186.

Drurey, C., H.T. Lindholm, G. Coakley, M.C. Poveda, S. Loser, R. Doolan, F. Gerbe, P. Jay, N. Harris, M.J. Oudhoff, and R.M. Maizels. 2022. Intestinal epithelial tuft cell induction is negated by a murine helminth and its secreted products. *J Exp Med*. 219.

Du, L., J.J. Kim, J. Shen, B. Chen, and N. Dai. 2017. KRAS and TP53 mutations in inflammatory bowel disease-associated colorectal cancer: a meta-analysis. *Oncotarget*. 8:22175-22186.

Duan, Y., Y. Sun, F. Zhang, W.K. Zhang, D. Wang, Y. Wang, X. Cao, W. Hu, C. Xie, J. Cuppoletti, T.M. Magin, H. Wang, Z. Wu, N. Li, and P. Huang. 2012. Keratin K18 increases cystic fibrosis transmembrane conductance regulator (CFTR) surface expression by binding to its C-terminal hydrophobic patch. *J Biol Chem*. 287:40547-40559.

Dupont, S., L. Morsut, M. Aragona, E. Enzo, S. Giulitti, M. Cordenonsi, F. Zanconato, J. Le Digabel, M. Forcato, S. Bicciato, N. Elvassore, and S. Piccolo. 2011. Role of YAP/TAZ in mechanotransduction. *Nature*. 474:179-183.

Durmus, S., M. van der Valk, S.F. Teunissen, J.Y. Song, E. Wagenaar, J.H. Beijnen, and A.H. Schinkel. 2019. ABC transporters Mdr1a/1b, Bcrp1, Mrp2 and Mrp3 determine the sensitivity to PhIP/DSS-induced colon carcinogenesis and inflammation. *Arch Toxicol*. 93:775-790.

Eaden, J.A., K.R. Abrams, and J.F. Mayberry. 2001. The risk of colorectal cancer in ulcerative colitis: a meta-analysis. *Gut*. 48:526-535.

Edgar, R.C., and H. Flyvbjerg. 2015. Error filtering, pair assembly and error correction for next-generation sequencing reads. *Bioinformatics*. 31:3476-3482.

Eger, A., A. Stockinger, G. Wiche, and R. Foisner. 1997. Polarisation-dependent association of plectin with desmoplakin and the lateral submembrane skeleton in MDCK cells. *J Cell Sci*. 110 (Pt 11):1307-1316.

Eisenhoffer, G.T., P.D. Loftus, M. Yoshigi, H. Otsuna, C.B. Chien, P.A. Morcos, and J. Rosenblatt. 2012. Crowding induces live cell extrusion to maintain homeostatic cell numbers in epithelia. *Nature*. 484:546-549.

Eissa, N., H. Hussein, H. Wang, M.F. Rabbi, C.N. Bernstein, and J.E. Ghia. 2016. Stability of Reference Genes for Messenger RNA Quantification by Real-Time PCR in Mouse Dextran Sodium Sulfate Experimental Colitis. *PLoS One*. 11:e0156289.

el Marjou, F., K.P. Janssen, B.H. Chang, M. Li, V. Hindie, L. Chan, D. Louvard, P. Chambon, D. Metzger, and S. Robine. 2004. Tissue-specific and inducible Cre-mediated recombination in the gut epithelium. *Genesis*. 39:186-193.

Elosegui-Artola, A., I. Andreu, A.E.M. Beedle, A. Lezamiz, M. Uroz, A.J. Kosmalska, R. Oria, J.Z. Kechagia, P. Rico-Lastres, A.L. Le Roux, C.M. Shanahan, X. Trepat, D. Navajas, S. Garcia-Manyes, and P. Roca-Cusachs. 2017. Force Triggers YAP Nuclear Entry by Regulating Transport across Nuclear Pores. *Cell*. 171:1397-1410 e1314.

Eluri, S., A.M. Parian, B.N. Limketkai, C.Y. Ha, S.R. Brant, S. Dudley-Brown, J.E. Efron, S.G. Fang, S.L. Gearhart, M.R. Marohn, S.J. Meltzer, S. Bashar, B. Truta, E.A. Montgomery, and M.G. Lazarev. 2017. Nearly a Third of High-Grade Dysplasia and Colorectal Cancer Is Undetected in Patients with Inflammatory Bowel Disease. *Dig Dis Sci*. 62:3586-3593.

Erdman, S.E., V.P. Rao, T. Poutahidis, M.M. Ihrig, Z. Ge, Y. Feng, M. Tomczak, A.B. Rogers, B.H. Horwitz, and J.G. Fox. 2003. CD4(+)CD25(+) regulatory lymphocytes require interleukin 10 to interrupt colon carcinogenesis in mice. *Cancer Res*. 63:6042-6050.

Evans, C.A., R. Rosser, J.S. Waby, J. Noirel, D. Lai, P.C. Wright, E.A. Williams, S.A. Riley, J.P. Bury, and B.M. Corfe. 2015. Reduced keratin expression in colorectal neoplasia and associated fields is reversible by diet and resection. *BMJ Open Gastroenterol*. 2:e000022.

Faust, U., N. Hampe, W. Rubner, N. Kirchgessner, S. Safran, B. Hoffmann, and R. Merkel. 2011. Cyclic stress at mHz frequencies aligns fibroblasts in direction of zero strain. *PLoS One*. 6:e28963.

Fernandez-Sanchez, M.E., S. Barbier, J. Whitehead, G. Bealle, A. Michel, H. Latorre-Ossa, C. Rey, L. Fouassier, A. Claperon, L. Brulle, E. Girard, N. Servant, T. Rio-Frio, H. Marie, S. Lesieur, C. Housset, J.L. Gennisson, M. Tanter, C. Menager, S. Fre, S. Robine, and E. Farge. 2015. Mechanical induction of the tumorigenic beta-catenin pathway by tumour growth pressure. *Nature*. 523:92-95.

Fish, E.M., K.R. Shumway, and B. Burns. 2024. Physiology, Small Bowel. *In* StatPearls, Treasure Island (FL).

Fishel, R., M.K. Lescoe, M.R. Rao, N.G. Copeland, N.A. Jenkins, J. Garber, M. Kane, and R. Kolodner. 1993. The human mutator gene homolog MSH2 and its association with hereditary nonpolyposis colon cancer. *Cell*. 75:1027-1038.

Flores, B.M., A. O'Connor, and A.C. Moss. 2017. Impact of mucosal inflammation on risk of colorectal neoplasia in patients with ulcerative colitis: a systematic review and meta-analysis. *Gastrointest Endosc*. 86:1006-1011 e1008.

Foisner, R., F.E. Leichtfried, H. Herrmann, J.V. Small, D. Lawson, and G. Wiche. 1988. Cytoskeleton-associated plectin: in situ localization, in vitro reconstitution, and binding to immobilized intermediate filament proteins. *J Cell Biol*. 106:723-733.

Foisner, R., and G. Wiche. 1987. Structure and hydrodynamic properties of plectin molecules. *J Mol Biol*. 198:515-531.

Fontao, L., J. Stutzmann, P. Gendry, and J.F. Launay. 1999. Regulation of the type II hemidesmosomal plaque assembly in intestinal epithelial cells. *Exp Cell Res*. 250:298-312.

Fornaro, R., M. Caratto, E. Caratto, G. Caristo, F. Fornaro, D. Giovinazzo, C. Sticchi, M. Casaccia, and E. Andorno. 2016. Colorectal Cancer in Patients With Inflammatory Bowel Disease: The Need for a Real Surveillance Program. *Clin Colorectal Cancer*. 15:204-212.

Franke, A., T. Balschun, T.H. Karlsen, J. Sventoraityte, S. Nikolaus, G. Mayr, F.S. Domingues, M. Albrecht, M. Nothnagel, D. Ellinghaus, C. Sina, C.M. Onnie, R.K. Weersma, P.C. Stokkers, C. Wijmenga, M. Gazouli, D. Strachan, W.L. McArdle, S. Vermeire, P. Rutgeerts, P. Rosenstiel, M. Krawczak, M.H. Vatn, I.s. group, C.G. Mathew, and S. Schreiber. 2008. Sequence variants in IL10, ARPC2 and multiple other loci contribute to ulcerative colitis susceptibility. *Nat Genet*. 40:1319-1323.

Friedrich, M., M. Pohin, and F. Powrie. 2019. Cytokine Networks in the Pathophysiology of Inflammatory Bowel Disease. *Immunity*. 50:992-1006.

Fuchs, P., M. Zorer, G.A. Rezniczek, D. Spazierer, S. Oehler, M.J. Castanon, R. Hauptmann, and G. Wiche. 1999. Unusual 5' transcript complexity of plectin isoforms: novel tissue-specific exons modulate actin binding activity. *Hum Mol Genet*. 8:2461-2472.

Gan, Z., L. Ding, C.J. Burckhardt, J. Lowery, A. Zaritsky, K. Sitterley, A. Mota, N. Costigliola, C.G. Starker, D.F. Voytas, J. Tytell, R.D. Goldman, and G. Danuser. 2016. Vimentin Intermediate Filaments Template Microtubule Networks to Enhance Persistence in Cell Polarity and Directed Migration. *Cell Syst*. 3:252-263 e258.

Gassler, N., C. Rohr, A. Schneider, J. Kartenbeck, A. Bach, N. Obermuller, H.F. Otto, and F. Autschbach. 2001. Inflammatory bowel disease is associated with changes of enterocytic junctions. *Am J Physiol Gastrointest Liver Physiol*. 281:G216-228.

Gauthier, N.C., and P. Roca-Cusachs. 2018. Mechanosensing at integrin-mediated cell-matrix adhesions: from molecular to integrated mechanisms. *Curr Opin Cell Biol*. 50:20-26.

Gayer, C.P., and M.D. Basson. 2009. The effects of mechanical forces on intestinal physiology and pathology. *Cell Signal*. 21:1237-1244.

Gehart, H., and H. Clevers. 2019. Tales from the crypt: new insights into intestinal stem cells. *Nat Rev Gastroenterol Hepatol*. 16:19-34.

Geiger, B., and K.M. Yamada. 2011. Molecular architecture and function of matrix adhesions. *Cold Spring Harb Perspect Biol*. 3.

Geisler, F., and R.E. Leube. 2016. Epithelial Intermediate Filaments: Guardians against Microbial Infection? *Cells*. 5.

Genua, F., V. Raghunathan, M. Jenab, W.M. Gallagher, and D.J. Hughes. 2021. The Role of Gut Barrier Dysfunction and Microbiome Dysbiosis in Colorectal Cancer Development. *Front Oncol*. 11:626349.

Goldman, R.D. 1971. The role of three cytoplasmic fibers in BHK-21 cell motility. I. Microtubules and the effects of colchicine. *J Cell Biol*. 51:752-762.

Gonzalez-Lama, Y., E. Ricart, A. Cabez, P. Fortes, S. Gomez, and F. Casellas. 2023. Medical consultation in ulcerative colitis: Key elements for improvement. *World J Gastroenterol*. 29:917-925.

Grady, W.M., and S. Markowitz. 2000. Genomic instability and colorectal cancer. *Curr Opin Gastroenterol*. 16:62-67.

Green, K.J., and C.A. Gaudry. 2000. Are desmosomes more than tethers for intermediate filaments? *Nat Rev Mol Cell Biol*. 1:208-216.

Gregor, M., S. Osmanagic-Myers, G. Burgstaller, M. Wolfram, I. Fischer, G. Walko, G.P. Resch, A. Jorgl, H. Herrmann, and G. Wiche. 2014. Mechanosensing through focal adhesion-anchored intermediate filaments. *FASEB J*. 28:715-729.

Gribble, F.M., and F. Reimann. 2016. Enteroendocrine Cells: Chemosensors in the Intestinal Epithelium. *Annu Rev Physiol*. 78:277-299.

Gribble, F.M., and F. Reimann. 2017. Signalling in the gut endocrine axis. *Physiol Behav*. 176:183-188.

Groschwitz, K.R., and S.P. Hogan. 2009. Intestinal barrier function: molecular regulation and disease pathogenesis. *J Allergy Clin Immunol*. 124:3-20; quiz 21-22.

Gross, A., L.A.P. Pack, G.M. Schacht, S. Kant, H. Ungewiss, M. Meir, N. Schlegel, C. Preisinger, P. Boor, N. Guldiken, C.A. Krusche, G. Sellge, C. Trautwein, J. Waschke, A. Heuser, R.E. Leube, and P. Strnad. 2018. Desmoglein 2, but not desmocollin 2, protects intestinal epithelia from injury. *Mucosal Immunol*. 11:1630-1639.

Gruenbaum, Y., and R. Foisner. 2015. Lamins: nuclear intermediate filament proteins with fundamental functions in nuclear mechanics and genome regulation. *Annu Rev Biochem*. 84:131-164.

Gruenbaum, Y., A. Margalit, R.D. Goldman, D.K. Shumaker, and K.L. Wilson. 2005. The nuclear lamina comes of age. *Nat Rev Mol Cell Biol*. 6:21-31.

Gu, S., D. Chen, J.N. Zhang, X. Lv, K. Wang, L.P. Duan, Y. Nie, and X.L. Wu. 2013. Bacterial community mapping of the mouse gastrointestinal tract. *PLoS One*. 8:e74957.

Gudipaty, S.A., J. Lindblom, P.D. Loftus, M.J. Redd, K. Edes, C.F. Davey, V. Krishnegowda, and J. Rosenblatt. 2017. Mechanical stretch triggers rapid epithelial cell division through Piezo1. *Nature*. 543:118-121.

Guerrera, D., J. Shah, E. Vasileva, S. Sluysmans, I. Mean, L. Jond, I. Poser, M. Mann, A.A. Hyman, and S. Citi. 2016. PLEKHA7 Recruits PDZD11 to Adherens Junctions to Stabilize Nectins. *J Biol Chem*. 291:11016-11029.

Guldiken, N., G. Kobazi Ensari, P. Lahiri, G. Couchy, C. Preisinger, C. Liedtke, H.W. Zimmermann, M. Ziol, P. Boor, J. Zucman-Rossi, C. Trautwein, and P. Strnad. 2016. Keratin 23 is a stress-inducible marker of mouse and human ductular reaction in liver disease. *J Hepatol*. 65:552-559.

Haberman, Y., R. Karns, P.J. Dexheimer, M. Schirmer, J. Somekh, I. Jurickova, T. Braun, E. Novak, L. Bauman, M.H. Collins, A. Mo, M.J. Rosen, E. Bonkowski, N. Gotman, A. Marquis, M. Nistel, P.A. Rufo, S.S. Baker, C.G. Sauer, J. Markowitz, M.D. Pfefferkorn, J.R. Rosh, B.M. Boyle, D.R. Mack, R.N. Baldassano, S. Shah, N.S. Leleiko, M.B. Heyman, A.M. Grifiths, A.S. Patel, J.D. Noe, B.J. Aronow, S. Kugathasan, T.D. Walters, G. Gibson, S.D. Thomas, K. Mollen, S. Shen-Orr, C. Huttenhower, R.J. Xavier, J.S. Hyams, and L.A. Denson. 2019. Ulcerative colitis mucosal transcriptomes reveal mitochondriopathy and personalized mechanisms underlying disease severity and treatment response. *Nat Commun*. 10:38.

Habtezion, A., D.M. Toivola, M.N. Asghar, G.S. Kronmal, J.D. Brooks, E.C. Butcher, and M.B. Omary. 2011. Absence of keratin 8 confers a paradoxical microflora-dependent resistance to apoptosis in the colon. *Proc Natl Acad Sci U S A*. 108:1445-1450.
Habtezion, A., D.M. Toivola, E.C. Butcher, and M.B. Omary. 2005. Keratin-8-deficient mice develop chronic spontaneous Th2 colitis amenable to antibiotic treatment. *J Cell Sci*. 118:1971-1980.
Hanauer, S.B. 2006. Inflammatory bowel disease: epidemiology, pathogenesis, and therapeutic opportunities. *Inflamm Bowel Dis*. 12 Suppl 1:S3-9.
Hanson, J., and J. Lowy. 1963. The structure of F-actin and of actin filaments isolated from muscle. *Journal of Molecular Biology*. 6:46-IN45.
Harris, T.J., and U. Tepass. 2010. Adherens junctions: from molecules to morphogenesis. *Nat Rev Mol Cell Biol*. 11:502-514.
Hartsock, A., and W.J. Nelson. 2008. Adherens and tight junctions: structure, function and connections to the actin cytoskeleton. *Biochim Biophys Acta*. 1778:660-669.
Has, C., and J. Fischer. 2019. Inherited epidermolysis bullosa: New diagnostics and new clinical phenotypes. *Exp Dermatol*. 28:1146-1152.
Hasegawa, R., M. Sano, S. Tamano, K. Imaida, T. Shirai, M. Nagao, T. Sugimura, and N. Ito. 1993. Dose-dependence of 2-amino-1-methyl-6-phenylimidazo[4,5-b]-pyridine (PhIP) carcinogenicity in rats. *Carcinogenesis*. 14:2553-2557.
Hayakawa, K., N. Sato, and T. Obinata. 2001. Dynamic reorientation of cultured cells and stress fibers under mechanical stress from periodic stretching. *Exp Cell Res*. 268:104-114.
He, S., P. Lei, W. Kang, P. Cheung, T. Xu, M. Mana, C.Y. Park, H. Wang, S. Imada, J.O. Russell, J. Wang, R. Wang, Z. Zhou, K. Chetal, E. Stas, V. Mohad, P. Bruun-Rasmussen, R.I. Sadreyev, R.A. Hodin, Y. Zhang, D.T. Breault, F.D. Camargo, O.H. Yilmaz, J.J. Fredberg, and N. Saeidi. 2023. Stiffness Restricts the Stemness of the Intestinal Stem Cells and Skews Their Differentiation Toward Goblet Cells. *Gastroenterology*. 164:1137-1151 e1115.
Heinemann, U., and A. Schuetz. 2019. Structural Features of Tight-Junction Proteins. *Int J Mol Sci*. 20.
Helenius, T.O., C.A. Antman, M.N. Asghar, J.H. Nystrom, and D.M. Toivola. 2016. Keratins Are Altered in Intestinal Disease-Related Stress Responses. *Cells*. 5.
Heo, S.J., T.P. Driscoll, S.D. Thorpe, N.L. Nerurkar, B.M. Baker, M.T. Yang, C.S. Chen, D.A. Lee, and R.L. Mauck. 2016. Differentiation alters stem cell nuclear architecture, mechanics, and mechano-sensitivity. *Elife*. 5.
Hoevenaar, W.H.M., A. Janssen, A.I. Quirindongo, H. Ma, S.J. Klaasen, A. Teixeira, B. van Gerwen, N. Lansu, F.H.M. Morsink, G.J.A. Offerhaus, R.H. Medema, G. Kops, and N. Jelluma. 2020. Degree and site of chromosomal instability define its oncogenic potential. *Nat Commun*. 11:1501.
Houtekamer, R.M., M.C. van der Net, M.M. Maurice, and M. Gloerich. 2022. Mechanical forces directing intestinal form and function. *Curr Biol*. 32:R791-R805.
Howitt, M.R., S. Lavoie, M. Michaud, A.M. Blum, S.V. Tran, J.V. Weinstock, C.A. Gallini, K. Redding, R.F. Margolskee, L.C. Osborne, D. Artis, and W.S. Garrett. 2016. Tuft cells, taste-chemosensory cells, orchestrate parasite type 2 immunity in the gut. *Science*. 351:1329-1333.
Hsieh, C.Y., H.Y. Hsiao, W.Y. Wu, C.A. Liu, Y.C. Tsai, Y.J. Chao, D.L. Wang, and H.J. Hsieh. 2009. Regulation of shear-induced nuclear translocation of the Nrf2 transcription factor in endothelial cells. *J Biomed Sci*. 16:12.
Hu, J.E., F. Weiss, C. Bojarski, F. Branchi, J.D. Schulzke, M. Fromm, and S.M. Krug. 2021. Expression of tricellular tight junction proteins and the paracellular macromolecule barrier are recovered in remission of ulcerative colitis. *BMC Gastroenterol*. 21:141.
Hu, X., F.M. Margadant, M. Yao, and M.P. Sheetz. 2017. Molecular stretching modulates mechanosensing pathways. *Protein Sci*. 26:1337-1351.
Huang, R., and P.K. Zhou. 2021. DNA damage repair: historical perspectives, mechanistic pathways and clinical translation for targeted cancer therapy. *Signal Transduct Target Ther*. 6:254.
Huebner, K., K. Erlenbach-Wuensch, J. Prochazka, I. Sheraj, C. Hampel, B. Mrazkova, T. Michalcikova, J. Tureckova, V. Iatsiuk, A. Weissmann, F. Ferrazzi, P. Kunze, E. Nalli, E. Sammer, A. Gehring, M.M. Cheema, M. Eckstein, E.M. Paap, A. Soederberg, C. Fischer, S. Paul, V. Mahadevan, B.

Ndreshkjana, M.A. Meier, S. Muehlich, C.I. Geppert, S. Merkel, R. Grutzmann, A. Roehe, S. Banerjee, A. Hartmann, R. Sedlacek, and R. Schneider-Stock. 2022. ATF2 loss promotes tumor invasion in colorectal cancer cells via upregulation of cancer driver TROP2. *Cell Mol Life Sci*. 79:423.

Hunter, G.L., L. He, N. Perrimon, G. Charras, E. Giniger, and B. Baum. 2019. A role for actomyosin contractility in Notch signaling. *BMC Biol*. 17:12.

Ichijima, Y., K. Yoshioka, Y. Yoshioka, K. Shinohe, H. Fujimori, J. Unno, M. Takagi, H. Goto, M. Inagaki, S. Mizutani, and H. Teraoka. 2010. DNA lesions induced by replication stress trigger mitotic aberration and tetraploidy development. *PLoS One*. 5:e8821.

Ikeda, K., I. Semenova, O. Zhapparova, and V. Rodionov. 2010. Melanophores for microtubule dynamics and motility assays. *Methods Cell Biol*. 97:401-414.

Imajo, M., M. Ebisuya, and E. Nishida. 2015. Dual role of YAP and TAZ in renewal of the intestinal epithelium. *Nat Cell Biol*. 17:7-19.

Indra, I., S. Hong, R. Troyanovsky, B. Kormos, and S. Troyanovsky. 2013. The adherens junction: a mosaic of cadherin and nectin clusters bundled by actin filaments. *J Invest Dermatol*. 133:2546-2554.

Irianto, J., Y. Xia, C.R. Pfeifer, A. Athirasala, J. Ji, C. Alvey, M. Tewari, R.R. Bennett, S.M. Harding, A.J. Liu, R.A. Greenberg, and D.E. Discher. 2017. DNA Damage Follows Repair Factor Depletion and Portends Genome Variation in Cancer Cells after Pore Migration. *Curr Biol*. 27:210-223.

Iskratsch, T., H. Wolfenson, and M.P. Sheetz. 2014. Appreciating force and shape-the rise of mechanotransduction in cell biology. *Nat Rev Mol Cell Biol*. 15:825-833.

Jacob, J.T., P.A. Coulombe, R. Kwan, and M.B. Omary. 2018. Types I and II Keratin Intermediate Filaments. *Cold Spring Harb Perspect Biol*. 10.

Jain, N., K.V. Iyer, A. Kumar, and G.V. Shivashankar. 2013. Cell geometric constraints induce modular gene-expression patterns via redistribution of HDAC3 regulated by actomyosin contractility. *Proc Natl Acad Sci U S A*. 110:11349-11354.

Janda, L., J. Damborsky, G.A. Rezniczek, and G. Wiche. 2001. Plectin repeats and modules: strategic cysteines and their presumed impact on cytolinker functions. *Bioessays*. 23:1064-1069.

Janker, L., D. Schuster, P. Bortel, G. Hagn, S.M. Meier-Menches, T. Mohr, J.C. Mader, A. Slany, A. Bileck, J. Brunmair, C. Madl, L. Unger, B. Hennlich, B. Weitmayr, G. Del Favero, D. Pils, T. Pukrop, N. Pfisterer, T. Feichtenschlager, and C. Gerner. 2023. Multiomics-empowered Deep Phenotyping of Ulcerative Colitis Identifies Biomarker Signatures Reporting Functional Remission States. *J Crohns Colitis*. 17:1514-1527.

Jefferson, J.J., C.L. Leung, and R.K. Liem. 2004. Plakins: goliaths that link cell junctions and the cytoskeleton. *Nat Rev Mol Cell Biol*. 5:542-553.

Jerabkova, B., J. Marek, H. Buckova, L. Kopeckova, K. Vesely, J. Valickova, J. Fajkus, and L. Fajkusova. 2010. Keratin mutations in patients with epidermolysis bullosa simplex: correlations between phenotype severity and disturbance of intermediate filament molecular structure. *Br J Dermatol*. 162:1004-1013.

Jirouskova, M., K. Nepomucka, G. Oyman-Eyrilmez, A. Kalendova, H. Havelkova, L. Sarnova, K. Chalupsky, B. Schuster, O. Benada, P. Miksatkova, M. Kuchar, O. Fabian, R. Sedlacek, G. Wiche, and M. Gregor. 2018. Plectin controls biliary tree architecture and stability in cholestasis. *J Hepatol*. 68:1006-1017.

Johansson, M.E., M. Phillipson, J. Petersson, A. Velcich, L. Holm, and G.C. Hansson. 2008. The inner of the two Muc2 mucin-dependent mucus layers in colon is devoid of bacteria. *Proc Natl Acad Sci U S A*. 105:15064-15069.

Joshi, V., P.R. Strege, G. Farrugia, and A. Beyder. 2021. Mechanotransduction in gastrointestinal smooth muscle cells: role of mechanosensitive ion channels. *Am J Physiol Gastrointest Liver Physiol*. 320:G897-G906.

Jung, C., J.P. Hugot, and F. Barreau. 2010. Peyer's Patches: The Immune Sensors of the Intestine. *Int J Inflam*. 2010:823710.

Kah, D., C. Durrbeck, W. Schneider, B. Fabry, and R.C. Gerum. 2020. High-Force Magnetic Tweezers with Hysteresis-Free Force Feedback. *Biophys J*. 119:15-23.

Kaneyasu, H., K. Takahashi, N. Ohta, S. Okada, S. Kimura, S. Yasuno, S. Murata, S. Katsura, N. Yamada, K. Shiraishi, J. Tsuda, S. Miyai, H. Kurahashi, S. Hasegawa, and Y. Shimomura. 2023. Novel compound heterozygous mutations in the PLEC gene in a neonate with epidermolysis bullosa simplex with pyloric atresia. *J Dermatol*. 50:239-244.

Karlinger, K., T. Gyorke, E. Mako, A. Mester, and Z. Tarjan. 2000. The epidemiology and the pathogenesis of inflammatory bowel disease. *Eur J Radiol*. 35:154-167.

Kaunas, R., S. Usami, and S. Chien. 2006. Regulation of stretch-induced JNK activation by stress fiber orientation. *Cell Signal*. 18:1924-1931.

Kaverina, I., O. Krylyshkina, M. Gimona, K. Beningo, Y.L. Wang, and J.V. Small. 2000. Enforced polarisation and locomotion of fibroblasts lacking microtubules. *Curr Biol*. 10:739-742.

Kechagia, Z., P. Saez, M. Gomez-Gonzalez, B. Canales, S. Viswanadha, M. Zamarbide, I. Andreu, T. Koorman, A.E.M. Beedle, A. Elosegui-Artola, P.W.B. Derksen, X. Trepat, M. Arroyo, and P. Roca-Cusachs. 2023. The laminin-keratin link shields the nucleus from mechanical deformation and signalling. *Nat Mater*. 22:1409-1420.

Ketema, M., M. Kreft, P. Secades, H. Janssen, and A. Sonnenberg. 2013. Nesprin-3 connects plectin and vimentin to the nuclear envelope of Sertoli cells but is not required for Sertoli cell function in spermatogenesis. *Mol Biol Cell*. 24:2454-2466.

Ketema, M., K. Wilhelmsen, I. Kuikman, H. Janssen, D. Hodzic, and A. Sonnenberg. 2007. Requirements for the localization of nesprin-3 at the nuclear envelope and its interaction with plectin. *J Cell Sci*. 120:3384-3394.

Kiela, P.R., and F.K. Ghishan. 2016. Physiology of Intestinal Absorption and Secretion. *Best Pract Res Clin Gastroenterol*. 30:145-159.

Kiesslich, R., C.A. Duckworth, D. Moussata, A. Gloeckner, L.G. Lim, M. Goetz, D.M. Pritchard, P.R. Galle, M.F. Neurath, and A.J. Watson. 2012. Local barrier dysfunction identified by confocal laser endomicroscopy predicts relapse in inflammatory bowel disease. *Gut*. 61:1146-1153.

Kippenberger, S., S. Loitsch, M. Guschel, J. Muller, Y. Knies, R. Kaufmann, and A. Bernd. 2005. Mechanical stretch stimulates protein kinase B/Akt phosphorylation in epidermal cells via angiotensin II type 1 receptor and epidermal growth factor receptor. *J Biol Chem*. 280:3060-3067.

Kiraly, O., G. Gong, W. Olipitz, S. Muthupalani, and B.P. Engelward. 2015. Inflammation-induced cell proliferation potentiates DNA damage-induced mutations in vivo. *PLoS Genet*. 11:e1004901.

Kiritsi, D., L. Tsakiris, and F. Schauer. 2021. Plectin in Skin Fragility Disorders. *Cells*. 10.

Knoop, K.A., J.K. Gustafsson, K.G. McDonald, D.H. Kulkarni, P.E. Coughlin, S. McCrate, D. Kim, C.S. Hsieh, S.P. Hogan, C.O. Elson, P.I. Tarr, and R.D. Newberry. 2017a. Microbial antigen encounter during a preweaning interval is critical for tolerance to gut bacteria. *Sci Immunol*. 2.

Knoop, K.A., J.K. Gustafsson, K.G. McDonald, D.H. Kulkarni, R. Kassel, and R.D. Newberry. 2017b. Antibiotics promote the sampling of luminal antigens and bacteria via colonic goblet cell associated antigen passages. *Gut Microbes*. 8:400-411.

Koch, P.J., and W.W. Franke. 1994. Desmosomal cadherins: another growing multigene family of adhesion molecules. *Curr Opin Cell Biol*. 6:682-687.

Kojima, R., S. Kuroda, T. Ohkishi, K. Nakamaru, and S. Hatakeyama. 2004. Oxazolone-induced colitis in BALB/C mice: a new method to evaluate the efficacy of therapeutic agents for ulcerative colitis. *J Pharmacol Sci*. 96:307-313.

Kono, K., D.A. Tamashiro, and V.B. Alarcon. 2014. Inhibition of RHO-ROCK signaling enhances ICM and suppresses TE characteristics through activation of Hippo signaling in the mouse blastocyst. *Dev Biol*. 394:142-155.

Kostan, J., M. Gregor, G. Walko, and G. Wiche. 2009. Plectin isoform-dependent regulation of keratin-integrin alpha6beta4 anchorage via Ca2+/calmodulin. *J Biol Chem*. 284:18525-18536.

Koster, J., D. Geerts, B. Favre, L. Borradori, and A. Sonnenberg. 2003. Analysis of the interactions between BP180, BP230, plectin and the integrin alpha6beta4 important for hemidesmosome assembly. *J Cell Sci*. 116:387-399.

Koster, J., I. Kuikman, M. Kreft, and A. Sonnenberg. 2001. Two different mutations in the cytoplasmic domain of the integrin beta 4 subunit in nonlethal forms of epidermolysis bullosa prevent interaction of beta 4 with plectin. *J Invest Dermatol*. 117:1405-1411.

Kostovcikova, K., S. Coufal, N. Galanova, A. Fajstova, T. Hudcovic, M. Kostovcik, P. Prochazkova, Z. Jiraskova Zakostelska, M. Cermakova, B. Sediva, M. Kuzma, H. Tlaskalova-Hogenova, and M. Kverka. 2019. Diet Rich in Animal Protein Promotes Pro-inflammatory Macrophage Response and Exacerbates Colitis in Mice. *Front Immunol*. 10:919.

Krupina, K., A. Goginashvili, and D.W. Cleveland. 2021. Causes and consequences of micronuclei. *Curr Opin Cell Biol*. 70:91-99.

Ku, N.O., S. Michie, R.G. Oshima, and M.B. Omary. 1995. Chronic hepatitis, hepatocyte fragility, and increased soluble phosphoglycokeratins in transgenic mice expressing a keratin 18 conserved arginine mutant. *J Cell Biol*. 131:1303-1314.

Kucherlapati, M.H., K. Lee, A.A. Nguyen, A.B. Clark, H. Hou, Jr., A. Rosulek, H. Li, K. Yang, K. Fan, M. Lipkin, R.T. Bronson, L. Jelicks, T.A. Kunkel, R. Kucherlapati, and W. Edelmann. 2010. An Msh2 conditional knockout mouse for studying intestinal cancer and testing anticancer agents. *Gastroenterology*. 138:993-1002 e1001.

Kuhn, R., J. Lohler, D. Rennick, K. Rajewsky, and W. Muller. 1993. Interleukin-10-deficient mice develop chronic enterocolitis. *Cell*. 75:263-274.

Kumar, A., S. Lnu, R. Malya, D. Barron, J. Moore, D.B. Corry, and A.M. Boriek. 2003. Mechanical stretch activates nuclear factor-kappaB, activator protein-1, and mitogen-activated protein kinases in lung parenchyma: implications in asthma. *FASEB J*. 17:1800-1811.

Lahdeniemi, I.A.K., J.O. Misiorek, C.J.M. Antila, S.K. Landor, C.A. Stenvall, L.E. Fortelius, L.K. Bergstrom, C. Sahlgren, and D.M. Toivola. 2017. Keratins regulate colonic epithelial cell differentiation through the Notch1 signalling pathway. *Cell Death Differ*. 24:984-996.

Lakatos, P.L., and L. Lakatos. 2008. Risk for colorectal cancer in ulcerative colitis: changes, causes and management strategies. *World J Gastroenterol*. 14:3937-3947.

Laly, A.C., K. Sliogeryte, O.J. Pundel, R. Ross, M.C. Keeling, D. Avisetti, A. Waseem, N. Gavara, and J.T. Connelly. 2021. The keratin network of intermediate filaments regulates keratinocyte rigidity sensing and nuclear mechanotransduction. *Sci Adv*. 7.

Landy, J., E. Ronde, N. English, S.K. Clark, A.L. Hart, S.C. Knight, P.J. Ciclitira, and H.O. Al-Hassi. 2016. Tight junctions in inflammatory bowel diseases and inflammatory bowel disease associated colorectal cancer. *World J Gastroenterol*. 22:3117-3126.

Laroui, H., S.A. Ingersoll, H.C. Liu, M.T. Baker, S. Ayyadurai, M.A. Charania, F. Laroui, Y. Yan, S.V. Sitaraman, and D. Merlin. 2012. Dextran sodium sulfate (DSS) induces colitis in mice by forming nano-lipocomplexes with medium-chain-length fatty acids in the colon. *PLoS One*. 7:e32084.

Le Berre, M., E. Zlotek-Zlotkiewicz, D. Bonazzi, F. Lautenschlaeger, and M. Piel. 2014. Methods for two-dimensional cell confinement. *Methods Cell Biol*. 121:213-229.

Le Guen, T., S. Ragu, J. Guirouilh-Barbat, and B.S. Lopez. 2015. Role of the double-strand break repair pathway in the maintenance of genomic stability. *Mol Cell Oncol*. 2:e968020.

Le, H.Q., S. Ghatak, C.Y. Yeung, F. Tellkamp, C. Gunschmann, C. Dieterich, A. Yeroslaviz, B. Habermann, A. Pombo, C.M. Niessen, and S.A. Wickstrom. 2016. Mechanical regulation of transcription controls Polycomb-mediated gene silencing during lineage commitment. *Nat Cell Biol*. 18:864-875.

Lea, T. 2015. Caco-2 Cell Line. *In* The Impact of Food Bioactives on Health: in vitro and ex vivo models. K. Verhoeckx, P. Cotter, I. Lopez-Exposito, C. Kleiveland, T. Lea, A. Mackie, T. Requena, D. Swiatecka, and H. Wichers, editors, Cham (CH). 103-111.

Leake, I. 2016. IBD: Treatment for acute severe ulcerative colitis. *Nat Rev Gastroenterol Hepatol*. 13:436.

Lechuga, S., N.G. Naydenov, A. Feygin, M. Cruise, J.M. Ervasti, and A.I. Ivanov. 2020. Loss of beta-Cytoplasmic Actin in the Intestinal Epithelium Increases Gut Barrier Permeability in vivo and Exaggerates the Severity of Experimental Colitis. *Front Cell Dev Biol*. 8:588836.

Lemaitre, C., and W.A. Bickmore. 2015. Chromatin at the nuclear periphery and the regulation of genome functions. *Histochem Cell Biol*. 144:111-122.

Lessey, L.R., S.C. Robinson, R. Chaudhary, and J.M. Daniel. 2022. Adherens junction proteins on the move-From the membrane to the nucleus in intestinal diseases. *Front Cell Dev Biol*. 10:998373.

Leung, C.L., K.J. Green, and R.K. Liem. 2002. Plakins: a family of versatile cytolinker proteins. *Trends Cell Biol*. 12:37-45.

Lewis, A.H., and J. Grandl. 2015. Mechanical sensitivity of Piezo1 ion channels can be tuned by cellular membrane tension. *Elife*. 4.

Li, C., H.C. Lau, X. Zhang, and J. Yu. 2022. Mouse Models for Application in Colorectal Cancer: Understanding the Pathogenesis and Relevance to the Human Condition. *Biomedicines*. 10.

Liang, J., C. Lin, F. Hu, F. Wang, L. Zhu, X. Yao, Y. Wang, and Y. Zhao. 2013. APC polymorphisms and the risk of colorectal neoplasia: a HuGE review and meta-analysis. *Am J Epidemiol*. 177:1169-1179.

Lin, F., and H.J. Worman. 1993. Structural organization of the human gene encoding nuclear lamin A and nuclear lamin C. *J Biol Chem*. 268:16321-16326.

Lindblom, A., P. Tannergard, B. Werelius, and M. Nordenskjold. 1993. Genetic mapping of a second locus predisposing to hereditary non-polyposis colon cancer. *Nat Genet*. 5:279-282.

Linggi, B., V. Jairath, G. Zou, L.M. Shackelton, D.P.B. McGovern, A. Salas, B. Verstockt, M.S. Silverberg, S. Nayeri, B.G. Feagan, and N. Vande Casteele. 2021. Meta-analysis of gene expression disease signatures in colonic biopsy tissue from patients with ulcerative colitis. *Sci Rep*. 11:18243.

Litjens, S.H., J.M. de Pereda, and A. Sonnenberg. 2006. Current insights into the formation and breakdown of hemidesmosomes. *Trends Cell Biol*. 16:376-383.

Liu, C., E.D. Liu, Y.X. Meng, X.M. Dong, Y.L. Bi, H.W. Wu, Y.C. Jin, K. Zhao, J.J. Li, M. Yu, Y.Q. Zhan, H. Chen, C.H. Ge, X.M. Yang, and C.Y. Li. 2017. Keratin 8 reduces colonic permeability and maintains gut microbiota homeostasis, protecting against colitis and colitis-associated tumorigenesis. *Oncotarget*. 8:96774-96790.

Liu, C.G., C. Maercker, M.J. Castanon, R. Hauptmann, and G. Wiche. 1996. Human plectin: organization of the gene, sequence analysis, and chromosome localization (8q24). *Proc Natl Acad Sci U S A*. 93:4278-4283.

Liu, F., D. Lagares, K.M. Choi, L. Stopfer, A. Marinkovic, V. Vrbanac, C.K. Probst, S.E. Hiemer, T.H. Sisson, J.C. Horowitz, I.O. Rosas, L.E. Fredenburgh, C. Feghali-Bostwick, X. Varelas, A.M. Tager, and D.J. Tschumperlin. 2015. Mechanosignaling through YAP and TAZ drives fibroblast activation and fibrosis. *Am J Physiol Lung Cell Mol Physiol*. 308:L344-357.

Lomakin, A.J., C.J. Cattin, D. Cuvelier, Z. Alraies, M. Molina, G.P.F. Nader, N. Srivastava, P.J. Saez, J.M. Garcia-Arcos, I.Y. Zhitnyak, A. Bhargava, M.K. Driscoll, E.S. Welf, R. Fiolka, R.J. Petrie, N.S. De Silva, J.M. Gonzalez-Granado, N. Manel, A.M. Lennon-Dumenil, D.J. Muller, and M. Piel. 2020. The nucleus acts as a ruler tailoring cell responses to spatial constraints. *Science*. 370.

Lombardi, M.L., D.E. Jaalouk, C.M. Shanahan, B. Burke, K.J. Roux, and J. Lammerding. 2011. The interaction between nesprins and sun proteins at the nuclear envelope is critical for force transmission between the nucleus and cytoskeleton. *J Biol Chem*. 286:26743-26753.

Long, A.G., E.T. Lundsmith, and K.E. Hamilton. 2017. Inflammation and Colorectal Cancer. *Curr Colorectal Cancer Rep*. 13:341-351.

Loranger, A., S. Duclos, A. Grenier, J. Price, M. Wilson-Heiner, H. Baribault, and N. Marceau. 1997. Simple epithelium keratins are required for maintenance of hepatocyte integrity. *Am J Pathol*. 151:1673-1683.

Lowery, J., E.R. Kuczmarski, H. Herrmann, and R.D. Goldman. 2015. Intermediate Filaments Play a Pivotal Role in Regulating Cell Architecture and Function. *J Biol Chem*. 290:17145-17153.

Lu, C., J. Schardey, T. Zhang, A. Crispin, U. Wirth, K.W. Karcz, A.V. Bazhin, J. Andrassy, J. Werner, and F. Kuhn. 2022. Survival Outcomes and Clinicopathological Features in Inflammatory Bowel Disease-associated Colorectal Cancer: A Systematic Review and Meta-analysis. *Ann Surg*. 276:e319-e330.

Luca, V.C., B.C. Kim, C. Ge, S. Kakuda, D. Wu, M. Roein-Peikar, R.S. Haltiwanger, C. Zhu, T. Ha, and K.C. Garcia. 2017. Notch-Jagged complex structure implicates a catch bond in tuning ligand sensitivity. *Science*. 355:1320-1324.

Luna, G., G.P. Lewis, C.D. Banna, O. Skalli, and S.K. Fisher. 2010. Expression profiles of nestin and synemin in reactive astrocytes and Muller cells following retinal injury: a comparison with glial fibrillar acidic protein and vimentin. *Mol Vis*. 16:2511-2523.

Mabbott, N.A., D.S. Donaldson, H. Ohno, I.R. Williams, and A. Mahajan. 2013. Microfold (M) cells: important immunosurveillance posts in the intestinal epithelium. *Mucosal Immunol*. 6:666-677.

Maiato, H., J. DeLuca, E.D. Salmon, and W.C. Earnshaw. 2004. The dynamic kinetochore-microtubule interface. *J Cell Sci*. 117:5461-5477.

Mammoto, T., and D.E. Ingber. 2010. Mechanical control of tissue and organ development. *Development*. 137:1407-1420.

Martini, E., S.M. Krug, B. Siegmund, M.F. Neurath, and C. Becker. 2017. Mend Your Fences: The Epithelial Barrier and its Relationship With Mucosal Immunity in Inflammatory Bowel Disease. *Cell Mol Gastroenterol Hepatol*. 4:33-46.

Massimino, L., L.A. Lamparelli, Y. Houshyar, S. D'Alessio, L. Peyrin-Biroulet, S. Vetrano, S. Danese, and F. Ungaro. 2021. The Inflammatory Bowel Disease Transcriptome and Metatranscriptome Meta-Analysis (IBD TaMMA) framework. *Nat Comput Sci*. 1:511-515.

Matthews, H.K., S. Ganguli, K. Plak, A.V. Taubenberger, Z. Win, M. Williamson, M. Piel, J. Guck, and B. Baum. 2020. Oncogenic Signaling Alters Cell Shape and Mechanics to Facilitate Cell Division under Confinement. *Dev Cell*. 52:563-573 e563.

Mazmanian, S.K., C.H. Liu, A.O. Tzianabos, and D.L. Kasper. 2005. An immunomodulatory molecule of symbiotic bacteria directs maturation of the host immune system. *Cell*. 122:107-118.

McCole, D.F. 2014. IBD candidate genes and intestinal barrier regulation. *Inflamm Bowel Dis*. 20:1829-1849.

McHugh, B.J., R. Buttery, Y. Lad, S. Banks, C. Haslett, and T. Sethi. 2010. Integrin activation by Fam38A uses a novel mechanism of R-Ras targeting to the endoplasmic reticulum. *J Cell Sci*. 123:51-61.

Mehta, S., A. Nijhuis, T. Kumagai, J. Lindsay, and A. Silver. 2015. Defects in the adherens junction complex (E-cadherin/ beta-catenin) in inflammatory bowel disease. *Cell Tissue Res*. 360:749-760.

Meier, S.M., D. Kreutz, L. Winter, M.H.M. Klose, K. Cseh, T. Weiss, A. Bileck, B. Alte, J.C. Mader, S. Jana, A. Chatterjee, A. Bhattacharyya, M. Hejl, M.A. Jakupec, P. Heffeter, W. Berger, C.G. Hartinger, B.K. Keppler, G. Wiche, and C. Gerner. 2017. An Organoruthenium Anticancer Agent Shows Unexpected Target Selectivity For Plectin. *Angew Chem Int Ed Engl*. 56:8267-8271.

Meira, L.B., J.M. Bugni, S.L. Green, C.W. Lee, B. Pang, D. Borenshtein, B.H. Rickman, A.B. Rogers, C.A. Moroski-Erkul, J.L. McFaline, D.B. Schauer, P.C. Dedon, J.G. Fox, and L.D. Samson. 2008. DNA damage induced by chronic inflammation contributes to colon carcinogenesis in mice. *J Clin Invest*. 118:2516-2525.

Melgar, S., L. Karlsson, E. Rehnstrom, A. Karlsson, H. Utkovic, L. Jansson, and E. Michaelsson. 2008. Validation of murine dextran sulfate sodium-induced colitis using four therapeutic agents for human inflammatory bowel disease. *Int Immunopharmacol*. 8:836-844.

Meng, W., Y. Mushika, T. Ichii, and M. Takeichi. 2008. Anchorage of microtubule minus ends to adherens junctions regulates epithelial cell-cell contacts. *Cell*. 135:948-959.

Meng, W., and M. Takeichi. 2009. Adherens junction: molecular architecture and regulation. *Cold Spring Harb Perspect Biol*. 1:a002899.

Metcalfe, C., N.M. Kljavin, R. Ybarra, and F.J. de Sauvage. 2014. Lgr5+ stem cells are indispensable for radiation-induced intestinal regeneration. *Cell Stem Cell*. 14:149-159.

Mills, K.D., D.O. Ferguson, and F.W. Alt. 2003. The role of DNA breaks in genomic instability and tumorigenesis. *Immunol Rev*. 194:77-95.

Misiorek, J.O., I.A.K. Lahdeniemi, J.H. Nystrom, V.M. Paramonov, J.A. Gullmets, H. Saarento, A. Rivero-Muller, T. Husoy, P. Taimen, and D.M. Toivola. 2016. Keratin 8-deletion induced colitis predisposes to murine colorectal cancer enforced by the inflammasome and IL-22 pathway. *Carcinogenesis*. 37:777-786.

Mitra, S.K., D.A. Hanson, and D.D. Schlaepfer. 2005. Focal adhesion kinase: in command and control of cell motility. *Nat Rev Mol Cell Biol*. 6:56-68.

Modesto, R., J. Estarreja, I. Silva, J. Rocha, R. Pinto, and V. Mateus. 2022. Chemically Induced Colitis-Associated Cancer Models in Rodents for Pharmacological Modulation: A Systematic Review. *J Clin Med*. 11.

Modos, D., J.P. Thomas, and T. Korcsmaros. 2021. A handy meta-analysis tool for IBD research. *Nat Comput Sci*. 1:571-572.

Moll, R., A. Lowe, J. Laufer, and W.W. Franke. 1992. Cytokeratin 20 in human carcinomas. A new histodiagnostic marker detected by monoclonal antibodies. *Am J Pathol*. 140:427-447.

Moorwood, C. 2008. Syncoilin, an intermediate filament-like protein linked to the dystrophin associated protein complex in skeletal muscle. *Cell Mol Life Sci*. 65:2957-2963.

Moretto, R., M.M. Germani, M. Giordano, V. Conca, A. Proietti, C. Niccoli, F. Pietrantonio, S. Lonardi, E. Tamburini, A. Zaniboni, A. Passardi, T.P. Latiano, V. Fanotto, S. Di Donato, M. Prisciandaro, F. Bergamo, G. Masi, G. Fontanini, C. Ugolini, and C. Cremolini. 2023. Trop-2 and Nectin-4 immunohistochemical expression in metastatic colorectal cancer: searching for the right population for drugs' development. *Br J Cancer*. 128:1391-1399.

Morgan, E., M. Arnold, A. Gini, V. Lorenzoni, C.J. Cabasag, M. Laversanne, J. Vignat, J. Ferlay, N. Murphy, and F. Bray. 2023. Global burden of colorectal cancer in 2020 and 2040: incidence and mortality estimates from GLOBOCAN. *Gut*. 72:338-344.

Muller, L., M. Hatzfeld, and R. Keil. 2021. Desmosomes as Signaling Hubs in the Regulation of Cell Behavior. *Front Cell Dev Biol*. 9:745670.

Munoz, J., D.E. Stange, A.G. Schepers, M. van de Wetering, B.K. Koo, S. Itzkovitz, R. Volckmann, K.S. Kung, J. Koster, S. Radulescu, K. Myant, R. Versteeg, O.J. Sansom, J.H. van Es, N. Barker, A. van Oudenaarden, S. Mohammed, A.J. Heck, and H. Clevers. 2012. The Lgr5 intestinal stem cell signature: robust expression of proposed quiescent '+4' cell markers. *EMBO J*. 31:3079-3091.

Murrell, M., P.W. Oakes, M. Lenz, and M.L. Gardel. 2015. Forcing cells into shape: the mechanics of actomyosin contractility. *Nat Rev Mol Cell Biol*. 16:486-498.

Murthy, S.E., A.E. Dubin, and A. Patapoutian. 2017. Piezos thrive under pressure: mechanically activated ion channels in health and disease. *Nat Rev Mol Cell Biol*. 18:771-783.

Musah, S., P.J. Wrighton, Y. Zaltsman, X. Zhong, S. Zorn, M.B. Parlato, C. Hsiao, S.P. Palecek, Q. Chang, W.L. Murphy, and L.L. Kiessling. 2014. Substratum-induced differentiation of human pluripotent stem cells reveals the coactivator YAP is a potent regulator of neuronal specification. *Proc Natl Acad Sci U S A*. 111:13805-13810.

Myllymaki, S.M., U.R. Kamarainen, X. Liu, S.P. Cruz, S. Miettinen, M. Vuorela, M. Varjosalo, and A. Manninen. 2019. Assembly of the beta4-Integrin Interactome Based on Proximal Biotinylation in the Presence and Absence of Heterodimerization. *Mol Cell Proteomics*. 18:277-293.

Mylonas, K.S., M. Hayes, L.N. Ko, C.L. Griggs, D. Kroshinsky, and P.T. Masiakos. 2019. Clinical outcomes and molecular profile of patients with Carmi syndrome: A systematic review and evidence quality assessment. *J Pediatr Surg*. 54:1351-1358.

Nader, G.P.F., S. Aguera-Gonzalez, F. Routet, M. Gratia, M. Maurin, V. Cancila, C. Cadart, A. Palamidessi, R.N. Ramos, M. San Roman, M. Gentili, A. Yamada, A. Williart, C. Lodillinsky, E. Lagoutte, C. Villard, J.L. Viovy, C. Tripodo, J. Galon, G. Scita, N. Manel, P. Chavrier, and M. Piel. 2021. Compromised nuclear envelope integrity drives TREX1-dependent DNA damage and tumor cell invasion. *Cell*. 184:5230-5246 e5222.

Nahidiazar, L., M. Kreft, B. van den Broek, P. Secades, E.M. Manders, A. Sonnenberg, and K. Jalink. 2015. The molecular architecture of hemidesmosomes, as revealed with super-resolution microscopy. *J Cell Sci*. 128:3714-3719.

Nava, M.M., Y.A. Miroshnikova, L.C. Biggs, D.B. Whitefield, F. Metge, J. Boucas, H. Vihinen, E. Jokitalo, X. Li, J.M. Garcia Arcos, B. Hoffmann, R. Merkel, C.M. Niessen, K.N. Dahl, and S.A. Wickstrom. 2020. Heterochromatin-Driven Nuclear Softening Protects the Genome against Mechanical Stress-Induced Damage. *Cell*. 181:800-817 e822.

Nenci, A., C. Becker, A. Wullaert, R. Gareus, G. van Loo, S. Danese, M. Huth, A. Nikolaev, C. Neufert, B. Madison, D. Gumucio, M.F. Neurath, and M. Pasparakis. 2007. Epithelial NEMO links innate immunity to chronic intestinal inflammation. *Nature*. 446:557-561.

Neurath, M.F., and S. Finotto. 2009. Translating inflammatory bowel disease research into clinical medicine. *Immunity*. 31:357-361.

Neurath, M.F., I. Fuss, B.L. Kelsall, E. Stuber, and W. Strober. 1995. Antibodies to interleukin 12 abrogate established experimental colitis in mice. *J Exp Med*. 182:1281-1290.

Nicetto, D., G. Donahue, T. Jain, T. Peng, S. Sidoli, L. Sheng, T. Montavon, J.S. Becker, J.M. Grindheim, K. Blahnik, B.A. Garcia, K. Tan, R. Bonasio, T. Jenuwein, and K.S. Zaret. 2019. H3K9me3-heterochromatin loss at protein-coding genes enables developmental lineage specification. *Science*. 363:294-297.

Nievers, M.G., I. Kuikman, D. Geerts, I.M. Leigh, and A. Sonnenberg. 2000. Formation of hemidesmosome-like structures in the absence of ligand binding by the (alpha)6(beta)4 integrin requires binding of HD1/plectin to the cytoplasmic domain of the (beta)4 integrin subunit. *J Cell Sci*. 113 (Pt 6):963-973.

Noethel, B., L. Ramms, G. Dreissen, M. Hoffmann, R. Springer, M. Rubsam, W.H. Ziegler, C.M. Niessen, R. Merkel, and B. Hoffmann. 2018. Transition of responsive mechanosensitive elements from focal adhesions to adherens junctions on epithelial differentiation. *Mol Biol Cell*. 29:2317-2325.

Nogales, E., S.G. Wolf, and K.H. Downing. 1998. Structure of the alpha beta tubulin dimer by electron crystallography. *Nature*. 391:199-203.

Obbink-Huizer, C., C.W. Oomens, S. Loerakker, J. Foolen, C.V. Bouten, and F.P. Baaijens. 2014. Computational model predicts cell orientation in response to a range of mechanical stimuli. *Biomech Model Mechanobiol*. 13:227-236.

Odenwald, M.A., and J.R. Turner. 2017. The intestinal epithelial barrier: a therapeutic target? *Nat Rev Gastroenterol Hepatol*. 14:9-21.

Ohmachi, T., F. Tanaka, K. Mimori, H. Inoue, K. Yanaga, and M. Mori. 2006. Clinical significance of TROP2 expression in colorectal cancer. *Clin Cancer Res*. 12:3057-3063.

Ohno, H. 2016. Intestinal M cells. *J Biochem*. 159:151-160.

Ohtani, N., and N. Kawada. 2019. Role of the Gut-Liver Axis in Liver Inflammation, Fibrosis, and Cancer: A Special Focus on the Gut Microbiota Relationship. *Hepatol Commun*. 3:456-470.

Omary, M.B., N.O. Ku, P. Strnad, and S. Hanada. 2009. Toward unraveling the complexity of simple epithelial keratins in human disease. *J Clin Invest*. 119:1794-1805.

Ortega, E., J.A. Manso, R.M. Buey, A.M. Carballido, A. Carabias, A. Sonnenberg, and J.M. de Pereda. 2016. The Structure of the Plakin Domain of Plectin Reveals an Extended Rod-like Shape. *J Biol Chem*. 291:18643-18662.

Osmanagic-Myers, S., M. Gregor, G. Walko, G. Burgstaller, S. Reipert, and G. Wiche. 2006. Plectin-controlled keratin cytoarchitecture affects MAP kinases involved in cellular stress response and migration. *J Cell Biol*. 174:557-568.

Osmanagic-Myers, S., S. Rus, M. Wolfram, D. Brunner, W.H. Goldmann, N. Bonakdar, I. Fischer, S. Reipert, A. Zuzuarregui, G. Walko, and G. Wiche. 2015. Plectin reinforces vascular integrity by mediating crosstalk between the vimentin and the actin networks. *J Cell Sci*. 128:4138-4150.

Owaribe, K., J. Kartenbeck, S. Stumpp, T.M. Magin, T. Krieg, L.A. Diaz, and W.W. Franke. 1990. The hemidesmosomal plaque. I. Characterization of a major constituent protein as a differentiation marker for certain forms of epithelia. *Differentiation*. 45:207-220.

Owens, D.W., N.J. Wilson, A.J. Hill, E.L. Rugg, R.M. Porter, A.M. Hutcheson, R.A. Quinlan, D. van Heel, M. Parkes, D.P. Jewell, S.S. Campbell, S. Ghosh, J. Satsangi, and E.B. Lane. 2004. Human keratin 8 mutations that disturb filament assembly observed in inflammatory bowel disease patients. *J Cell Sci*. 117:1989-1999.

Pabst, O., M.W. Hornef, F.G. Schaap, V. Cerovic, T. Clavel, and T. Bruns. 2023. Gut-liver axis: barriers and functional circuits. *Nat Rev Gastroenterol Hepatol*. 20:447-461.

Pascal, V., M. Pozuelo, N. Borruel, F. Casellas, D. Campos, A. Santiago, X. Martinez, E. Varela, G. Sarrabayrouse, K. Machiels, S. Vermeire, H. Sokol, F. Guarner, and C. Manichanh. 2017. A microbial signature for Crohn's disease. *Gut*. 66:813-822.

Pastorelli, L., C. De Salvo, J.R. Mercado, M. Vecchi, and T.T. Pizarro. 2013. Central role of the gut epithelial barrier in the pathogenesis of chronic intestinal inflammation: lessons learned from animal models and human genetics. *Front Immunol*. 4:280.

Patteson, A.E., A. Vahabikashi, K. Pogoda, S.A. Adam, K. Mandal, M. Kittisopikul, S. Sivagurunathan, A. Goldman, R.D. Goldman, and P.A. Janmey. 2019. Vimentin protects cells against nuclear rupture and DNA damage during migration. *J Cell Biol*. 218:4079-4092.

Perler, B.K., R. Ungaro, G. Baird, M. Mallette, R. Bright, S. Shah, J. Shapiro, and B.E. Sands. 2019. Presenting symptoms in inflammatory bowel disease: descriptive analysis of a community-based inception cohort. *BMC Gastroenterol*. 19:47.

Peter, M., G.T. Kitten, C.F. Lehner, K. Vorburger, S.M. Bailer, G. Maridor, and E.A. Nigg. 1989. Cloning and sequencing of cDNA clones encoding chicken lamins A and B1 and comparison of the primary structures of vertebrate A- and B-type lamins. *J Mol Biol*. 208:393-404.

Peterson, L.W., and D. Artis. 2014. Intestinal epithelial cells: regulators of barrier function and immune homeostasis. *Nat Rev Immunol*. 14:141-153.

Pfaffl, M.W. 2001. A new mathematical model for relative quantification in real-time RT-PCR. *Nucleic Acids Res*. 29:e45.

Pfeifer, C.R., C.M. Alvey, J. Irianto, and D.E. Discher. 2017. Genome variation across cancers scales with tissue stiffness - an invasion-mutation mechanism and implications for immune cell infiltration. *Curr Opin Syst Biol*. 2:103-114.

Pfeifer, C.R., Y. Xia, K. Zhu, D. Liu, J. Irianto, V.M.M. Garcia, L.M.S. Millan, B. Niese, S. Harding, D. Deviri, R.A. Greenberg, and D.E. Discher. 2018. Constricted migration increases DNA damage and independently represses cell cycle. *Mol Biol Cell*. 29:1948-1962.

Piche, T., G. Barbara, P. Aubert, S. Bruley des Varannes, R. Dainese, J.L. Nano, C. Cremon, V. Stanghellini, R. De Giorgio, J.P. Galmiche, and M. Neunlist. 2009. Impaired intestinal barrier integrity in the colon of patients with irritable bowel syndrome: involvement of soluble mediators. *Gut*. 58:196-201.

Pinheiro, D., and Y. Bellaiche. 2018. Mechanical Force-Driven Adherens Junction Remodeling and Epithelial Dynamics. *Dev Cell*. 47:3-19.

Polari, L., M. Tenhami, S. Anttila, T. Helenius, H. Kujari, M. Kallajoki, M. Voutilainen, and D.M. Toivola. 2022. Colonocyte keratin 7 is expressed de novo in inflammatory bowel diseases and associated with pathological changes and drug-resistance. *Sci Rep*. 12:22213.

Pollard, T.D. 2016. Actin and Actin-Binding Proteins. *Cold Spring Harb Perspect Biol*. 8.

Pora, A., S. Yoon, R. Windoffer, and R.E. Leube. 2019. Hemidesmosomes and Focal Adhesions Treadmill as Separate but Linked Entities during Keratinocyte Migration. *J Invest Dermatol*. 139:1876-1888 e1874.

Poritz, L.S., K.I. Garver, C. Green, L. Fitzpatrick, F. Ruggiero, and W.A. Koltun. 2007. Loss of the tight junction protein ZO-1 in dextran sulfate sodium induced colitis. *J Surg Res*. 140:12-19.

Porter, E.M., C.L. Bevins, D. Ghosh, and T. Ganz. 2002. The multifaceted Paneth cell. *Cell Mol Life Sci*. 59:156-170.

Potten, C.S., and M. Loeffler. 1990. Stem cells: attributes, cycles, spirals, pitfalls and uncertainties. Lessons for and from the crypt. *Development*. 110:1001-1020.

Powrie, F., M.W. Leach, S. Mauze, S. Menon, L.B. Caddle, and R.L. Coffman. 1994. Inhibition of Th1 responses prevents inflammatory bowel disease in scid mice reconstituted with CD45RBhi CD4+ T cells. *Immunity*. 1:553-562.

Prechova, M., Z. Adamova, A.L. Schweizer, M. Maninova, A. Bauer, D. Kah, S.M. Meier-Menches, G. Wiche, B. Fabry, and M. Gregor. 2022. Plectin-mediated cytoskeletal crosstalk controls cell tension and cohesion in epithelial sheets. *J Cell Biol*. 221.

Prechova, M., K. Korelova, and M. Gregor. 2023. Plectin. *Curr Biol*. 33:R128-R130.

Price, A.J., A.L. Cost, H. Ungewiss, J. Waschke, A.R. Dunn, and C. Grashoff. 2018. Mechanical loading of desmosomes depends on the magnitude and orientation of external stress. *Nat Commun*. 9:5284.

Pulli, B., M. Ali, R. Forghani, S. Schob, K.L. Hsieh, G. Wojtkiewicz, J.J. Linnoila, and J.W. Chen. 2013. Measuring myeloperoxidase activity in biological samples. *PLoS One*. 8:e67976.

Pytela, R., and G. Wiche. 1980. High molecular weight polypeptides (270,000-340,000) from cultured cells are related to hog brain microtubule-associated proteins but copurify with intermediate filaments. *Proc Natl Acad Sci U S A*. 77:4808-4812.

Rajamaki, K., A. Taira, R. Katainen, N. Valimaki, A. Kuosmanen, R.M. Plaketti, T.T. Seppala, M. Ahtiainen, E.V. Wirta, E. Vartiainen, P. Sulo, J. Ravantti, S. Lehtipuro, K.J. Granberg, M. Nykter, T. Tanskanen, A. Ristimaki, S. Koskensalo, L. Renkonen-Sinisalo, A. Lepisto, J. Bohm, J. Taipale, J.P. Mecklin, M. Aavikko, K. Palin, and L.A. Aaltonen. 2021. Genetic and Epigenetic Characteristics of Inflammatory Bowel Disease-Associated Colorectal Cancer. *Gastroenterology*. 161:592-607.

Reitmair, A.H., J.C. Cai, M. Bjerknes, M. Redston, H. Cheng, M.T. Pind, K. Hay, A. Mitri, B.V. Bapat, T.W. Mak, and S. Gallinger. 1996. MSH2 deficiency contributes to accelerated APC-mediated intestinal tumorigenesis. *Cancer Res*. 56:2922-2926.

Reitmair, A.H., R. Schmits, A. Ewel, B. Bapat, M. Redston, A. Mitri, P. Waterhouse, H.W. Mittrucker, A. Wakeham, B. Liu, and et al. 1995. MSH2 deficient mice are viable and susceptible to lymphoid tumours. *Nat Genet*. 11:64-70.

Research, W.C.R.F.A.I.f.C. 2018. Diet, nutrition, physical activity and colorectal cancer: Continuous Update Project Expert Report. American Institute for Cancer Research.

Rezniczek, G.A., C. Abrahamsberg, P. Fuchs, D. Spazierer, and G. Wiche. 2003. Plectin 5'-transcript diversity: short alternative sequences determine stability of gene products, initiation of translation and subcellular localization of isoforms. *Hum Mol Genet*. 12:3181-3194.

Rezniczek, G.A., J.M. de Pereda, S. Reipert, and G. Wiche. 1998. Linking integrin alpha6beta4-based cell adhesion to the intermediate filament cytoskeleton: direct interaction between the beta4 subunit and plectin at multiple molecular sites. *J Cell Biol*. 141:209-225.

Ridley, A.J., M.A. Schwartz, K. Burridge, R.A. Firtel, M.H. Ginsberg, G. Borisy, J.T. Parsons, and A.R. Horwitz. 2003. Cell migration: integrating signals from front to back. *Science*. 302:1704-1709.

Robles, A.I., G. Traverso, M. Zhang, N.J. Roberts, M.A. Khan, C. Joseph, G.Y. Lauwers, F.M. Selaru, M. Popoli, M.E. Pittman, X. Ke, R.H. Hruban, S.J. Meltzer, K.W. Kinzler, B. Vogelstein, C.C. Harris, and N. Papadopoulos. 2016. Whole-Exome Sequencing Analyses of Inflammatory Bowel Disease-Associated Colorectal Cancers. *Gastroenterology*. 150:931-943.

Rodriguez, M.L., M. Brignoni, and P.J. Salas. 1994. A specifically apical sub-membrane intermediate filament cytoskeleton in non-brush-border epithelial cells. *J Cell Sci*. 107 (Pt 11):3145-3151.

Rogakou, E.P., D.R. Pilch, A.H. Orr, V.S. Ivanova, and W.M. Bonner. 1998. DNA double-stranded breaks induce histone H2AX phosphorylation on serine 139. *J Biol Chem*. 273:5858-5868.

Rothenberg, K.E., and R. Fernandez-Gonzalez. 2019. Forceful closure: cytoskeletal networks in embryonic wound repair. *Mol Biol Cell*. 30:1353-1358.

Ruhrberg, C., and F.M. Watt. 1997. The plakin family: versatile organizers of cytoskeletal architecture. *Curr Opin Genet Dev*. 7:392-397.

Salas, P.J., R. Forteza, and A. Mashukova. 2016. Multiple roles for keratin intermediate filaments in the regulation of epithelial barrier function and apico-basal polarity. *Tissue Barriers*. 4:e1178368.

Samak, G., K.K. Chaudhry, R. Gangwar, D. Narayanan, J.H. Jaggar, and R. Rao. 2015. Calcium/Ask1/MKK7/JNK2/c-Src signalling cascade mediates disruption of intestinal epithelial tight junctions by dextran sulfate sodium. *Biochem J*. 465:503-515.

Samuel, M.S., J.I. Lopez, E.J. McGhee, D.R. Croft, D. Strachan, P. Timpson, J. Munro, E. Schroder, J. Zhou, V.G. Brunton, N. Barker, H. Clevers, O.J. Sansom, K.I. Anderson, V.M. Weaver, and M.F. Olson. 2011. Actomyosin-mediated cellular tension drives increased tissue stiffness and beta-catenin activation to induce epidermal hyperplasia and tumor growth. *Cancer Cell*. 19:776-791.

Sartor, R.B. 1995. Current concepts of the etiology and pathogenesis of ulcerative colitis and Crohn's disease. *Gastroenterol Clin North Am*. 24:475-507.

Sartor, R.B. 2006. Mechanisms of disease: pathogenesis of Crohn's disease and ulcerative colitis. *Nat Clin Pract Gastroenterol Hepatol*. 3:390-407.

Satelli, A., and S. Li. 2011. Vimentin in cancer and its potential as a molecular target for cancer therapy. *Cell Mol Life Sci*. 68:3033-3046.

Sato, T., J.H. van Es, H.J. Snippert, D.E. Stange, R.G. Vries, M. van den Born, N. Barker, N.F. Shroyer, M. van de Wetering, and H. Clevers. 2011. Paneth cells constitute the niche for Lgr5 stem cells in intestinal crypts. *Nature*. 469:415-418.

Schindelin, J., I. Arganda-Carreras, E. Frise, V. Kaynig, M. Longair, T. Pietzsch, S. Preibisch, C. Rueden, S. Saalfeld, B. Schmid, J.Y. Tinevez, D.J. White, V. Hartenstein, K. Eliceiri, P. Tomancak, and A. Cardona. 2012. Fiji: an open-source platform for biological-image analysis. *Nat Methods*. 9:676-682.

Schlegel, N., K. Boerner, and J. Waschke. 2021. Targeting desmosomal adhesion and signalling for intestinal barrier stabilization in inflammatory bowel diseases-Lessons from experimental models and patients. *Acta Physiol (Oxf)*. 231:e13492.

Schmidt, A., M. Kaakinen, T. Wenta, and A. Manninen. 2022. Loss of alpha6beta4 Integrin-Mediated Hemidesmosomes Promotes Prostate Epithelial Cell Migration by Stimulating Focal Adhesion Dynamics. *Front Cell Dev Biol*. 10:886569.

Schmidt, C., and A. Stallmach. 2005. Etiology and pathogenesis of inflammatory bowel disease. *Minerva Gastroenterol Dietol*. 51:127-145.

Schmidt, W.M., M.H. Uddin, S. Dysek, K. Moser-Thier, C. Pirker, H. Hoger, I.M. Ambros, P.F. Ambros, W. Berger, and R.E. Bittner. 2011. DNA damage, somatic aneuploidy, and malignant sarcoma susceptibility in muscular dystrophies. *PLoS Genet*. 7:e1002042.

Schniers, A., R. Goll, Y. Pasing, S.W. Sorbye, J. Florholmen, and T. Hansen. 2019. Ulcerative colitis: functional analysis of the in-depth proteome. *Clin Proteomics*. 16:4.

Schweizer, J., L. Langbein, M.A. Rogers, and H. Winter. 2007. Hair follicle-specific keratins and their diseases. *Exp Cell Res*. 313:2010-2020.

Selinger, C.P., J.M. Andrews, A. Titman, I. Norton, D.B. Jones, C. McDonald, G. Barr, W. Selby, R.W. Leong, and I.B.D.C.S.G. Sydney. 2014. Long-term follow-up reveals low incidence of colorectal cancer, but frequent need for resection, among Australian patients with inflammatory bowel disease. *Clin Gastroenterol Hepatol*. 12:644-650.

Serres, M.P., M. Samwer, B.A. Truong Quang, G. Lavoie, U. Perera, D. Gorlich, G. Charras, M. Petronczki, P.P. Roux, and E.K. Paluch. 2020. F-Actin Interactome Reveals Vimentin as a Key Regulator of Actin Organization and Cell Mechanics in Mitosis. *Dev Cell*. 52:210-222 e217.

Sevcik, J., L. Urbanikova, J. Kost'an, L. Janda, and G. Wiche. 2004. Actin-binding domain of mouse plectin. Crystal structure and binding to vimentin. *Eur J Biochem*. 271:1873-1884.

Shah, P., C.M. Hobson, S. Cheng, M.J. Colville, M.J. Paszek, R. Superfine, and J. Lammerding. 2021. Nuclear Deformation Causes DNA Damage by Increasing Replication Stress. *Curr Biol*. 31:753-765 e756.

Shih, I.M., W. Zhou, S.N. Goodman, C. Lengauer, K.W. Kinzler, and B. Vogelstein. 2001. Evidence that genetic instability occurs at an early stage of colorectal tumorigenesis. *Cancer Res*. 61:818-822.

Shirai, T., M. Sano, S. Tamano, S. Takahashi, M. Hirose, M. Futakuchi, R. Hasegawa, K. Imaida, K. Matsumoto, K. Wakabayashi, T. Sugimura, and N. Ito. 1997. The prostate: a target for carcinogenicity of 2-amino-1-methyl-6-phenylimidazo[4,5-b]pyridine (PhIP) derived from cooked foods. *Cancer Res*. 57:195-198.

Shiu, J.Y., L. Aires, Z. Lin, and V. Vogel. 2018. Nanopillar force measurements reveal actin-cap-mediated YAP mechanotransduction. *Nat Cell Biol*. 20:262-271.

Silva, I., J. Solas, R. Pinto, and V. Mateus. 2022. Chronic Experimental Model of TNBS-Induced Colitis to Study Inflammatory Bowel Disease. *Int J Mol Sci*. 23.

Small, J.V., and A. Sobieszek. 1977. Studies on the function and composition of the 10-NM(100-A) filaments of vertebrate smooth muscle. *J Cell Sci*. 23:243-268.

Snoeck, V., B. Goddeeris, and E. Cox. 2005. The role of enterocytes in the intestinal barrier function and antigen uptake. *Microbes Infect*. 7:997-1004.

Sohn, O.S., E.S. Fiala, S.P. Requeijo, J.H. Weisburger, and F.J. Gonzalez. 2001. Differential effects of CYP2E1 status on the metabolic activation of the colon carcinogens azoxymethane and methylazoxymethanol. *Cancer Res*. 61:8435-8440.

Sonnenberg, A., A.M. Rojas, and J.M. de Pereda. 2007. The structure of a tandem pair of spectrin repeats of plectin reveals a modular organization of the plakin domain. *J Mol Biol*. 368:1379-1391.

Spagnol, S.T., and K.N. Dahl. 2016. Spatially Resolved Quantification of Chromatin Condensation through Differential Local Rheology in Cell Nuclei Fluorescence Lifetime Imaging. *PLoS One*. 11:e0146244.

Staszewska, I., I. Fischer, and G. Wiche. 2015. Plectin isoform 1-dependent nuclear docking of desmin networks affects myonuclear architecture and expression of mechanotransducers. *Hum Mol Genet*. 24:7373-7389.

Steiner-Champliaud, M.F., Y. Schneider, B. Favre, F. Paulhe, S. Praetzel-Wunder, G. Faulkner, P. Konieczny, M. Raith, G. Wiche, A. Adebola, R.K. Liem, L. Langbein, A. Sonnenberg, L. Fontao, and L. Borradori. 2010. BPAG1 isoform-b: complex distribution pattern in striated and heart muscle and association with plectin and alpha-actinin. *Exp Cell Res*. 316:297-313.

Stenling, R., J. Lindberg, J. Rutegard, and R. Palmqvist. 2007. Altered expression of CK7 and CK20 in preneoplastic and neoplastic lesions in ulcerative colitis. *APMIS*. 115:1219-1226.

Stenvall, C.A., J.H. Nystrom, C. Butler-Hallissey, T. Jansson, T.R.H. Heikkila, S.A. Adam, R. Foisner, R.D. Goldman, K.M. Ridge, and D.M. Toivola. 2022. Cytoplasmic keratins couple with and maintain nuclear envelope integrity in colonic epithelial cells. *Mol Biol Cell*. 33:ar121.

Stenvall, C.A., M. Tayyab, T.J. Gronroos, M.A. Ilomaki, K. Viiri, K.M. Ridge, L. Polari, and D.M. Toivola. 2021. Targeted deletion of keratin 8 in intestinal epithelial cells disrupts tissue integrity and predisposes to tumorigenesis in the colon. *Cell Mol Life Sci*. 79:10.

Stephens, A.D., E.J. Banigan, S.A. Adam, R.D. Goldman, and J.F. Marko. 2017. Chromatin and lamin A determine two different mechanical response regimes of the cell nucleus. *Mol Biol Cell*. 28:1984-1996.

Stooke-Vaughan, G.A., and O. Campas. 2018. Physical control of tissue morphogenesis across scales. *Curr Opin Genet Dev*. 51:111-119.

Strouhalova, K., M. Prechova, A. Gandalovicova, J. Brabek, M. Gregor, and D. Rosel. 2020. Vimentin Intermediate Filaments as Potential Target for Cancer Treatment. *Cancers (Basel)*. 12.

Sturlan, S., G. Oberhuber, B.G. Beinhauer, B. Tichy, S. Kappel, J. Wang, and M.A. Rogy. 2001. Interleukin-10-deficient mice and inflammatory bowel disease associated cancer development. *Carcinogenesis*. 22:665-671.

Sung, H., J. Ferlay, R.L. Siegel, M. Laversanne, I. Soerjomataram, A. Jemal, and F. Bray. 2021. Global Cancer Statistics 2020: GLOBOCAN Estimates of Incidence and Mortality Worldwide for 36 Cancers in 185 Countries. *CA Cancer J Clin*. 71:209-249.

Suzuki, T. 2013. Regulation of intestinal epithelial permeability by tight junctions. *Cell Mol Life Sci*. 70:631-659.

Svec, J., M. Stastna, L. Janeckova, D. Hrckulak, M. Vojtechova, J. Onhajzer, V. Kriz, K. Galuskova, E. Sloncova, J. Kubovciak, L. Pfeiferova, J. Hrudka, R. Matej, P. Waldauf, L. Havluj, M. Kolar, and V. Korinek. 2022. TROP2 Represents a Negative Prognostic Factor in Colorectal Adenocarcinoma and Its Expression Is Associated with Features of Epithelial-Mesenchymal Transition and Invasiveness. *Cancers (Basel)*. 14.

Szeverenyi, I., A.J. Cassidy, C.W. Chung, B.T. Lee, J.E. Common, S.C. Ogg, H. Chen, S.Y. Sim, W.L. Goh, K.W. Ng, J.A. Simpson, L.L. Chee, G.H. Eng, B. Li, D.P. Lunny, D. Chuon, A. Venkatesh, K.H. Khoo, W.H. McLean, Y.P. Lim, and E.B. Lane. 2008. The Human Intermediate Filament Database: comprehensive information on a gene family involved in many human diseases. *Hum Mutat*. 29:351-360.

Takeda, N., R. Jain, M.R. LeBoeuf, Q. Wang, M.M. Lu, and J.A. Epstein. 2011. Interconversion between intestinal stem cell populations in distinct niches. *Science*. 334:1420-1424.

Talwar, S., N. Jain, and G.V. Shivashankar. 2014. The regulation of gene expression during onset of differentiation by nuclear mechanical heterogeneity. *Biomaterials*. 35:2411-2419.

Taman, H., C.G. Fenton, I.V. Hensel, E. Anderssen, J. Florholmen, and R.H. Paulssen. 2018. Transcriptomic Landscape of Treatment-Naive Ulcerative Colitis. *J Crohns Colitis*. 12:327-336.

Tao, G.Z., K.S. Looi, D.M. Toivola, P. Strnad, Q. Zhou, J. Liao, Y. Wei, A. Habtezion, and M.B. Omary. 2009. Keratins modulate the shape and function of hepatocyte mitochondria: a mechanism for protection from apoptosis. *J Cell Sci*. 122:3851-3855.

Tao, G.Z., P. Strnad, Q. Zhou, A. Kamal, L. Zhang, N.D. Madani, S. Kugathasan, S.R. Brant, J.H. Cho, M.B. Omary, and R.H. Duerr. 2007. Analysis of keratin polypeptides 8 and 19 variants in inflammatory bowel disease. *Clin Gastroenterol Hepatol*. 5:857-864.

Thebaut, A., M. Aumar, A. Gardin, M. Almes, A. Davit-Spraul, and E. Jacquemin. 2024. Failure of cholic acid therapy in a child with a bile acid synthesis defect and harboring plectin mutations. *J Pediatr Gastroenterol Nutr*. 78:1203-1204.

Tijore, A., M. Yao, Y.H. Wang, A. Hariharan, Y. Nematbakhsh, B. Lee Doss, C.T. Lim, and M. Sheetz. 2021. Selective killing of transformed cells by mechanical stretch. *Biomaterials*. 275:120866.

Tiwari, V., and D.M. Wilson, 3rd. 2019. DNA Damage and Associated DNA Repair Defects in Disease and Premature Aging. *Am J Hum Genet*. 105:237-257.

Toivola, D.M., S. Krishnan, H.J. Binder, S.K. Singh, and M.B. Omary. 2004. Keratins modulate colonocyte electrolyte transport via protein mistargeting. *J Cell Biol*. 164:911-921.

Toivola, D.M., Q. Zhou, L.S. English, and M.B. Omary. 2002. Type II keratins are phosphorylated on a unique motif during stress and mitosis in tissues and cultured cells. *Mol Biol Cell*. 13:1857-1870.

Tsuruta, D., T. Hashimoto, K.J. Hamill, and J.C. Jones. 2011. Hemidesmosomes and focal contact proteins: functions and cross-talk in keratinocytes, bullous diseases and wound healing. *J Dermatol Sci*. 62:1-7.

Uitto, J., L. Bruckner-Tuderman, J.A. McGrath, R. Riedl, and C. Robinson. 2018. EB2017-Progress in Epidermolysis Bullosa Research toward Treatment and Cure. *J Invest Dermatol*. 138:1010-1016.

Vahidnezhad, H., L. Youssefian, N. Harvey, A.R. Tavasoli, A.H. Saeidian, S. Sotoudeh, A. Varghaei, H. Mahmoudi, P. Mansouri, N. Mozafari, O. Zargari, S. Zeinali, and J. Uitto. 2022. Mutation update: The spectra of PLEC sequence variants and related plectinopathies. *Hum Mutat*. 43:1706-1731.

van Steensel, B., and A.S. Belmont. 2017. Lamina-Associated Domains: Links with Chromosome Architecture, Heterochromatin, and Gene Repression. *Cell*. 169:780-791.

Verma, K.P., S.J. Robertson, and I.M. Winship. 2020. Phenotypic discordance between siblings with junctional epidermolysis bullosa-pyloric atresia. *Clin Exp Dermatol*. 45:793-795.

Viedma-Poyatos, A., M.A. Pajares, and D. Perez-Sala. 2020. Type III intermediate filaments as targets and effectors of electrophiles and oxidants. *Redox Biol*. 36:101582.

Vivinus-Nebot, M., G. Frin-Mathy, H. Bzioueche, R. Dainese, G. Bernard, R. Anty, J. Filippi, M.C. Saint-Paul, M.K. Tulic, V. Verhasselt, X. Hebuterne, and T. Piche. 2014. Functional bowel symptoms

in quiescent inflammatory bowel diseases: role of epithelial barrier disruption and low-grade inflammation. *Gut*. 63:744-752.

Walko, G., M.J. Castanon, and G. Wiche. 2015. Molecular architecture and function of the hemidesmosome. *Cell Tissue Res*. 360:363-378.

Walko, G., N. Vukasinovic, K. Gross, I. Fischer, S. Sibitz, P. Fuchs, S. Reipert, U. Jungwirth, W. Berger, U. Salzer, O. Carugo, M.J. Castanon, and G. Wiche. 2011. Targeted proteolysis of plectin isoform 1a accounts for hemidesmosome dysfunction in mice mimicking the dominant skin blistering disease EBS-Ogna. *PLoS Genet*. 7:e1002396.

Walter, M.C., P. Reilich, S. Krause, M. Hiebeler, S. Gehling, H.H. Goebel, B. Schoser, and A. Abicht. 2021. Congenital myopathy and epidermolysis bullosa due to PLEC variant. *Neuromuscul Disord*. 31:1212-1217.

Wanders, L.K., M. Cordes, Q. Voorham, D. Sie, S.D. de Vries, G. d'Haens, N.K.H. de Boer, B. Ylstra, N.C.T. van Grieken, G.A. Meijer, E. Dekker, and B. Carvalho. 2020. IBD-Associated Dysplastic Lesions Show More Chromosomal Instability Than Sporadic Adenomas. *Inflamm Bowel Dis*. 26:167-180.

Wang, J.H., P. Goldschmidt-Clermont, J. Wille, and F.C. Yin. 2001. Specificity of endothelial cell reorientation in response to cyclic mechanical stretching. *J Biomech*. 34:1563-1572.

Wang, L., S. Srinivasan, A.L. Theiss, D. Merlin, and S.V. Sitaraman. 2007a. Interleukin-6 induces keratin expression in intestinal epithelial cells: potential role of keratin-8 in interleukin-6-induced barrier function alterations. *J Biol Chem*. 282:8219-8227.

Wang, Q., G.M. Garrity, J.M. Tiedje, and J.R. Cole. 2007b. Naive Bayesian classifier for rapid assignment of rRNA sequences into the new bacterial taxonomy. *Appl Environ Microbiol*. 73:5261-5267.

Wang, W., A. Zuidema, L. Te Molder, L. Nahidiazar, L. Hoekman, T. Schmidt, S. Coppola, and A. Sonnenberg. 2020. Hemidesmosomes modulate force generation via focal adhesions. *J Cell Biol*. 219.

Wang, X., Q. Ouyang, and W.J. Luo. 2004. Oxazolone-induced murine model of ulcerative colitis. *Chin J Dig Dis*. 5:165-168.

Watson, A.J., and K.R. Hughes. 2012. TNF-alpha-induced intestinal epithelial cell shedding: implications for intestinal barrier function. *Ann N Y Acad Sci*. 1258:1-8.

Weber, C.R., D.R. Raleigh, L. Su, L. Shen, E.A. Sullivan, Y. Wang, and J.R. Turner. 2010. Epithelial myosin light chain kinase activation induces mucosal interleukin-13 expression to alter tight junction ion selectivity. *J Biol Chem*. 285:12037-12046.

Wehkamp, J., H. Chu, B. Shen, R.W. Feathers, R.J. Kays, S.K. Lee, and C.L. Bevins. 2006. Paneth cell antimicrobial peptides: topographical distribution and quantification in human gastrointestinal tissues. *FEBS Lett*. 580:5344-5350.

Wenta, T., A. Schmidt, Q. Zhang, R. Devarajan, P. Singh, X. Yang, A. Ahtikoski, M. Vaarala, G.H. Wei, and A. Manninen. 2022. Disassembly of alpha6beta4-mediated hemidesmosomal adhesions promotes tumorigenesis in PTEN-negative prostate cancer by targeting plectin to focal adhesions. *Oncogene*. 41:3804-3820.

Wiche, G. 2021. Plectin-Mediated Intermediate Filament Functions: Why Isoforms Matter. *Cells*. 10.

Wiche, G., B. Becker, K. Luber, G. Weitzer, M.J. Castanon, R. Hauptmann, C. Stratowa, and M. Stewart. 1991. Cloning and sequencing of rat plectin indicates a 466-kD polypeptide chain with a three-domain structure based on a central alpha-helical coiled coil. *J Cell Biol*. 114:83-99.

Wilen, C.B., S. Lee, L.L. Hsieh, R.C. Orchard, C. Desai, B.L. Hykes, Jr., M.R. McAllaster, D.R. Balce, T. Feehley, J.R. Brestoff, C.A. Hickey, C.C. Yokoyama, Y.T. Wang, D.A. MacDuff, D. Kreamalmayer, M.R. Howitt, J.A. Neil, K. Cadwell, P.M. Allen, S.A. Handley, M. van Lookeren Campagne, M.T. Baldridge, and H.W. Virgin. 2018. Tropism for tuft cells determines immune promotion of norovirus pathogenesis. *Science*. 360:204-208.

Wilhelmsen, K., S.H. Litjens, I. Kuikman, N. Tshimbalanga, H. Janssen, I. van den Bout, K. Raymond, and A. Sonnenberg. 2005. Nesprin-3, a novel outer nuclear membrane protein, associates with the cytoskeletal linker protein plectin. *J Cell Biol*. 171:799-810.

Wilson, C.L., A.J. Ouellette, D.P. Satchell, T. Ayabe, Y.S. Lopez-Boado, J.L. Stratman, S.J. Hultgren, L.M. Matrisian, and W.C. Parks. 1999. Regulation of intestinal alpha-defensin activation by the metalloproteinase matrilysin in innate host defense. *Science*. 286:113-117.

Worthington, J.J., F. Reimann, and F.M. Gribble. 2018. Enteroendocrine cells-sensory sentinels of the intestinal environment and orchestrators of mucosal immunity. *Mucosal Immunol*. 11:3-20.

Wu, C. 2007. Focal adhesion: a focal point in current cell biology and molecular medicine. *Cell Adh Migr*. 1:13-18.

Wu, S.H., J.S. Hsu, H.L. Chen, M.M. Chien, J.F. Wu, Y.H. Ni, B.Y. Liou, M.C. Ho, Y.M. Jeng, M.H. Chang, P.L. Chen, and H.L. Chen. 2019. Plectin Mutations in Progressive Familial Intrahepatic Cholestasis. *Hepatology*. 70:2221-2224.

Xia, Y., C.R. Pfeifer, K. Zhu, J. Irianto, D. Liu, K. Pannell, E.J. Chen, L.J. Dooling, M.P. Tobin, M. Wang, I.L. Ivanovska, L.R. Smith, R.A. Greenberg, and D.E. Discher. 2019. Rescue of DNA damage after constricted migration reveals a mechano-regulated threshold for cell cycle. *J Cell Biol*. 218:2545-2563.

Xiong, Z., X. Zhu, J. Geng, Y. Xu, R. Wu, C. Li, D. Fan, X. Qin, Y. Du, Y. Tian, and Z. Fan. 2022. Intestinal Tuft-2 cells exert antimicrobial immunity via sensing bacterial metabolite N-undecanoylglycine. *Immunity*. 55:686-700 e687.

Yaeger, R., M.A. Shah, V.A. Miller, J.R. Kelsen, K. Wang, Z.J. Heins, J.S. Ross, Y. He, E. Sanford, R.K. Yantiss, S. Balasubramanian, P.J. Stephens, N. Schultz, M. Oren, L. Tang, and D. Kelsen. 2016. Genomic Alterations Observed in Colitis-Associated Cancers Are Distinct From Those Found in Sporadic Colorectal Cancers and Vary by Type of Inflammatory Bowel Disease. *Gastroenterology*. 151:278-287 e276.

Yamashiro, Y., B.Q. Thang, K. Ramirez, S.J. Shin, T. Kohata, S. Ohata, T.A.V. Nguyen, S. Ohtsuki, K. Nagayama, and H. Yanagisawa. 2020. Matrix mechanotransduction mediated by thrombospondin-1/integrin/YAP in the vascular remodeling. *Proc Natl Acad Sci U S A*. 117:9896-9905.

Yan, K.S., L.A. Chia, X. Li, A. Ootani, J. Su, J.Y. Lee, N. Su, Y. Luo, S.C. Heilshorn, M.R. Amieva, E. Sangiorgi, M.R. Capecchi, and C.J. Kuo. 2012. The intestinal stem cell markers Bmi1 and Lgr5 identify two functionally distinct populations. *Proc Natl Acad Sci U S A*. 109:466-471.

Yokochi, T., K. Poduch, T. Ryba, J. Lu, I. Hiratani, M. Tachibana, Y. Shinkai, and D.M. Gilbert. 2009. G9a selectively represses a class of late-replicating genes at the nuclear periphery. *Proc Natl Acad Sci U S A*. 106:19363-19368.

Yonemura, S., Y. Wada, T. Watanabe, A. Nagafuchi, and M. Shibata. 2010. alpha-Catenin as a tension transducer that induces adherens junction development. *Nat Cell Biol*. 12:533-542.

Yu, Y., W. Yang, Y. Li, and Y. Cong. 2020. Enteroendocrine Cells: Sensing Gut Microbiota and Regulating Inflammatory Bowel Diseases. *Inflamm Bowel Dis*. 26:11-20.

Yuan, A., M.V. Rao, T. Sasaki, Y. Chen, A. Kumar, Veeranna, R.K. Liem, J. Eyer, A.C. Peterson, J.P. Julien, and R.A. Nixon. 2006. Alpha-internexin is structurally and functionally associated with the neurofilament triplet proteins in the mature CNS. *J Neurosci*. 26:10006-10019.

Yuan, C., M. Graham, C. Staley, and S. Subramanian. 2020. Mucosal Microbiota and Metabolome along the Intestinal Tract Reveal a Location-Specific Relationship. *mSystems*. 5.

Yui, S., L. Azzolin, M. Maimets, M.T. Pedersen, R.P. Fordham, S.L. Hansen, H.L. Larsen, J. Guiu, M.R.P. Alves, C.F. Rundsten, J.V. Johansen, Y. Li, C.D. Madsen, T. Nakamura, M. Watanabe, O.H. Nielsen, P.J. Schweiger, S. Piccolo, and K.B. Jensen. 2018. YAP/TAZ-Dependent Reprogramming of Colonic Epithelium Links ECM Remodeling to Tissue Regeneration. *Cell Stem Cell*. 22:35-49 e37.

Yun, K., A.E. Merrie, J. Gunn, L.V. Phillips, and J.L. McCall. 2000. Keratin 20 is a specific marker of submicroscopic lymph node metastases in colorectal cancer: validation by K-RAS mutations. *J Pathol*. 191:21-26.

Zbar, A.P., C. Simopoulos, and A.J. Karayiannakis. 2004. Cadherins: an integral role in inflammatory bowel disease and mucosal restitution. *J Gastroenterol*. 39:413-421.

Zhang, Y., and M. Jasin. 2011. An essential role for CtIP in chromosomal translocation formation through an alternative end-joining pathway. *Nat Struct Mol Biol*. 18:80-84.

Zhao, X.H., C. Laschinger, P. Arora, K. Szaszi, A. Kapus, and C.A. McCulloch. 2007. Force activates smooth muscle alpha-actin promoter activity through the Rho signaling pathway. *J Cell Sci*. 120:1801-1809.

Zhong, B., Q. Zhou, D.M. Toivola, G.Z. Tao, E.Z. Resurreccion, and M.B. Omary. 2004. Organ-specific stress induces mouse pancreatic keratin overexpression in association with NF-kappaB activation. *J Cell Sci*. 117:1709-1719.

Zhou, J., W. Zhang, W. Liu, J. Sheng, M. Li, X. Chen, and R. Dong. 2020. Histological study of intestinal goblet cells, IgA, and CD3+ lymphocyte distribution in Huang-huai white goat. *Folia Morphol (Warsz)*. 79:303-310.

Zihni, C., C. Mills, K. Matter, and M.S. Balda. 2016. Tight junctions: from simple barriers to multifunctional molecular gates. *Nat Rev Mol Cell Biol*. 17:564-580.

Zink, D., A.H. Fischer, and J.A. Nickerson. 2004. Nuclear structure in cancer cells. *Nat Rev Cancer*. 4:677-687.

8 Publications

This thesis is mainly based on the following publications:

Plectin ensures intestinal epithelial integrity and protects colon against colitis

Alzbeta Krausova*, Petra Buresova*, Lenka Sarnova, Gizem Oyman-Eyrilmez, Jozef Skarda, Pavel Wohl, Lukas Bajer, Eva Sticova, Lenka Bartonova, Jiri Pacha, Gizela Koubkova, Jan Prochazka, Marina Spörrer, Christopher Dürrbeck, Zuzana Stehlikova, Martin Vit, Natalia Ziolkowska, Radislav Sedlacek, Daniel Jirak, Miloslav Kverka, Gerhard Wiche, Ben Fabry, Vladimir Korinek & Martin Gregor

*These authors contributed equally: Alzbeta Krausova, Petra Buresova.

Mucosal Immunol **14**, 691–702 (2021). DOI: 10.1038/s41385-021-00380-z.

Petra Buresova (Novotna) conducted the following experiments: DSS-induced colitis and DAI scoring, depletion of gut microbiota by ATB treatment, liquid diet feeding, histology of mice and patient samples (H&E, SR, Alcian Blue, PAS staining), IHC and immunofluorescence (samples from mouse models), protein extraction and immunoblotting, cell stretching, radial shear assay, magnetic tweezer microrheology, high salt extraction of Caco-2 cells, histological and morphometric analyses, image acquisition and processing, statistics evaluation.

Plectin in Colorectal Carcinoma: Mechanical Stress Drives DNA Damage and Carcinogenesis

Miloslava Maninova*, Petra Novotna*, Lenka Sarnova, Vera Getmanchuk-Zaporoshchenko, Magdalena Prechova, Jakub Gemperle, Tomas Venit, Jozef Skarda, Jiri Novotny, Ronja M. Houtekamer, Libor Macurek, Samuel M Meier, Vladimir Korinek, Ben Fabry, Michal Kolar, Piergiorgio Percipalle, Gerhard Wiche, Martijn Gloerich, Alzbeta Krausova, Martin Gregor

*These authors contributed equally: Petra Novotna, Miloslava Maninova.

Manuscript in preparation

Petra Novotna conducted the following experiments: cells and CRISPR-mediated targeting of plectin, AOM-induced sporadic CRC, AOM/DSS-induced CA-CRC, depletion of gut microbiota by ATB treatment, histology of mice (H&E), IHC and immunofluorescence (samples from mouse models), protein extraction and immunoblotting, qRT-PCR, cell stretching (CEC, 2D organoids, last biological replicate of RPE monolayers for analysis of nuclear envelope

wrinkles), cell confinement (RPE cells), CEC and organoid experiments, DSB repair assay (exposure of Caco-2 and RPE cells to irradiation), histological and morphometric analyses (samples from mouse models, Ferret's diameter and cell body measurement of Caco-2 cells), image acquisition and processing, statistics evaluation.

Limited Validity of Mayo Endoscopic Subscore in Ulcerative Colitis with Concomitant Primary Sclerosing Cholangitis

Pavel Wohl, Alzbeta Krausova, Petr Wohl, Ondrej Fabian, Lukas Bajer, Jan Brezina, Pavel Drastich, Mojmír Hlavaty, Petra Novotna, Michal Kahle, Julius Spicak, Martin Gregor

medRxiv **2024**, 2024.2004.2008.24305005. DOI: 10.1101/2024.04.08.24305005.

Petra Novotna conducted the following experiments: data analysis.

Plectin-mediated cytoskeletal cross-talk as a target for inhibition of hepatocellular carcinoma growth and metastasis

Zuzana Outla, Gizem Oyman-Eyrilmez, Katerina Korelova, Magdalena Prechova, Lukas Frick, Lenka Sarnova, Piyush Bisht, Petra Novotna, Jan Kosla, Patricia Bortel, Yasmin Borutzki, Andrea Bileck, Christopher Gerner, Mohammad Rahbari, Nuh Rahbari, Emrullah Birgin, Bibiana Kvasnicova, Martin Vit, Natalia Ziolkowska, Katerina Sulkova, Andreas Bauer, Eva Sticova, Marketa Jirouskova, Ben Fabry, Martin Otahal, Daniel Jirak, Mathias Heikenwälder, Gerhard Wiche, Samuel M Meier-Menches, Martin Gregor

Manuscript in preparation

Petra Novotna conducted the following experiments: technical and material support.